Graduate Aeronautical Laboratories

California Institute of Technology

Chemical Reactions in Turbulent Mixing Flows

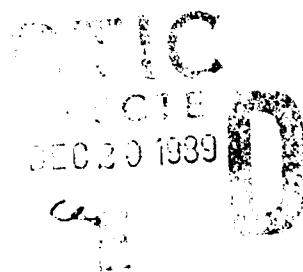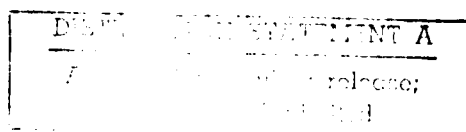Paul E. Dimotakis[*], James E. Broadwell[**] and Anthony Leonard[†]

15 October 1989

Firestone Flight Sciences Laboratory

Guggenheim Aeronautical Laboratory

Karman Laboratory of Fluid Mechanics and Jet Propulsion

Pasadena

REPORT DOCUMENTATION PAGE

Form Approved
OMB No. 0704-0188

1a. REPORT SECURITY CLASSIFICATION	1b RESTRICTIVE MARKINGS
Unclassified	

2a. SECURITY CLASSIFICATION AUTHORITY	3. DISTRIBUTION / AVAILABILITY OF REPORT
	Approved for public release;
2b. DECLASSIFICATION / DOWNGRADING SCHEDULE	distribution is unlimited.

4. PERFORMING ORGANIZATION REPORT NUMBER(S)	5. MONITORING ORGANIZATION REPORT NUMBER(S)
	AFOSR·TR· 89-1690

6a. NAME OF PERFORMING ORGANIZATION	6b. OFFICE SYMBOL (If applicable)	7a. NAME OF MONITORING ORGANIZATION
California Institute of Technology		AFOSR/NA

6c. ADDRESS (City, State, and ZIP Code)	7b. ADDRESS (City, State, and ZIP Code)
Graduate Aeronautical Laboratories Mail Stop 301-46 Pasadena, CA 91125	Building 410, Bolling AFB DC 20332-6448

8a. NAME OF FUNDING / SPONSORING ORGANIZATION	8b. OFFICE SYMBOL (If applicable)	9 PROCUREMENT INSTRUMENT IDENTIFICATION NUMBER
AFOSR/NA		AFOSR-88-0155

8c. ADDRESS (City, State, and ZIP Code)	10. SOURCE OF FUNDING NUMBERS			
Building 410, Bolling AFB DC 20332-6448	PROGRAM ELEMENT NO.	PROJECT NO.	TASK NO	WORK UNIT ACCESSION NO.
	61102F	2308	A2	

11. TITLE (Include Security Classification)

(U)Chemical Reactions in Turbulent Mixing Flows

12. PERSONAL AUTHOR(S)
Paul E. Dimotakis, James E. Broadwell and Anthony Leonard

13a. TYPE OF REPORT	13b. TIME COVERED	14. DATE OF REPORT (Year, Month, Day)	15. PAGE COUNT
Annual	FROM 16Apr88 TO 15Apr89	15 October 1989	140

16. SUPPLEMENTARY NOTATION

17. COSATI CODES			18. SUBJECT TERMS (Continue on reverse if necessary and identify by block number)
FIELD	GROUP	SUB-GROUP	Turbulence, shear layers, jets, mixing, combustion, numerical simulation, light detection diagnostics
21	01		
21	02		

19. ABSTRACT (Continue on reverse if necessary and identify by block number)

The purpose of this research has been to conduct fundamental investigations of turbulent mixing chemical reactions and combustion processes in turbulent, subsonic and supersonic flows. This program is comprised of several efforts. In particular, an experimental effort, an analytical effort, a modeling effort, a computational effort and a diagnostics development and data-acquisition effort -- the latter as dictated by specific needs of the experimental part of the overall program.

Our approach has been to carry out a series of detailed theoretical and experimental studies primarily in two well-defined, fundamentally important flow fields: Free shear layers and axisymmetric jets. To elucidate molecular transport effects, experiments and theory concern themselves with both liquids and gases. Modeling efforts have been focused on both shear layers and turbulent jets with an effort to include the physics of the molecular transport processes, as well as formulations of models that permit the full chemical kinetics of the combustion process to be incorporated. Our recent analytical efforts have concentrated on a

20. DISTRIBUTION / AVAILABILITY OF ABSTRACT	21. ABSTRACT SECURITY CLASSIFICATION
☒ UNCLASSIFIED/UNLIMITED ☒ SAME AS RPT ☒ DTIC USERS	Unclassified

22a. NAME OF RESPONSIBLE INDIVIDUAL	22b. TELEPHONE (Include Area Code)	22c. OFFICE SYMBOL
Julian M Tishkoff	(202) 767-	AFOSR/NA

DD Form 1473, JUN 86   Previous editions are obsolete.   SECURITY CLASSIFICATION OF THIS PAGE

19. (continued)
hydrodynamic analysis of the stability of compressible shear layers. The computational
studies are, at present, focused at fundamental issues pertaining to the computational
simulation of both compressible and incompressible flows./ /

B

GRADUATE AERONAUTICAL LABORATORIES
CALIFORNIA INSTITUTE of TECHNOLOGY
Pasadena, California 91125

Chemical Reactions in Turbulent Mixing Flows

Paul E. Dimotakis*, James E. Broadwell** and Anthony Leonard[†]

15 October 1989

---

* Professor, Aeronautics & Applied Physics.

** Senior Scientist, Aeronautics.

† Professor, Aeronautics.

Abstract

The purpose of this research has been to conduct fundamental investigations of turbulent mixing, chemical reaction and combustion processes in turbulent. subsonic and supersonic flows. This program is comprised of several efforts. In particular,

    a. an experimental effort,

    b. an analytical effort.

    c. a modeling effort,

    d. a computational effort.

and

    e. a diagnostics development and data-acquisition effort,

the latter as dictated by specific needs of the experimental part of the overall program.

Our approach has been to carry out a series of detailed theoretical and experimental studies primarily in two well-defined. fundamentally important flow fields: free shear layers and axisymmetric jets. To elucidate molecular transport effects, experiments and theory concern themselves with both liquids and gases. Modeling efforts have been focused on both shear layers and turbulent jets, with an effort to include the physics of the molecular transport processes, as well as formulations of models that permit the full chemical kinetics of the combustion process to be incorporated. Our recent analytical efforts have concentrated on a hydrodynamic analysis of the stability of compressible shear layers. The computational studies are, at present, focused at fundamental issues pertaining to the computational simulation of both compressible and incompressible flows.

1. Introduction

Progress in the effort under the sponsorship of this Grant, for the period ending 15 April 1989, has been realized in several areas. In particular,

    a. in chemically reacting, gas phase, subsonic shear layers with unequal free stream densities;

    b. in the investigations of turbulent jets[‡], namely

        1. investigations of gas phase, chemically reacting jets;

        2. liquid phase jet mixing and interface topology studies;

        3. the development of jet mixing models that permit the inclusion of full chemical kinetics calculations;

    c. supersonic shear layers, namely:

        1. hydrodynamic linear stability analysis of homogeneous compressible free (unbounded) and confined shear layers;

    and

        2. the design and fabrication of the supersonic shear layer combustion facility.

    d. in the computational effort:

        1. the development of lagrangian computational methods for compressible, unsteady flows;

    and

        2. the development of efficient algorithms for vortex dynamics calculations.

Finally, in our diagnostics effort,

    e. we have taken the opportunity to document some of our progress in the measurement and processing of low intensity signals, derived from laser scattering experiments.

These will be discussed below.

[‡] The investigations of turbulent mixing and combustion in turbulent jets are co-sponsored by the Gas Research Institute.

2. Mixing and combustion in turbulent shear layers

An extended review of shear layer mixing and combustion, including issues that are likely to prove important in the context of compressible shear layers and which we will specifically address in the upcoming research, was presented at the 27th *AIAA Aerospace Sciences Meeting (Reno, Nevada)*, 9–12 January 1989), and again, with several extensions, at the 9th *International Symposium on Air Breathing Engines (Athens, Greece)*, 3–9 September 1989 (Dimotakis 1989). A copy is included in this report as Appendix A.

2.1 Heat release effects

The archival documentation of the work on heat release effects, undertaken under the sponsorship of this Program, as part of the Ph.D. research effort of Dr. J. C. Hermanson, is included in this report as Appendix B.

2.2 Free stream density ratio effects

A Ph. D. thesis documenting this part of the effort in subsonic shear layer ming and combustion, as well as other related work, is presently being prepared by Mr. C. E. Frieler.

2.3 Supersonic shear layer combustion facility

The preponderant fraction of the effort in this part of the program has been directed towards bringing the new supersonic shear layer facility on line. The previous version (3.0) of the Design Review Report (Hall, Dimotakis, Papamoschou & Frieler 1988) has been updated (Hall & Dimotakis 1989). It includes engineering drawings and summarizes the design and some of the fabrication details of the facility. It is presently on file at the GALCIT library. Copies are available from P. E. Dimotakis on application.

At this writing, the development of the algorithm for the on-line feedback control of the rotary throttling valve is in progress. It is being tested using a reduced sonic throat area* for the plenum nozzle to conserve gas during the development phase.

The control strategy is based on a program control part, which initiates the flow and compensates for the drop in the tank pressure in the course of the run, and a feedback control part, which maintains the plenum pressure to the requisite tolerances and uses a system model based on a linearization of the system response, following the program control actuation.

---

* $3\,in^2$ *vs.* roughly the $8\,in^2$ required for the $M_1 = 1.5$ (high speed stream Mach number) flow planned for the first set of runs.

This effort is part of the Ph.D. research of Mr. Jeffery Hall, with the participation of Dr. Henning Rosemann, who has recently joined the program as a Post Doctoral Research Fellow in Aeronautics.

2.4 Hydrodynamic instability of compressible shear layers

The instability behavior of both free and confined compressible plane mixing layers with respect to two-dimensional, spatially growing wave disturbances are investigated using linear stability analysis. Studies were made for the case of inviscid flow under the assumptions that the main flow can be treated as parallel, that the gases in the two parallel streams are non-reactive, non-heat-conducting and that the molecular diffusion processes of the flows are neglected. The disturbances in the flows are taken as of small amplitudes. The effect of

a. the free stream Mach number,

b. the velocity ratio,

c. the gas constant (molecular weight) ratio,

d. temperature ratio and temperature profile

and

e. the ratio of the specific heats

on the linear spatial instability characteristics of a plane mixing layer were determined. The effect of the convective Mach number, which has been suggested by Bogdanoff (1983) and by Papamoschou & Roshko (1988) as the compressibility-effect parameter, on the growth rate of the mixing layers was studied.

In a finite thickness mixing layer, all *mean* quantities, such as the velocity, density, temperature, gas constants, concentration and the ratio of the specific heats, vary gradually across the mixing layer. To carry out the numerical calculations, we took the mean velocity profile of the mixing layer to be a hyperbolic tangent profile. The mean temperature distribution was obtained using both the Crocco-Busemann relation and a hyperbolic tangent profile. The concentration profile of the mixing layer was also assumed to be a hyperbolic tangent. The range of the unstable frequencies and wave numbers were numerically calculated using a Runge-Kutta method combined with a shooting technique.

For a free mixing layer with subsonic convective Mach numbers, there is only one unstable mode propagating with the phase velocity C_p, approximately equal to the convective velocity of the large scale structures U_c. As the convective Mach number approaches or exceeds unity, there are always two unstable modes. One is with a phase velocity $C_p < U_c$ and the other is with a phase velocity $C_p > U_c$. As we increase the convective Mach number, the phase velocities of the two unstable modes will further decrease or increase. A nearly universal dependence of the normalized maximum amplification rate on the convective Mach number was found. This amplification rate decreases significantly with increasing convective Mach number in the subsonic region and goes to zero as the convective Mach

number M_{c1} or $M_{c2} \gg 1$. Some of this work was documented in a paper presented at the 1st *National Fluid Dynamic Congress* (Zhuang, Kubota & Dimotakis 1988) and, with some minor revisions and extensions, has since been accepted by the *AIAA J.* for publication. A copy of the revised paper (Zhuang, Kubota & Dimotakis 1989), as submitted to the *AIAA J.* is included as Appendix C. It was also found that decreasing the thickness of the total temperature profile relative to the velocity profile or that adding a wake component in the velocity profile can make this normalized amplification rate decrease slower for subsonic convective Mach numbers and approach an asymptotic value for supersonic convective Mach numbers.

For a mixing layer inside parallel flow guide walls, the effect of walls on a spatially growing shear layer was also investigated. It was shown that, in this case, if the convective Mach number exceeds the critical value, which is about 1, there are many unstable modes. The effort is continuing with calculations of the instability characteristics of the unstable modes, the contour plots of the pressure perturbation fields and the streaklines of the flows. It should be noted that this, more recent, part of the work has suggested some strategies for flow control that would only be realizable under supersonic flow conditions. No documentation of this part of the effort is, as yet, available.

This effort is part of the Ph.D. research of Ms. Mei Zhuang, which is performed in collaboration with Prof. Toshi Kubota of GALCIT.

3. Mixing and combustion in turbulent jets

The part of the research effort dealing with mixing, chemical reactions and combustion in turbulent jets is co-sponsored by the Gas Research Institute[**].

3.1 High Pressure jet Combustion Facility

The first preliminary experiments in this facility are under way. These are focused on investigating the dependence of turbulent jet flame length on the flow Reynolds number. The diagnostics utilized in these experiments are designed to give a sensible and accurate measure of flame length. Long ($58\,cm$), small diameter ($25\,\mu m$), $Pt-10\%Rh$ wires are stretched across the jet centerline at positions beginning at $x/d = 20$ (the start of the self-similar region) to $x/d = 200$. Sixteen wires are spaced at axial locations selected to give equal spacing on a $\log(x/d)$ axis (see Fig. 1). Platinum was chosen for its high coefficient of resistivity and rhodium was chosen to increase the strength. The wires are welded to $5\,cm$ long inconel prongs, which serve as cantilevered springs maintaining tension in the wires. The resistance of these wires, when stretched across the flame, yields an accurate estimate of the line-integrated heat release (temperature rise) resulting from the chemical reaction.

Beyond the end of the reaction zone (flame length), the heat released is simply diluted by the subsequently entrained fluid. Temperature becomes a conserved scalar obeying the similarity law

$$\frac{\Delta T(x,y)}{\Delta T_0} = \kappa \frac{d^*}{x - x_0} g(\eta) \, . \tag{1a}$$

where x is the streamwise (jet axis) coordinate, y is normal to it, $\Delta T(x,y)$ is the temperature rise at (x,y), κ and ΔT_0 are constants determined by experiment, d^* is the momentum diameter of the jet, g is the similarity mean profile function (determined by experiment), and

$$\eta \equiv \frac{y}{x - x_0} \tag{1b}$$

is the similarity variable with x_0 the virtual origin. See Fig. 1.

Taking the line integral of Eq. 1 along y, at constant x (along a wire), yields

$$\frac{1}{L} \int_{-L/2}^{L/2} \frac{\Delta T(x,y)}{\Delta T_0} dy = \kappa \frac{d^*/L}{x - x_0} \int_{-\infty}^{\infty} g(\eta)\, dy$$

$$= \kappa \left(\frac{d^*}{L}\right) \int_{-\infty}^{\infty} g(\eta)\, d\eta$$

where L is the span (length) of the wire, or, for $x > x_f$, where x_f is the flame tip,

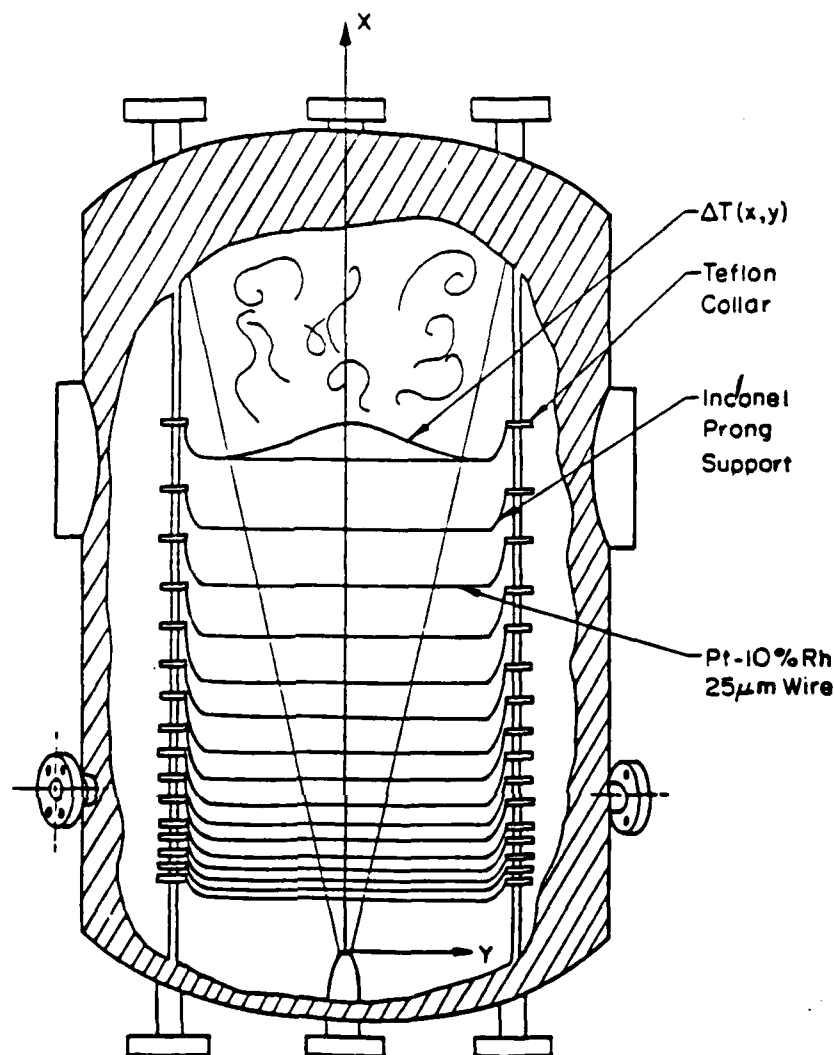$$\frac{1}{L} \int_{-L/2}^{L/2} \frac{\Delta T(x,y)}{\Delta T_0} dy \neq \text{fn}(x) \, . \tag{2}$$

FIG. 1 Schematic of the diagnostics with the coordinate axes indicated. Note that the virtual origin x_0 of the flow field can be adjusted by translating the nozzle assembly with respect to the fixed wire assembly.

We conclude that the (time-averaged), line-integrated mean temperature rise measured at each wire beyond the flame tip at x_f is expected to asymptote to a constant value. Accordingly, the line integral will *rise* to that asymptotic value, as dictated by the cumulative mixing and chemical product formation (heat release) to that station, for values of x/d smaller than x_f/d, the end of the flame region. The law with which this asymptotic behavior is attained is at present controversial; an issue that will have to be resolved both theoretically as well as with the planned for experiments. A sample plot of one of our first runs is included as Fig. 2. The data support one of the original guesses of a (close to) logarithmic dependence on x/d; the reason for installing the wires with such a spacing to start with.
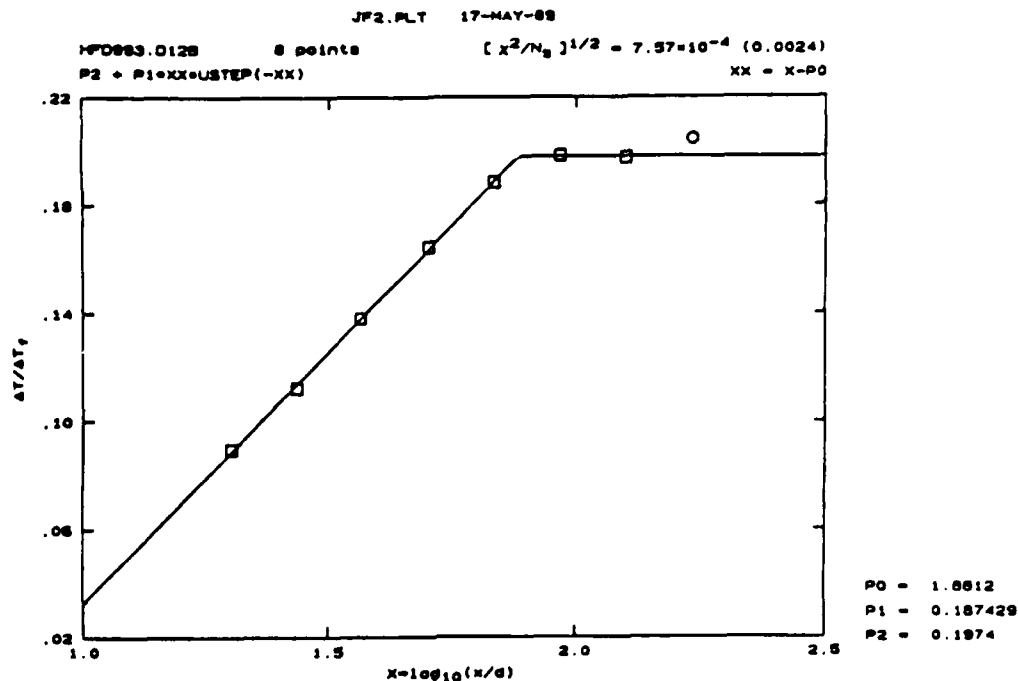
FIG. 2 Mean temperature rise, normalized by the adiabatic flame temperature rise ΔT_f for the chemical reaction (preliminary data).

The primary purpose of the first set of experiments is to examine whether the adage of the Reynolds number independence of these quantities is correct. We are excited in that our proposed definition of flame length appears to represent a significant advance in the way this imporant quantity should be understood. The outcome of these experiments is of considerable significance in the broader context of our understanding and modeling of mixing in high Reynolds number, turbulent flows.

This effort is part of the Ph.D. research of Mr. Rick Gilbrech.

3.2   Turbulent structure and mixing in high Schmidt number jets

Our work with high resolution (both spatial and temporal) measurements in the passive scalar field of the turbulent jet is continuing. To date, these experiments have yielded several new and interesting results. Among these is our finding that the scalar interface geometry *cannot* be characterized by a constant fractal dimension, contrary to previous and continuing claims in the literature.

The geometry of scalar interfaces, and in particular, the surface-to-volume ratio, is of great interest in modeling reacting, turbulent flows. We find that a stochastic, log-normal model agrees well with the results at lower Reynolds numbers ($Re \leq 12,000$), while behavior at higher Reynolds numbers appears to be somewhat more complicated. This corroborates

previous findings that jet flow is undergoing a transition at a Reynolds number in this vicinity. A paper covering this material was presented at the *ASME* (La Jolla) meeting last July, and has also been submitted to *Physics of Fluids*. A similar presentation will also be given at the Thanksgiving APS Fluid Dynamics meeting. A copy of this paper (Miller & Dimotakis 1989) has been included in this report as Appendix D[†].

A second very interesting, and, to the best of our knowledge, new finding is that the normalized rms, *i.e.* $c'/\bar{c}$, scalar fluctuations in the high Schmidt number jet vary with Reynolds number[‡]. Since the normalized rms is a measure of the degree of mixing (unmixedness), this has important implications for mixing, chemical reaction and combustion. To further explore the behavior of the rms and the geometric description of the scalar interface, additional experiments are in progress.

Modifications are presently underway to further increase the resolution of the measurements, which will permit an increase in the range of Reynolds numbers which may be studied in this manner. These changes should allow us to examine the scalar field with an adequate resolution to Reynolds numbers as high as 100,000, or more, complementing our gas phase reacting jet work (see Sec. 3.1). Comparison between these two experiments, as well as the completed work in the non-reacting gas phase jet (Dowling 1988[*], Dowling & Dimotakis 1988[*]), should make it possible to discern aspects of the fluid dynamics of mixing in the jet which are specific to the gas phase from those which are not, *i.e.* Schmidt number effects. In addition, mixing in certain gas flows may behave with a very high effective Schmidt number, such as in the presence of soot, or other particulates, in which case the high Schmidt number results will be useful for direct application.

This effort is part of the Ph.D. research of Mr. Paul Miller.

[†] An effort was made in that paper to list the plausible reasons for the discrepance between the findings of other investigators and our recent results. We feel that the resolution of this issue will help advance our fundamental understanding of these phenomena.

[‡] We appreciate that this finding could be construed as indicative of inadequate resolution in our measurements. We have taken particular pains to address this issue, however, and can ascertain that the result stands.

[*] Appended as part of the 1988 Annual Report (Dimotakis *et al.* 1987).

4. Computational effort

Our computational effort is focused in two areas: numerical simulation of compressible flows and the advancement of vortex methods for incompressible flows. These will be discussed below.

4.1 Compressible flows

A promising new Lagrangian technique for the numerical simulation of unsteady compressible flows, including chemical reactions, is under development. For the non-reacting case, this method can be classified as a shock-capturing Godunov-type method. It is characterized, however, many new and interesting features which permit very accurate results. *e.g.* perfect discontinuities as in shock-fitting methods, while retaining the robust character of shock-capturing methods. The basis for the spatial discretization is a number of Lagrangian computational cells, *i.e.* cells whose boundaries are permitted to move either with the local fluid velocity, or with a different velocity in regions where there are discontinuities or reaction zones. This scheme injects to the numerical simulation the physics of shocks**, permitting the capturing of shocks as perfect discontinuities, for example.

As a first step, we have implemented the scheme in one-dimension without chemical reactions. In the figure we show the results for a standard shock-tube problem, *i.e.* unsteady, one-dimensional flow (*e.g.* Sod 1978). Our results are already *better than any other known numerical method* that has been used in such flows. Sample plots, capturing an instant in the unsteady shock/expansion process are included as Figs. 3a, through 3c.

The next step, presently in progress, is to extend the method to include chemical reactions, *e.g.* detonation waves. Following this, we plan to address unsteady, compressible flows in two dimensions.

This effort is part of the Ph.D. thesis of Mr. Tasso Lappas.

** Cells which are in the vicinity of, or are about to experience, shocks are computed separately solving a local Riemann problem at each time-step.
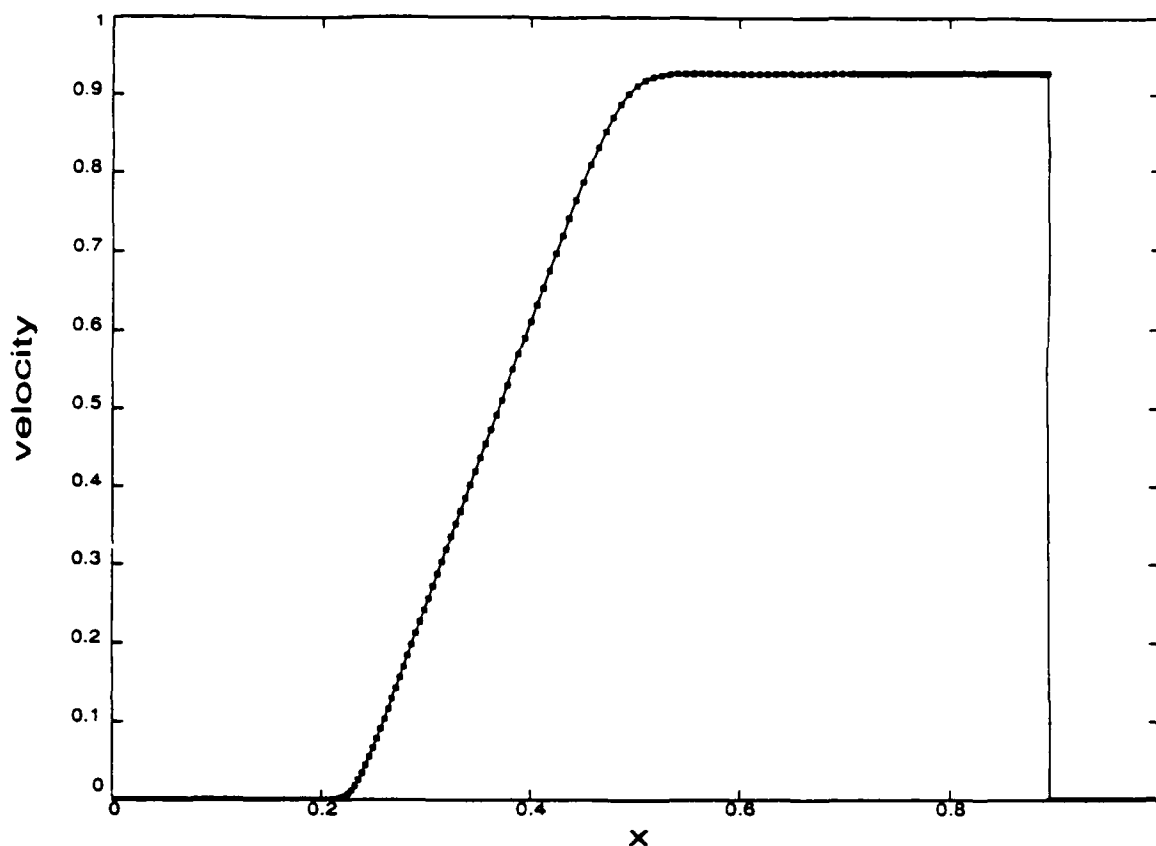
FIG. 3a Shock tube problem: Velocity profile at $t = 0.225$ (flow computed using 300 lagrangian cells).

4.2 Fast vortex algorithms and parallel computing

Vortex methods represent a powerful technique for the numerical simulation of incompressible, two- and three-dimensional flows at high Reynolds numbers. In a typical simulation, the time evolution of a vortex element is influenced by all the other elements in the domain. Consequently, the required CPU time for standard algorithms grows like the square of N, where N is the number of computational elements. As a result, reasonable computing times cannot be obtained for N larger than a few thousand. To make the calculation more efficient, it has been proposed that one should approximate the interaction of distant groups of vortices. Pairwise interactions between individual elements of the groups are replaced by a simpler cluster-to-cluster interaction. In the context of this approximation, a group of vortices could be replaced by a single vortex judiciously sized and located. The cluster-to-cluster approximation is computed as if only two vortices were involved. The resulting induced velocities are applied to all the members of the respective groups. This simple approximation is very fast but requires groups which are tightly bounded and very far apart, otherwise significant errors are made in the evaluation of the velocities. These cluster-to-cluster approximations cannot be used on large groups where the potential speed-up is the most important. As a result, this approach is not much faster than the regular $N2$ algorithm. More sophisticated approximations are needed to compute the interactions of large clusters accurately. In one suggested technique, the
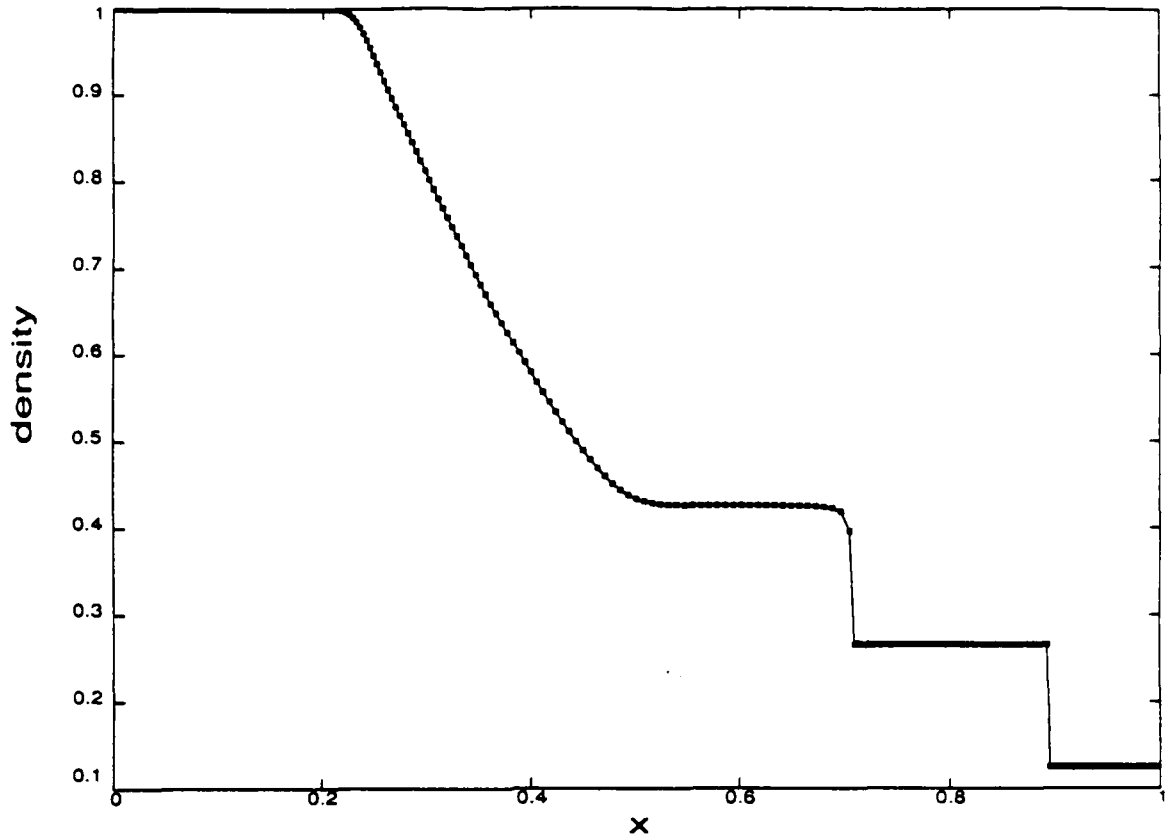
FIG. 3b Shock tube problem: Density profile at $t = 0.225$. Note shock discontinuity and discontinuity across the driver/driven gas contact surface.

inducting effect of a cluster can be represented by a multipole expansion (in 2-D), while a Taylor series describes the velocity induced within a group. Any level of accuracy can be obtained by keeping more terms in the expansions. It can be shown that the error due to any given approximation is bounded by $(dr/r)^p$, where dr is the radius of the largest group, r is the distance between the groups, and p is the number of terms in the expansions. Since these quantities are known, an error estimate can easily be obtained. If this estimate is large than some criterion, ϵ, the approximation is rejected. Smaller groups are sought until valid approximations, consistently with the imposed tolerable error specification, are found. Ultimately, the influence of the nearby vortex elements is computed using pairwise interactions. At that level, the short range core effects can be included.

Regardless of the approximation used, the binary tree is the most appropriate date structure to efficiently implement the algorithm. Each cluster is composed of two subclusters; it has two children. When an approximation is rejected, pointers are used to have access to the information concerning the subclusters. A hierarchy of "meshes" is produced and interactions are computed at the coarsest possible level. This binary tree is actually built from the bottom up. Neighboring vortex elements are grouped into clusters. Pairs of nearby clusters are assembled into a larger structure and so forth. This data structure is grid free and moves with the vortex elements on top of which it resides. Slight readjustments of the tree are made at every time step to insure that the groups remain as compact
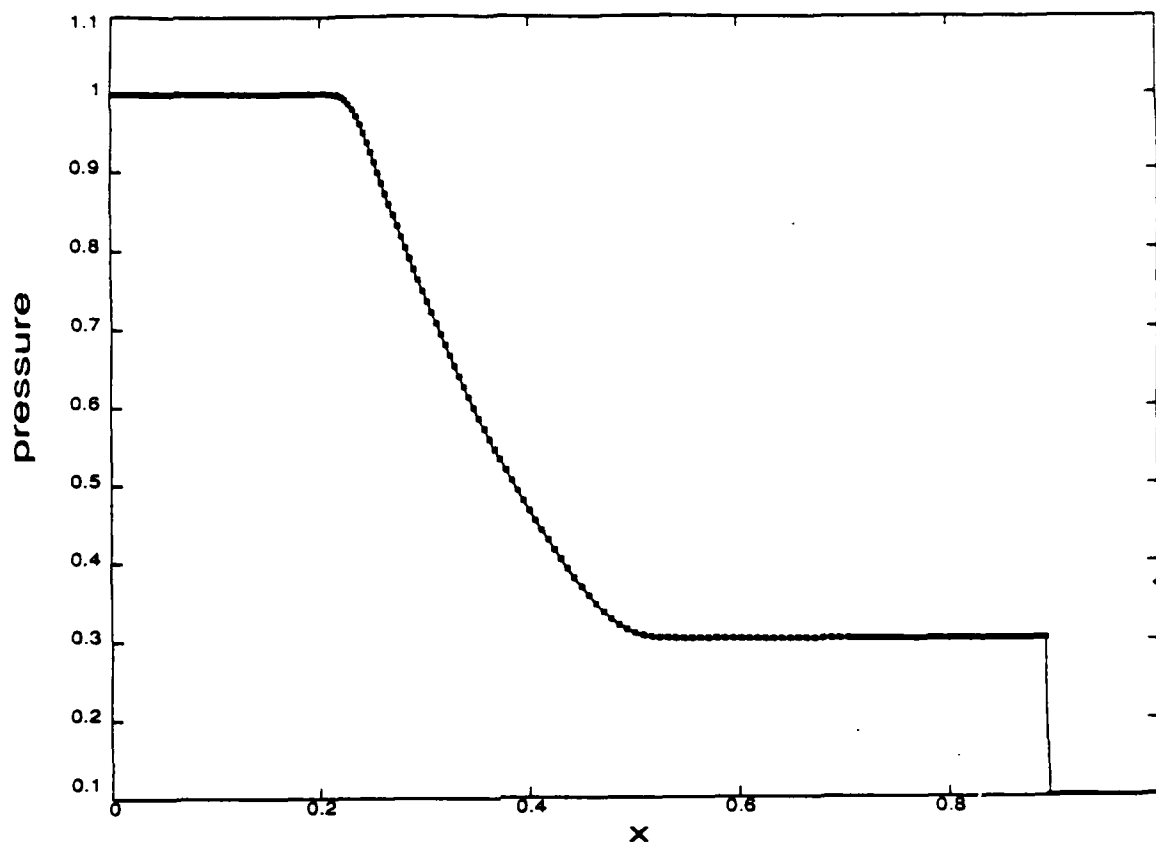
FIG. 3c Shock tube problem: Pressure profile at $t = 0.225$. Note continuity across contact surface (cf. Fig. 3b).

as possible. To realize the potential efficiency gains, the data structure must reflect the organization existing in the flow.

Because of its unpredictability, this algorithm is difficult to vectorize, but its implementation on a parallel processor (Caltech Mark III) is underway. The preliminary results are encouraging. Several promising strategies have been proposed that should lead to reasonable load balancing.

This effort is part of the Ph.D. research of Mr. Francois Pepin.

5. Modeling effort

Several modeling efforts are in progress. In particular, an effort to model mixing and chemical reactions in turbulent shear layers, including finite chemical kinetic rate effects, based on the ideas put forth by Broadwell and Breidenthal (1982), has recently been published (Broadwell & Mungal 1988) and is included as Appendix E. In addition, a co-operative modeling/computational effort[†] to simulate turbulent jet mixing, also using the Broadwell-Breidenthal ideas, and a full chemical kinetic description of the combustion process, utilizing the CHEMKIN code package (Kee *et al.* 1980), is also in progress with the SANDIA Combustion Research Facility. This effort attempts to simulate such effects as the formation of oxides of nitrogen in turbulent jet diffusion flames, a process which relies on multiple flow and chemical kinetic time scales, as well as the results of our flame length experiments currently in progress, described in this report in Sec. 3.1.

6. Diagnostics effort

We have traditionally not permitted the development of diagnostics methods to become an end in themselves. Nevertheless, as part of the larger effort under the sponsorship of this program, several significant advances in diagnostics have been realized, over the years, which have permitted measurements to be realized that would otherwise have been out of reach of the state-of-the-art at the time. One of these is the development of very high signal-to-noise ratio measurements of light, using solid state detectors coupled to transimpedance amplifiers, as usually arise in laser scattering experiments[‡].

This technique was recently documented (Dowling, Lang & Dimotakis 1989). A reprint has been included as part of this report as Appendix F. We would like to draw the reader's attention to Fig. 6 in that paper, where the spectrum of the jet fluid concentration fluctuations, measured using Rayleigh scattering techniques, is shown with a spectral signal-to-noise ratio (SNR) of, roughly, $60\,dB$[*].

We note that does not represent the maximum we have attained to date. In particular, measurements with a spectral SNR of $80\,dB$ have been realized in water laser scattering experiments[**]. The signal processing and spectrum estimation techniques that were utilized for this estimate have also been developed under the sponsorship of this program over the years. A preliminary account was given in Dowling (1988). We, unfortunately, have not had the opportunity to fully document the latter as yet.

[†] Cosponsored by the Gas Research Institute.

[‡] The conventional wisdom is that at such low light levels, only photomultiplier tubes (PMT) can be used. We have, in effect, lowered the light intensity threshold by a very large factor at which the PMT becomes the detector of choice.

[*] Ratio of highest spectral power to the noise level.

[**] Note that these $SNRs$ are achieved using 12-bit A/D converters (resolution of 1 part in 4,096 of full scale). The maximum spectral $SNRs$ we have attained (with 12-bit data) is $\sim 100\,dB$ (in some recent measurements of hydroacoustic spectra).

7. Personnel

In addition to the Principal Investigators:

P. E. Dimotakis: Professor, Aeronautics & Applied Physics;

J. E. Broadwell: Senior Scientist, Aeronautics;

A. Leonard: Professor, Aeronautics;

other personnel who have participated directly in the effort during the current reporting period are listed below:

E. Dahl: Member of the technical Staff, Aeronautics;

D. R. Dowling: Graduate Research Assistant, Aeronautics[†];

C. E. Frieler: Graduate Research Assistant, Aeronautics;

R. J. Gilbrech: Graduate Research Assistant, Aeronautics;

J. A. Hall: Graduate Research Assistant, Aeronautics;

D. B. Lang: Staff Engineer, Aeronautics;

T. Lappas: Graduate Research Assistant, Aeronautics;

T. Kubota: Professor, Aeronautics;

R. Miake-Lye: Senior Research Fellow, Aeronautics[‡];

P. L. Miller: Graduate Research Assistant, Applied Physics;

F. Pepin: Graduate Research Assistant, Aeronautics;

M. Zhuang: Graduate Research Assistant, Aeronautics;

In addition, Dr. H. Rosemann is now participating in this program, as of July 1989, as a Post-doctoral Research Fellow in Aeronautics.

[†] Presently, Research Fellow, University of Washington.

[‡] Presently, with Lincoln Labs, Mass.

8. References

BOGDANOFF, D. W. [1983] "Compressibility Effects in Turbulent Shear Layers", *AIAA J.* **21**(6), 926-927 (TN).

BROADWELL, J. E. and BREIDENTHAL, R. E. [1982] "A Simple Model of Mixing and Chemical Reaction in a Turbulent Shear Layer", *J. Fluid Mech.* **125**, 397-410.

BROADWELL, J. E. and MUNGAL, M. G. [1988] "Molecular Mixing and Chemical Reactions in Turbulent Shear Layers", *22nd Symposium (International) on Combustion* (The Combustion Institute), 579-587.

DIMOTAKIS, P. E. [1989] "Turbulent Free Shear Layer Mixing and Combustion", 9th ISABE (Athens, Greece), 3-9 September 1989.

DIMOTAKIS, P. E., BROADWELL, J. E. and LEONARD, A. [1987] "Chemical Reactions in Turbulent Mixing Flows", California Institute of Technology , AFOSR-83-0213 Annual Report (June 1987).

DOWLING, D. R. [1988] *Mixing in gas phase turbulent jets*, Ph.D. thesis, California Institute of Technology.

DOWLING, D. R. and DIMOTAKIS, P. E. [1988] "On Mixing and Structure of the Concentration Field of Turbulent Jets", Proceedings, *First National Fluid Dynamics Congress*, 25-28 July 1988 (Cincinatti, Ohio), **II**, 982-988.

HALL, J., DIMOTAKIS, P., PAPAMOSCHOU, D. and FRIELER, C. [1988] "Design Overview of the Supersonic Hydrogen-Fluorine Facility (V3.0)", GALCIT Internal Report (6 May 1988).

HALL, J. and DIMOTAKIS, P. E. [1989] "Design Overview of the Supersonic Hydrogen-Fluorine Facility (V4.0)", GALCIT Internal Report (30 August 1989).

KEE, R. J., MILLER, J. A. and JEFFERSON, T. H. [1980] "CHEMKIN: A General Purpose, Problem-independent, Transportable, Fortran Chemical Kinetics Code Package", SANDIA Report SAND80-8003.

MILLER, P. L. and DIMOTAKIS, P. E. [1989] "Stochastic Geometric Properties of Scalar Interfaces", *ASME Fluids Engineering Conference* (La Jolla, California), 10-12 July 1989, session on *Fractal Structures*.

PAPAMOSCHOU, D. and ROSHKO, A. [1988] "The Compressible Turbulent Shear Layer: An Experimental Study", *J. Fluid Mech.* **197**, 453-477.

SOD, G. S. [1978] "A Survey of Several Finite Difference Methods for Systems of Nonlinear Hyperbolic Conservation Laws", *J. Comp. Phys.* **27**(1), 1-31.

ZHUANG, M., KUBOTA, T. and DIMOTAKIS, P. E. [1988] "On the Stability of Inviscid,

Compressible Free Shear Layers", Proceedings, *First National Fluid Dynamics Congress*, 25-28 July 1988 (Cincinatti, Ohio), **II**, 768-773.

ZHUANG, M., KUBOTA, T. and DIMOTAKIS, P. E. [1989] "On the Instability of Inviscid, Compressible Free Shear Layers", submitted for publication, *AIAA J.* .

Appendix A

DIMOTAKIS, P. E. [1989] "Turbulent Free Shear Layer Mixing and Combustion", 9th ISABE (Athens, Greece), 3–9 September 1989.

Turbulent free shear layer mixing and combustion[*]

by

Paul E. Dimotakis[**]

Graduate Aeronautical Laboratories
California Institute of Technology
Pasadena, California 91125

Some experimental data on turbulent free shear layer growth, mixing, and chemical reactions are reviewed. The depen-
dence of these phenomena on such fluid and flow parameters as Reynolds number, Schmidt number and Mach number
are discussed with the aid of some direct consequences deducible from the large scale organization of the flow as well as
from some recent models.

1. Introduction

The mixing of two or more fluids that are entrained into a turbulent region is an important process from both a scientific and an applications vantage point. If the issue of mixing arises in the context of chemical reactions and combustion, we recognize that only fluid mixed on a *molecular* scale can contribute to chemical product formation and associated heat release. The discussion in this paper will be limited to this level of mixing.

The theoretical importance of the study of molecular mixing by turbulence is in that it provides a test for models of the behavior of the smallest scales of turbulence. These correspond to a spectral regime that can be treated in a rather more cavalier fashion if one need only address the momentum transport properties of the turbulent region (Brown & Roshko 1974), for example, but must be described with some deference to the physics at those scales if molecular mixing is to be accounted for correctly. From an experimental point of view, molecular mixing and chemical reactions in high Reynolds number flows provide us with an important probe of diffusion length and time scales that would otherwise remain beyond the reach of any conceivable direct measurement diagnostics. Matters are no better computationally, with the requisite spatial/temporal resolution long recognized to be out of reach (Von Neumann 1949), a situation that must still be accepted as the case for high Reynolds number flow for the foreseeable future (e.g. Leonard 1983, Rogallo & Moin 1984). Finally, from a technological vantage point, mixing in a turbulent environment may well dictate the performance of many devices that rely on the details of the turbulent mixing process, such as high fuel efficiency internal combustion engines, chemical lasers, hypersonic propulsion, etc. It is also likely to prove to be an important consideration in other contexts, such the local and global environmental issues involving chemistry in the turbulent atmospheric environment, the dynamics of stellar atmospheres and interiors, etc.

The discussion here will be limited to that of mixing in turbulent shear layers, formed between two uniform free streams of unequal velocity — not necessarily of equal density — at high Reynolds numbers. In particular, at least for subsonic flow, for values of the local Reynolds number given by

$$Re \equiv \frac{\delta \Delta U}{\nu} > 10^4 , \tag{1}$$

where $\delta = \delta(x)$ is the (local) transverse extent of the turbulent shear layer region,

$$\Delta U = U_1 - U_2 \tag{2}$$

is the velocity difference across the shear layer, and ν is some appropriate measure of the kinematic viscosity. In the discussion that follows, issues pertaining to gas phase mixing will be addressed, for which the Schmidt number,

$$Sc \equiv \frac{\nu}{\mathcal{D}} , \tag{3}$$

with ν the kinematic viscosity and $\mathcal{D}$ the diffusing/mixing species diffusivity, is near unity. Mixing in liquid phase flows, for which $Sc \gg 1$ (e.g. $Sc_{water} \approx 600$), will also be discussed. The difference in the mixing between these two cases is important in that it provides important clues in the behavior of the smallest scales of the flow.

While the two-dimensional shear layer flow geometry may not be germane to all the issues alluded to above, many of the phenomena that need to be addressed are generic and two-dimensional turbulent free shear layer flows provide a useful arena in which they can be studied. Additionally, however, the flow within the turbulent region formed between the two free streams is capable of sustaining relatively rapid mixing, and one that can be further enhanced by a variety of flow manipulation means. This is a consequence of the property of shear-driven turbulence, which at least for sub-sonic flow conditions can generate interfacial surface area between fluids inducted from each of the two streams

at very high rates. At the high Reynolds numbers of interest here, the relatively small (molecular) diffusivity can result in a total diffusive flux across this very large interface that may come close to accommodating the rate at which the free stream fluids are inducted into the turbulent region at the largest scales of the flow. As a consequence, at least for subsonic, high Reynolds number, gas phase flows, one finds that the expected fraction δ_m/δ of the turbulent region occupied by molecularly mixed fluid can be significant. It's not called a *mixing* layer for nought!

It is useful to view the molecular mixing process and any associated chemical product formation at a particular station z of the flow as resolved into a sequence of Lagrangian stages in the "life" of entrained fluid elements bearing the chemical reactants. These fluid elements must:

    i. be inducted into the mixing zone of relative transverse extent δ/z,

then

    ii. mix molecularly to occupy some fraction δ_m/δ, of $\delta(z)$ at z,

before

    iii. reacting to form the chemical product. which represents, in turn, some fraction δ_P/δ_m of the mixed fluid.

This suggests expressing the expected chemical product between the virtual origin ($z = 0$) of the shear layer flow and the station at z as a product of factors of the form:

$$\frac{\delta_P}{z} = \frac{\delta}{z} \times \frac{\delta_m}{\delta} \times \frac{\delta_P}{\delta_m} . \tag{4}$$

The first factor, δ/z, measures the *growth* of the mixing layer region, the second, δ_m/δ, the *mixing* within the shear layer, while the third, δ_P/δ_m, the *chemical reactions* that can take place within the molecularly mixed fluid in the layer. This partition, at least in the case of high Reynolds numbers is justified by the fact that the various stages represented by these factors occur in a *succession of Lagrangian times*. This resolution also provides a useful framework within which turbulent mixing and chemical reactions in two-dimensional shear layers can be discussed and reviewed, and will be adopted in the discussion that follows.

2. Shear layer growth: δ/x

At the high Reynolds numbers of interest and for Schmidt numbers which, if not large, are not much smaller than unity, the shear layer growth rate δ/z is an important quantity. It measures the angle of the wedge-shaped turbulent mixing region which confines the mixed fluid and chemical product. Conversely, the width of the turbulent region δ/z, represents an upper bound for the amount of mixed fluid we can hope for in the layer, corresponding to a scenario in which the entrained fluids are mixed instantly, on a molecular scale, as soon as they enter the turbulent region within the transverse extent δ.

The transverse extent δ/z of the shear layer is known to depend on several dimensionless parameters of the flow, i.e.

$$r \equiv \frac{U_2}{U_1} \quad \text{and} \quad s \equiv \frac{\rho_2}{\rho_1} , \tag{5}$$

the free stream velocity and density ratios, respectively, the (convective) Mach numbers of the two streams, i.e.

$$M_{c_1} = \frac{U_1 - U_c}{a_1} \quad \text{and} \quad M_{c_2} = \frac{U_c - U_2}{a_2} , \tag{6a}$$

where

$$U_2 < U_c < U_1 \tag{6b}$$

is the convection velocity of the large scale structures in the shear layer, and $a_{1,2}$ are the speeds of sound in the high and low speed free stream, respectively. In the case of combusting flow, it also depends on the relative mean density reduction $\Delta\rho/\rho$ in the interior of the chemically reacting shear layer owing to heat release. For equal free stream densities ($\rho_1 = \rho_2 = \rho_0$), this can be expressed in terms of the parameter

$$q \equiv \frac{\rho_0 - \bar{\rho}}{\rho_0} = \frac{\Delta\rho}{\rho_0} , \tag{7}$$

where $\bar{\rho}$ is the (reduced) mean density of the flow within the δ/z shear layer wedge. Finally, the shear layer growth rate is influenced by the presence of streamwise pressure gradients. We note, however, that if $dp/dz \neq 0$ (accelerating/decelarating flow), the shear layer will not grow linearly, unless it so happens that the dynamic pressures in the two free streams are matched, i.e. if $\rho_1 U_1^2 = \rho_2 U_2^2$ (Rebollo 1973). Experimental information as well as some theoretical understanding of the dependence of δ/z on these parameters is available, even though the picture is as yet far from complete or satisfactory.

By δ, in this discussion, we will denote the local transverse extent of the sheared region that contains the molecularly mixed fluid in a boundary layer sense, i.e. the distance between the shear layer edges outside which the expected concentration of molecularly mixed fluid is less than some small fraction, say 1%, of its peak value. This definition yields a local width which closely matches the measurements of the "visible" shear layer width δ_{vis}, as would be measured in a schlieren or shadowgraph picture of the layer (e.g. Brown & Roshko 1971, 1974). It is also very close to the 1% width δ_1 in the case of a chemically reacting layer, defined as the distance between the two points across the layer where the mean product concentration, or temperature rise owing to heat release, has dropped to 1% of its peak value (see Mungal & Dimotakis 1984, Koochesfahani & Dimotakis 1986). As a result of the similarity properties of this flow at high Reynolds numbers (Eq. 1) we can argue that other transverse scales must be fixed multiples of this δ. By way of example, the vorticity (or maximum slope) thickness δ_ω of the mean streamwise velocity profile $U(y)$, defined by

$$\frac{1}{\delta_\omega} \equiv \frac{1}{\Delta U} \left[\frac{dU(y)}{dy} \right]_{max} , \tag{8}$$

is found to be roughly half of δ.

2.1 Dependence on velocity and density ratio

Abramowich (1963) and Sabin (1965) proposed an expression for the shear layer growth rate given by

$$\frac{\delta}{x} \approx C_\delta \frac{1-r}{1+r} , \qquad (9)$$

where C_δ is taken as a constant. This was found to be in reasonable accord with experimental data of incompressible shear layers with equal free stream densities. The dependence on the free stream density ratio was addressed in the seminal experiments by Brown & Roshko (1971, 1974), originally undertaken to investigate whether the observed reduction in growth rate in supersonic shear layers could be attributed to density ratio effects. Using different gases for each free stream and subsonic free stream velocities, they found that while the growth rate depended on the free stream density ratio, compressibility effects could not be identified with density ratio effects. In subsequent experiments, Konrad (1976) provided further documentation of the dependence on the density ratio and also noted that a shear layer entrained asymmetrically from each of the free streams.

Brown (1974) proposed an account of these phenomena based on similarity arguments which recognized the significance of a Galilean frame translating at the convection velocity U_c of the large structures. Growth and entrainment is to be understood as taking place in this frame, whose convection velocity is a function of both the density and velocity ratio. His theory, which applied to a temporally growing shear layer, was in reasonable accord with the observed growth rate density ratio effects, but — as appropriate for a temporal model — predicted no asymmetry in the entrainment ratio for matched free stream densities, contrary to Konrad's observations.

In a subsequent proposal (Dimotakis 1984), the difference between temporal vs. spatial growth of a shear layer was noted and exploited to explain the entrainment ratio asymmetry, yielding also an expression for the growth rate of a spatially growing shear layer given by,

$$\frac{\delta}{x}(r,s;M \to 0) \approx C_\delta \frac{(1-r)(1+s^{1/2})}{2(1+s^{1/2}r)}$$

$$\times \left\{ 1 - \frac{(1-s^{1/2})/(1+s^{1/2})}{1+2.9\left(\frac{1+r}{1-r}\right)} \right\} , \qquad (10)$$

where the coefficient C_δ is independent of the velocity ratio r and/or the density ratio s. The factor multiplying the braces describes the growth rate of a temporally growing shear layer and is the same as the Brown (1974) proposal for shear layer growth. The observed (and predicted) dependence of the growth rate on the density ratio is not weak and is plotted for density ratios in the range $0.1 < s < 8$ in Fig. 1, computed for a fixed velocity ratio of $r = 0.4$ and the value of $C_\delta = 0.37$, along with the experimental values of Brown & Roshko (1974) for $s = 1/7, 7$, and the measurement of Mungal & Dimotakis (1984) for $s = 1$. Also plotted for comparison is the Brown (1974) prediction for the temporally growing shear layer. As can be seen, the difference between the two predicted growth rates is not large. It vanishes for equal free stream densities ($s = 1$), where the quantity in the
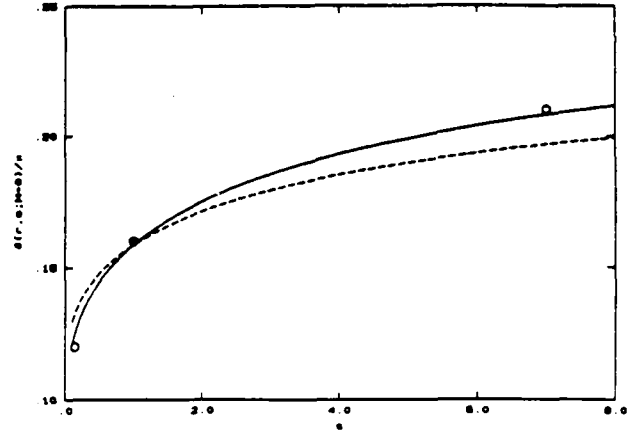

FIG. 1 Incompressible growth rate for fixed velocity ratio $r = U_2/U_1 = 0.4$ and density ratios $0.1 < s = \rho_2/\rho_1 < 8$ (Eq. 10; $C_\delta = 0.37$). Solid line: spatially growing layer (Eq. 10), open symbols: Brown & Roshko (1974; $s = 1/7, 7$), filled symbol: Mungal & Dimotakis (1984; $s = 1$). Dashed line: temporally growing shear layer (Brown 1974).

braces becomes equal to unity, and where the proposed expression reduces to the Abramowich–Sabin relation (Eq. 9).

For a free shear layer with no external disturbances[†], the value of the coefficient C_δ is found to be in the range of

$$C_\delta \approx 0.25 \text{ to } 0.45 \qquad (11)$$

for the total thickness δ, or roughly half that for the maximum slope thickness δ_ω (see, for example, data compiled by Brown & Roshko 1974, Fig. 10). An understanding, much less an accounting, of this rather large spread of values of the coefficient C_δ, which cannot be attributed to experimental errors, must await further investigations. It is not even clear, at this writing, whether the values in Eq. 11 represent bounds or not. What is clear, is that this coefficient depends in some way on the initial conditions of the flow (e.g. Batt 1975, Hussain 1978, Browand & Latigo 1979, Weisbrot, Einav & Wygnanski 1982, Lang 1985, Dziomba & Fiedler 1985).

It has been recognized for some time (Bradshaw 1966) that the shear layer is sensitive to its initial conditions. Bradshaw suggests that a minimum of several hundred of the initial momentum thicknesses θ_0 is required for the shear layer to assume its asymptotic behavior. In view of the dynamics and interactions of the large scale structures in the flow, it can even be argued that this estimate may not be conservative enough (Dimotakis & Brown 1976). These caveats notwithstanding, there exist sufficient experimental data to suggest that a turbulent shear layer will exhibit *linear* growth, even within the Bradshaw x/θ_0 specification, but that the growth rate may not be a unique function of the free stream density and velocity ratio. This is illustrated in the schlieren data in Fig. 2 of a shear layer with equal free stream

---

[†] As opposed to a *forced* or *driven* shear layer (e.g. Oster & Wygnanski 1982, Hussain & Hussain 1983, Ho & Huerre 1984, Roberts & Roshko 1985, Roberts 1985, Wygnanski & Petersen 1987, Koochesfahani & Dimotakis 1988).

densities ($s = 1$), as the flow velocity was increased. keeping the free stream velocity *ratio* fixed at $r = 0.4$. As can be seen. the reduction in the shear layer growth rate with increasing flow velocity is appreciable. It is clear. that this behavior cannot be attributable to effects scaled by the *local* Reynolds number. for example. which increases linearly with x for this flow (see Eq. 1). Were that the case. or if *decaying* remnants of the effects of the initial conditions were responsible. the shear layer would be growing with curved edges rather than along (straight line) rays emanating from the (virtual) origin.
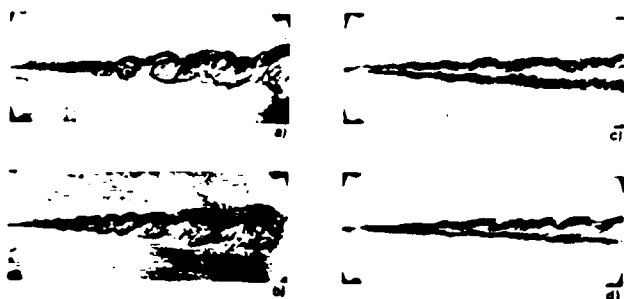
FIG. 2 Shear layer growth at a fixed velocity ratio ($r = 0.4$) and equal free stream densities. as a function of flow velocity (field of view $\approx 25\,cm$). Flow here is made visible by changes in the index of refraction owing to the (small) heat release from a diluted reactant $H_2 + F_2$ chemical reaction. (a) $U_1 = 13\ m/s$, (b) $U_1 = 22\ m/s$. (c) $U_1 = 44\ m/s$. (d) $U_1 = 83\ m/s$. Unpublished data by Mungal, Hermanson & Dimotakis.

This behavior is perhaps better illustrated in the schlieren data in Fig. 3, formed as a composite of two pairs of pictures, which cover roughly half a meter of flow, and an x/θ_0 of several thousand. The reader is invited to sight along the shear layer edges of Fig. 3a. which is characterized by the better contrast, to ascertain the claim. Note that the highest high speed stream velocity (U_1) in these data (Fig. 2) was 83 m/s, with the free stream fluid primarily comprised of N_2 (diluent) gas. As a consequence, the observed reduction in growth rate cannot be attributed to compressibility (Mach number) effects. which will be discussed below.
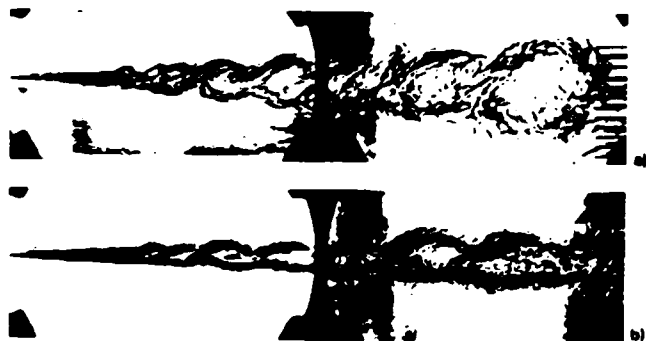

FIG. 3 Composite schlieren data of the same shear layer (probe array at far right at $z = 45\,cm$). (a) $U_1 = 14\ m/s$. (b) $U_1 = 88\ m/s$. Unpublished data by Mungal, Hermanson & Dimotakis.

It is intriguing that shear layer growth, *as far downstream as several thousand of the original splitter plate boundary layer momentum thicknesses*, appears dependent on. if not determined by, the initial conditions. It is also intriguing that the large scale structure spacing appears to be the same in the low and high speed flow data in Fig. 3, even as their transverse extent is being reduced: what does appear to be changing is the large scale structure aspect ratio.

A clue into this behavior may, perhaps, be found in terms of the notions of *convective* and *global* instabilities, first developed in the context of plasma instabilities (Briggs 1964, Bers 1975). By that criterion and the results of temporal, linear stability analysis the fluctuations in a (co-flowing) plane shear layer must be classified as the former, as discussed in Huerre & Monkewitz (1985). It can then argued that the shear layer should be regarded as an amplifier of the externally imposed disturbances, possessing a non-unique growth rate thereby, as opposed to the behavior of an oscillator, which could be characterized by its own growth rate. That analysis. however, must be amended to include the contribution to the overall stability of the initial development region, which is characterized by the influence of the wake introduced into the flow by the splitter plate (Koch 1983, 1985) as Huerre & Monkewitz discuss. See also Lang (1985), Koochesfahani & Frieler (1987) and Sandam & Reynolds (1987). In addition. the differences between a temporally growing layer and the spatially growing shear layers of interest here must also be contended with. Finally, one would have to incorporate additional feedback mechanisms present in the real flow in the analysis, such as the ones that act on the initial region owing to the long-range velocity fluctuations induced by the downstream structures, spanning a range of *lower* frequencies. as well as owing to pressure fluctuations feeding back to the splitter plate tip as the last structures leave the shear layer flow domain (test section), as dictated by the facility-dependent outflow boundary conditions (Dimotakis & Brown 1976). The question of the applicability of linear stability analysis to the description of these phenomena aside for the moment. it is difficult to say at this time whether a proper accounting of all of these influences would alter these qualitative conclusions.

2.2 Compressibility effects

It has been known for some time that two-dimensional shear layer growth diminishes as the flow Mach number increases, even after the coupling of the flow Mach number to the free stream density and velocity ratio that would result in a typical flow facility is accounted for (Brown & Roshko 1974. Sec. 7.1). Recent analysis (Bogdanoff 1983) and experimental investigations of compressible shear layers (Papamoschou & Roshko 1988) have suggested that the effects of compressibility are scaled by the *convective* Mach numbers of the shear layer large scale structures with respect to the two streams, which measure the relative free stream Mach numbers as seen from the Galilean frame of these structures (Eq. 6). It is interesting that one can argue for a similar scaling on the basis of linear stability analysis of compressible shear flow, if the convection velocity U_c is identified with the (real) phase velocity

c_r of the unstable mode in the flow (Mack 1975, Ragab & Wu 1988, Zhuang et al. 1988).

For incompressible flow, the convection velocity U_c can be estimated by recognizing (Coles 1981) that, in the large scale structure Galilean convection frame, there exist stagnation points in between each adjacent pair of structures. Continuity in the pressure at these points (Dimotakis 1984 and Coles 1985), i.e.

$$p_1 + \frac{1}{2}\rho_1(U_1 - U_c)^2 \approx p_2 + \frac{1}{2}\rho_2(U_c - U_2)^2 , \qquad (12)$$

then yields, for $p_1 \approx p_2$,

$$\frac{U_1 - U_c}{U_c - U_2} \approx \sqrt{\frac{\rho_2}{\rho_1}} , \qquad (13)$$

or,

$$\frac{U_c}{U_1} \approx \frac{1 + r\,s^{1/2}}{1 + s^{1/2}} . \qquad (13')$$

This agrees with the differently derived Brown (1974) result, the few estimates of this quantity from the (x,t) data in Brown & Roshko (1974), as well as the measurements of Wang (1984) in curved shear layers (see Coles 1985, Fig. 7 and related discussion).

For compressible flow, the corresponding result can be similarly estimated from the isentropic relation for the total pressure, i.e.

$$\frac{p_{ti}}{p_i} = \left[1 + \frac{\gamma_i - 1}{2}\left(\frac{U_i - U_c}{a_i}\right)^2 \right]^{\frac{\gamma_i}{\gamma_i - 1}} , \qquad (14a)$$

with $i = 1,2$ corresponding to the high and low speed streams, γ_i the ratios of specific heats, and a_i the speeds of sound for the high speed and low speed stream fluids, respectively. Approximately equal pressure recovery from each free stream at the large structure interstitial stagnation points then yields (for $p_1 \approx p_2$)

$$\frac{p_{t1}}{p_1} \approx \frac{p_{t2}}{p_2} . \qquad (14b)$$

This is the same result as the one arrived at by Bogdanoff (1983) using different arguments (see also discussion in Papamoschou & Roshko 1988). It also agrees with the linear stability estimates of this quantity (Zhuang et al. 1988), at least for subsonic convective Mach numbers. Note that, for equal ratios of specific heats ($\gamma_1 = \gamma_2$), e.g. both free streams composed of diatomic gases, we have

$$M_{c1} = M_{c2} \qquad (15)$$

and the compressible flow relation reverts to the incompressible result (cf. Eq. 13).

It should be noted that these results are more robust than the assumption that the pressure recovered at the large scale structure interstitial stagnation points can be computed using the (isentropic) Bernoulli equation for the total pressure. It suffices to assume that, if only a fraction of the total pressure is recovered at these points, that the fractional losses from each side are roughly the same, in the mean. Considering the symmetries of the flow, even when viewed as an unsteady process, such an assumption may well be justified, at least for subsonic convective Mach numbers, and yields results in accord with the experimental data cited, as well as the computational (Lele 1989) evidence to date. Secondly, we should note that the pressure matching condition (Eqs.
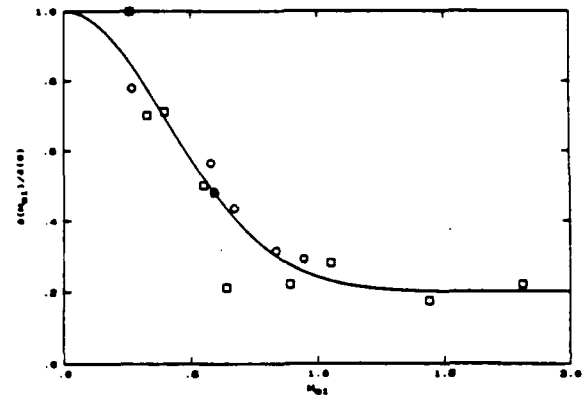

FIG. 4 Compressible shear layer growth data for a range of free stream velocity and density ratios. Shear layer width normalized by the incompressible value, estimated at the same free stream density and velocity ratio for each run. Squares: Papamoschou & Roshko (1988) data. Circles: growth rates estimated from the Chinzei et al. (1986) data (see text). Smooth curve drawn to provide an estimate of the effect (Eq. 17).

12, 14) is not a force balance condition; the large scale structure is not some intervening impermeable body between the two streams. Were that the case, a small "imbalance" that would momentarily decrease the velocity difference with respect to one stream would provide a positive feedback and drive the velocity difference with respect to the same stream to zero. This relation show' ... .er be viewed as a non-linear, quasi-stationary phase condition for the large scale structures: any non-abiding flow substructure is subject to accelerations in its own frame, which will ultimately convect it with one or the other stream by the force of the positive feedback mechanism argument above. Perhaps the robustness of the large scale flow structures in this flow can be understood in this light. The positive feedback convection velocity mechanism strips away all other structures! The success of linear stability analyses of these phenomena, at least for subsonic convective Mach numbers, can perhaps also be understood in the same light, since the dominant surviving mode must abide by the same considerations.

Papamoschou & Roshko find that the compressible shear layer growth rate, when normalized by the corresponding incompressible flow growth rate estimated at the same velocity and density ratio, is only a function of the convective Mach number, say, M_{c1}, i.e.

$$\frac{\frac{\delta}{2}(r, s; M_{c1})}{\frac{\delta}{2}(r, s; M_{c1} = 0)} \approx \text{fn}(M_{c1}) . \qquad (16)$$

The Papamoschou & Roshko data are plotted in Fig. 4. The smooth curve is a plot of the function

$$f(M_{c1}) = (1 - f_\infty)e^{-3M_{c1}^2} + f_\infty , \qquad (17)$$

which is drawn as a rough estimate of the effect, with a value for the asymptotic value, f_∞, of 0.2. Also plotted in the same figure are shear layer growth rate estimates computed from the earlier data of Chinzei et al. (1986), which were processed to estimate M_{c1} for each of their runs and normalized to the value of $\delta(M_{c1})/\delta(0)$ at one point (filled circle). See also Bogdanoff (1983) for an additional compilation of earlier data.

5

As can be seen in the data in Fig. 4, the convective Mach number need not be very large for compressibility effects to be significant. Secondly, for $M_{c1} > 0.8$, the growth rate appears to reach an asymptotic value roughly 0.2 of its incompressible counterpart. This is at variance with the results of two-dimensional, linear shear layer stability analyses (e.g. Gropengiesser 1970, Ragab & Wu 1988, Zhuang et al. 1988), which find that the growth rate tends to very small values, as $M_{c1} \to \infty$. Accepting the stability analsis results at face value, the question of the applicability of such an analysis aside for the moment, the discrepancy could be attributable to other factors. In particular, it is possible that three-dimensional modes are more unstable in the limit of large Mach numbers, as was suggested by Sandam & Reynolds (1989). Alternatively, the Papamoschou & Roshko experiments were conducted in an enclosed test section, as opposed to the stability analyses which were carried out for unbounded flow. For supersonic convective Mach numbers, a closed test section can act as a wave guide, providing a feedback mechanism between the growing shear layer structures and the compression/expansion wave system whose energy would otherwise be radiated to the far field (Tam & Morris 1980, Tam & Hu 1988). Finally, recalling our aside, we should at least note that for supersonic (or near supersonic) convective Mach numbers, we expect shocks to form in the flow, a feature that cannot adequately be captured by linear stability analysis.

It should be noted that it is not clear at this writing whether the value of the ratio $\delta(M_{c1})/\delta(0)$, for $M_{c1} \gg 1$, is intrinsic to the behavior of the fully developed compressible shear layer, or depends on the details of the flow geometry, e.g. the distance of the upper and lower flow guidewalls from the layer, whether only one or both streams are supersonic, etc. We recognize that in the context of the potential for hypersonic propulsion, whether the growth rate tends to zero with increasing Mach number or not is an important issue; an ever decreasing shear layer growth with increasing Mach number hardly bodes well for efficient supersonic mixing and combustion!

Papamoschou (1989), subsequently conducted a series of experiments in which he investigated the convection velocity of the large scale structures, for a range of free stream Mach numbers and various gases. In those experiments he found that at high convective Mach numbers the large scale structures seemed to be "dragged" by one stream or another, at variance with the matched pressure recovery model of Eq. 14. See Fig. 5. Papamoschou offered a qualitative description of how shocks could be responsible for this behavior, crediting D. Coles for the suggestion (made before the experiments were conducted) that the effects of shocks needed to be incorporated in the analysis.

We should appreciate that, for supersonic, or transonic, convective Mach numbers, the free stream flow over the turbulent large scale structures can support a system of expansions and shocks. Such a system may serve to isolate, in effect, the large scale turbulent mixing structures from exposure to the full relative free stream velocities. To explore this ansatz a little further, we note that the assumption of isentropic (or approximately matched) pressure recovery from each stream (Eq. 14) will generally be grossly unrealistic at supersonic convective Mach numbers.
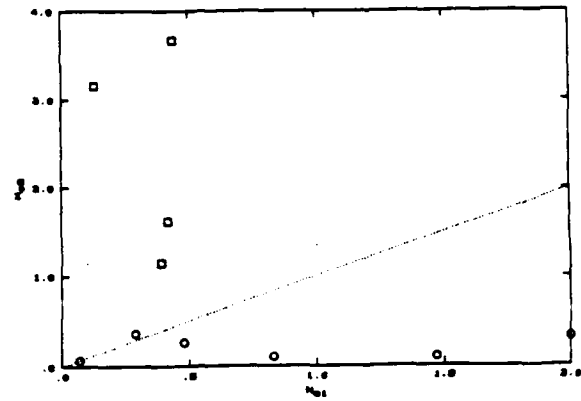

FIG. 5 Experimentally estimated convective Mach numbers for supersonic shear layers. Squares: $M_2 < 1$, circles: $M_2 > 1$. Dotted line corresponds to $M_{c1} = M_{c2}$ and is included for reference (Papamoschou 1989).

In that case, streamlines that end up on interstitial stagnation points from each free stream will have to traverse a shock, or a system of shocks for turbulent flow, to connect to the free stream static conditions and are likely to have suffered a loss in total pressure that may be reasonably well approximated by that of a normal shock. This leads to the following possibilities, depending on which stream has, or can support, shocks. In particular, we can have

a. shocks in the high speed stream, with a shock-free low speed stream, i.e.

$$\frac{p_{t1}/p_1}{p_{t1}/p_{o1}} \approx \frac{p_{t2}}{p_2} ; \qquad (18a)$$

b. low speed stream shocks, shock-free high speed stream, i.e.

$$\frac{p_{t1}}{p_1} \approx \frac{p_{t2}/p_2}{p_{t2}/p_{o2}} ; \qquad (18b)$$

while

c. for shocks in both streams, we must have

$$\frac{p_{t1}/p_1}{p_{t1}/p_{o1}} \approx \frac{p_{t2}/p_2}{p_{t2}/p_{o2}} . \qquad (18c)$$

In these expressions, p_t/p is the isentropic total-to-static pressure ratio (Eq. 14) and p_t/p_o is the pre-/post-normal shock total pressure ratio, given by (for $M_o > 1$),

$$\frac{p_t}{p_o} = \left[1 + \frac{2\gamma}{\gamma + 1} \left(M_o^2 - 1 \right) \right]^{-\frac{1}{\gamma-1}} \left[\frac{2 + (\gamma - 1) M_o^2}{(\gamma + 1) M_o^2} \right]^{-\frac{\gamma}{\gamma-1}} > 1 \qquad (19)$$

(e.g. Liepmann & Roshko 1957, Sec. 2.13). For the purposes of this discussion, this ratio will be estimated using the corresponding convective Mach number(s) M_{ci} for the normal shock Mach number(s) M_o, in each case[‡]. This situation is depicted in the examples in Figs. 6a and 6b, which will be discussed below.

[‡] While the proposed scheme for estimating the total pressure loss may not always be justified (especially for low Reynolds number flow), the important conclusions this simple model affords should not be deferred in the interest of exactitude!
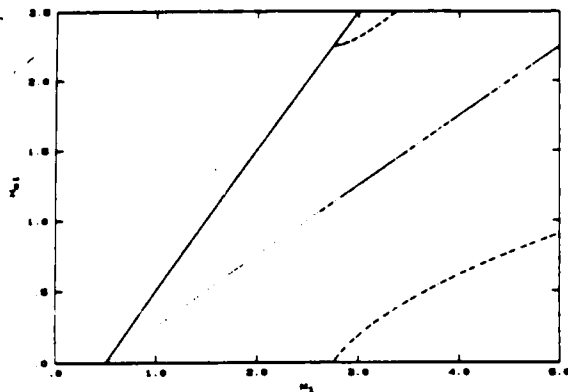
6

FIG. 6a Convective high speed stream Mach number. computed for a fixed (lab frame) subsonic low speed Mach number ($M_2 = 0.5$), as a function of M_1, for $\gamma_1 = \gamma_2 = 1.4$ and matched static speeds of sound. Dotted line: isentropic prediction (no shocks, Eq. 14). Dashed line: high speed stream shock (Eq. 18a). Dot-dash-dash: low speed shock (Eq. 18b). Dot-dot-dash-dash: shocks in both streams (Eq. 18c). Solid line: $U_c = U_2$ ($M_{c1} = \Delta U/a_1$). Realizable solutions ($U_2 < U_c < U_1$) lie below this line.

Several important conclusions can be drawn from the example in Fig. 6a, computed for $\gamma_1 = \gamma_2$ and matched static speeds of sound ($a_1 = a_2$). In this simple model, no shocks can be sustained in a particular free stream unless the corresponding convective Mach number exceeds unity (note that $M_{c1} = M_{c2}$ in this case). That requires relatively high values of the high speed Mach number, even though the low speed Mach number was selected to be low (subsonic), and would require even higher values if both streams were supersonic. In a realistic calculation, shocks would first form for convective Mach numbers close to — but somewhat less than — unity, for much the same reasons as they do on the lifting side of transonic airfoils. For a normal shock (or equivalent total pressure loss) in one stream (upper dashed curve for high speed stream, lower dash-dash-dot curve for low speed stream), the fractional total pressure loss on the side that bears it is such that the shear layer large structures are now essentially carried by the other side. If our pressure balance, quasi-stationary phase condition is to be upheld, the first appearance of a shock in one stream must result in a significant decrease in the relative velocity between the turbulent region large scale structures and that of the *other* free stream. It requires a substantial additional increase in the shock-bearing free stream velocity before the relative velocity with respect to the other stream can increase to the point where shocks could appear there too. Finally, the third possibility, representing a probably precarious balance of (weaker) shocks in both streams, is represented by the dot-dot-dash-dash curve. As expected for this test case (matched γ's, matched a's), the same values of the convection velocity are obtained in the presence of shocks as with the isentropic expression (Eq. 14), since equal pressure recovery is realized from both streams.

A second example, with free stream $\gamma_1 = 5/3$, $\gamma_2 = 1.4$ and fixed *stagnation* speeds of sound in the ratio $a_{2t}/a_{1t} = 0.3$ (*e.g.* $\approx$ helium/air), is presented in Fig. 6b (we note here that the difference between maintaining constant static speeds of sound, *vs.* constant stagnation speeds of sound, is small; the latter perhaps representing the more typical experimental scenario, however). In

this case, the lower speed of sound in the low speed free stream results in the possibility of shocks at a much lower high speed (lab frame) free stream Mach number, than in Fig. 6a. If we imagine the flow first establishing M_2 and then increasing M_1 to some final value, we note that we will initially be on the shock-free branch (dotted line). Shocks are predicted to first appear in the low speed stream, at $M_1 \approx 1.4$. If the flow assumes this configuration, a (lab frame) high speed stream Mach number of $M_1 \approx 2.4$ must be attained before M_{c1} can again become supersonic. Beyond that point, shocks should be expected in *both* streams (dot-dot-dash-dash curve). The predicted behavior for the convection velocity is now different (recall $\gamma_1 \neq \gamma_2$ here) than for the shock-free case. Substantial reductions in the shear supported across major portions of the mixing zone, as well as in the imposed strain rate in the vicinity of the interstitial stagnation points, would be associated with such a flow configuration. In this context, it is interesting that the normalized Papamoschou & Roshko growth rate data (Fig. 4; squares) become independent of the convective Mach number around about where (transonic flow) shocks are first expected (see also Papamoschou 1988, Papamoschou 1989). This observation lends credence to the *ansatz* and should not escape unnoticed.
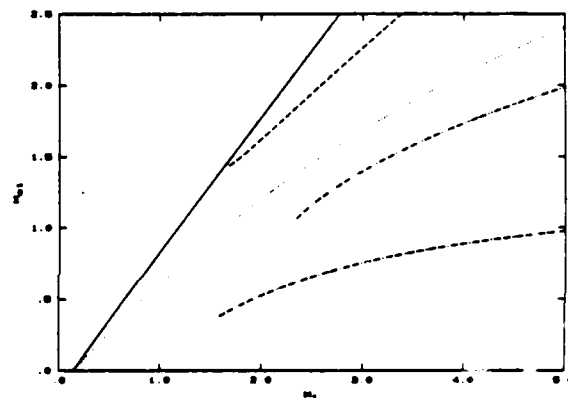

FIG. 6b Convective Mach number with respect to the high speed stream, estimated for $\gamma_1 = 5/3$, $\gamma_2 = 1.4$ and stagnation speed of sound ratio of $a_{2t}/a_{1t} = 0.3$. Other legend as in Fig. 6a.

It may seem strange, at least in the context of this simple model, that the relative free stream velocity in the large structure frame *jumps* to ΔU, or zero, as soon as shocks can form. One might argue, for shock Mach numbers close to unity and since total pressure losses increase very slowly with shock Mach number, that the convection velocity might transition rather more slowly than with a jump. That is not correct, however, since once an imbalance starts, however small, the positive feedback mechanism is operative and the system is driven completely one way or the other.

How the flow chooses which shock configuration it will assume (high speed stream, low speed stream, or both), must await further investigations. It is plausible, however, that under certain flow conditions the flow will make the selection depending on the *downstream pressure/outflow condition*. However strange this may seem in the hyperbolic flow environment of interest here, we should recognize that, in the presence of shocks, total pressure

losses along each of the "free streams", in each case, are quite different. One can hypothesize that the situation is akin to the manner in which supersonic flow over a ramp selects the weak or strong oblique shock solution, depending on the *downstream* pressure condition, the hyperbolic nature of the flow notwithstanding. See, for example, discussion in Courant & Friedrichs (1948, §123). It is interesting that in the Papamoschou (1989) data, it appears that the flow placed the shocks in the low speed stream ($M_{c1} < 1$), when that stream was subsonic ($M_2 < 1$); and in the high speed stream ($M_{c1} > 1$), when that stream was supersonic ($M_2 > 1$). While this difference could be significant in a variety of contexts. we should note that a subsonic low speed stream entends an elliptical flow domain all the way up to the splitter plate tip. changing the manner in which pressure is communicated along the extent of the shear layer. Additionally, in the regime of multiple possible solutions for the convective Mach numbers, and depending on the separate inflow and downstream outflow/pressure conditions. the flow may well exhibit *hysteresis*, as was intimated in the preceding discussion. At Mach numbers that are high enough. however, the flow has little choice but to support shocks in both streams, with Eq. 18c the more appropriate expression for estimating the large scale structure convection velocity U_c. It is interesting that this does not appear to be the case for the highest Mach number runs in the Papamoschou (1989) data (Fig. 5)[*]. The resolution of this and many other issues must await the results of many investigations currently in progress.

Finally, we note that this behavior is likely to prove significant in a different context, with important implications for the entrainment ratio and the mixed fluid composition in the shear layer, as will be discussed below.

2.3 Heat release effects

Some experimental investigations have studied the effects of heat release on the growth rate of chemically reacting shear layers (e.g. Wallace 1981, Hermanson & Dimotakis 1989), as well as experiments with combusting shear layers at high levels of heat release (e.g. Ganji & Sawyer 1980, Pitz & Daily 1983, Daily & Lundquist 1984, Keller & Daily 1985). Important information has also been derived from computations (e.g. McMurtry et al. 1986, McMurtry & Riley 1987), which is in qualitative accord with the experimental findings, even though these computations have perforce been conducted at Reynolds numbers that do not meet the fully developed flow criterion of Eq. 1.

One might argue that dilatation owing to heat release in a chemically reacting shear layer, which is confined to the shear layer wedge, might result in an *increase* in shear layer growth. While the basis of that intuition is well founded, the inference is not. One does observe a *displacement* velocity in the far field away from the shear layer, that increases with the amount of heat released. This can be measured experimentally as a displacement thickness δ^*/x, by noting the angle of, say, the lower free stream flow guide wall

[*] We should note, however, that the diagnostic used for those estimates would tend to be more sensitive to the behavior of small structures at the free stream edges, rather than the convection velocity of the largest scales of the flow in the interior of the layer.

required to maintain a non-accelerating flow ($dp/dx = 0$), as a function of the amount of heat release. See Fig. 7.
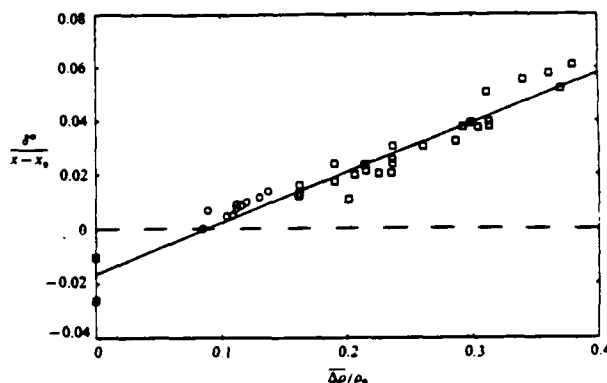

FIG. 7 Normalized shear layer displacement thickness vs. heat release. Circles: Mungal (unpublished) data. Squares: Hermanson & Dimotakis (1989).

At least for subsonic flow and equal free stream densities, other parameters held constant, one observes a *decrease* in the shear layer growth rate, with increasing heat release. This behavior is depicted in the data of the 1% thickness in Fig. 8, taken from Hermanson & Dimotakis (1989, Fig. 5). Note that, in these experiments, the pressure gradient was maintained close to zero by adjusting the lower stream guide wall as necessary. These data suggest that the decrease in the shear layer growth rate with heat release is approximately given by ($q = \Delta\rho/\rho$, see Eq. 7)

$$\frac{\frac{\delta}{x}(r = 0.4, s = 1; q)}{\frac{\delta}{x}(r = 0.4, s = 1; q = 0)} \approx 1 - C_q q, \quad \text{with} \quad C_q \approx 0.05 . \tag{20}$$

While these experiments were conducted at a fixed velocity ratio $r = 0.4$ and matched free stream densities ($s = 1$), one can speculate that heat release effects manifest themselves as a reduction in the growth rate coefficient C_δ (Eqs. 9, 10), with Eq. 20 expressing the dependence of C_δ on q. In any event, the effect of heat release on the growth rate is slight (see also Daily & Lundquist 1984).
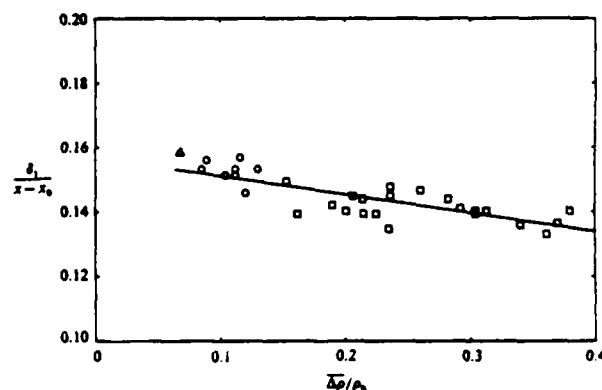

FIG. 8 Normalized 1% thickness vs. heat release. Triangle: Wallace (1981), circles: Mungal (unpublished data), squares: Hermanson & Dimotakis (1989). Note displaced origin.

8

The physical implication is that the outward displacement velocity owing to heat release impedes the entrainment process to an extent that more than offsets the effects of dilatation. It is interesting that this reduction in growth rate is also found to be consistent with the assumption that the heat release and dilatation effects leave the $\overline{u'v'}$ velocity correlation largely unaltered. The reduction in the growth rate can then be approximately accounted for by noting the reduction in the turbulent stress $\tau = \overline{\rho u'v'}$ in the layer; a result of the reduction in the density profile $\rho(y/x)$ owing to heat release. It should be noted that it would probably be difficult to argue for such an assumption *a priori*. See discussion in Hermanson & Dimotakis (1989, Secs. 5.2 and 5.4).

At high Reynolds numbers, a substantial volume fraction in the turbulent shear layer is taken by fluid that is *not* molecularly mixed (independently estimated to be roughly 1/2 at the conditions of the Hermanson & Dimotakis experiments) so that, even with fast chemical reactions characterized by very large adiabatic flame temperatures, there will be a limiting value of the expected reduction in $\Delta\rho/\rho$ within the layer owing to heat release. This is a consequence of the large pockets of unmixed fluid, whose density is essentially unaltered by the combustion process. This behavior is illustrated by the data in Fig. 9, where the estimated mean density reduction $\Delta\rho/\rho_0$ is plotted *vs.* the normalized adiabatic temperature rise $\Delta T_f/T_0$. These data were recorded at high Reynolds numbers ($Re \approx 6 \times 10^4$), for several values of the free stream stoichiometric mixture ratio ϕ, an important quantity that we will discuss below in the context of chemical reactions.
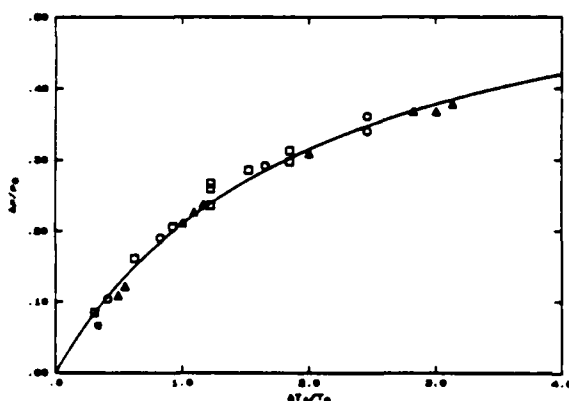

FIG. 9 Mean density reduction $\Delta\rho/\rho$ *vs.* adiabatic flame temperature rise $\Delta T_f/T_0$, where T_0 is the (common) free stream temperature. Squares/asterisk: $\phi = 1$; circles: $\phi = 1/2$; triangles: $\phi = 1/4$. Solid symbols: Mungal & Dimotakis (1984); open symbols: Hermanson & Dimotakis (1989); asterisk: Wallace (1981). Smooth line computed using Eq. 21 (see text).

A useful test model of the behavior with increasing heat release is one in which vortical structures tend to a configuration of low density, (hot) cores and are surrounded by irrotational, recently entrained, unmixed (cold) fluid. Using this cartoon, the expected mean density reduction in the combustion zone can be

estimated. In the notation of Eq. 4, we find

$$\frac{\Delta\rho}{\rho_0} \approx \frac{\left(\frac{\delta_P}{\delta}\right)\frac{\Delta T_f}{T_0}}{1 + \left(\frac{\delta_P}{\delta_m}\right)\frac{\Delta T_f}{T_0}} . \tag{21a}$$

The smooth line in Fig. 9 was computed using this expression, with the constant (heat release independent) values of

$$\frac{\delta_m}{\delta} = 0.63 , \quad \text{and} \quad \frac{\delta_P}{\delta_m} = 0.5 . \tag{21b}$$

It is interesting that the resulting curve does as well as it does, suggesting that the simple model may have merit even at modest values of the heat release. As we shall see, the inferred value of 0.63 of the mixed fluid fraction δ_m/δ is a little high. It should be noted, however, that the mean density reduction values in Fig. 9 were estimated using the reciprocal of the mean temperature measured in the combustion zone, as opposed to the mean of the reciprocal temperature, which would have provided better estimates. Additionally, of course, the mixed fluid fraction is not likely to be exactly constant, *i.e.* independent of $\Delta T_f/T_0$.

2.4 Pressure gradient effects

The effects of pressure gradient on shear layer growth were discussed by Sabin (1965) and have been investigated in non-reacting shear layers (Rebollo 1973), and in reacting shear layers (Keller & Daily 1985, Hermanson & Dimotakis 1989) for incompressible flow conditions. In the case of a favorable pressure gradient ($dp/dx < 0$) and equal free stream densities ($s = \rho_2/\rho_1 = 1$), it was found (Hermanson & Dimotakis 1989) that the decrease in the growth could be accounted by interpreting Eq. 9 as a local relation. The argument, which was suggested by M. Koochesfahani and is akin to some of the ideas put forth by Sabin (1965), is summarized below.

The local rendition of the Abramowich-Sabin relation (Eq. 9) becomes

$$\frac{d\delta}{dx} \approx C_\delta \frac{1 - r(x)}{1 + r(x)} , \tag{22a}$$

with

$$r(x) = \frac{U_2(x)}{U_1(x)} \tag{22b}$$

the local velocity ratio. This can be computed by applying the Bernoulli equation in each of the free streams, and yields

$$r(x) = r_0 \sqrt{\frac{1 - C_{p_2}(x)}{1 - s r_0^2 C_{p_2}(x)}} , \tag{23a}$$

where

$$r_0 \equiv \frac{U_2(0)}{U_1(0)} \tag{23b}$$

is the free stream velocity ratio at $x = 0$,

$$C_{p_2}(x) \equiv \frac{p(x) - p(0)}{\frac{1}{2}\rho_2 U_2^2(0)} \tag{23c}$$

is the local pressure coefficient normalized by the low speed stream dynamic head at $x = 0$, and $s = \rho_2/\rho_1$ is the free stream density ratio. It can be seen that a favorable pressure gradient is expected to decrease or increase the shear layer growth rate, depending on whether the product $s r_0^2$ is less or greater than unity, respectively. Conversely for an unfavorable pressure gradient.

9

For a specified pressure gradient, Eq. 23 for the local velocity ratio can be used to integrate the local growth rate Eq. 22 to yield the local shear layer width $\delta\left[C_{p_2}(x)\right]$ at the station x. The results of this procedure are in accord with the observed effects, at least for the range of values of the pressure coefficient at the measuring station that were investigated (Hermanson & Dimotakis 1989, Sec. 8).

3. Mixing: δ_m/δ

As alluded to in the preceding discussions, one finds that, at sufficiently high Reynolds numbers, a substantial fraction of the fluid within the δ/x shear layer wedge is not molecularly mixed. Additionally, at least for incompressible shear layers, the available evidence suggests that the mixed fluid in a turbulent shear layer exhibits the following characteristics:

a. The mixed fluid composition (averaged across the shear layer width δ/x) is *not* generally centered around a 50:50 mixture, but favors a composition that is a function of the free stream density and velocity ratio.

b. The amount of mixed fluid, beyond the downstream location where the shear layer has attained fully developed, three-dimensional flow status (*e.g.* Eq. 1), depends weakly on the local flow Reynolds number. The evidence suggests that, at least for gas phase flows, it decreases as the Reynolds number increases.

Finally,

c. the mixed fluid fraction δ_m/δ is found to depend on the fluid Schmidt number $Sc \equiv \nu/\mathcal{D}$ (Eq. 3).

A large number of models are employed today in efforts to account for the observed turbulent shear layer mixing phenomena and while they all differ in the details of their implementation, they can be classified, in my opinion, into two main categories: models that ultimately rely on some form of Reynolds averaging and/or turbulent gradient transport, and ones that do not. In the discussion that follows, models which cannot account for the characteristics listed above will not be considered in the attempt to account for shear layer mixing phenomena. While it *could* be argued that this need not be so, this criterion — to the best of my knowledge — presently eliminates models which rely on gradient transport ideas. For an opposing viewpoint the reader is directed to the review article by Bilger (1989). Unfortunately, since molecular mixing takes place throughout the spectrum of spatial and temporal scales, direct computations at high Reynolds numbers are out of the question for now, at least, and we must resort to some kind of modeling for some time.

It may appear surprising that *Schmidt* number effects are given so much weight, when it could be argued that most turbulent mixing/combustion phenomena are encountered in gas phase flows. There are two issues here. First, while it may be that *most* turbulent combustion occurs in gas phase flows, it is certainly not so that *all* of it does (*cf.* underwater, liquid metal, particulate combustion, *etc.*). Secondly, if we are to formulate

models on which we must rely for predictions and design outside the range of experience that was used to validate them — and not just use them as interpolative french curves — we must at least require that they adequately account for the *known* turbulent mixing behavior. In the case of Schmidt number effects, the issue is particularly important, in as much as those effects are a direct manifestation of, and provide important clues to, the role of the small mixing scales of the problem, which *must* be correctly accounted for (if not described) by turbulent mixing models.

3.1 The mixing transition

The flow in a two-dimensional shear layer issuing from a smooth splitter plate with a sharp trailing edge and low turbulence level free streams originally develops as two-dimensional flow. This flow is characterized by large, two-dimensional, vortical structures (*e.g.* Winant & Browand 1974, Corcos & Sherman 1984), but is susceptible to a three-dimensional instability mode of counter-rotating streamwise vortices (Konrad 1976, Bernal 1981, Alvarez & Martinez-val 1984, Corcos & Lin 1984, Daily & Lundquist 1984, Browand 1986, Bernal & Roshko 1986, Metcalfe *et al.* 1987, Knio & Ghoniem 1988, Lasheras & Choi 1988), which spawn the transition to three-dimensional, fully developed turbulent flow, leading to substantial increases in the mixed fluid fraction (Konrad 1976, Bernal *et al.* 1979, Breidenthal 1981, Roberts 1985, Koochesfahani & Dimotakis 1986). This is illustrated in the liquid phase flow laser-induced fluorescence data reproduced in Fig. 10, recorded before ($Re \approx 2 \times 10^3$) and after ($Re \approx 2.3 \times 10^4$) the mixing transition, respectively. Note that in the pre-mixing-transition data the entrained fluids *participate in the large scale motion but remain essentially un-mixed*. Under these conditions, the surface-to-volume ratio of the two-dimensional interfacial area between the two entrained fluids is relatively small. In particular, when multiplied in water ($\mathcal{D} \approx \nu/600$) with the small local transverse diffusion thickness straddling this interface, *i.e.*

$$\lambda_\mathcal{D} \propto \sqrt{\mathcal{D}/\sigma}\,, \tag{24}$$

where σ is the (local) strain rate[**], it yields a negligible mixed fluid volume fraction δ_m/δ within the shear layer width δ/x.

The attendant explosive increase in interfacial area following the mixing transition changes this tally, resulting in a mixed fluid fraction, under these conditions, of

$$\delta_m/\delta \approx \begin{cases} 0.26\,, & \text{in water;} \\ 0.49\,, & \text{in gas phase flow} \end{cases} \tag{25}$$

(we will substantiate these values below).

It is interesting that the growth rate of the shear layer does not appear to respond to this mixing transition, suggesting that it is dominated by the two-dimensional large scale dynamics (see Fig. 3 and also discussion in Corcos & Lin 1984). The evolution of $\delta(x)$ and $\delta_m(x)$ through the mixing transition is sketched in Fig. 11.

[**] See Marble & Broadwell (1977), Broadwell & Breidenthal (1982), and Dimotakis (1987, Sec. 2.2).

FIG. 10 Liquid phase shear layer mixing digital (y, t) image data at a fixed streamwise location x (Koochesfahani & Dimotakis 1986). Left image: pre–mixing-transition ($Re \approx 2 \times 10^3$). Right image: post–mixing-transition ($Re \approx 2.3 \times 10^4$).
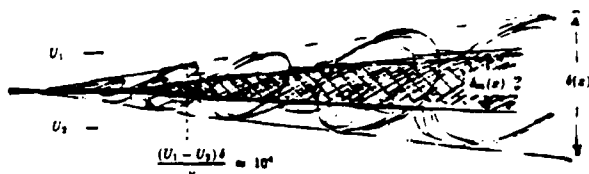

FIG. 11 Sketch of the shear layer and gas phase mixed fluid thickness growth through the mixing transition.

It is not clear how this picture is altered by compressibility effects, or even whether the criterion of a minimum local Reynolds number of 10^4 will be good when the convective Mach numbers become large. The depressed growth rate of the two-dimensional Kelvin-Helmholz disturbances, discussed in the previous section, may well alter the environment in which the three-dimensional motions develop, which are vital for the large interfacial area generation. See also Demetriades (1980); Demetriades, Ortwerth & Moeny (1981); and Demetriades & Brower (1982). At higher convective Mach numbers, shocks must certainly be expected to play an important role in this process. Whether that role enhances a transition to three-dimensionality and improved mixing, or not, must also await future investigations.

3.2 Entrainment ratio

We can think of the growth of the shear layer region δ/x as the increasing participation of free stream fluid in the turbulent process, i.e. the *entrainment*, as the downstream distance from the splitter plate increases. From this point of view, the preceding discussion on shear layer growth addresses the *total* entrainment flux from each of the two free streams, without regard as to the relative amounts from free stream, i.e. the entrainment flux *ratio*. It is clear, however, that the entrainment flux ratio, supplied to the mixing processes of turbulence, must be taken into account in the tally of the resulting range of compositions of the mixed fluid.

An important conclusion drawn by Konrad (1976) was that *a shear layer entrains fluid from each of the two free streams in an asymmetric way*, even for equal free stream densities. In particular, for equal free stream densities ($s = 1$) and a free stream speed ratio of $r = 0.38$, Konrad estimated a volume flux entrainment ratio of $E \approx 1.3$. For a free stream density ratio of $s = 7$ (high speed He, low speed N_2) and the same velocity ratio, he estimated an entrainment ratio of $E \approx 3.4$.

Brown (1974) proposed an estimate for the entrainment based on the free stream velocity ratio, as seen from the frame of the large scale structures, i.e. $E \approx (U_1 - U_c)/(U_c - U_2) \approx s^{1/2}$. The density ratio dependence of this proposal is in accord with the ratio ($3.4/1.3 \approx 2.6 \approx \sqrt{7}$) of the two estimates from Konrad, but cannot account for the asymmetric entrainment ratio for equal free stream densities. This behavior can be understood, however, in terms of the upstream/downstream asymmetry that a given large scale vortical structure sees in a spatially growing shear layer and the fact, also noted by Fiedler (1975) in a different context, that a vortex entrains from each stream from its "lee side". See Fig. 12. Simple arguments (Dimotakis 1984) suggest that, for a similarly growing shear layer, the volume flux entrainment ratio can be estimated by the expression

$$E \approx \frac{U_1 - U_c}{U_c - U_2} \left(1 + \frac{\ell}{x} \right) , \qquad (26)$$

where ℓ/x is the large structure spacing-to-position ratio. The quantity in parentheses is always greater than unity and the consequence of the spatial growth of the shear layer and the self-similarly increasing large structure spacing with streamwise distance. It would be equal to unity for a temporally growing layer. Fitting the available data, one finds that the relation ($r = U_2/U_1$),

$$\frac{\ell}{x} \approx C_\ell \frac{1 - r}{1 + r} , \qquad (27a)$$

with

$$C_\ell \approx 0.68 , \qquad (27b)$$

is a good representation for ℓ/x, independently of the free stream density ratio.

We argued that, for incompressible flow, $(U_1 - U_c)/(U_c - U_2) \approx s^{1/2}$ (Eq. 13). Consequently, for matched free stream densities and Konrad's free stream speed ratio of 0.38, we estimate (Eq. 26)

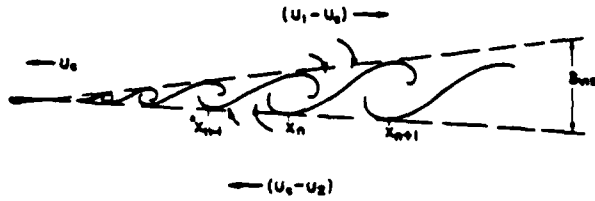$$E(r = 0.38, s = 1) \approx \left(1 + \frac{\ell}{x} \right) \approx 1.3 .$$

11

FIG. 12 Large structure array and induction velocities in vortex convection frame.

For the He/N_2 shear layer data at the same speed ratio, we estimate

$$E(r = 0.38, s = 7) \approx 7^{1/2} \times 1.3 \approx 3.4 ,$$

in rather good agreement with Konrad's experimental values. The arguments that lead to the proposed expression for the entrainment ratio (Eq. 26) should also be valid for compressible flow, noting, however, that U_c must now be computed accordingly (i.e. Eqs. 14 or 18, as appropriate). We also expect that a revision of Eq. 27 would be necessary. A first guess is that it might scale with δ/x as it does for subsonic flow, i.e.

$$\frac{\ell}{x}(r, s; M_{c1} \to 0) \propto \frac{\delta}{x}(r, s = 1; M_{c1} \to 0) ,$$

with a plausible extension of the form

$$\frac{\ell}{x}(r, s; M_{c1}) \approx C_\ell \frac{1-r}{1+r} f(M_{c1}) , \qquad (28)$$

where $f(M_{c1})$ is an estimate of the Papamoschou & Roshko compressibility effect in the shear layer growth, e.g. Eq. 17, as was assumed by Dimotakis & Hall (1987).

It is useful to keep track of the mixing process and the resulting range of compositions by defining a conserved scalar ξ denoting the volume (or mole) fraction of high speed stream fluid in the mixture (e.g. Bilger 1980). Accordingly, $\xi = 0$ corresponds to pure low speed stream fluid, $\xi = 1$ represents pure high speed stream fluid, and $\xi = 1/2$ represents a 50:50 mixture. We call this a *conserved* scalar because its integral over any volume V can only change as a result of ξ-fluxes through the bounding surfaces of V. In particular, it cannot be altered by any turbulent/mixing/chemical processes in its interior. In this notation, the entrainment ratio E measures the flux of $\xi = 1$ fluid that is entering the turbulent mixing region, per unit flux of $\xi = 0$ fluid.

The asymmetric entrainment ratio suggests a zeroth order model for mixing in a two-dimensional shear layer, entraining $\xi = 1$ and $\xi = 0$ fluid from each of the free streams at a ratio E, respectively, that was assumed by Konrad (1976) in the analysis of his concentration fluctuation data. The two entrained fluids are mixed by the efficient action of the turbulence, and can be expected to tend towards a mixed fluid composition of

$$\xi_E = \frac{E}{E+1} . \qquad (29)$$

A useful cartoon (Fig. 13) is that of a bucket being filled by two faucets running with unequal flow rates, as a laboratory stirring device mixes the effluents. We can also think of a hot/cold water faucet and the (average) temperature in the bucket; it is only a function of the ratio of the two flow rates. For all the complexity of the ensuing turbulent motion, we would expect to find a probability density function (PDF) of mixed fluid compositions in the bucket clustered around the value of the mixture fraction given by Eq. 29, where E in our cartoon corresponds to the ratio of the flux from each of the two faucets. Fluid homogenized at this composition is an important component in the mixing model by Broadwell & Breidenthal (1982), as we will discuss below. One can appreciate that the range of compositions one should expect to encounter in the bucket depends on the relative rate of inflow to mixing. As we lower the combined faucet flow rate, keeping the ratio and the stirring fixed, we expect the mixed fluid to be homogenized with a composition PDF tending to a Dirac delta function at ξ_E, i.e.

$$p(\xi)d\xi \to p_H(\xi)d\xi = \delta_D(\xi - \xi_E)d\xi , \qquad (30)$$

in the limit. Similarly for a fixed faucet flow rate as the stirring rate is increased. See, for example, Levenspiel (1962).
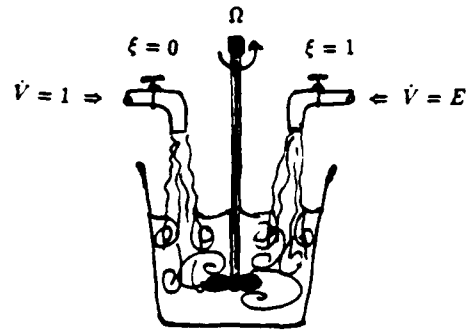

FIG. 13 Stirred bucket mixing. E corresponds to the right/left faucet flow rate ratio. Note that as the stirring rate is increased, at fixed faucet flow rate, $p(\xi)d\xi \to \delta_D(\xi - \xi_E)d\xi$, where $\xi_E = E/(1 + E)$.

The effects of the asymmetric entrainment ratio can be seen in the PDF measurements by Konrad (1976) made in a gas phase, matched free stream density ($\frac{1}{3}He : \frac{2}{3}Ar)/N_2$ shear layer experiment, using an aspirating probe (Brown & Rebollo 1972). See Fig. 14. Note that the most probable value of the high speed fluid fraction ξ, denoted as $C(N_2)$ in the figure, is very close to $\xi_E \approx E/(1 + E) = 0.57$, corresponding to the (independently) estimated matched density entrainment ratio of $E \approx 1.3$ (see Konrad 1976 for details).

Similar results were obtained in water (Koochesfahani & Dimotakis 1986), where the PDF was measured using laser induced fluorescence techniques in a shear layer at the same velocity ratio. See Fig. 15. Note that the most probable value of the composition is again very close to the $\xi_E \approx 0.57$ value. Notable in both sets of measurements is the fact that this most probable value is observed
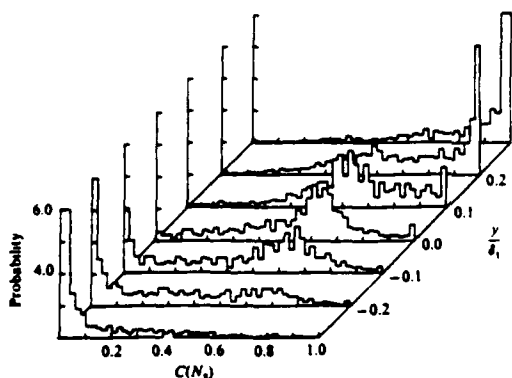
FIG. 14 Gas phase, high speed fluid mixture fraction PDF measurements (Konrad 1976) in a matched density, $r = U_2/U_1 \approx 0.4$ shear layer beyond the mixing transition. High speed fluid mixture fraction ξ is denoted by $C(N_2)$.

throughout the shear layer. This can be understood in terms of the circumferential velocities, in the frame of the large scale vortical structures, which can transport a fluid element from one side of the turbulent region to the other, before it has much chance to alter its own internal mean composition. A comparison of the gas phase and liquid phase data suggest that, as expected at the higher Schmidt numbers in the latter case, this is more the case in the liquid than in the gas. It should be noted, however, that lower resolution in the gas phase measurements could account for some of the observed trends. These observations are at variance with the results of gradient transport based PDF modeling efforts (*e.g.* Pope 1981, Kollmann & Janicka 1982), which yield a most *probable value of ξ for the mixed fluid that is close to the local* value of the mean mixture fraction profile (mixed and unmixed), *i.e.* $\bar{\xi}(y)$.
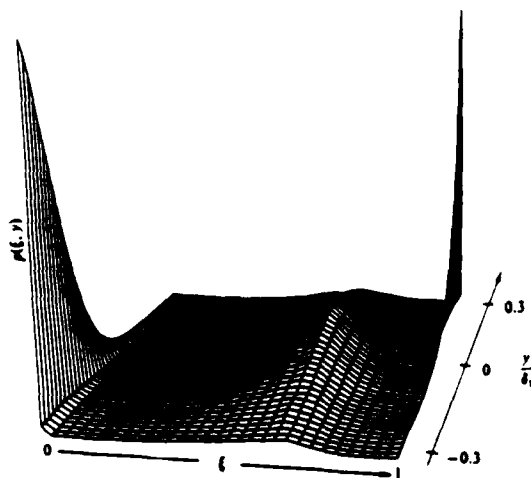

FIG. 15 High speed fluid mixture fraction PDF measurements in a liquid phase (matched density), $r = U_2/U_1 \approx 0.38$ shear layer at $Re = 2.3 \times 10^4$ (Koochesfahani & Dimotakis 1986, PDF computed from the run that yielded the post-mixing-transition image in Fig. 10).

Important consequences of the asymmetric entrainment ratio and the resulting "tilt" in the mixed fluid composition are to be

found in chemically reacting shear layers. In particular, in the case where the reactant concentrations are not carried by the free streams at the stoichiometric ratio, which side carries the *lean* reactant can make an easily discernible difference in the amount of chemical product formed in the layer. This was illustrated in the liquid phase "flip" experiments of Koochesfahani *et al.* (1985) in which the mixed fluid at a range of compositions $0 < \xi < 0.36$ was compared in a complementary run to the mixed fluid at a range of compositions $0.64 < \xi < 1$, using a pH–sensitive, laser induced fluorescence technique. See Fig. 16. The "chemical product" is many times larger in the second case, which marks the high values of ξ in the local composition. Note also that there is no systematic gradient in the labeled mixed fluid concentration across the shear layer δ/x width. It should be emphasized that these experiments, which were designed to illustrate the potential of this effect, were conducted in the mixing transition region where the remnants of the much larger asymmetries in the initial roll-up have yet to be amortized with entrainment at the asymptotic values of the entrainment ratio (*e.g.* Eq. 26). See pre-mixing-transition image in Fig. 10 data and Koochesfahani & Dimotakis (1986, Fig. 12 and related discussion). Similar conclusion were drawn by Masutani & Bowman (1986), in their gas phase measurements in the mixing transition region, and by Sandam & Reynolds (1987), in their computational modeling of the shear layer at low Reynolds number.

FIG. 16 Mixing transition laser induced fluorescence "flip" experiment. Left picture: Fluorescence from mixed fluid compositions in the range $0 < \xi < 0.36$. Right picture: fluorescence from compositions in the range $0.64 < \xi < 1$ (from Koochesfahani *et al.* 1985).

A sufficient distance beyond the mixing transition, the observed asymmetries are consistent with the asymptotic values of E and the associated "tilt" in the mixed fluid composition PDF in Fig. 15. See chemically reacting data at higher Reynolds numbers in Koochesfahani & Dimotakis (1986, Figs. 16 and 17). These and other mixing issues in subsonic turbulent shear layers will be discussed in the context of chemically reacting shear layers, which must be relied on for data at the high Reynolds numbers of interest here.

4. Chemical reactions: δ_P/δ

In the case where the entrained fluids are not premixed and can react, the associated chemical product formation can obviously proceed no faster than the rate at which the reactants are mixed on a molecular scale by the turbulent flow. Considering a vertical slice of the turbulent region of streamwise extent dz, located at some downstream location z, the mixed fluid fraction δ_m/δ within the transverse extent δ of the turbulent region occupied by molecularly mixed fluid (in the mean) represents an important upper bound for the expected chemical product fraction δ_P/δ within the layer at that location. In the case of (non-premixed reactant) combustion, it also bounds the heat release corresponding to the amount of chemical product formed.

In the limit of fast chemistry, i.e. a chemical kinetic rate that is sufficiently large so as not to be the limiting process in the rate of chemical product formation, the fraction of molecularly mixed fluid that is converted to chemical product, i.e. δ_P/δ_m, depends on the resulting PDF $p(\xi)\,d\xi$ of molecular mixture compositions within the turbulent region. In particular, it depends on the distribution of mixture fractions ξ of high-speed fluid to low-speed fluid in the molecularly mixed fluid, relative to the stoichiometric mixture fraction ξ_ϕ required for complete consumption of the available (entrained) reactants, as we will discuss below.

If the chemical kinetics are not sufficiently fast by the previous measure, the chemical product formation will lag behind the rate at which the reactants are mixed on a molecular scale by the turbulence. As a consequence, δ_P/δ_m will be smaller, depending also on the ratio (Damköhler number)

$$Da \equiv \frac{\tau_m}{\tau_\chi} . \tag{31}$$

of the expected time τ_m required for mixing, to the time τ_χ required to complete the ensuing chemical reactions. What is also important from a diagnostics vantage point is the recognition that, for chemical/flow systems that can be regarded as kinetically fast, i.e. in the limit of $Da \to \infty$, measurements of the chemical product volume fraction δ_P/δ can be combined to provide us with reliable estimates of molecular mixing and δ_m/δ, as well as the distribution of compositions of the molecularly mixed fluid, as we will discuss below. This often obviates the need for direct measurements of these quantities, which would, for the most part, have been infeasible at the high Reynolds numbers of interest here. Direct computations fair no better, as the behavior of fast chemical systems can result in reaction zones that are even thinner that the expected diffusion scales (e.g. Eq. 24) under these conditions.

In the context of mixing, we will restrict the discussion that follows to the behavior in the limit of fast chemical kinetics ($Da \to \infty$). Chemical product formation for finite Damköhler numbers, however, is important theoretically in as much as it depends not only on the state of the flow at the measurement location but also on the flow history. It is also important from an applications vantage point, for example, as the impetus for ever increasing flight speeds is forcing us to consider chemical product formation at high Mach numbers that is not only limited by the rate of mixing but also by the chemical kinetics.

Data on the Damköhler number dependence of the product volume fraction in a gas phase, subsonic shear layer were documented by Mungal & Frieler (1988). An analysis of these data in terms of the Broadwell-Breidenthal-Mungal model we will discuss below can be found in Broadwell & Mungal (1988). An attempt to incorporate a more realistic account of a complex chemical system was made by Dimotakis & Hall (1987), using the bucket zeroth order mixing model described above (Fig. 13). The reader is directed to those references for an account.

4.1 Dependence on the stoichiometric mixture ratio

Consider the idealized case of the high speed stream carrying a reactant at a concentration (mole fraction) X_{01}, and the low speed stream carrying a reactant at a concentration X_{02}, which can react infinitely fast to form a chemical product, associated with an enthalpy release $\Delta\mathcal{H}$. An important quantity, in this context, is the *stoichiometric mixture ratio* ϕ, defined as the volume (number of moles) of high speed fluid that carries sufficient reactants to consume a unit volume (mole) of low speed fluid, i.e.

$$\phi \equiv \frac{X_{02}/X_{01}}{(X_{02}/X_{01})_{st}} , \tag{32}$$

where the quantity subscripted by "st" in the denominator denotes the concentration ratio of a stoichiometric mixture. For example, a (free stream) stoichiometric mixture ratio of $\phi = 4$ implies that a mixture of 4 parts of high speed fluid per part of low speed fluid is required for complete consumption of all reactants. Accordingly, complete consumption of all reactants will occur at a stoichiometric (high speed fluid) mixture *mole fraction*

$$\xi_\phi = \frac{\phi}{\phi+1} . \tag{33}$$

We can see that a mixture fraction of $\xi < \xi_\phi$, for example, will be lean in high speed fluid reactants, and will result in unreacted low speed chemicals. Similar definitions can also be employed on a mass basis (e.g. Kuo 1986, Sec. 1.8).

Consider, for example, the chemical reaction between hydrogen and fluorine which, in the limit of fast chemistry, we can simplify as a one step reaction (see Mungal & Dimotakis 1984 for details)

$$H_2 + F_2 \longrightarrow 2HF \quad \text{with} \quad \Delta\mathcal{H} = -130\,kcal/mole . \tag{34}$$

and which was used in many of the experiments that will be cited below. A mixture of 1% H_2 in 99% N_2 and an equal volume of 1% F_2 in 99% N_2 is stoichiometric and will result in an adiabatic (flame) temperature rise owing to the heat released of $\Delta T_f = 93\,K$. A shear layer with a high speed stream fluid comprised of 4% H_2 + 96% N_2, and a low speed stream fluid of 1% F_2 + 99% N_2 would be characterized by $\phi = 1/4$, i.e. 1/4 parts of high speed fluid must be mixed, per part of low speed fluid, for complete reaction.

For equal heat and species diffusivities, i.e. for Lewis numbers $Le \equiv \kappa/\mathcal{D} = Sc/Pr = 1$, the adiabatic flame temperature rise $\Delta T_f(\phi)$ is the highest temperature rise that can be observed in the flow and serves as a convenient normalization of the observed mean temperature rise $\Delta T(y,\phi)$ in the reaction zone. Note that in a mixture where X_{01} is kept constant and the stoichiometric mixture ratio ϕ is changed by varying X_{02} (Eq. 32), keeping the heat capacities constant in the process, the dependence of the adiabatic flame temperature rise on ϕ is given by

$$\Delta T_f(\phi) = \frac{2\phi}{\phi+1}\,\Delta T_f(1) = 2\xi_\phi\,\Delta T_f(1) . \tag{35}$$

Experimental data for the normalized mean temperature rise, for matched free stream density ($s = 1$), a free stream velocity ratio of $r \approx 0.4$, gas phase reacting shear layers at low heat release, are plotted in Fig. 17 for $\phi = 1/8, 1$, and 8. The plotted quantity reflects the local mean fraction of the total chemical product (heat release) possible under the circumstances. There is a shift towards the lean side of the location of the peak mean temperature rise. There is also a marked asymmetry in the total amount of product (heat release) between the low-ϕ and the high-ϕ runs, which, in view of the the relation between the entrainment ratio E and the (required) stoichiometric mixture ratio ϕ, is clear in this context. In particular, for $\phi < E$, for example, fluid homogenized at the entrainment ratio will be low speed stream reactant lean ($\xi_\phi < \xi_E$) and result in unconsumed high speed stream reactants.
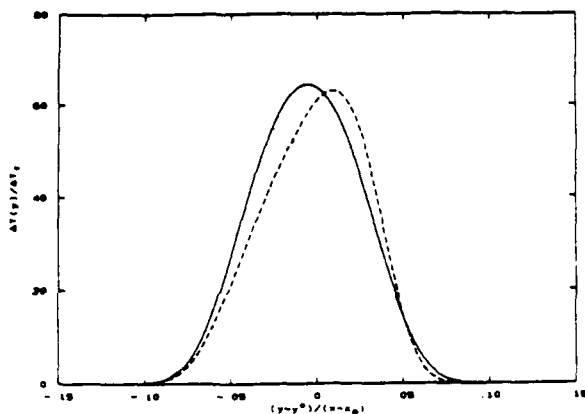
FIG. 17 Gas phase shear layer: Normalized chemical product at low heat release. Solid line: $\phi = 1$, dashed line: $\phi = 8$. dotted line: $\phi = 1/8$ (Mungal & Dimotakis 1984; $s = 1$, $r \approx 0.4$). Note peak temperature rise tilt towards the lean side for $\phi \neq 1$ and the larger total chemical product for $\phi \gg 1$ relative to $\phi \ll 1$, corresponding to an entrainment ratio of $E > 1$.

The maximum amount of product is expected at $\phi \approx E$, with more product for $\phi \gg 1$ than for $\phi \ll 1$, for $E > 1$ (recall that $E \approx 1.3$ under these conditions). Note also that, consistently with our observation that a substantial fraction of fluid is unmixed within the shear layer, the mean temperature rise is everywhere less than $0.65 \Delta T_f$.

It is interesting to compare these ⊥ ɯ to the corresponding data from a liquid phase (matched density) ..emically reacting shear layer at the same free stream speed at· ,·· = 0.4). These are depicted in Fig. 18, for $\phi = 1/10$ and $\phi = 10$. Note the reduced amount of product *relative to the gas phase results, the asymmetry between the high-ϕ and low-ϕ runs* ($E \approx 1.3$ here also), but that the tilt towards the lean side is no longer there. We can understand the differences attributable to Schmidt number effects on the basis of our preceding discussions. In particular, the reduction in the total chemical product is attributable to the reduction in the amount of molecularly mixed fluid at the higher Schmidt number (lower species diffusivity). The absence of a tilt of the peak mean temperature towards the lean side is the result of the delayed (slower) molecular mixing which provides a longer Langrangian time for homogenization to occur at the larger than diffusion scales across the whole shear layer transverse extent, owing to the large structure motion (recall discussion of data in Fig. 15). See also discussion in Broadwell & Mungal (1988).

4.2 Relation to the PDF. Schmidt number effects

These results would all be derivable from the local PDF $p(\xi, y)$ of the mixture fraction at the measuring station at z, if that were available. In particular, the product (or heat release) that can be produced corresponding to a particular value of the mixture fraction ξ is easily computed by assuming complete consumption of the lean reactant. This yields two straight lines in ξ, joining at ξ_ϕ where the normalized product is equal to unity, i.e.

$$\theta(\xi;\xi_\phi) = \begin{cases} \dfrac{\xi}{\xi_\phi}, & \text{for } 0 \le \xi \le \xi_\phi ; \\[2mm] \dfrac{1-\xi}{1-\xi_\phi}, & \text{for } \xi_\phi \le \xi \le 1 \end{cases} \tag{36}$$

(see, for example, Kuo 1986, Sec. 1.9). This dependence is depicted in Fig. 19 for $\phi = 1/8, 1, 8$.
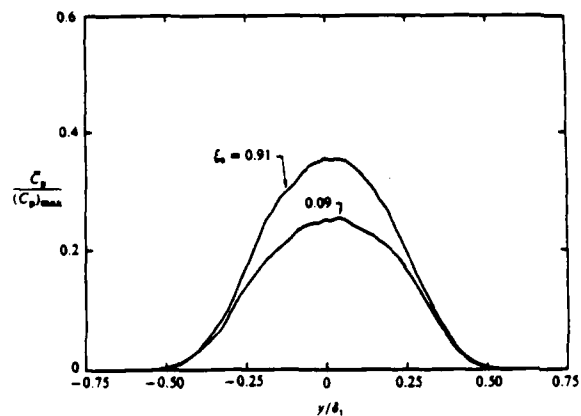

FIG. 18 Liquid phase shear layer: Normalized chemical product at low heat release, for $\phi = 1/10, 11$ (Koochesfahani & Dimotakis 1986; $s = 1$, $r \approx 0.4$). Note symmetric chemical product distribution for both $\phi \gg 1$ and $\phi \ll 1$. ξ_s in the figure denotes ξ_ϕ (Eq. 33).
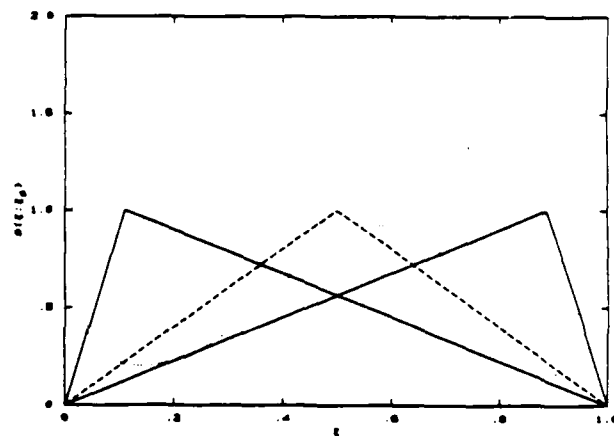

FIG. 19 Normalized chemical product function $\theta(\xi;\xi_\phi)$ for $\phi = 1/8, 8$ (solid lines), and $\phi = 1$ (dashed line). PDF is sketched (dotted line) for reference, corresponding to $E \approx 1.3$ (cf. Fig. 17).

The average chemical product volume (mole) fraction δ_P/δ can be computed as the integral of the normalized product profile in the interior of the shear layer,

$$\frac{\delta_P(\xi_\phi)}{\delta} = \frac{1}{\delta} \int_{-\infty}^{\infty} \frac{\Delta T(y, \phi)}{\Delta T_f(\phi)} \, dy , \tag{37a}$$

or as an integral over the PDF of mixture fractions, since

$$\frac{\Delta T(y, \phi)}{\Delta T_f(\phi)} = \int_0^1 \theta(\xi;\xi_\phi) p(\xi, y) \, d\xi , \tag{37b}$$

where $\theta(\xi;\xi_\phi)$ is the triangular normalized product function (Eq. 36). Experimental values of this quantity are included in Fig. 20, for a gas phase reacting shear layer at $Re = 6.4 \times 10^4$ (Mungal & Dimotakis 1984), as a function of the stoichiometric mixture fraction ξ_ϕ. Also included in that figure is a point at $\phi = 10$ (Koochesfahani & Dimotakis 1986, $\xi_\phi = 0.91$) for a liquid phase shear layer at a comparable Reynolds number ($Re = 7.8 \times 10^4$).

The triangular normalized product function $\theta(\xi;\xi_\phi)$ suggests the use of chemically reacting experiments to estimate some statistics of the mixed fluid PDF. In particular, for $\xi_\phi \to 0$ and $\xi_\phi \to 1$, the ratio of the corresponding product volume fractions can be used to estimate the
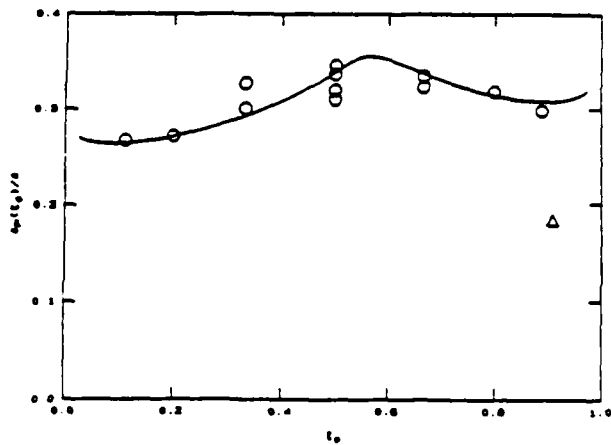
FIG. 20 Chemical product volume fraction δ_P/δ vs. ξ_ϕ for $r \approx 0.4$ and matched free stream densities. Circles: gas phase data (Mungal & Dimotakis 1984) $Re = 6.4 \times 10^4$. Triangle: liquid phase data (Koochesfahani & Dimotakis 1986) $Re = 7.8 \times 10^4$. Smooth curve drawn to aid the eye.

average composition $\bar{\xi}_m$ in the mixed fluid. For a small $\xi = \xi_0 - 0$, we find

$$\bar{\xi}_m \approx \frac{\delta_P(1 - \xi_0)}{\delta_P(\xi_0) + \delta_P(1 - \xi_0)} . \tag{38}$$

sing the experimentally determined liquid phase values of

$$\frac{\delta_P(\xi_\phi)}{\delta} = \begin{cases} 0.125 , & \text{at } \xi_\phi = \xi_0 = 0.09 ; \\ 0.165 , & \text{at } \xi_\phi = 1 - \xi_0 = 0.91 . \end{cases} \tag{39}$$

we then estimate a value of $\bar{\xi}_m \approx 0.57$ (Koochesfahani & Dimotakis 1986). This agrees with the value of $\xi_E = E/(E + 1)$, calculated with the independently estimated value of the volume flux entrainment ratio $E \approx s^{1/2}(1 + \ell/z) \approx 1.3$ (Eqs. 26, 27, 13).

This idea was also used to estimate the dependence of the mean mixed fluid composition in a recent set of experiments (Frieler & Dimotakis 1988) in subsonic, low heat release, gas phase shear layers with unequal free stream densities ($s \neq 1$), for which the expected asymmetries in the entrainment ratio can be large (Eqs. 13 and 26). The resulting data are plotted in Fig. 21 for free stream density ratios in the range of $0.1 < s < 4$, and compared to the estimated value of ξ_E, using the subsonic expression for the volume flux entrainment ratio discussed in the previous paragraph.

Comparing the triangular product functions for small and large ξ_ϕ, we also note that, except for omitting the end-points, they are essentially the complements of each other. Consequently, for the case of negligible heat release, we find

$$\frac{\delta_m}{\delta} \approx (1 - \xi_0)\left[\frac{\delta_P(\xi_0)}{\delta} + \frac{\delta_P(1 - \xi_0)}{\delta}\right] .$$

This represents the mixed fluid fraction, if the edge contributions from the regions $0 < \xi < \epsilon$ and $1 - \epsilon < \xi < 1$ are excluded from the mixed fluid tally. In this approximation, $\epsilon \approx \xi_0/2$, corresponding to the gas phase chemical reaction product function, and $\epsilon \approx \xi_0$ for the liquid phase data. Using the values for the liquid phase chemically reacting layer (Eq. 39), with $\epsilon \approx \xi_0 = 0.09$, we then estimate ($s = 1$)

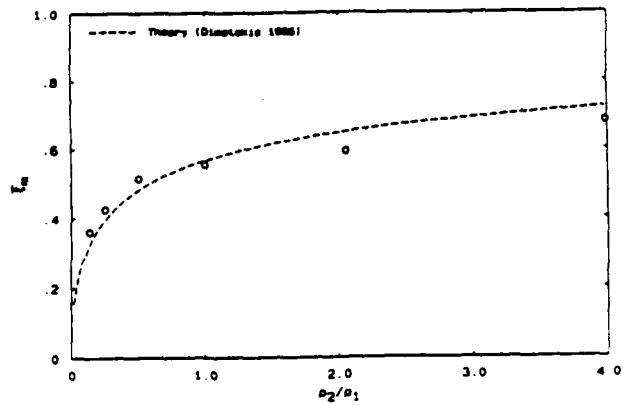$$\left(\frac{\delta_m}{\delta}\right)_{liq} \approx 0.26 . \tag{40a}$$

FIG. 21 Estimated average high speed fluid mixture fraction as a function of the density ratio (Frieler & Dimotakis 1988). Dashed line depicts the estimated dependence of ξ_E on the density ratio.

A similar calculation was also made using the results of the low heat release gas phase data vs. free stream density ratio of Frieler & Dimotakis. Small dilatation corrections were applied to those data, which are of first order for this quantity. The results are plotted in Fig. 22 as a function of the free stream density ratio. It is significant that the mixed fluid fraction is found to be essentially independent of the density ratio, even as the mixed fluid composition depends rather strongly on it. The mixed fluid fraction derived from these data for matched free stream densities is then found to be ($\epsilon \approx \xi_0/2 \approx 0.05$)

$$\left(\frac{\delta_m}{\delta}\right)_{gas} \approx 0.49 . \tag{40b}$$

The estimates in Eqs. 40a and 40b were the values quoted in Eq. 25 for this quantity.
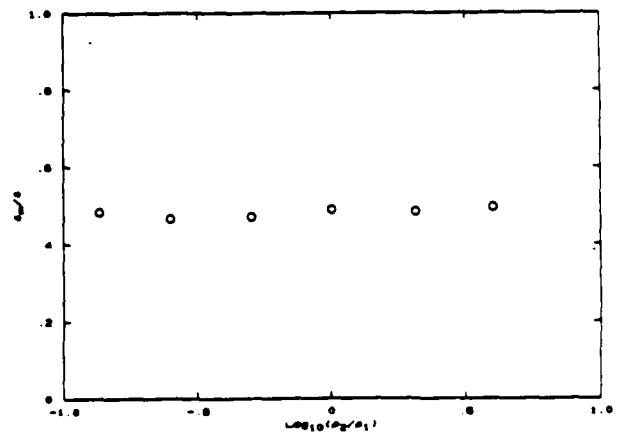

FIG. 22 Mixed fluid fraction as a function of the free stream density ratio $s = \rho_2/\rho_1$. Gas phase data from Frieler & Dimotakis (1988).

4.3 Reynolds number effects

The existing experimental evidence suggests that chemical product formation and the resulting chemical product volume fraction observed at a station x is a (weak) function of the local Reynolds number, at least in the case of gas phase flows. The corresponding gas phase and liquid phase data appear in Fig. 23. Note that for the gas phase data, the product volume fraction is found to decrease slowly with increasing Reynolds number. Liquid phase data exhibit an even weaker Reynolds number dependence, if any, even though the lower Reynolds number value of $Re \approx 2.3 \times 10^4$ in those data may not be sufficiently above the mixing transition to be used for the comparison. It should also be noted that the shear layer growth rate in these runs was also changing. While this variation was normalized out by taking the ratio of the product thickness δ_P and the shear layer (1%) thickness $\delta_{1\%} \approx \delta_{vis}$, to compute the chemical product volume fraction, it should be noted that the shear layer thickness also changed with Reynolds number, sometimes by a larger amount than the change in the estimated product volume fraction documented in Fig. 23 (recall Figs. 2 and 3 and related discussion).
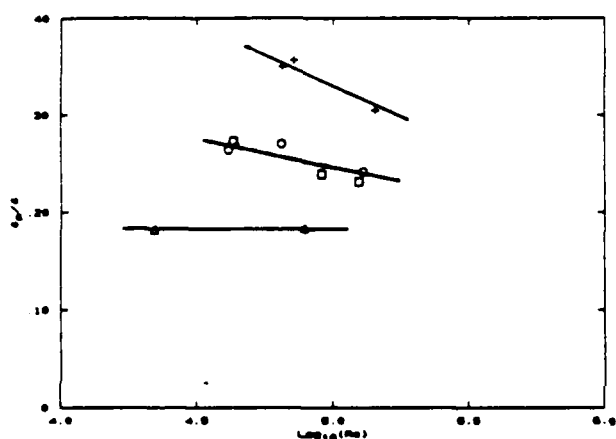

FIG. 23 Reynolds number dependence of product fraction δ_P/δ. Gas phase data: Circles (laminar initial boundary layer) and squares (turbulent boundary layer) from low heat release data of Mungal et al. (1985, $\phi = 1/8$, $\Delta T_f \approx 186 K$). Crosses from the higher heat release data of Hermanson & Dimotakis (1989, $\phi = 1$, $\Delta T_f \approx 368 K$). Liquid phase data: Triangles from Koochesfahani & Dimotakis (1986, $\phi = 10$).

A proposal for an explanation of Reynolds number and Schmidt number effects was first made by Broadwell & Breidenthal (1982). The suggestion in that model was that the mixed fluid PDF can be modeled as a superposition of the $p_H(\xi)$ PDF corresponding to the homogeneously mixed fluid in the bucket cartoon, and the contribution from thin interfacial diffusion layers interspersed in the shear layer, and which separate pure $\xi = 0$ and $\xi = 1$ fluid. Some revisions and clarifications were made in the more recent discussion of this model by Broadwell & Mungal (1988). The Broadwell-Breidenthal-Mungal (BBM) model then yields for the mixed fluid PDF, i.e. for $\xi \neq 0$ and $\xi \neq 1$,

$$p(\xi)\,d\xi \approx \left[C_H\,\delta_D(\xi - \xi_E) + \frac{C_F}{\sqrt{Sc\,Re}}\,p_F(\xi) \right] d\xi .\qquad (41)$$

where $\delta_D(\xi)$ denotes the Dirac delta function. The Reynolds number and Schmidt number dependence in this superposition arises from modeling the amount of mixed fluid taken as residing in the diffusive interfaces ("flame sheets"). The coefficients C_H and C_F are assumed to be constants of the flow and, in particular, independent of the Schmidt and Reynolds number. The proposed Schmidt number and Reynolds number dependence in the BBM model is equivalent to the assumption that

the interfacial diffusion layer thicknesses can be modeled by scaling the relevant strain rate using the local outer flow variables, i.e. $\sigma \sim \Delta U/\delta$ (see Eq. 24), and that the associated interfacial surface-to-volume ratio is independent of the Reynolds number. It should be noted, however, that BBM base their model on Lagrangian arguments, for which the reader is directed to the references cited. These authors suggest that the model should apply for $Re \gg 1$, $\sqrt{Sc\,Re} \gg 1$ and $\sqrt{Re} \gg \ln Sc$, even though the latter inequality would automatically be satisfied at the Reynolds numbers of interest here (Broadwell & Mungal 1988).

Integrating the proposed PDF over ξ, excluding the contributions of the unmixed fluid at $\xi = 0$ and $\xi = 1$, we then obtain for the BBM model estimate of the mixed fluid fraction

$$\frac{\delta_m}{\delta} \approx C_H + \frac{C_F}{\sqrt{Sc\,Re}} .\qquad (42)$$

A similar result is obtained for the product fraction $\delta_P(\xi_\phi)/d$, in which the dependence of the homogeneous mixture contribution on ξ_ϕ is given by (see Eq. 36) $\theta(\xi_E;\xi_\phi)$, and the dependence of the flame sheet contribution is given by (see Broadwell & Mungal 1988)

$$F(\xi_\phi) = \frac{e^{-z_\phi^2}}{\sqrt{\pi}\,\xi_\phi(1-\xi_\phi)} , \qquad \text{where} \qquad \text{erf}\,z_\phi = 2(\xi_\phi - \frac{1}{2}) \quad (43)$$

The constants C_H and C_F in the BBM model are to be determined by fitting the data, e.g. the Schmidt number dependence of δ_m/δ (Eq. 42). The proposed PDF is depicted in Fig. 24, with the Dirac delta function contribution represented by a narrow gaussian of the appropriate area, corresponding to an entrainment ratio of $E = 1.3$.
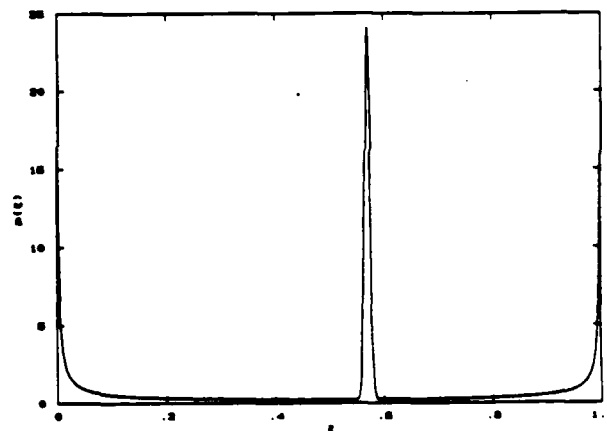

FIG. 24 Broadwell-Breidenthal-Mungal model PDF. See Broadwell & Breidenthal (1982).

In the BBM estimates for δ_m/δ and δ_P/δ, the "flame sheet" contribution vanishes at large Schmidt numbers. The gas/liquid difference is then accounted for by noting that the mixed fluid, in that case, is limited to the homogeneously mixed fluid at the composition $\xi \approx \xi_E$. Similarly, the gas phase expressions asymptote to the liquid value at high Reynolds numbers. Conversely, the BBM model predicts that there should be no Schmidt number dependence at high Reynolds numbers. For gas phase flow, the predicted BBM dependence on Reynolds number is stronger (algebraic) than the one (logarithmic) suggested by the data (Fig. 23), but nicely simulates the much weaker Reynolds number dependence of the liquid phase data. Finally, we should note that, according to the BBM model, the mixed fluid and chemical product volume fraction does not depend on the fluid kinematic viscosity, being a function of the Peclet number, $Pe \equiv \Delta U\,\delta/D = Sc \times Re$, only. See Broadwell & Mungal (1988) for more details.

17

It is interesting that similar conclusions have also been arrived at by Kerstein (1988, 1989), using a phenomenological Monte-Carlo model to represent the mechanics of turbulent transport and mixing. In his numerical simulations, Kerstein arrives at results for the mixed fluid and chemical product formed in a shear layer that are in accord with the BBM result expressed in the form of Eq. 42.

It could be argued that the strain rate at the interfacial surface formed by the turbulent flow between the entrained pure fluids from each of the free streams should be estimated as a function of the distribution of spatial scales associated with that interface. In particular, one could argue that the predominant fraction of the surface-to-volume ratio S would be associated with the smallest scales in the flow, which, for $Sc \approx 1$, would be in the vicinity of the Kolmogorov (1941) scale

$$\lambda_K = \left(\frac{\varepsilon^3}{\nu}\right)^{1/4} , \qquad (44a)$$

where $\varepsilon \propto (\Delta U)^3/\delta$ is the expected local kinetic energy dissipation rate per unit mass. This yields

$$S \sim \frac{1}{\lambda_K} \sim \frac{1}{\delta} Re^{3/4} , \qquad (45)$$

in the limit of large Reynolds numbers. The expected strain rate at those spatial scales would be proportional to the reciprocal of the Kolmogorov time $t_K = \sqrt{\nu/\varepsilon}$, or in terms of the outer variables of the flow,

$$\sigma_K \propto \frac{\Delta U}{\delta} Re^{1/2} . \qquad (44b)$$

For $Sc \approx 1$, an estimate of the mixed fluid fraction scaling might be obtained as the product of the expected diffusion thickness $\lambda_D \sim \sqrt{D/\sigma}$ (Eq. 24), at the small scales, and the surface-to-volume ratio S of Eq. 45. It is interesting that this simple tally yields a *Reynolds number independent estimate*, to leading behavior, *for the mixed fluid fraction* (see also discussion in Dimotakis 1987, Sec. 3.3).

As a rebuttal to this argument, we recognize that the interfacial surface will be characterized by the full spectrum of turbulent scales and the associated distribution of strain rates. Accordingly, one might attempt a tally in which this distribution is accounted for, with closure requiring the assignment of a normalized statistical weight to each scale λ within the bounds of the turbulent flow. Such a model has been attempted (Dimotakis 1987), where it was argued that the statistical weight $w(\lambda) d\lambda$ of a scale λ in the self-similar inertial range must be given by

$$w(\lambda) d\lambda \propto \frac{d\lambda}{\lambda} \qquad (46)$$

as the only scale-invariant group that can be formed, and that the flow behavior below the Kolmogorov scale cannot alter this distribution in the range $\lambda_B < \lambda < \lambda_K$, where $\lambda_B = \lambda_K/\sqrt{Sc}$ is the (Batchelor 1959) diffusion scale. This is equivalent to assuming that all scales are equally probable and that the statistical weight of a scale λ is therefore given by the surface-to-volume ratio of that scale, i.e. $S(\lambda) \sim 1/\lambda$ (see Dimotakis 1987 for details). This leads to an estimate for the mixed fluid fraction of

$$\frac{\delta_m}{\delta} \approx \frac{B_1(Sc)}{B_0(Sc) + \frac{3}{4}(1 - \frac{x}{4})\ln(Re/Re_{cr})} , \qquad (47)$$

where the functions $B_0(Sc)$ and $B_1(Sc)$ are determined by the calculation, $\mu \approx 0.3$ is the dissipation rate fluctuation coefficient (Kolmogorov 1962, Oboukhov 1962), and $Re_{cr} \approx 26$. The model is in accord with the observed dependence of the chemical product on the stoichiometry of the free streams, as well as the Schmidt number and Reynolds number dependence of the chemical product and mixed fluid volume fractions. It also predicts an ever decreasing chemical product and mixed fluid fraction with increasing Schmidt number (decreasing species diffusivity). As can be seen in the resulting expression for δ_m/δ, however, it predicts that

the mixed fluid volume fraction is also an ever decreasing function of the Reynolds number, albeit slowly. This is a rather robust consequence of the $w(\lambda) d\lambda$ statistical weight distribution that was assumed. On the other hand, *small* departures from this distribution would alter this behavior in the limit, without resulting in discernible differences within the range of Reynolds numbers typically achievable in the laboratory.

It need not be emphasized that the dependence and limiting behavior of the mixing processes on Reynolds number is of considerable significance not only theoretically but also from an applications vantage point.

5. Discussion and conclusions

For all the progress that has been made in addressing problems of mixing and combustion in turbulent shear flows, it is clear that important issues remain, yet to be resolved. Many of these arise from the complexity and constraints imposed on these flows for a diverse set of reasons, which fundamental research often has the luxury of ignoring. Just as significant, however, are the problems that can be considered important and fundamental from any perspective, whose resolution would not only advance our understanding of turbulence, mixing and combustion, but would also have a direct impact on technology and applications. As Boltzmann used to say: *There is nothing more practical than a good theory!*

While there are many problems that emerge from the preceding discussion, there are three, in my opinion, that merit closer future scrutiny. They are: the apparent dependence of the far field behavior of high Reynolds number flows on initial conditions, the limiting behavior of high Reynolds number turbulence as the Reynolds number is increased to very large values, and the nature of turbulence under compressible flow conditions. The discussion that follows on these is necessarily more in the nature of speculation. In Sir Arthur's words: *It is dangerous to theorize without data!*

To paraphrase one of the conclusions of the discussion on shear layer growth, it is surprising that the initial conditions seem to determine what appears to be the asymptotic behavior of the turbulent shear layer. Should that interpretation survive future scrutiny, it must be considered a remarkable manifestation of what the equations of motion are clearly capable of doing in principle, but flies in the face of traditional assumptions about the behavior of turbulence in the limit of high Reynolds numbers. Additionally, unless an explanation and an accounting can be formulated for this behavior, it also complicates the analysis, simulation and modeling of these flows in that this behavior will appear as a non-unique response to seemingly similar flow conditions. To the extent that we cannot mix any faster than the shear layer grows, the stakes, both theoretically and from an applications standpoint, are not small, as measured by the range of empirical values of the shear layer growth coefficient C_δ of almost a factor of 2 (Eqs. 10, 11).

Turning the coin around, we can see the potential for substantial benefits from flow control: if we can get, or ...lose, a factor of 2 by doing hardly anything at all, think what we can do if we try! There is a growing body of evidence that the suggestion is not without merit, as can be seen from the work cited on the response of shear layers to external forcing (footnote, Sec. 2.1), many others that have not been included here, as well work currently in progress.

It is important to understand the mechanism by which the initial conditions are felt by the flow thousands of momentum thicknesses downstream of the splitter plate trailing edge. It will be interesting to examine this issue and the clues that may be offered by the various research efforts

in supersonic shear layers in progress. As the flow change from elliptic to hyperbolic, the communication channels between different portions of the flow become a function of the Mach number of the two streams as well as the respective convective Mach numbers that result. In that context, however, we must also recall the strong suggestion of non-unique, possibly hysteretic behavior within a range of Mach numbers and/or flow history and conditions, that may wreak havoc with the actual operation and performance of mixing devices in this regime. We will return to this point later.

In considering Reynolds number effects, it may be useful to think about a *gedanken* experiment in which the Reynolds number is varied by controlling the test section or combustor *pressure*, at fixed geometry and free stream speeds. This would control the Reynolds number (at fixed Schmidt number) through a change in the molecular diffusivity coefficients, leaving most other flow parameters unaltered. Such a scheme would still change the Reynolds number of the initial conditions (recall Figs. 2, 3, related caveats and previous discussion), as well as the expected number of large scale structures between the splitter plate trailing edge and a fixed measuring station (Dimotakis & Brown 1976). *Nevertheless, it would leave the scaling with respect to the local outer flow variables unaltered* and make it easier to argue for (or even discern, should such experiments be undertaken in the future) the subtle dependence of turbulence and mixing on the fluid Reynolds number, at fixed Schmidt number. If the dynamic range of Reynolds numbers in such experiments are large enough, one might obtain important clues about the behavior of turbulence as the Reynolds number is increased without limit. This is all the more important as the experimental evidence suggests that the mixed fluid fraction is decreasing with increasing Reynolds *number, in a Reynolds number regime untouchable by the foreseeable* computing community, conventional models silent on the issue, and disagreement between two models that have stuck their necks out at this writing!

Even in the unlikely event that compressible turbulence proves to be an even better mixer than its incompressible counterpart, it seems clear that we should expect to find a reduced overall mixing rate at high Mach numbers, relative to incompressible flow. If the growth rate, absent external disturbances and mixing devices, is diminished by a factor of five, or so, there is little the turbulent interior can do to offset this reduction.

A second potentially important difference in behavior can be gleaned from the discussion of the entrainment ratio and the behavior of the large scale structure convection velocity under supersonic conditions. In particular, in a flow regime where the evidence and simple arguments suggest that shocks may be borne by one free stream or another, but not both, *we expect much larger potential asymmetries in the entrainment* ratio than in incompressible flow. To make matters worse, it is possible that it may prove difficult to predict or control which direction the asymmetry may be realized. This is of considerable significance in the context of the expected composition of the mixed fluid, to the extent that one may not be able to predict and design for even the stoichiometry at which the combustion may have to be asked to take place within a shear layer zone. Moreover, it is a behavior that may exhibit large changes in response with small changes in Mach number.

As regards the mixing process itself, it is an issue about which we can only speculate, at present. Our views of compressible turbulence are limited and not well substantiated. Some of the mainstays of incompressible turbulence, like the Kolmogorov similarity theories, may have to be revised if not abandoned as supersonic convective Mach numbers admit shocks running through the flow. There is evidence that in cases where the driving field can generate eddies at intermediate scales, these similarity ideas cease to apply. In the case of shocks running through a

turbulent flow characterized by density inhomogeneities, baroclinic generation of vorticity will form such eddies (*e.g.* Haas & Sturtevant 1987, Brouillette 1989), which will both influence and be influenced by subsequent shocks that visit (*e.g.* Hesselink & Sturtevant 1988). Secondly, in an environment that is characterized by limits in the *speed*, on the one hand, and couples density fluctuations particularly efficiently to acoustically radiated power, as the Mach number increases, fluctuations and mixing may become dear commodities. On the other hand, this behavior could depend rather strongly on whether this is confined or open flow, as noted in our discussion on stability analysis (Tam & Morris 1980, Tam & Hu 1988, Sec. 2.2) and by H. Hornung in private discussions, with the *sign* of the outcome possibly dependent on the details!

It may be worth concluding by stating what is perhaps obvious, namely that, from an applications point of view, *enhancement* of shear layer growth and mixing is not always the objective. While it may be, if one is interested in combustion efficiency and propulsion, it certainly is not in the case of film cooling of hypersonic propulsion devices, aerodynamic windows for high power chemical lasers, *etc.* What is at a premium here is the mastering of the fundamental physics of these phenomena, which will permit the optimization and control of their behavior for the specific, complex and sometimes unanticipated purposes at the outset, in each case.

7. References

ABRAMOWICH, G. N. [1963] *The Theory of Turbulent Jets* (MIT Press).

ALVAREZ, C. and MARTINEZ-VAL, R. [1984] "Visual measurement of streamwise vorticity in the mixing layer", *Phys. Fluids* 27(9), 2367-2368.

BATCHELOR, G. K. [1959] "Small-scale variation of convected quantities like temperature in turbulent fluid. Part 1. General discussion and the case of small conductivity", *J. Fluid Mech.* 5, 113-133.

BATT, R. G. [1975] "Some Measurements on the Effect of Tripping the Two-Dimensional Shear Layer", *AIAA J.* 13(2), 245-247.

BERNAL, L. P. [1981] *The Coherent Structure of Turbulent Mixing Layers. I. Similarity of the Primary Vortex Structure. II. Secondary Streamwise Vortex Structure*, Ph. D. thesis, California Institute of Technology.

BERNAL, L. P., BREIDENTHAL, R. E., BROWN, G. L., KONRAD, J. H. and ROSHKO, A. [1979] "On the Development of Three Dimensional Small Scales in Turbulent Mixing Layers", 2nd Int. Symposium on Turb. Shear Flows (Imperial College, London), 2-4 July 1979, published in: Turbulent Shear Flows 2 (Eds. Bradbury, L. J. S. et al., Springer-Verlag), 305-313.

BERNAL, L. P. and ROSHKO, A. [1986] "Streamwise vortex structure in plane mixing layers", J. Fluid Mech. 170, 499-525.

BERS, A. [1975] "Linear waves and instabilities", In Physique des Plasmas (eds. C. DeWitt & J. Peyraud), 117-213 (Gordon and Breach, New York).

BILGER, R. W. [1980] "Turbulent Flows with Nonpremixed Reactants", Turbulent Reacting Flows (Springer-Verlag, Topics in Applied Physics 44 (1980, Ed. P. A. Libby, F. A. Williams), 65-113.

BILGER, R. W. [1989] "Turbulent Diffusion Flames", Ann. Rev. Fluid Mech. 21, 101-135.

BRIGGS, R. J. [1964] "Electron-stream interaction in plasmas", Research Monograph No. 29, Cambridge, Mass. (M.I.T. Press).

BOGDANOFF, D. W. [1983] "Compressibility Effects in Turbulent Shear Layers", AIAA J. 21(6), 926-927 (TN).

BRADSHAW, P. [1966] "The Effect of Initial Conditions on the Development of a Free Shear Layer", J. Fluid Mech. 26(2), 225-236.

BREIDENTHAL, R. E. [1981] "Structure in Turbulent Mixing Layers and Wakes Using a Chemical Reaction", J. Fluid Mech. 109, 1-24.

BROADWELL, J. E. and BREIDENTHAL, R. E. [1982] "A Simple Model of Mixing and Chemical Reaction in a Turbulent Shear Layer", J. Fluid Mech. 125, 397-410.

BROADWELL, J. E. and MUNGAL, M. G. [1988] "Molecular Mixing and Chemical Reactions in Turbulent Shear Layers", 22nd International Symposium of Combustion (Seattle, Wash.), 14-18 August 1988 (to appear).

BROUILLETTE, M. [1989] On the Interaction of Shock Waves with Contact Surfaces Between Gases of Different Densities, Ph. D. thesis, California Institute of Technology.

BROWAND, F. K. [1986] "The Structure of the Turbulent Mixing Layer", Physica D 18, 135-148.

BROWAND, F. K. and LATIGO, B. O. [1979] "Growth of the Two-Dimensional Mixing Layer from a Turbulent and Non-Turbulent Boundary Layer", Phys. Fluids 22(6), 1011-1019.

BROWN, G. L. [1974] "The Entrainment and Large Structure in Turbulent Mixing Layers", 5th Australasian Conf. on Hydraulics and Fluid Mechanics, 352-359.

BROWN, G. L. and REBOLLO, M. R. [1972] "A Small, Fast-Response Probe to Measure Composition of a Binary Gas Mixture", AIAA J. 10(5), 649-652.

BROWN, G. L. and ROSHKO, A. [1971] "The Effect of Density Difference on the Turbulent Mixing Layer", Turbulent Shear Flows, AGARD-CP-93, 23.1-12.

BROWN, G. L. and ROSHKO, A. [1974] "On Density Effects and Large Structure in Turbulent Mixing Layers", J. Fluid Mech. 64(4), 775-816.

COLES, D. [1981] "Prospects for Useful Research on Coherent Structure in Turbulent Shear Flow", Proc. Indian Acad. Sci. (Eng. Sci.) 4(2), 111-127.

COLES, D. [1985] "Dryden Lecture: The Uses of Coherent Structure", 23rd AIAA Aerospace Sciences Meeting, 14-17 January 1985 (Reno, Nevada), AIAA Paper 85-0506.

CORCOS, G. M. and LIN, S. J. [1984] "The mixing layer: deterministic models of the turbulent flow. Part 2. The origin of the three-dimensional motion.", J. Fluid Mech. 139, 67-95.

CORCOS, G. M. and SHERMAN, F. S. [1984] "The mixing layer: deterministic models of the turbulent flow. Part 1. Introduction and the two-dimensinoal flow", J. Fluid Mech. 139, 29-65.

COURANT, R. and FRIEDRICHS, K. O. [1948] Supersonic Flow and Shock Waves (Interscience, New York).

DAILY, J. W. and LUNDQUIST, W. J. [1984] "Three dimensional structure in a turbulent combusting mixing layer", 20th Symposium (International) on Combustion (The Combustion Institute), 487-494.

DEMETRIADES, A. [1980] "Necessary conditions for transition in a free shear layer", AFOSR-TR-80-0442.

DEMETRIADES, A. and BROWER, T. L. [1982] "Experimental Study of Transition in a Compressible Shear Layer", Annual Report (Montana State U.), AFOSR Grant No. 80-0267, distributed as AFOSR-TR-83-0144.

DEMETRIADES, A., ORTWERTH, P. J. and MOENY, W. M. [1981] "Laminar-Turbulent Transition in Free Shear Layers", AIAA J. 19(9), 1091-1092 (SYN).

DIMOTAKIS, P. E. [1984] "Two-dimensional shear-layer entrainment", 22nd AIAA Aerospace Sciences Meeting, 9-12 January 1984 (Reno, Nevada), Paper 84-0368. Published, AIAA J. 24(11), 1791-1796 (1976).

DIMOTAKIS, P. E. [1987] "Turbulent shear layer mixing with fast chemical reactions", US-France Workshop on Turbulent Reactive Flows (Rouen, France), 7-10 July 1987. Turbulent Reactive Flows, (eds.) R. Borghi and S. N. B. Murthy Lecture Notes in Engineering 40 (Springer-Verlag, New York, 1989), 417-485.

DIMOTAKIS, P. E. and BROWN, G. L. [1976] "The Mixing Layer at High Reynolds Number: Large-Structure Dynamics and Entrainment", J. Fluid Mech. 78(3), 535-560 + 2 plates.

DIMOTAKIS, P. E. and HALL, J. L. [1987] "A simple model for finite chemical kinetics analysis of supersonic turbulent shear layer combustion", AIAA/SAE/ASME/ASEE 23rd Joint Propulsion Meeting (La Jolla, CA), 29 June - 1 July 1987, AIAA Paper 87-1879.

DZIOMBA, B. and FIEDLER, H. E. [1985] "Effect of initial conditions on two-dimensional free shear layers", J. Fluid Mech. 152, 419-442.

FIEDLER, H. E. [1975] "On Turbulence Structure and Mixing Mechanism in Free Turbulent Shear Flows", Turbulent Mixing in Non-Reactive and Reactive Flows (ed. S. N. B. Murthy, Plenum Press), 381-409.

FRIELER, C. E. and DIMOTAKIS, P. E. [1988] "Mixing and Reaction at Low Heat Release in the Non-Homogeneous Shear Layer", First National Fluid Dynamics Congress, 24-28 July 1988 (Cincinatti, Ohio). AIAA Paper 88-3626.

GANJI, A. R. and SAWYER, R. F. [1980] "Experimental Study of a Two-Dimensional Premixed Turbulent Flame", AIAA J. 18(7), 817-824.

GROPENGIESSER, H. [1970] "Study of the Stability of Boundary Layers in Compressible Fluids", NASA-TT-F-12, 786.

HAAS, J. F. and STURTEVANT, B. [1987] "Interaction of weak shock waves with cylindrical and spherical gas inhomogeneities", J. Fluid Mech. 181, 41–76.

HERMANSON, J. C. [1985] Heat Release Effects in a Turbulent, Reacting Shear Layer Ph. D. thesis, California Institute of Technology.

HERMANSON, J. C. and DIMOTAKIS, P. E. [1989] "Effects of heat release in a turbulent reacting shear layer", J. Fluid Mech. 199, 333–375.

HESSELINK, L. and STURTEVANT, B. [1988] "Propagation of weak shocks through a random medium", J. Fluid Mech. 196, 513–553.

HO, C.-M. and HUERRE, P. [1984] "Perturbed Free Shear Layers", Ann. Rev. Fluid Mech. 16, 365–424.

HUERRE, P. and MONKEWITZ, P. A. [1985] "Absolute and convective instabilities in free shear layers", J. Fluid Mech. 159, 151-168.

HUSAIN, Z. D. and HUSSAIN, A. K. M. F. [1983] "Natural Instability of Free Shear Layers", AIAA J. 21(11), 1512–1517.

HUSSAIN, A. K. M. F. [1978] "Initial Condition Effect on Free Turbulent Shear Flows", Proceedings, Structure and Mechanisms of Turbulence I. Published in: Lecture Notes in in Physics 75 (Springer-Verlag, 1977, ed. H. Fiedler), 103-107.

KELLER, J. O. and DAILY, J. W. [1985] "The Effect of Highly Exothermic Chemical Reaction on a Two-Dimensional Mixing Layer", AIAA J. 23(12), 1937-1945.

KERSTEIN, A. [1988] "A linear-eddy model of turbulent scalar transport and mixing", Comb. Sc. & Tech. 60, 391.

KERSTEIN, A. [1989] "Linear-Eddy Modeling of Turbulent Transport II: Application to Shear Layer Mixing", Comb. & Flame 75, 397–413.

KOOCHESFAHANI, M. M. and FRIELER, C. E. [1987] "Inviscid Instability Characteristics of Free Shear Layers with non-Uniform Density", 25th AIAA Aerospace Sciences Meeting, 12–15 January 1987 (Reno, Nevada), AIAA Paper 87-0047.

KNIO, O. M. and GHONIEM, A. F. [1988] "On the formation of streamwise vorticity in turbulent shear flows", 26th AIAA Aerospace Sciences Meeting, 11–14 January 1988 (Reno, Nevada), AIAA Paper 88-0728.

KOLLMANN, W. and JANICKA, J. [1982] "The Probability Density Function of a Passive Scalar in Turbulent Shear Flows", Phys. Fluids 25, 1755-1769.

KOLMOGOROV, A. N. [1941] "Local structure of turbulence in an incompressible viscous fluid at very high Reynolds numbers", Dokl. Akad. Nauk SSSR 30, 299. Reprinted in: Usp. Fiz. Nauk 93, 476–481 (1967). Translated into English in: Sov. Phys. Usp. 10(6), 734-736 (1968).

KOLMOGOROV, A. N. [1962] "A refinement of previous hypotheses concerning the local structure of turbulence in a viscous incompressible fluid at high Reynolds number", J. Fluid Mech. 13, 82–85.

KONRAD, J. H. [1976] An Experimental Investigation of Mixing in Two-Dimensional Turbulent Shear Flows with Applications to Diffusion-Limited Chemical Reactions, Ph. D. thesis, California Institute of Technology (also Project SQUID Technical Report CIT-8-PU, December 1976).

KOOCHESFAHANI, M. M. and DIMOTAKIS, P. E. [1986] "Mixing and chemical reactions in a turbulent liquid mixing layer", J. Fluid Mech. 170, 83–112.

KOOCHESFAHANI, M. M. and DIMOTAKIS, P. E. [1988] "A Cancellation Experiment in a Forced Turbulent Shear Layer", First National Fluid Dynamics Congress, 25–28 July 1988 (Cincinatti, Ohio), Proceedings II, 1204-1208.

KOOCHESFAHANI, M. M., DIMOTAKIS, P. E. and BROADWELL, J. E. [1985] "A 'Flip' Experiment in a Chemically Reacting Turbulent Mixing Layer", AIAA J. 23(8), 1191-1194.

KUO, K. K.-Y. [1986] Principles of Combustion (John Wiley & Sons).

LANG, D. B. [1985] Laser Doppler Velocity and Vorticity Measurements in Turbulent Shear Layers, Ph. D. th California Institute of Technology.

LASHERAS, J. C. and CHOI, H. [1988] "Three-dimensional instability of a plane shear layer: an experimental study of the formation and evolution of streamwise vortices", J. Fluid Mech. 189, 53–86.

LELE, S. K. [1989] "Direct Numerical Simulation of Compressible Free Shear Flows", 27th AIAA Aerospace Sciences Meeting, 9–12 January 1989 (Reno, Nevada), AIAA Paper 89–0374.

LEONARD, A. [1983] "Numerical simulation of Turbulent Fluid Flows", (NASA TM-84320). Published in Proc. 3rd Int. Symp. on Numerical Methods in Engineering (Paris, France), 45–63.

LEVENSPIEL, O. [1962] Chemical Reaction Engineering. An Introduction to the Design of Chemical Reactors. (John Wiley).

LIEPMANN, H. W. and ROSHKO, A. [1957] Elements of Gasdynamics (GALCIT Aeronautical Series, John Wiley & Sons, Inc.).

MACK, L. M. [1975] "Linear Stability and the Problem of Supersonic Boundary-layer Transition", AIAA J. 13, 278–289.

MARBLE, F. E. and BROADWELL, J. E. [1977] "The Coherent Flame Model for Turbulent Chemical Reactions", Project SQUID TRW-9-PU.

MASUTANI, S. M. and BOWMAN, C. T. [1986] "The structure of a chemically reacting plane mixing layer", J. Fluid Mech. 172, 93-126.

McMURTRY, P. A., JOU, W. H., RILEY, J. W. and METCALFE, R. W. [1986] "Direct Numerical Simulations of a Reacting Mixing Layer with Chemical Heat Release", AIAA J. 24(6), 962-970.

McMURTRY, P. A. and RILEY, J. J. [1987] "Mechanisms by which heat release affects the flow field in a chemically reacting turbulent mixing layer", 25th AIAA Aerospace Sciences Meeting, 12–15 January 1987 (Reno, Nevada), AIAA Paper 87-0131.

METCALFE, R. W., ORZAG, S. A., BRACHET, M. E., MENON, S. and RILEY, J. J. [1987] "Secondary Instability of a Temporally Growing Mixing Layer", J. Fluid Mech. 184, 207-244.

MUNGAL, M. G. and DIMOTAKIS, P. E. [1984] "Mixing and combustion with low heat release in a turbulent mixing layer", J. Fluid Mech. 148, 349-382.

MUNGAL, M. G. and FRIELER, C. E. [1988] "The Effects of Damköhler Number in a Turbulent Shear Layer", Comb. & Flame 71, 23-34.

OBOUKHOV, A. M. [1962] "Some specific features of atmospheric turbulence", J. Fluid Mech. 13, 77-81.

21

OSTER, D. and WYGNANSKI, I. [1982] "The forced mixing layer between parallel streams", *J. Fluid Mech.* 123, 91-130.

PAPAMOSCHOU, D. [1986] *Experimental Investigation of Heterogeneous Compressible Shear Layers*, Ph. D. thesis, California Institute of Technology.

PAPAMOSCHOU, D. [1988] "Outstanding issues in the area of compressible mixing", *International Workshop on the Physics of Compressible Mixing*, Princeton U. (October 1988). Proceedings to be published by Springer-Verlag, *Lecture Notes in Engineering*.

PAPAMOSCHOU, D. [1989] "Structure of the compressible turbulent shear layer", 27th *AIAA Aerospace Sciences Meeting*, 9–12 January 1989 (Reno, Nevada), AIAA Paper 89–0126.

PAPAMOSCHOU, D. and ROSHKO, A. [1988] "The Compressible Turbulent Shear Layer: An Experimental Study", *J. Fluid Mech.* 197, 453–477.

PITZ, R. W. and DAILY, J. W. [1983] "Combustion in a Turbulent Mixing Layer at a Rearward-Facing Step", *AIAA J.* 21(11), 1565-1570.

POPE, S. B. [1981] "A Monte Carlo method for the PDF equations of turbulent reactive flow", *Comb. Sc. & Tech.* 25, 159-174.

RAGAB, S. A. and WU, J. L. [1988] "Instabilities in the Free Shear Layer Formed by Two Supersonic Streams", 26th *AIAA Aerospace Sciences Meeting*, 11–14 January 1988 (Reno, Nevada), AIAA-88-0038.

REBOLLO, M. R. [1973] *Analytical and Experimental Investigation of a Turbulent Mixing Layer of Different Gases in a Pressure Gradient*, Ph. D. thesis, California Institute of Technology.

ROBERTS, F. A. [1985] *Effects of a Periodic Disturbance on Structure and Mixing in Turbulent Shear Layers and Wakes*, Ph. D. thesis, California Institute of Technology.

ROBERTS, F. A. and ROSHKO, A. [1985] "Effects of Periodic Forcing on Mixing in Turbulent Shear Layers and Wakes", AIAA Shear Flow Control Conference, 12-14 March 1985 (Boulder, CO), AIAA Paper No. 85-0570.

ROGALLO, R. S. and MOIN, P. [1984] "Numerical Simulation of Turbulent Flows", *Ann. Rev. Fluid Mech.* 16, 99-137.

SABIN, C. M. [1965] "An analytical and experimental investigation of the plane, incompressible, turbulent free-shear layer with arbitrary velocity ratio and pressure gradient", *Trans. ASME.* D 87, 421–428.

SANDAM, N. D. and REYNOLDS, W. C. [1987] "Some Inlet-Plane Effects on the Numerically Simulated Spatially-Developing Mixing Layer", 6th International Symp. on Turb. Shear Flows (1987). Published in: *Turbulent Shear Flows* 6 (Springer Verlag), 441–454.

SANDAM, N. and REYNOLDS, W. C. [1989] "The Compressible Mixing Layer: Linear Theory and Direct Simulation", 27th *AIAA Aerospace Sciences Meeting*, 9–12 January 1989 (Reno, Nevada), AIAA-89-0371.

TAM, C. K. W. and MORRIS, P. J. [1980] "The radiation of sound by the instability waves of a compressible plane turbulent shear layer", *J. Fluid Mech.* 98, 349-381.

TAM, C. K. W. and HU, F. Q. [1988] "Instabilities of supersonic mixing layers inside a rectangular channel", Proceedings, *First National Fluid Dynamics Congress*, 25–28 July 1988 (Cincinatti, Ohio), II, 1073-1086.

VON NEUMANN, J. [1949] "Recent Theories of Turbulence". Report to the Office of Naval Research, reprinted in: *Collected Works* VI (A. H. Taub, ed. 1963 McMillan Co., New York), 437-472.

WALLACE, A. K. [1981] *Experimental Investigation on the Effects of Chemical Heat Release in the Reacting Turbulent Plane Shear Layer*, Ph. D. thesis, University of Adelaide (also distributed as AFOSR-TR-84-0650).

WANG, C. [1984] *The effects of curvature on turbulent mixing layers*, Ph. D. thesis, California Institute of Technology.

WEISBROT, I., EINAV. S. and WYGNANSKI, I. [1982] "The Non Unique Rate of Spread of the Two-Dimensional Mixing Layer", *Phys. Fluids* 25(10), 1691-1693.

WINANT, C. D. and BROWAND, F. K. [1974] "Vortex Pairing: The Mechanism of Turbulent Mixing Layer Growth at Moderate Reynolds Number", *J. Fluid Mech.* 63(2), 237-255.

WYGNANSKI, I. J. and PETERSEN, R. A. [1987] "Coherent Motion in Excited Free Shear Flows", *AIAA J.* 25(2), 201-213.

ZHUANG, M., KUBOTA, T. and DIMOTAKIS, P. E. [1987] "On the Stability of Inviscid, Compressible Free Shear Layers". Proceedings, *First National Fluid Dynamics Congress*, 25–28 July 1988 (Cincinatti, Ohio), II, 768-773.

Appendix B

HERMANSON, J. C. and DIMOTAKIS, P. E. [1989] "Effects of heat release in a turbulent reacting shear layer", *J. Fluid Mech.* **199**, 333–375.

Effects of heat release in a turbulent, reacting shear layer

By J. C. HERMANSON† AND P. E. DIMOTAKIS

Graduate Aeronautical Laboratories. California Institute of Technology.
Pasadena', CA 91125. USA

Experiments were conducted to study the effects of heat release in a planar. gas-phase. reacting mixing layer formed between two free streams. one containing hydrogen in an inert diluent. the other. fluorine in an inert diluent. Sufficiently high concentrations of reactants were utilized to produce adiabatic flame temperature rises of up to 940 K (corresponding to 1240 K absolute). The temperature field was measured at eight fixed points across the layer. Flow visualization was accomplished by schlieren spark and motion picture photography. Mean velocity information was extracted from Pitot-probe dynamic pressure measurements. The results showed that the growth rate of the layer. for conditions of zero streamwise pressure gradient. decreased slightly with increasing heat release. The overall entrainment into the layer was substantially reduced as a consequence of heat release. *A posteriori* calculations suggest that the decrease in layer growth rate is consistent with a corresponding reduction in turbulent shear stress. Large-scale coherent structures were observed at all levels of heat release in this investigation. The mean structure spacing decreased with increasing temperature. This decrease was more than the corresponding decrease in shear-layer growth rate. and suggests that the mechanisms of vortex amalgamation are. in some manner. inhibited by heat release. The mean temperature rise profiles, normalized by the adiabatic flame temperature rise. were not greatly changed in shape over the range of heat release of this investigation. A small decrease in normalized mean temperature rise with heat release was however observed. Imposition of a favourable pressure gradient in a mixing layer with heat release resulted in an additional decrease in layer growth rate. and caused only a very slight increase in the mixing and amount of chemical product formation. The additional decrease in layer growth rate is shown to be accounted for in terms of the change in free-stream velocity ratio induced by the pressure gradient.

1. Introduction

Combustion processes in turbulent flows are of great interest and are significant in many practical applications. Because chemical reactions can occur only when the reactants become molecularly mixed. understanding the flow processes leading to mixing is vital to an understanding of turbulent combustion. Alternatively. the amount and location of chemical product formation can provide an important ·window· into the fluid mechanics of combustion. The amount of chemical product formed as a result of mixing cannot exceed the amount of reactant species entrained into the layer. and the entrainment itself is related to the dynamics of the turbulent flow structure.

† Presently at United Technologies Research Center. East Hartford. CT 06108.

A major advance in understanding turbulent shear flow was the discovery that important aspects of the flow processes in a shear layer are dominated by large-scale organized structures. This was reported by Brown & Roshko (1971, 1974). Winant & Browand (1974). Dimotakis & Brown (1976). and others. The discovery of large-scale organization has motivated new measurements of composition. Konrad (1976) measured the probability density function of the concentration of individual species in a non-reacting gas-phase layer. Those results allowed an estimation of the amount of product that would be obtained in a chemically reacting shear layer. Another significant finding reported in that work was an asymmetry in the shear-layer entrainment. with more high-speed than low-speed fluid entrained. Detailed concentration measurements were performed in a liquid-phase shear layer by Koochesfahani & Dimotakis (1986). Those measurements affirmed that species transport in the layer is dominated by large-scale structures. It was also shown that. at high Reynolds numbers. the composition of the mixed fluid is quite uniform within individual structures.

The amount of mixing and product formation in a gas-phase shear flow with chemical reaction was studied by Mungal & Dimotakis (1984). utilizing the hydrogen–fluorine reaction. The effects of Reynolds number and chemical reaction rate were addressed in the same facility by Mungal. Hermanson & Dimotakis (1985) and Mungal & Frieler (1985). respectively. In addition. the structure of a gas-phase chemically reacting mixing layer prior to the mixing transition was examined by Masutani & Bowman (1986) using the nitric oxide–ozone reaction. Those investigations were all conducted under conditions of low heat release. with no apparent coupling between heat release and the fluid mechanics. Exploratory studies of reacting shear layers in liquid were performed by Dimotakis & Brown (1976). more systematically by Breidenthal (1981). who determined the integral amount of product in the layer. and by Koochesfahani & Dimotakis (1986). who were able to provide detailed measurements of product concentration and its average profile across the layer.

Much of the recent research in flows with combustion has been directed toward understanding the effects of the flow field on the combustion process. These considerations have led to the development of analytical models – for example. the strained-flame models of Marble & Broadwell (1977) and Broadwell & Breidenthal (1982). and models for the probability density function of a passive scalar proposed by Pope (1981). Kollman & Janicka (1982). and Effelsberg & Peters (1983). Little research effort has been directed. however. at the reverse problem : understanding how the combustion processes affect the flow field. and. in particular. the layer growth. entrainment. and large-scale structure dynamics. The study of these effects was the primary focus of the present investigation.

An exploratory investigation into the effects of heat release was conducted by Wallace (1981). who used the nitric oxide–ozone reaction to study the mixing and combustion in a reacting shear layer. The maximum adiabatic flame temperature rise attained in that investigation was about 400 K. Studies in reacting shear layers at high temperatures ($\approx$ 1400 K flame temperature rise) were performed by Ganji & Sawyer (1980). Keller & Daily (1983) and Pitz & Daily (1983).

The present work is a sequel to the experiments of Mungal & Dimotakis (1984) and can be considered to fill the gap between the low-heat-release studies of Mungal & Dimotakis (1984). and Wallace (1981). and the high-heat-release investigations of Ganji & Sawyer (1980). Keller & Daily (1983) and Pitz & Dailey (1983). The reactants employed in the present experiments. hydrogen and fluorine. allowed the

systematic study of heat release effects over a wide range of temperatures. In this work the adiabatic flame temperature rise ranged from 186 K to 940 K. placing the adiabatic flame temperature rise normalized by the ambient temperature in the range $0.62 \leqslant \Delta T_f/T_0 \leqslant 3.1$.

Heat release might be expected to alter both the macroscopic properties of a mixing layer (such as the layer growth. entrainment and large-scale structure dynamics) and the microscopic layer properties (for example. the mixing and the amount of chemical product formation). It is not obvious *a priori*. for example. whether the release of heat by a reacting flow would serve to increase or decrease the rate of growth and entrainment of a shear layer. One might expect that the wedge-like geometry of a shear layer would result in an increased rate of growth owing to the dilatation and consequent displacement effects caused by an increase in temperature in the mixing zone. The earlier results of Wallace (1981). however. suggested a slight *decrease* in layer growth rate with increasing heat release. Wallace (1981) also found some decrease in layer entrainment with heat release. An interesting. related question is what effect heat release might have on the entrainment ratio.

The amount of mixing that occurs in a shear layer can be measured or inferred by means of various techniques. Two methods which have been employed are the so-called passive-scalar technique and the chemical-reaction technique. In the passive-scalar technique. the concentration of a non-reacting entity serving as a conserved scalar in the fluid (e.g. dye or a selected species) is measured and then used to determine the amount of mixing (Rebollo 1973 and Konrad 1976 in gases: Koochesfahani & Dimotakis 1986 in liquids). The chemical-reaction method relies on the molecular mixing to allow the formation of some sort of product. which once measured is used to infer the amount of molecular mixing that occurred (in gas. Wallace 1981. Mungal & Dimotakis 1984 and Masutani & Bowman 1986: in liquid Breidenthal 1981 and Koochesfahani & Dimotakis 1986). The present work used the chemical-reaction technique. with the measured temperature rise (heat release) used to determine the amount of product formed.

The effects of pressure gradient in reacting flow are of interest because many practical devices have fixed geometry and do not have a means of manipulating the pressure gradient. Some investigators. for example Bray & Libby (1981) and Spalding (1986). have suggested that a pressure gradient might serve to enhance the mixing and combustion in a reacting flow. The effects of pressure gradient on layer growth and flow structure were investigated by Rebollo (1973) in a non-reacting shear layer. In some cases reported in the present work. a favourable pressure gradient was imposed on the flow. and the layer growth and product formation were also investigated under these conditions.

The experimental facility and measuring techniques will be discussed in §2. Sections 3 and 4 contain discussions on the chemistry and run conditions. The effects of heat release on the growth and entrainment of the layer are examined in §5. The amount of product formation and the large-scale structure dynamics are discussed in §§6 and 7. respectively. Finally. the effects of a favourable pressure gradient on the growth and product formation of a reacting mixing layer are presented in §8.

2. Experimental facility and instrumentation

2.1. *Flow apparatus*

The experiments described here were conducted in the blow-down facility documented by Mungal & Dimotakis (1984). which was partly modified as described
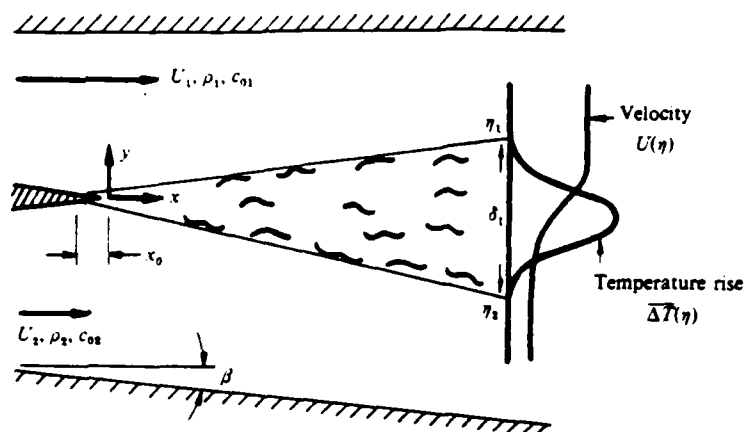
FIGURE 1. Turbulent shear-layer geometry. $\eta = y/(x - x_0)$.

by Hermanson (1985). Specifically. a planar shear flow was established between free streams resulting from the discharge of separate mixtures of fluorine in an inert diluent. and hydrogen premixed with a small amount of nitric oxide in an inert diluent. The densities of the free streams were matched for most cases by using a gas mixture consisting of nitrogen and a small amount of helium. on the fluorine side. and a mixture of nitrogen and a small amount of argon on the hydrogen side. This procedure was also used to match the heat capacities of the two free streams. allowing the measured temperature rise to be simply related to the heat release in the flow. The high-speed stream emerged from a 6:1 contraction with an exit area of 5 × 20 cm. and the low-speed stream from a 4:1 contraction with a 7.5 × 20 cm exit area. The gas mixtures were discharged into the contraction section through sonic orifices. Small adjustments in throat areas were made to minimize variations in free-stream velocity from run to run which would have resulted from the differences in gas properties of the various mixtures employed. The two streams met at the tip of a horizontal stainless steel splitter plate with an included angle of 3.8°. The test section geometry is shown schematically in figure 1.

The high-speed upper wall was fixed for all runs at 0° (horizontal). The divergence angle of the low-speed lower wall was adjusted before each run for the desired streamwise pressure gradient. The wedge-like geometry of the planar shear-layer displacement allows this simple means of accommodating or imposing a pressure gradient. Most of the runs in the present investigation were performed with the upper and lower walls adjusted to the requisite divergence angle to ensure a zero streamwise pressure gradient. For some runs. the walls were left fixed at the angle required for zero pressure gradient at zero heat release. which allowed the heat release to induce a favourable streamwise pressure gradient (accelerating flow), as a result of the combustion displacement effects.

2.2 Instrumentation

Five diagnostic techniques were employed in this investigation: schlieren/ shadowgraph flow visualization. cold-wire resistance thermometer and thermocouple temperature measurement. Pitot-probe measurements of the mean dynamic pressure transverse profiles and measurements of two-point streamwise pressure gradient.

High-time-resolution spark schlieren photographs were taken with a spark source ($\approx 3\ \mu s$ duration). synchronized with a motor-driven 35 mm camera. at a rate of

approximately three frames per second. Motion picture data were taken with a high-speed pin register camera (Teledyne Model DBS 55) at a rate of 450 frames per second. For the latter, continuous illumination was provided by a 200 W mercury vapour lamp. The schlieren method is more sensitive than the shadowgraph technique and is better suited for low-heat-release runs. It was found for the conditions of this investigation, even at the higher flow temperatures, that the schlieren technique resulted in better large-scale structure resolution than the shadowgraph method. A circular source mask and a circular hole spatial filter were used in place of the conventional source slit and knife edge in an effort to give equal weights to gradients in index of refraction in all directions and thus better resolve the large-scale vortical structure of the flow. The hole sizes were increased with increasing flow temperature to adjust the sensitivity as necessary.

Temperature data were recorded with a rake of eight $2.5\,\mu$m diameter platinum–10% rhodium cold wires, with a wire span of 1–1.5 mm, welded to sharpened Inconel prongs of 0.014 in. (0.36 mm) diameter. In the highly corrosive environment of these experiments, it was found that the $2.5\,\mu$m resistance wires in the hottest regions did not survive runs in which the adiabatic flame temperature rise exceeded approximately 600 K (corresponding to 900 K absolute). For this reason, a rake of 25 μm Chromel–Alumel thermocouples was employed for the hottest runs. The leads of the 25 μm thermocouple junctions (Omega Engineering CHAL-001) were welded to prongs consisting of Chromel and Alumel wires of 0.010 in. (250 μm) diameter. Both the cold wire and thermocouple rakes were positioned across the transverse extent of the layer. The probes were equally spaced at nominal intervals of 1 cm, which sufficed to capture the mean temperature profile. The total data rate for the resistance wires was 80 kHz, corresponding to 10 kHz per probe. This rate was consistent with the estimated frequency response of the wires (see Mungal & Dimotakis 1984). From that work it can be concluded that the characteristic thickness of the reaction zones (flame sheets) as well as the Kolmogorov scales (calculated using either a hot or cold value of kinematic viscosity) were beyond the resolution capabilities of the resistance wire probes. The thermocouples were sampled at 500 Hz each, for a total data rate of 4 kHz: their considerably lower frequency response did not warrant a higher rate.

Thermocouples normally do not require calibration. The resistance wires were calibrated as described in Mungal *et al.* (1985) using hot and cold jets of known temperature, yielding calibration constants to convert voltage to temperature rise. An additional correction was applied to the output signal voltage in the present experiments to account for the nonlinearity (quadratic coefficient) in the resistivity of the platinum–10% rhodium wire element at elevated temperatures (see Caldwell 1962). Using methods presented in Scadron & Warshawsky (1952), it was determined that for neither the thermocouple nor the resistance wires was there significant radiation error for the temperatures in this investigation. Conduction to the support prongs could, however, have resulted in excursions from the mean temperature being in error (low) by as much as 10% to 20% for the cold wires and up to 40% for the thermocouples. Both diagnostics nonetheless produced accurate mean temperatures, as during a small fraction of the course of the run (before data acquisition began) the tips of the support prongs equilibrated to the local mean value. Good agreement (typically within 5%) was obtained in runs in which both sets of probes were employed. Errors resulting from differences in the thermal conductivities between the free streams were small (Hermanson 1985).

The mean velocity was extracted from the mean dynamic pressure profile, which

was measured by a Pitot probe rake of 15 probes connected to a miniature manometer bank filled with a fluorine resistant oil (Hooker Chemical Fluorolube FS-5). The bank had an adequate time response to yield a reliable mean dynamic pressure profile during each run. The bank was photographed by a second motor-driven 35 mm camera. The photographic data were digitized using a Hewlett-Packard HP9874 digitizer and processed to yield dynamic pressure profiles. This technique of measuring the Pitot pressure was estimated to be accurate to approximately 5%. Rebollo (1973) estimated that the accuracy of extracting mean velocities from Pitot and test-section wall static pressures in a flow with a free-stream density ratio of $\rho_1/\rho_2 = 7$ is about 4–5%. In the present experiment. the density ratio of the cold free streams to the hot layer centre is at most three. suggesting that the Rebollo error estimate represents an upper bound under these conditions.

Streamwise pressure gradient information was obtained from pressure taps on the low-speed lower wall. The static pressure was measured at two downstream locations ($x = 5.1$ cm. $x = 30.0$ cm) and recorded as a differential using a Datametrics type 573 fluorine-resistant Barocel sensor.

3. Chemistry

The chemical kinetics of the hydrogen–fluorine system are summarized in Mungal & Dimotakis (1984). The reaction yields a temperature rise of 93 K for 1% F_2 and 1% H_2 in N_2 diluent under constant-pressure. adiabatic conditions (this is the so-called adiabatic flame temperature rise). Proper chain initiation requires some free F atoms. which were generated in these experiments by premixing a trace amount (3% of the free-stream F_2 concentration) of nitric oxide into the hydrogen-carrying stream.

For all flows reported here. the resulting chemical timescales were fast compared with the fluid mechanical timescales. The chemical timescales for the reaction. over the entire range of concentrations. were estimated using the CHEMKIN chemical kinetics program developed by Kee. Miller & Jefferson (1980). The chemical rate data for the reactions involved were taken from Cohen & Bott (1982) and Baulch *et al.* (1981). The Damköhler number (ratio of mixing time to chemical time) based on the local. large-scale characteristic time ($\delta_1/\Delta U$. where δ_1 is the width indicated by the 1% level of the mean temperature profile and $\Delta U = U_1 - U_2$ is the free-stream velocity difference) ranged from 25 to 130 with increasing reactant concentrations. The work of Mungal & Frieler (1985) suggests that the chemistry can be regarded as being fast when the Damköhler number for the large scales exceeds 10. A threshold Damköhler number of 10 for the large scales is also suggested by the results of Masutani & Bowman (1986). Chemical kinetics are. consequently. not an issue in the present investigation. where the chemistry was much faster as a result of the higher reactant concentrations and combustion temperatures.

4. Run conditions

The nominal flow velocities for this investigation were

$$U_1 = 22 \text{ m/s}. \quad U_2 = 8.8 \text{ m/s}. \quad r \equiv U_2/U_1 = 0.40.$$

with nominal equal free-stream densities. i.e.

$$s \equiv \frac{\rho_2}{\rho_1} = 1.$$
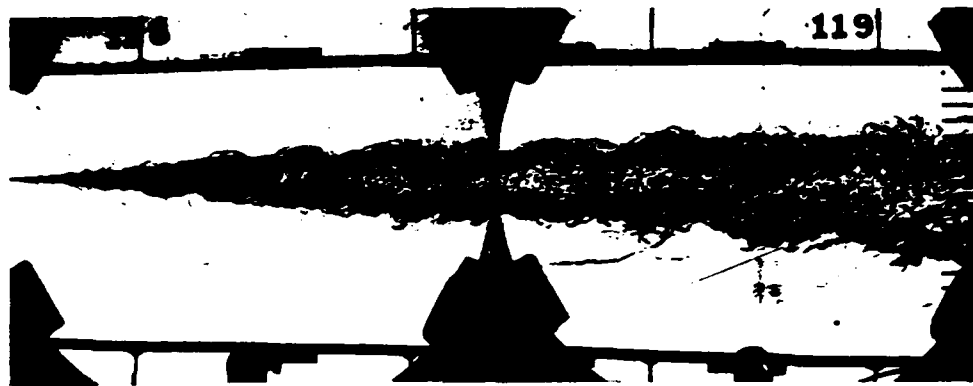
at one atmosphere pressure.

FIGURE 2. Composite spark schlieren photograph. Flow is from left to right. Top stream. 5%
H_2. $U_1 = 22$ m/s: lower stream: 5% F_2. $U_2 = 8.8$ m/s. $\Delta T_f = 457$ K: $Re_{\delta_1} = 6.2 \times 10^4$.

Reactant concentrations ranged from 2% fluorine and 2% hydrogen up to 6%
fluorine and 24% hydrogen. corresponding to an adiabatic flame temperature rise in
the range

$$186 \text{ K} \leqslant \Delta T_f \leqslant 940 \text{ K}$$

resulting in a maximum local mean temperature rise in the range

$$125 \text{ K} \leqslant \overline{\Delta T}_{max} \leqslant 550 \text{ K}.$$

The density changes corresponding to the adiabatic flame temperature rise were

$$0.38 \leqslant \frac{\Delta \rho_f}{\rho_0} \leqslant 0.76.$$

where $\Delta \rho_f$ is the density difference between the cold free streams and the density in
the layer. calculated using the adiabatic flame temperature rise and neglecting small
differences in static pressure in the layer. The corresponding density changes
calculated using the maximum local mean temperature rise were

$$0.29 \leqslant \frac{\Delta \rho_{max}}{\rho_0} \leqslant 0.65.$$

A composite spark schlieren photograph of two different runs is shown in figure 2.
The flow is from left to right with the high-speed free stream in the upper half of the
figure. The splitter plate tip and the temperature and Pitot probe rakes at the
measuring station are visible at the extreme left and right edges of the figure.
respectively.

The local Reynolds number at the measuring station was typically

$$Re_{\delta_1} \equiv \Delta U \delta_1 / \nu \approx 6 \times 10^4.$$

where ν is the cold free-stream kinematic viscosity. This value of the Reynolds number
is well above that for the mixing transition as reported by Konrad (1976).
Breidenthal (1981) and Bernal *et al.* (1979). Mungal & Dimotakis (1984) and
Koochesfahani & Dimotakis (1986) report that the width δ_1 correlates well with the
layer visual thickness δ_{vis} as defined by Brown & Roshko (1974): this was also
confirmed in the present study. The measuring station for the cold wires and Pitot
was at $x = 45.7$ cm downstream of the splitter plate trailing edge for all runs. The

thermocouple rake was normally positioned at $x = 44.8$ cm. The corresponding Reynolds number based on the high-speed free-stream velocity and on the downstream distance was typically $Re_x \equiv U_1 x/\nu \approx 6 \times 10^5$. The momentum thickness of the high-speed boundary layer on the splitter plate. θ_1. was calculated by Thwaite's method and yielded a Reynolds number based on momentum thickness of $U_1 \theta_1/\nu \approx 240$. At the measuring station the normalized distance to the splitter-plate tip was estimated to be $x/\theta_1 \approx 2800$. This is substantially larger than the value of $x/\theta_1 = 1000$ which Bradshaw (1966) suggests may be required for the layer to become self-similar. This value of x/θ_1 is in the range of other shear-layer investigations. for example $x/\theta_1 \approx 2300$ in Dimotakis & Brown (1976). $x/\theta_1 \approx 2900$ in Browand & Latigo (1979). and $x/\theta_1 \approx 4000$ for Brown & Roshko (1974).

The stoichiometric mixture ratio, ϕ. is defined here as the ratio of the low-speed free-stream molar concentration. c_{02}. to the high-speed free-stream molar concentration. c_{01}. divided by the low-speed to high-speed molar stoichiometric ratio:

$$\phi \equiv \frac{(c_{02}/c_{01})}{(c_{02}/c_{01})_s}.$$ (1)

or, in this case,
$$\phi = \frac{c_{02}}{c_{01}}.$$ (2)

since the hydrogen–fluorine stoichiometric ratio is unity. Equations (1) and (2) can be regarded as representing the volume (or mass) of high-speed free-stream fluid necessary to react completely with a unit volume (or mass) of low-speed free-stream fluid. Volume and mass. if differential diffusion effects are ignored. are interchangeable in this discussion because the free-stream densities in this experiment were nominally equal. For this investigation. the stoichiometric mixture ratio was in the range $\phi = 1$ to $\phi = \frac{1}{8}$, with the lean reactant. fluorine. always on the low-speed side of the layer. As the heat release was increased. it was determined that no obvious deviation from the simple trends with heat release (to be discussed later) warranted extending the heat release further. This consideration. in addition to issues of safety. restricted the use of high-speed free-stream hydrogen concentrations to a maximum of 24%. As a consequence. for the higher levels of heat release the extreme value of stoichiometric mixture ratio was $\phi = \frac{1}{4}$.

All the flows in the present investigation were momentum-dominated with negligible effects of buoyancy. For the present investigation. the maximum value of the Richardson number is

$$Ri \approx \frac{\Delta\rho}{\rho_0}\frac{g\delta_1}{(\Delta U)^2} \approx 0.004.$$

where g is the gravitational constant. Koop & Browand (1979) suggest that a minimum value of $Ri \approx 0.05$ is required in a shear layer for the effects of buoyancy to become important.

5. Shear-layer growth and entrainment

5.1 Shear-layer growth rate

The thickness of the shear layer, as indicated by the width of the mean temperature profile at a fixed downstream location, decreased slightly with increasing heat release. The observed 1% temperature profile thickness at zero pressure gradient. normalized by the downstream distance $x - x_0$ (here taken to be constant), is plotted
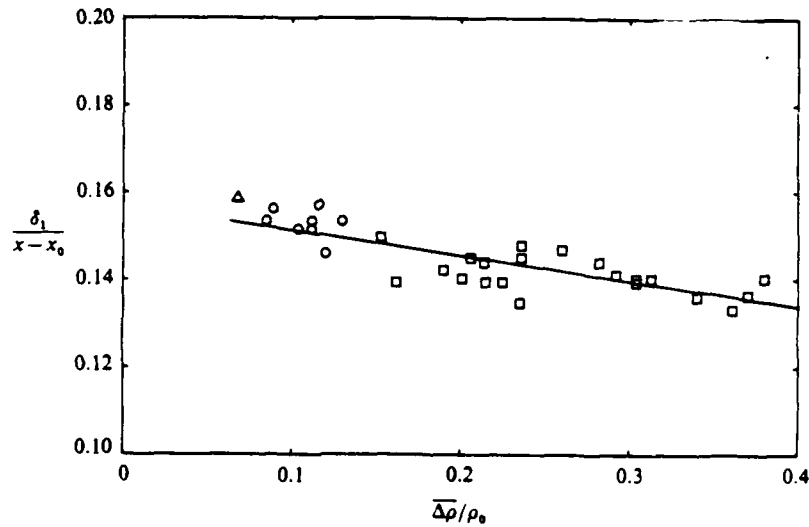
FIGURE 3. Temperature profile thickness growth rate *vs.* heat release. $\triangle$. Wallace (1981):
$\bigcirc$. Mungal & Dimotakis (1984): $\square$. present results.

in figure 3 versus the mean density reduction parameter. $\overline{\Delta\rho}/\rho_0$. Results obtained from Mungal & Dimotakis (1984) and Wallace (1981) are also presented. The parameter $\overline{\Delta\rho}/\rho_0 = (\rho_0 - \bar{\rho})/\rho_0$ represents the mean normalized density reduction in the layer due to heat release. where $\bar{\rho}$ is the mean density in the layer and $\rho_0 = \frac{1}{2}(\rho_1 + \rho_2)$ is the average (cold) density of the free streams. The mean density is defined here as

$$\bar{\rho} = \rho_0 \int_{\eta_2}^{\eta_1} \frac{T_0}{T_0 + \overline{\Delta T}} d\eta. \tag{3}$$

where $\eta_{1,2}$ are the 1% points of the mean temperature profile on the high- and low-speed sides. respectively (see figure 1), T_0 is the ambient temperature. and $\overline{\Delta T}$ is the time-averaged temperature rise at each point across the layer. This calculation neglects the small changes in pressure across the layer by taking the pressure to be constant. Small variations in the free-stream speed and density ratios from run to run (see Hermanson, Mungal & Dimotakis 1987) have been corrected for by use of a formula proposed by Dimotakis (1986)

$$\frac{\delta}{x} = \epsilon \left(\frac{1-r}{1+s^{\frac{1}{2}}r} \right) \left(1 + s^{\frac{1}{2}} - \frac{1 - s^{\frac{1}{2}}}{1 + 2.9\frac{1+r}{1-r}} \right). \tag{4}$$

where $s = \rho_2/\rho_1$. $r = U_2/U_1$. and ϵ is a constant. The correction consisted of using (4) to normalize each point in figure 3 by the ratio of the expected thickness for a cold layer with the actual speed and density ratio to that of a cold layer with the nominal values of $s = 1$. $r = 0.4$. A linear least-squares fit to the data in figure 3 suggests that the layer thinning. for a mean density reduction of 40%. may be as high as 15%. Extrapolation of the data in figure 3 indicates that the layer will retain a finite thickness even for the extreme case of zero mean density in the layer ($\overline{\Delta\rho}/\rho_0 = 1.0$). The largest mean density reduction presented in this work. $\overline{\Delta\rho}/\rho_0 = 0.38$. corresponds to a run with an adiabatic flame temperature rise of $\Delta T_f = 940$ K and a mean temperature rise in the layer of $\langle \overline{\Delta T} \rangle = 248$ K. No dependence of the thinning trend on stoichiometric mixture ratio (at a given value of $\overline{\Delta\rho}/\rho_0$) was observed.

The decrease in layer width with increasing heat release was noted by Wallace (1981) and was confirmed in the present set of experiments. in which the maximum mean flow temperature increase was about three times greater than that of Wallace. The implication of the results presented in figure 3 is that the rate at which the layer grows with downstream distance is reduced by heat release. The parameter $\delta_1/(x-x_0)$ represents the growth rate of a linearly growing shear layer. The location of the virtual origin. x_0. is a complicating factor. and the trend in layer growth rate suggested here does allow the possiblity that a shift in the virtual origin with heat release could result in slightly different growth rates than those suggested by figure 3. The location of the virtual origin in this work was determined visually from the intersection of the apparent layer edges. as revealed by spark schlieren photographs (see Brown & Roshko 1974). This yielded values of x_0 in the range $-5 < x_0 < -1$ cm. but did not. however. suggest any systematic change in the location of the virtual origin with heat release. A representative value of $x_0 = -3.2$ cm was used for all normalizations in this investigation. It should be noted that initial conditions can have a significant effect on layer growth as has been shown. for example. by Batt (1975) and Browand & Latigo (1979). In this investigation the initial conditions were essentially fixed.

Although the actual thickness of the layer decreased slightly with increasing heat release. the density decrease in the layer due to the increased temperature was nevertheless responsible for a displacement velocity in the external flow. At zero pressure gradient. this displacement deflected the low-speed free stream away from the layer and also deflected the layer away from the high-speed upper wall (the latter effect is a consequence of maintaining a fixed high-speed upper-wall orientation). The low-speed lower-wall divergence required for zero streamwise pressure gradient is. neglecting wall boundary layers. a direct measure of the displacement thickness of the layer. δ^*. where $\delta^*/(x-x_0)$ indicates the tangent of the angle. β. by which the low-speed free streamline is deflected owing to the presence of the shear layer (see figure 1). Note that the displacement thickness is less than zero for a layer with no heat release. and increases steadily with heat release. as shown in figure 4. Some unpublished data of Mungal are included in the figure with the present results. Since the streamwise pressure gradient for a given run was typically not exactly zero (see table 2. §8.1). each data point in figure 4 was corrected empirically to correspond to the approximate wall setting that would have resulted in a zero value of pressure gradient.

The slight reduction in layer thickness (and growth rate) with increasing heat release is also confirmed by the mean velocity data. The shear-layer vorticity thickness. δ_ω. can be defined by normalization of the maximum slope of the mean velocity profile by the free-stream velocity difference. as follows:

$$\frac{1}{\delta_\omega} = \frac{1}{\Delta U} \left(\frac{dU}{dy}\right)_{max}.$$

A plot of the vorticity thickness variation with heat release. again corrected for small variations in speed ratio and density ratio. is shown in figure 5. The solid line represents the change in vorticity thickness. δ_ω. implied by the reduction in 1% thickness. δ_1. assuming that $\delta_\omega/\delta_1 \approx 0.55 =$ constant. Brown & Roshko (1974) report a somewhat lower value of $\delta_\omega/\delta_1 \approx 0.48$. Each point was normalized by a representative value for the vorticity thickness at zero heat release. The portion of the present results at moderate heat release. including some unpublished data of
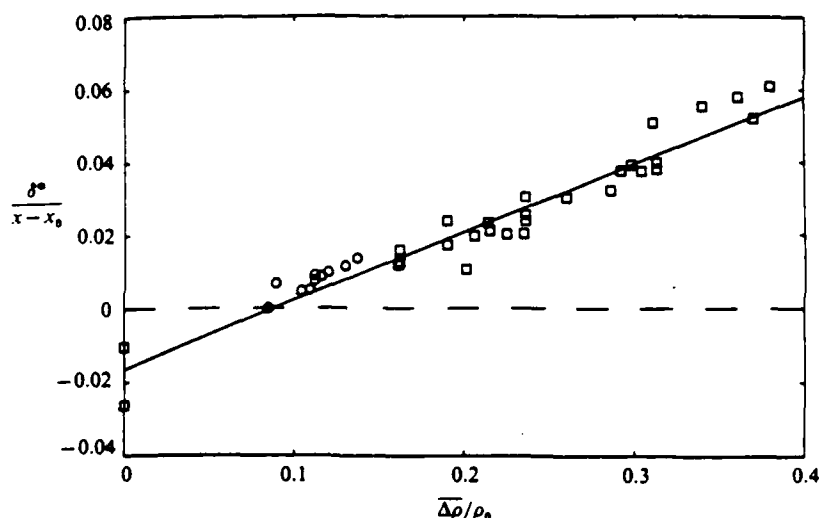
FIGURE 4. Normalized layer displacement *vs.* heat release: ○. Mungal (unpublished data):
□. present results.

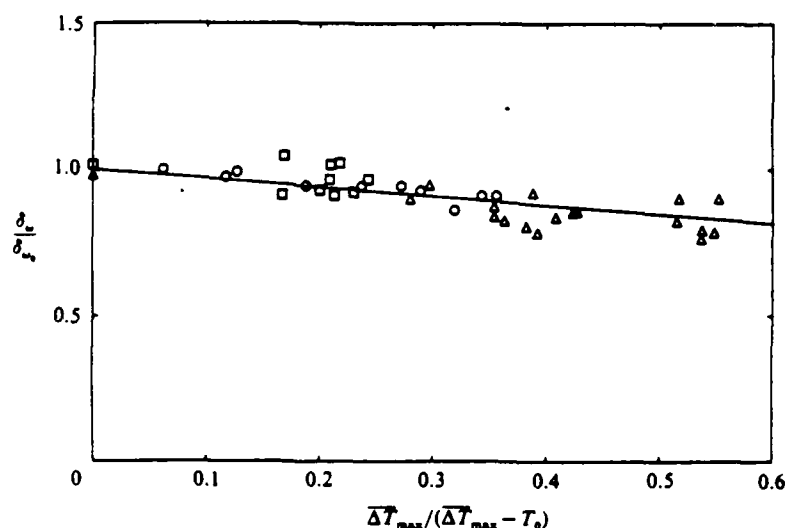FIGURE 5. Normalized vorticity thickness *vs.* heat release. ○. Wallace (1981): □. Mungal
(unpublished data); △. present results. δ_{ω_0} is vorticity thickness at zero heat release.

Mungal, are in good agreement with Wallace. Since the data of Wallace were
originally given in terms of $\overline{\Delta T}_{max}/T_0$, the maximum time-averaged temperature rise
over the ambient temperature, it was necessary to use the quantity $\overline{\Delta T}_{max}/$
$(\overline{\Delta T}_{max} + T_0)$ for the abscissa parameter of figure 5. This quantity is slightly different
from $\overline{\Delta\rho}/\rho_0$ because the density is not a linear function of the temperature rise.

In addition to an increase in maximum slope with heat release. the mean velocity
profile was also observed to change somewhat in shape. Velocity profiles at low and
high heat release are plotted in figure 6. against the normalized transverse coordinate
$(y - y_c)/\delta_\omega$. where y_c is the location of the centre of each profile (i.e. where
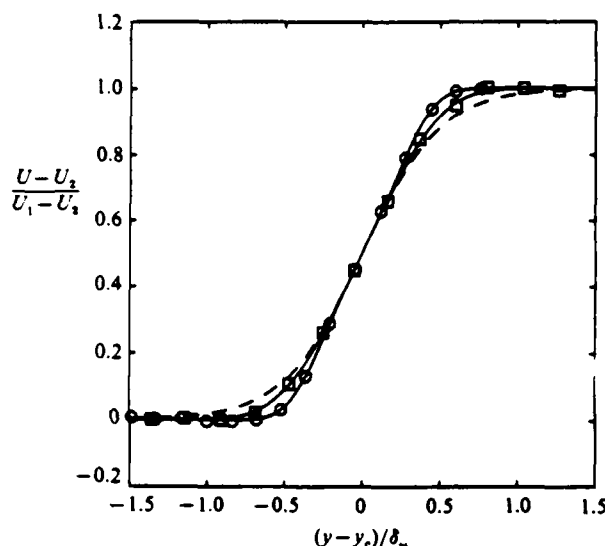
FIGURE 6. Velocity profile shape change with heat release: $\bigcirc$. unreacting flow. $\delta_\omega/(x-x_0) = 0.090$: $\square$. reacting flow. $\Delta T_f = 457$ K. $\delta_\omega/(x-x_0) = 0.079$. Dashed line is hyperbolic tangent profile.

$U = \frac{1}{2}(U_1 + U_2)$. The dashed line represents a hyperbolic tangent profile with the same maximum slope as the velocity profiles. The profile at high temperature appears fuller than the corresponding low-temperature profile. A modified fit of the form

$$\frac{U(y-y_c)-U_1}{U_1-U_2} = \frac{1}{2}+\frac{1}{2}\tanh\left[2\left(\frac{y-y_c}{\delta_\omega}\right)+b\left(\frac{y-y_c}{\delta_\omega}\right)^3\right]$$

provides a good fit to mean velocity profiles over all temperatures in this investigation. The parameter b can be regarded as a measure of how the profile differs in fullness from a pure hyperbolic-tangent profile; b decreases with increasing temperature as the profile becomes more like a hyperbolic tangent.

Experiments performed at higher temperatures than those in this work by Pitz & Daily (1983) in a combusting mixing layer formed downstream of a rearward-facing step indicated that the vorticity thickness did not appear to change between their cold runs and high-heat-release runs. Keller & Daily (1983), however, report that in a reacting mixing layer between a cold premixed reactant stream and a preheated combustion product stream the vorticity thickness increased significantly with increasing temperature. Direct numerical simulations of two-dimensional flow in a reacting mixing layer performed by McMurtry *et al.* (1986) suggest a decrease in layer growth rate when exothermic reactions occur, in qualitative agreement with the present results. Similar trends have been seen in subsequent three-dimensional simulations by McMurtry & Riley (1987). Additional discussion of heat release effects on layer growth is presented in §5.4.

5.2 *Shear-layer entrainment*

That the layer growth rate does not increase with increasing temperature, in conjunction with a substantially reduced density in the layer, implies that the total volumetric entrainment of free-stream fluid into the layer must be reduced by heat release. A method which approximates the overall entrainment is to use the

% F_2/% H_2	ΔT_f(K)	$\overline{\Delta\rho}/\rho_0$	η_1	η_2	β	r
1/1	93.0	0.085	0.0734	−0.0842	0.0103	0.388
1/8	165.0	0.120	0.0717	−0.0835	0.0174	0.380
2/2	186.3	0.153	0.0632	−0.0819	0.0221	0.411
2/4	247.6	0.190	0.0642	−0.0881	0.0179	0.373
3/3	278.1	0.206	0.0615	−0.0870	0.0216	0.392
4/4	368.2	0.260	0.0608	−0.0897	0.0334	0.390
5/5	456.8	0.286	0.0525	−0.0945	0.0329	0.393
4/16	600.3	0.311	0.0544	−0.0951	0.0509	0.373
6/6	553.8	0.313	0.0520	−0.0943	0.0436	0.382
6/12	737.4	0.361	0.0484	−0.1001	0.0619	0.364

TABLE 1. Selected values of layer geometry parameters. $\Delta T_f \equiv$ adiabatic flame temperature rise: $\overline{\Delta\rho}/\rho_0 \equiv$ mean density reduction: $\eta_1 \cdot \eta_2 \equiv$ similarity coordinate at 1 % points of mean temperature-rise profiles on the high-speed and low-speed sides. respectively: $\beta \equiv$ low-speed lower sidewall deflection angle: $r \equiv$ free-stream speed ratio. The first two data points listed are from Mungal (unpublished data).

geometry of the layer as shown in figure 1 to derive (Brown 1978: Dimotakis 1986)

$$\frac{\dot{V}}{U_1(x-x_0)} = \eta_1 - r(\eta_2 + \tan\beta),$$ (5)

where $\dot{V}$ is the volume flux into the layer per unit span. $r = U_2/U_1$, $\eta_{1,2}$ are the similarity coordinate edges of the shear layer and β is the deflection angle of the low-speed lower wall. Certain assumptions about the nature of the vertical component of velocity are implicit in this formulation. Equation (5) neglects the displacement of the wall boundary layers by taking the free-stream vertical component of velocity to be zero at the high-speed upper wall and to have the value implied by the angle β near the low-speed lower wall. These values of the free-stream vertical velocity are taken in (5) to also be those at the corresponding layer edges. By continuity. the change in mean horizontal velocity across the layer implies a corresponding change in the mean vertical velocity. At the outer edges of the layer. for example at the locations indicated by the 1 % points in the mean temperature profiles. the mean vertical velocity components do have values nearly equal to those in the free stream. That is not the case. however. for points deeper inside the layer. Equation (5) will be referred to as the geometric entrainment calculation method. Representative values of η_1. η_2. and β are presented in table 1 for varying amounts of heat release.

The entrainment into the layer can also be calculated from the mean velocity and density (i.e. temperature) profiles as follows:

$$\frac{\dot{V}}{U_1(x-x_0)} = \int_{\eta_2}^{\eta_1} \frac{\rho U}{\rho_0 U_1} d\eta.$$ (6)

Unlike the geometric relation (5). the integral relation (6) does not make any assumptions about the nature of the vertical velocity components. This expression assumes that the layer is self-similar at the station at which the integral is performed. Results from Mungal *et al.* (1985) suggest that there is a weak Reynolds-number dependence on product formation. Since the growth rate does appear to be a function of the product formation (i.e. heat release). strictly speaking. the flow cannot be

expected to be exactly self-similar. The quantity $\rho U'$ was estimated by $\bar{\rho}U'$, which was used here as an approximation for the density–velocity correlation $\overline{\rho u}$, where u and U' are the instantaneous and mean downstream velocity components, respectively. Equation (6) will be referred to as the integral entrainment calculation method.

A common difficulty of both the integral and geometric entrainment calculation methods involves selection of appropriate values for η_1 and η_2. Konrad (1976) was able to circumvent the difficulty of edge point selection by incorporating an estimate for the intermittency obtained from species concentration data. The resulting expression for the entrainment can be expressed in integral form as

$$\frac{V}{U_1(x-x_0)} = \int_{-x}^{+x} \hat{\gamma}(\eta)\frac{\rho U'}{\rho_0 U_1'}\,\mathrm{d}\eta. \tag{7}$$

where $\hat{\gamma}(\eta)$ is the intermittency, that is, the mean fraction of the time that turbulent (or mixed) fluid is encountered. Expressions (5) and (6) can be thought of as indicating the amount of fluid that is entrained into the overall boundaries of the layer: (7) estimates the amount that actually enters the turbulence (and becomes mixed). Equation (7) will be referred to as the intermittency-weighted entrainment calculation method.

An estimate for the intermittency can be made by relating it to the probability of finding mixed fluid at a given location in the layer. Koochesfahani & Dimotakis (1986) showed that the total mixed-fluid probability, $P_m(y)$, can be related to the sum of the normalized (mean) product concentrations, $\overline{c_P}$, at very high and very low stoichiometric mixture ratios, as follows:

$$P_m(y) = \frac{\overline{c_P}(y:\phi = \infty)}{c_{01}} + \frac{\overline{c_P}(y:\phi = 0)}{c_{02}}. \tag{8}$$

The mean product concentration can, at low heat release, be related to the mean temperature rise (see Mungal & Dimotakis 1984), giving for the mixed-fluid probability

$$P_m(y) = \frac{\hat{C}_p}{\Delta Q}\frac{\overline{\Delta T}(y:\phi = \infty)}{c_{01}} + \frac{\hat{C}_p}{\Delta Q}\frac{\overline{\Delta T}(y:\phi = 0)}{c_{02}}. \tag{9}$$

where ΔQ is the molar heat release of the chemical reaction and $\hat{C}_p$ is the molar specific heat capacity. It was shown by Mungal & Dimotakis (1984) that the amount of product formed is close to the asymptotic limits for $\phi = 8$ and $\phi = \frac{1}{8}$. These limits mean physically that the (mixed) lean reactant has been nearly fully consumed. Taking, as an approximation, the intermittency to be equal to the total mixed-fluid probability gives, in similarity coordinates,

$$\hat{\gamma}(\eta:\hat{q}) \approx \frac{\hat{C}_p}{\Delta Q}\frac{\overline{\Delta T}(\eta:\phi = 8)}{c_{01}} + \frac{\hat{C}_p}{\Delta Q}\frac{\overline{\Delta T}(\eta:\phi = \frac{1}{8})}{c_{02}}. \tag{10}$$

The parameter $\hat{q}$ is added to indicate a possible functional dependence on heat release: a possible choice is $\hat{q} \equiv \overline{\Delta\rho}/\rho_0$.

It is not clear exactly how intermittency changes with heat release, as in this investigation the cases $\phi = 8$ and $\phi = \frac{1}{8}$ were not investigated at high heat release. It will be seen in §6, however, that there is some decrease in the heights of the mean temperature-rise profiles normalized by the adiabatic flame temperature rise, with heat release. This allows the possibility that intermittency may be affected by heat release.
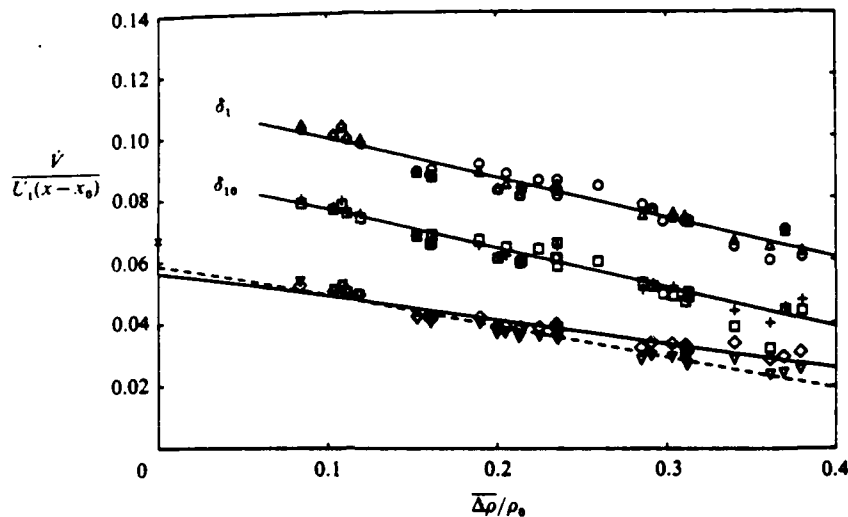
FIGURE 7. Dependence of volumetric entrainment on heat release: $\bigcirc$, $\square$, geometric entrainment calculation method: $\triangle$, $+$, integral entrainment calculation method: $-\diamondsuit-$, intermittency-weighted method using $\hat{\gamma}(y:0)$: $-\nabla-$, intermittency-weighted method using $\hat{\gamma}(y:\hat{q})$: $\times$, Konrad (1976). See text for explanation. Data for $0 < \overline{\Delta\rho}/\rho_0 < 0.13$ calculated from Mungal (unpublished data).

The resulting entrainment data. using the geometric, integral, and intermittency-weighted entrainment calculation methods, are presented in figure 7. Results calculated from unpublished data of Mungal are also included. The data sets labelled δ_1 and δ_{10} were calculated without intermittency using for edge points the 1% and 10% points in the mean temperature profiles. respectively. The solid and dashed lines are linear least-squares fits to the data.

The lowest sets of data in figure 7 were calculated by the intermittency-weighted method. The intermittency used in calculating the data set labelled $\hat{\gamma}(y:0)$ was estimated using the low-heat-release results of Mungal & Dimotakis and (10). For the data set labelled $\hat{\gamma}(y:\hat{q})$. the height of the intermittency profile was taken to decrease in direct proportion to the decrease in the normalized mean temperature profiles at $\phi = \frac{1}{4}$ with heat release. as discussed in §6. The data with changing intermittency do not suggest a significantly different trend than the results calculated incorporating the intermittency estimated from the low-heat-release results. It should be emphasized that this change in intermittency with heat release is speculative and that the actual dependence of the intermittency on temperature is yet to be established.

Regardless of the choice of method or reference points. the inference is that the total entrainment into the layer is strongly reduced with increasing heat release. amounting to a decrease of about 50%. for a mean density in the layer of 40% below its nominal cold value. That the entrainment reduction is in excess of the mean density reduction suggests that the decrease in entrainment flux with heat release more than compensates for the displacement effects due to density change. yielding a thinner layer thereby. The entrainment reported by Konrad (1976) for a non-reacting shear layer. estimated using intermittency. is included for comparison in figure 7. The value shown was scaled for comparison by the estimated growth rate at zero heat release in the present experiment. and is in fair agreement with the

present results. The linear least-squares fits shown in figure 7. if extrapolated to higher values of mean density reduction. would cross the x-axis and indicate zero entrainment into the layer for a value of $\overline{\Delta\rho}/\rho_0 \approx 0.8$. It will be argued in §7 that $\overline{\Delta\rho}/\rho_0$ may never reach that value. even for very high flame temperatures but will rather tend to a limiting value that is substantially less.

The difference between the integral and geometric methods can be used to infer. in an approximate fashion. the amount by which the time-averaged quantity $\overline{\rho u}$ differs from the approximation $\bar{\rho}U^{\cdot}$ used for the computations in this section. The difference is the fluctuation correlation term $\overline{\rho' u'}$. In view of the good agreement between the integral and geometric methods shown in figure 7 over all values of heat release. the quantity $\overline{\rho' u'}/\bar{\rho}U^{\cdot}$ does not appear to be greater than about 4% over the width of the layer. If it is assumed that the profile $\overline{\rho' u'}$ (η) is Gaussian-like. the maximum error near the centerline of the layer could be about 9%. Since the mean velocity itself is estimated to be accurate only to about 4% (Rebollo 1973) however. the data do allow the possibility that $\overline{\rho' u'}$ could on average be much smaller than 4% of $\bar{\rho}U^{\cdot}$. or. in fact. zero.

5.3. *Entrainment ratio*

Methods analogous to the integral and geometric methods for total entrainment can be developed to give estimates of the volumetric entrainment ratio. that is. the ratio of high-speed entrained fluid to low-speed entrained fluid. The geometric result is developed in Brown (1978) and Dimotakis (1986) and is

$$E_v \approx \frac{U_1^{\cdot}}{U_2^{\cdot}}\frac{\eta_1}{-\eta_2-\tan\beta}. \tag{11}$$

As noted by Dimotakis. (11) assumes that the ratio of the fluid inducted into the layer from each of the free streams is the same as the ratio of the fluid fluxes intercepting the corresponding (mean) visual edges of the shear layer. For the entrainment calculations in this investigation. the edges of the layer were taken to be those indicated by specific points in the mean temperature profiles. as explained earlier. An integral method for estimating the entrainment velocities into the layer can be derived from formulas presented in Konrad (1976). here expressed in terms of linear similarity coordinates :

$$\frac{V_{e_1}^{\cdot}}{U_1^{\cdot}} = \int_{\eta_0}^{\eta_1} \frac{\bar{\rho}U^{\cdot}}{\rho_0 U_1^{\cdot}} \,\mathrm{d}\eta \tag{12}$$

and

$$\frac{V_{e_2}^{\cdot}}{U_1^{\cdot}} = \int_{\eta_2}^{\eta_0} \frac{\bar{\rho}U^{\cdot}}{\rho_0 U_1^{\cdot}}\mathrm{d}\eta. \tag{13}$$

where $V_{e_{1,2}}^{\cdot}$ are the entrainment velocities into the high-speed and low-speed sides of the layer. respectively. and η_0 is the location of the dividing streamline. η_0 is obtainable from the following commonly employed relation. derived from combining the continuity and momentum equations :

$$\int_{-x}^{\eta_0} \frac{\bar{\rho}U^{\cdot}}{\rho_0 U_1^{\cdot}}\left(\frac{U^{\cdot}}{U_1^{\cdot}}-r\right)\mathrm{d}\eta = \int_{\eta_0}^{x} \frac{\bar{\rho}U^{\cdot}}{\rho_0 U_1^{\cdot}}\left(1-\frac{U^{\cdot}}{U_1^{\cdot}}\right)\mathrm{d}\eta. \tag{14}$$

The corresponding integral formulas incorporating intermittency are

$$\frac{V_{e_1}^{\cdot}}{U_1^{\cdot}} = \int_{\eta_0}^{x} \hat{\gamma}(\eta)\frac{\bar{\rho}U^{\cdot}}{\rho_0 U_1^{\cdot}}\,\mathrm{d}\eta \tag{15}$$
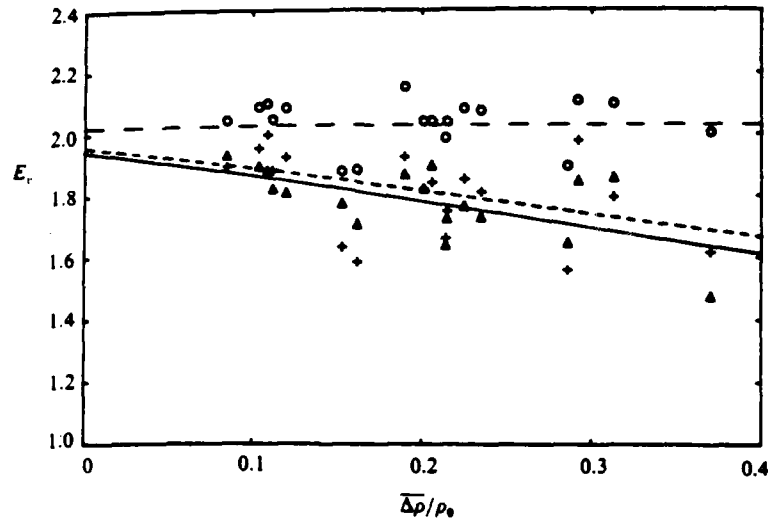
FIGURE 8. Effect of heat release on entrainment ratio: $\bigcirc$, based on 1% thickness of mean temperature profiles; $\triangle$, based on 10% thickness; $+$, calculated with intermittency. Lines shown are least-squares fit to data.

and
$$\frac{V_{e_2}}{U_1} = \int_{-x}^{\eta_0} \dot{\gamma}(\eta)\frac{\rho U'}{\rho_0 U_1} d\eta. \tag{16}$$

The volumetric entrainment ratio is given by

$$E_v = \frac{V_{e_1}}{V_{e_2}}.$$

The issue again arises, for the calculations without intermittency, of how to choose the values of η_1 and η_2. This issue is much more critical here than in the evaluation of the methods for the total entrainment, since small inaccuracies in V_{e_1} and V_{e_2} (resulting from errors in η_1 and η_0, for example) can result in large errors in the ratio E_v. The fact that only eight temperature probes were employed across the width of the layer made precise determination of the values of η_1 and, to a lesser extent, η_{10} difficult in this investigation. Note that the same cautionary remarks made in the previous section concerning the nature of the mean vertical velocity components also apply to the present discussion. In particular, in the geometric calculation (11) the boundary layer on the low-speed lower wall adds to the apparent layer displacement and can result in an observed value of β which exceeds the actual $\delta^*/(x-x_0)$ of the layer. This could cause (11) to indicate a substantially higher entrainment ratio than actually occurs in the flow.

The calculations from the present data and also those of Mungal using integral entrainment formulas, (12) and (13), are presented in figure 8, using as before the 1% and 10% points of the mean temperature profile to get η_1 and η_2. Linear least-square fits were performed for each data set. Each data point in figure 8 has been corrected for run-to-run variations in speed and density ratio by using, in a similar fashion to the growth rate correction applied in §5.1, the following formula derived by Dimotakis (1986) for the entrainment ratio:

$$E_v \approx s^{\frac{1}{2}}\left(1 + 0.68\frac{1-r}{1+r}\right). \tag{17}$$

The 1% data indicate no systematic change in volumetric entrainment ratio. The corresponding 10% results indicate a decrease in volumetric entrainment ratio with heat release of up to about 15% for a mean density reduction in the layer of 40%. The results employing the integral formulas with intermittency. (15) and (16). are also shown in figure 8 and indicate a comparable trend with the results calculated using the 10% points of the mean temperature profile. In this calculation. the intermittency was taken to be unchanging with heat release. An additional estimate of the change in entrainment ratio with heat release. using large-scale structure statistical information. is presented in §7. and is consistent with these results.

It is worth noting that the actual values of the entrainment ratio estimated by the methods without intermittency. using the 1% points. appear to exceed substantially the values calculated taking intermittency into account. and also the value given by Konrad of $E_v \approx 1.3$ for the non-reacting layer at comparable speed ratio. This suggests that the amount of high-speed fluid within the outside boundaries of the layer (as suggested by the width of the mean temperature profile). but yet unmixed. may exceed the corresponding amount of low-speed fluid by a factor greater than 1.3.

5.4. *Discussion of heat release effects on layer growth*

The observed heat release effects on layer growth and entrainment may be related to a decrease in the turbulent shear stress in the layer. The experimental data in fact suggest a decrease in shear stress which can be attributed to the density reduction in the layer caused by heat release. The following arguments are included as an *a posteriori* effort to estimate the magnitudes of the various effects that enter in the accounting of the growth rate of the shear layer. The discussion describes what is essentially a self-consistent calculation; it is not proposed here that such arguments could have been used to predict these results prior to their establishment by experiment.

The turbulent shear stress can be calculated from the time-averaged equations for conservation of mass and x-momentum. These equations for this flow can be developed by expressing the components of velocity and density as the sum of mean and fluctuating parts. i.e. $\tilde{u} = U + u'.\tilde{v} = V + v'.$ and $\tilde{\rho} = \rho + \rho'.$ where the primes indicate the fluctuating parts. The mean quantities are shown here with no diacritical marks. The equations are

$$\frac{\partial}{\partial x}(\rho U) + \frac{\partial}{\partial y}(\rho \tilde{V}) \approx 0. \tag{18}$$

$$\frac{\partial}{\partial x}(\rho U^2) + \frac{\partial}{\partial y}(\rho U\tilde{V}) \approx -\frac{\partial p}{\partial x} + \frac{\partial \tau}{\partial y}. \tag{19}$$

where $\rho\tilde{V} = \rho V + \overline{\rho' v'}.$ the bar being used to denote the time average. It is assumed here (as supported by the discussion in §5.2) that $\overline{\rho' u'} \ll \rho U.$ that the Reynolds stresses are much larger than the viscous stresses. and that all fluctuation correlations in u ($\rho\overline{u'^2}$. $2U\overline{\rho' u'}$. and $\overline{\rho' u'^2}$) are small compared with the product of ρU^2. The gradients in the y-direction are assumed to be much larger than gradients of similar quantities in the x-direction. The quantity τ in the x-momentum equation (19) is the turbulent shear stress. where $\tau = -\rho\overline{u' v'}.$ the Reynolds stress. plus higher-order terms ($\overline{\rho' u' v'}.$ $U\overline{\rho' v'}.$ and $V\overline{\rho' u'}$). For the purposes of this discussion. it is not necessary to state exactly which fluctuation terms constitute τ.

The x-momentum and continuity equations can be combined by introducing a

similarity variable and also a stream function. Taking here $\eta \equiv y/\delta(x)$[†], where $\delta(x)$ is a characteristic layer width (e.g. δ_1), allows rewriting of the x-momentum equation (19) to give

$$-\eta\rho U \cdot \frac{\mathrm{d}U}{\mathrm{d}\eta}\frac{\mathrm{d}\delta}{\mathrm{d}x} + \rho\tilde{V}\frac{\mathrm{d}U}{\mathrm{d}\eta} = \frac{\mathrm{d}\tau}{\mathrm{d}\eta} - \eta\frac{\mathrm{d}p}{\mathrm{d}\eta}\frac{\mathrm{d}\delta}{\mathrm{d}x}. \tag{20}$$

The continuity equation (18) is identically satisfied if the two-dimensional mean velocity components are derived in the usual manner in terms of a stream function of the form $\Psi = \rho_0 U_1 \delta(x) f(\eta)$ where the velocity–density products are given by

$$\rho U = \frac{\partial\Psi}{\partial y}, \quad \rho\tilde{V} = -\frac{\partial\Psi}{\partial x}. \tag{21}$$

Expressing (21) in terms of linear similarity coordinates gives the following relations for the velocity components:

$$U = U_1 \hat{s}\frac{\mathrm{d}f}{\mathrm{d}\eta} \tag{22}$$

and

$$\tilde{V} = U_1\hat{s}\left(\eta\frac{\mathrm{d}f}{\mathrm{d}\eta} - f\right)\frac{\mathrm{d}\delta}{\mathrm{d}x}. \tag{23}$$

where $\hat{s}(\eta) \equiv \rho_0/\rho$. Combining (20) and (21) with (22) and (23) thus gives

$$-\frac{U_1^2}{\Delta U^2}\frac{\mathrm{d}\delta}{\mathrm{d}x}f\left[\frac{\mathrm{d}\hat{s}}{\mathrm{d}\eta}f + \hat{s}\frac{\mathrm{d}^2 f}{\mathrm{d}\eta^2}\right] = \frac{1}{\rho_0 \Delta U^2}\frac{\mathrm{d}\tau}{\mathrm{d}\eta} - \frac{\eta}{\rho_0 \Delta U^2}\frac{\mathrm{d}p}{\mathrm{d}\eta}\frac{\mathrm{d}\delta}{\mathrm{d}x}. \tag{24}$$

Equation (24) provides, for given $f(\eta)$ and $\hat{s}(\eta)$ profiles, a means of estimating the shear-stress profile. The second term on the right-hand side (pressure term) is small.

Equation (24) can be integrated with respect to η to determine the layer shear-stress profile. Performing this calculation may result in a computed shear-stress profile that indicates a non-zero shear stress in one of the free streams. (see, for example. Spencer & Jones 1971). The calculated shear stress can be ensured to tend to zero in both free streams if the following condition, which is essentially a statement of conservation of mass for the top (i.e. high-speed) half of the layer, is enforced:

$$\eta_h = \int_{\eta_0}^{\eta_h} \frac{\rho U}{\rho_1 U_1}\,\mathrm{d}\eta. \tag{25}$$

where η_h is an arbitrary point in the high-speed free stream outside the layer. The dividing streamline. η_0, corresponds to the location at which $\rho\tilde{V} = \eta\rho U$, and is also the point at which the shear stress in the layer is a maximum. In the computations of Lang (1985) for a non-reacting layer, the shear stress was fixed at zero in the free streams by specifying the value of the vertical velocity component in the low-speed free stream. The vertical velocity component in the high-speed free stream was then obtained from integrating the continuity equation (18).

Calculated turbulent shear-stress profiles are shown in figure 9. Model density and velocity profiles, obtained from experimental results, provided the functions $f(\eta)$ and $\hat{s}(\eta)$. The changes in mean velocity profile with heat release were discussed in §5.1; the changes in mean temperature profile will be discussed in §6. For the purposes of

---

† In this discussion. this form is more convenient than the form $\eta = y/(x - x_0)$ used in previous sections.
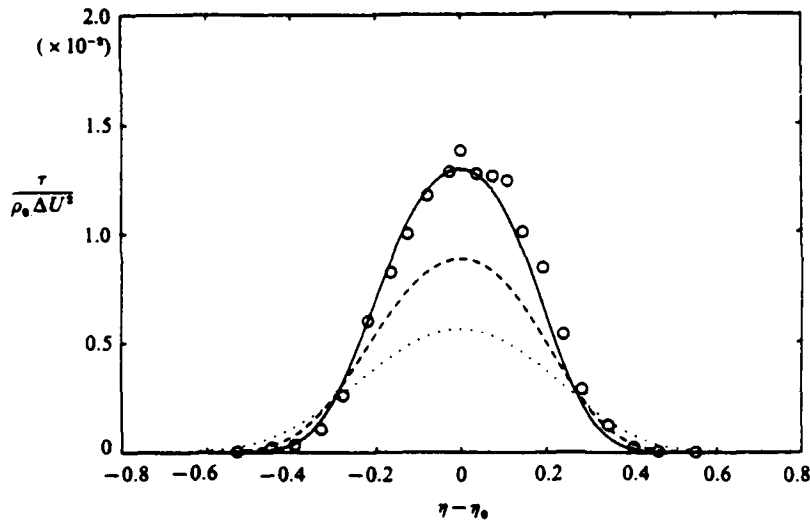
FIGURE 9. Calculated shear-stress profiles: —. $\overline{\Delta\rho}/\rho_0 = 0$: -·-. $\Delta\rho/\rho_0 = 0.2$: ·····. $\overline{\Delta\rho}/\rho_0 = 0.4$: O. data of Spencer & Jones (1971). η_0 is the location of the dividing streamline.

the computations performed in this section, symmetric model density (i.e. temperature) and velocity profiles were assumed, whose fit parameters were varied to match the observed changes in the profiles with heat release. The growth rate, $d\delta/dx$, was taken from the data of $\delta_1/(x-x_0)$ depicted in figure 3. It can be seen that with increasing heat release a marked decrease in shear stress is indicated. A broadening of the shear-stress profile with heat release is also apparent; this results from the broadening of the mean velocity profile $U(\eta)$ as was seen in figure 6. The calculated shear stress at zero heat release agrees well with the values of $\tau = -\rho\overline{u'v'}$ reported by Spencer & Jones (1971) for non-reacting flow (scaled here in width to match the present data, which are at a different speed ratio). A decrease in shear stress with heat release is also consistent with the results of direct numerical simulations by McMurtry & Riley (1987), which indicate that a density reduction due to heat release serves to both suppress the turbulent shear stress as well as to lower the generation rate of turbulent kinetic energy.

It is interesting to note that the decrease in shear stress with heat release is also consistent with the mixing-length scaling argument of Prandtl (1925):

$$\tau \approx \mu_t \frac{\partial U}{\partial y}, \quad \mu_t = \rho \hat{l}^2 \left|\frac{\partial U}{\partial y}\right|,$$

where $\hat{l}$ is the mixing length. Expressing $\partial U/\partial y$ in similarity coordinates gives

$$\tau \approx \rho \frac{\hat{l}^2}{\delta^2} \left|\frac{dU}{d\eta}\right| \frac{dU}{d\eta}. \tag{26}$$

Assuming $\hat{l} \sim \delta$, (26) suggests that if the similarity mean velocity profile is not strongly altered by heat release, the shear stress will decrease with decreasing density. An alternative argument is that if the correlation $\overline{u'v'}$ is not greatly altered by heat release, then the Reynolds stress, $\tau = -\rho\overline{u'v'}$, will decrease with heat release owing to the decreasing density. It should be pointed out, however, that some change in the velocity field does evidently occur with increasing heat release. This was seen

in the present work by the broadening of the mean velocity profiles in figure 6. An argument presented by Wallace (1981) suggests that the vorticity distribution within the large structures is altered by heat release owing to the action of the baroclinic torque which arises from non-aligned density gradient and acceleration vectors. This implies a change both in the mean velocity and in the fluctuating velocity correlation terms. The effects of thermal expansion in addition to those of baroclinic torque have been examined in detail by the direct numerical simulations of McMurtry *et al.* (1986) and McMurtry & Riley (1987). The results of those simulations clearly show a redistribution of vorticity leading to a decrease in the vorticity in the structure cores. Some changes in the shape of the mean velocity profiles with heat release were also indicated by those simulations. However. as quantified in the following discussion. the density change alone appears to be sufficient to result in decreased values of turbulent shear stress consistent with the observed decrease in layer growth rate. This, in addition to the observed relative insensitivity of the mean velocity profile to heat release. suggests that. as concerns the shear stress. the change in density dominates over changes in the velocity field.

There appear to be several possible values of density to employ in estimating the turbulent shear-stress reduction caused by heat release. One choice is the mean density at the given transverse station in the layer. Another possibility is suggested by considering the large-scale nature of the flow. Rajagopalan & Antonia (1981) found in a non-reacting flow that at least 80 % of the total shear stress appeared to be contained within the large-scale structures. As discussed in §7. large-scale structures persisted at all levels of heat release in this investigation. This suggests that an appropriate method for estimating the shear stress in a flow with heat release might consist of a combination of the shear stress found in unreacting flow and some representative large-scale structure shear stress. The shear stress could be expressed as

$$\tau(\eta) = (1 - \hat{a})\tau_0(\eta) + \hat{a}\tau_0(\eta)\frac{\rho^*}{\rho_0}. \tag{27}$$

where $\tau_0(\eta)$ is the shear-stress profile for the non-reacting flow. ρ^* is the structure density (here taken to be uniform within the structure). and $\hat{a}$ is the fraction of total stress contributed by the large-scale structure.

In order to obtain an estimate for the temperature in the structures from the mean temperature profile. it must be kept in mind. as pointed out by Mungal & Dimotakis (1984). that cold tongues of fluid penetrate well into the layer. This will be seen in §6 to also be the case at high heat release. These statements imply a value of a representative homogeneous large-scale structure temperature somewhat higher than the maximum mean temperature. The structure density can thus be expressed as

$$\frac{\rho^*}{\rho_0} = \frac{T_0}{T_0 + \hat{c}\overline{\Delta T}_{\max}}. \tag{28}$$

where $\overline{\Delta T}_{\max}$ is the maximum mean temperature rise in the layer and $\hat{c}$ is a weighting factor of value greater than unity.

The dependence of the peak shear stress on heat release is shown in figure 10. The solid line represents the peak shear stress calculated from the mean velocity and density profiles. The dashed and dotted lines correspond to the peak shear stress predicted by the method of (27). assuming values of $\hat{a} = 0.8$. $\hat{c} = 1.0$ and $\hat{a} = 1.0$. $\hat{c} = 1.1$. respectively. These two curves are above and below the result calculated from the mean velocity and density profiles. This method does not allow deter-
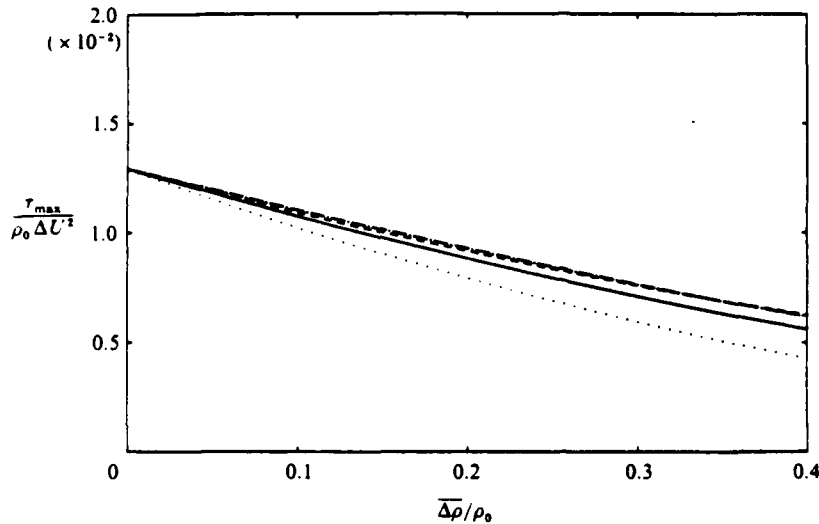
FIGURE 10. Reduction in maximum shear stress with heat release : —. calculated from ρ. U profiles : ···. $\hat{a} = 0.8$. $\hat{c} = 1.0$; ····. $\hat{a} = 1.0$. $\hat{c} = 1.1$; ——. δ/x = constant. See text for explanation.

mination of $\hat{a}$ and $\hat{c}$ separately. It does. however. suggest that the scaling of (27) is reasonable and is consistent with the possibility that at least 80% of the shear stress is contributed by the large-scale structures. Also included in figure 10 is the trend in maximum shear stress that would occur if the layer growth rate were constant and unchanged by heat release. The implication is that. even if the layer growth rate were constant. a substantial decrease in the turbulent shear stress would occur with heat release.

6. Temperature rise and amount of product formation

Time-resolved temperature measurements were performed using the cold-wire probes described in §2.2. Sample time traces are presented in figure 11(a). corresponding to a run with 2% F_2 and 2% H_2. with an adiabatic flame temperature rise of 186 K. Similar traces were presented. for conditions of low heat release. by Mungal & Dimotakis (1984). Figure 11(a) consists of individual traces representing the temperature rise recorded by the individual probes. with the high-speed free stream toward the top of the figure. Each horizontal axis represents 51.2 ms of real time. The vertical coordinate of each trace is $\Delta T/\Delta T_{max}$. where ΔT_{max} is the maximum temperature rise recorded by any probe. The traces are representations of the temperatures sensed by the probes as the hot and cold fluid elements flow past them : hence. the leading edge of any fluid element appears in the figure to the left of the corresponding trailing edge. Each time axis corresponds to a geometric distance which represents the product of the local flow velocity and the given time interval : to represent these distances each time axis would need to be shown substantially larger in the figure to be to scale with the probe spacings shown. The amount of compression in this sense ranges from a factor of about 9 for probes near the high-speed free-stream to roughly 4 for probes near the low-speed free stream. Time traces corresponding to a 4% F_2 and 4% H_2 run ($\Delta T_f = 368$ K) and a 6% F_2 and 6% H_2 run ($\Delta T_f = 554$ K) are shown in figures 11(b) and 11(c). respectively.

It can be observed in figure 11(a-c) that there are large. hot structures. separated
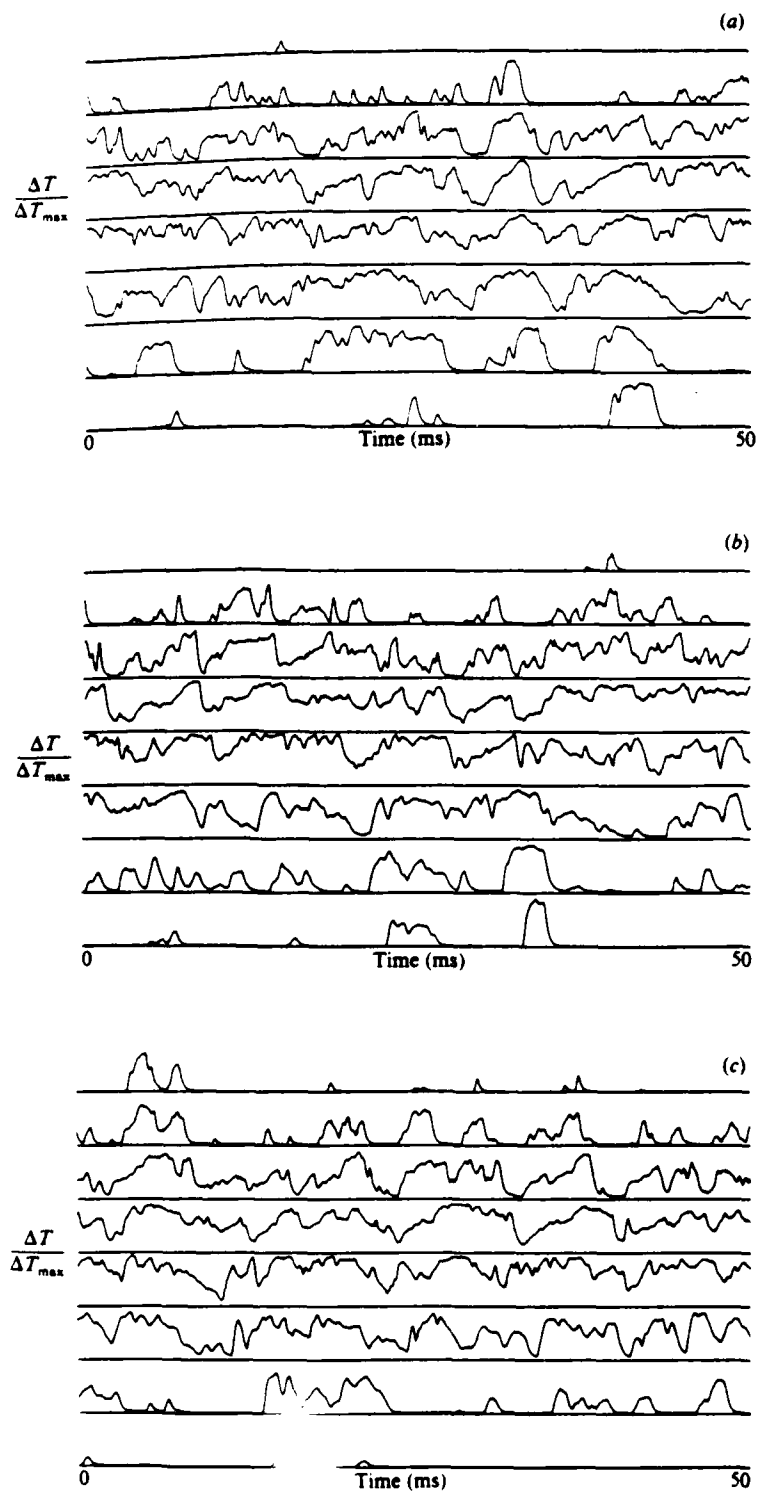
FIGURE 11. Temperature *vs.* time trace: $\phi = 1$; high-speed fluid on top. (a) $2\%F_2$, $2\%H_2$, $\Delta T_f = 186$ K. $\Delta T_{max} = 171$ K. (b) $4\%F_2$, $4\%H_2$. $\Delta T_f = 368$ K. $\Delta T_{max} = 348$ K. (c) $6\%F_2$, $6\%H_2$. $\Delta T_f = 554$ K. probe $\Delta T_{max} = 496$ K.
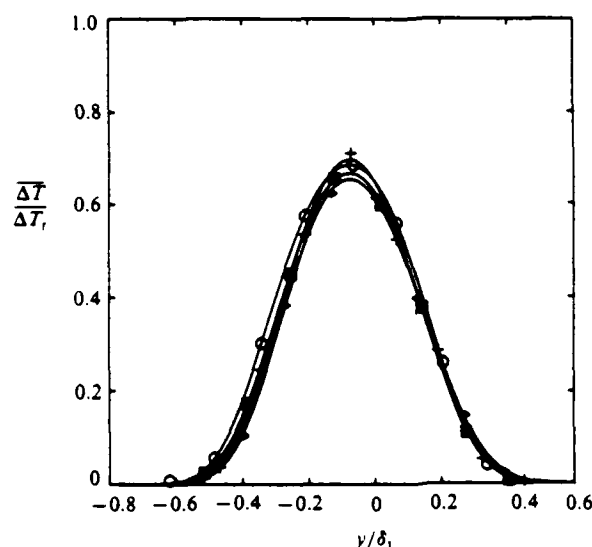
FIGURE 12. Mean temperature-rise profiles. $\phi = 1$: $\bigcirc$, $2\%F_2$:$2\%H_2$, $\overline{\Delta\rho}/\rho_0 = 0.162$: $\square$, $3\%F_2$, $3\%H_2$, $\overline{\Delta\rho}/\rho_0 = 0.206$: $\triangle$, $4\%F_2$:$4\%H_2$, $\overline{\Delta\rho}/\rho_0 = 0.260$:$+$, $5\%F_2$:$5\%H_2$, $\Delta\rho/\rho = 0.286$: $\Diamond$, $6\%F_2$:$6\%H_2$, $\overline{\Delta\rho}/\rho_0 = 0.313$. Profiles shifted to coincide with peak of $2\%F_2$:$2\%H_2$ case.

by cold tongues of cool free-stream fluid which penetrate deep into the layer. These observations are consistent with the findings of Mungal & Dimotakis (1984). The dynamics of the layer structures will be discussed in §7. The convection velocity and mean structure spacing suggest that roughly seven large structures passed the measuring station during the time interval represented by each time trace in those figures. It should be noted that conduction error (Scadron & Warshawsky 1952; Paranthoen, Lecordier & Petit 1982) prevented the probes near the centre of the layer from indicating a zero temperature rise, which would correspond to the cool, unreacted tongues of recently entrained fluid.

The average, over an entire run, of all time trace records results in the mean temperature profile. Several profiles, normalized by the corresponding adiabatic flame temperatures, are shown in figures 12, 13 and 14. Each of the figures presents profiles at a given stoichiometric mixture ratio ($\phi = 1$, $\frac{1}{2}$, $\frac{1}{4}$). The transverse coordinate. y/δ_1, indicates the distances from the splitter-plate tip normalized by the corresponding value of δ_1 for each run, with positive values toward the high-speed side of the layer. This coordinate was employed to enable easy comparison between profiles with different layer thicknesses. Following Mungal & Dimotakis (1984), an empirical function of the form

$$\frac{\Delta T}{\Delta T_f} = \exp\left(c_1 + c_2 y + c_3 y^2 + c_4 y^3 + c_5 y^4\right)$$

was employed to represent the local mean temperature rise profile. The coefficients for the present investigation were determined by a nonlinear least-squares fit, and the resulting function generally provided a good fit to the local mean temperature rise data. In each of the figures 12, 13 and 14, the profiles representing runs with more than 2% F_2 were shifted in y/δ_1 to coincide with the peak of the 2% F_2 profiles to aid comparison.
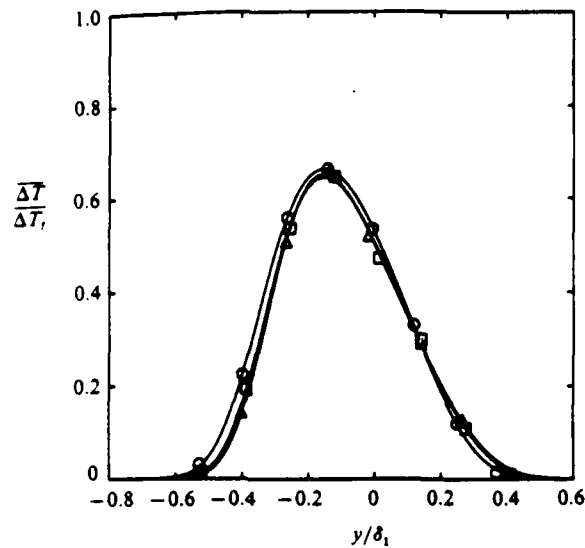
FIGURE 13. Mean temperature-rise profiles. $\phi = \frac{1}{2}$: O. $2\%F_2:4\%H_2$, $\overline{\Delta\rho}/\rho_0 = 0.190$; □. $4\%F_2$: $8\%H_2$. $\overline{\Delta\rho}/\rho_0 = 0.292$; △. $6\%F_2:12\%H_2$. $\overline{\Delta\rho}/\rho_0 = 0.361$. Profiles shifted to coincide with peak of $2\%F_2:4\%H_2$ case.
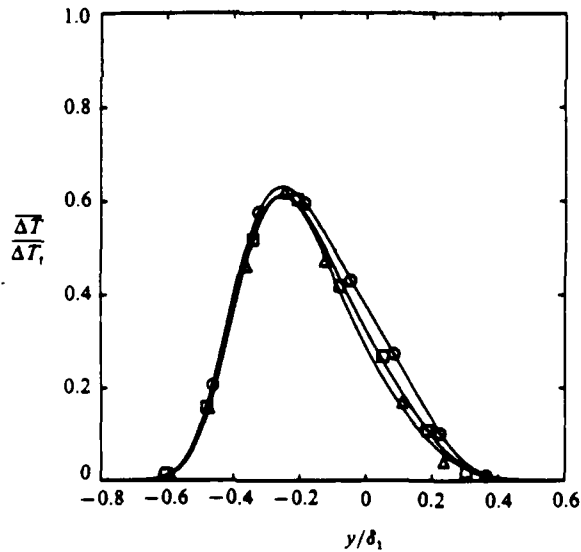

FIGURE 14. Mean temperature-rise profiles. $\phi = \frac{1}{4}$: O. $2\%F_2:8\%H_2$. $\overline{\Delta\rho}/\rho_0 = 0.214$; □. $4\%F_2$: $16\%H_2$. $\overline{\Delta\rho}/\rho_0 = 0.311$; △. $6\%F_2:24\%H_2$. $\overline{\Delta\rho}/\rho_0 = 0.370$. Profiles shifted to coincide with peak of $2\%F_2:8\%H_2$ case.

An interesting result is that at a given stoichiometric mixture ratio the shape of the mean temperature profiles. normalized by the adiabatic flame temperatures. did not change greatly in spite of the large values of heat release. There appears to be no qualitative change in the profiles at $\phi = 1$ and $\phi = \frac{1}{2}$. At $\phi = \frac{1}{4}$. a slight reduction in the profile height on the high-speed side can be observed.

Wallace (1981) and Mungal & Dimotakis (1984) observed that the mean temperature at any point in the layer was substantially below the adiabatic flame
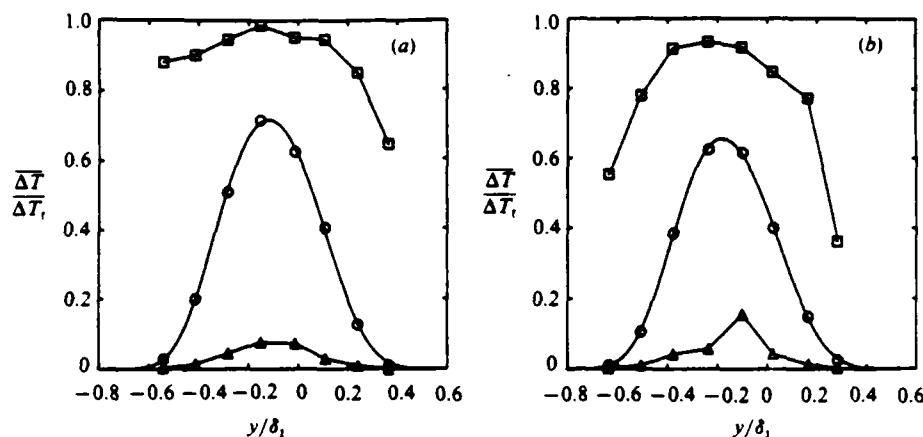
FIGURE 15. Temperature-rise profiles with maxima and minima. $\phi = 1$: $\bigcirc$. mean: $\square$. maximum: $\triangle$. minimum. (a) 4%F_2:4%H_2. $\Delta T_f = 368$ K: (b) 6%F_2:6%H_2. $\Delta T_f = 554$ K.

temperature. This was also observed in the present experiments at high heat release. This suggests that the mean temperature profiles. as at low temperature. result largely from a 'duty-cycle' phenomenon by which each probe spends a greater or lesser portion of the run time immersed in hot structure fluid. depending on its location in the layer, as proposed by Mungal & Dimotakis (1984). This is consistent with the data shown in figure 11 (a–c). where fairly distinct large. hot regions of fluid persist in the layer at elevated temperature. This gives a higher mean temperature near the centre of the layer and a lower value out near the layer edges. Employing an excess of high-speed reactant (i.e. $\phi < 1$) results in a shift in the mean temperature-rise profile toward the side containing the lean reactant. consistent with the low-heat-release results of Wallace (1981) and Mungal & Dimotakis (1984).

Konrad (1976) and Koochesfahani & Dimotakis (1986) demonstrated that. in shear flows with no heat release. the composition of the mixed fluid is fairly uniform across the layer. This was also seen in the low-heat-release work of Mungal & Dimotakis (1984) and appeared to persist. to some extent. in the present experiments. The extent to which the temperature in the large structures was uniform can be inferred by considering the maximum recorded temperatures at each point across the layer. The mean profiles at two selected values of heat release for $\phi = 1$. and also the maximum and minimum temperatures recorded during the course of the entire run. are shown in figure 15(a. b). A similar comparison for $\phi = \frac{1}{4}$ is made in figure 16(a. b). In both figure sets. it can be seen that at lower temperatures the maximum temperatures in the central portions of the layer are relatively uniform. suggesting a fairly uniform temperature in the large structures. However. above about $\Delta T_f \approx 500$ K. the maxima appear somewhat more peaked near the centre of the layer. suggesting that at higher temperatures the core regions of the structures become relatively hotter than the structure edges. As in Mungal & Dimotakis (1984). none of these data were compensated for conduction error (see §2.2). and one must assume that the probes were incapable of resolving the highest instantaneous temperature rise (near the adiabatic flame temperature rise). as well as the lowest instantaneous temperature rise (near zero for cold free-stream fluid).

It is possible to define a variety of parameters to quantify the trends in the amount of heat released and product formed. In the following discussion. two different
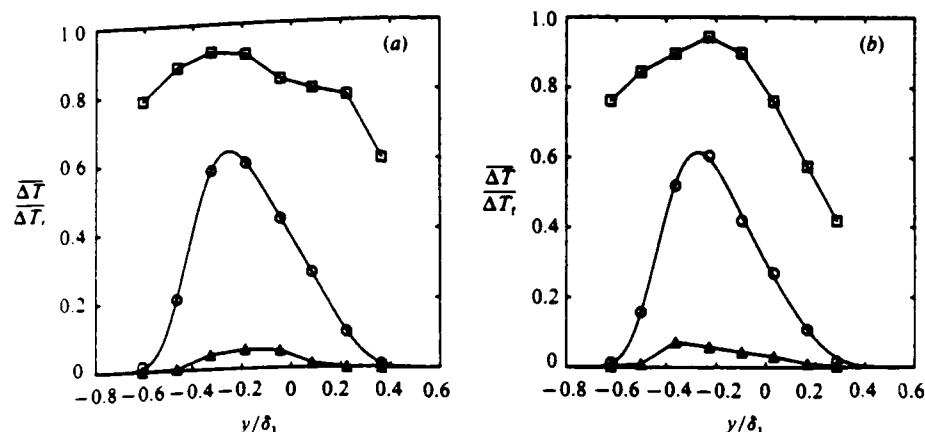
FIGURE 16. Temperature-rise profiles with maxima and minima. $\phi = \frac{1}{4}$: $\bigcirc$. mean: $\square$. maximum:
$\triangle$. minimum. (a) $2\%F_2 : 8\%H_2$. $\Delta T_f = 302$ K: (b) $4\%F_2 : 16\%H_2$. $\Delta T_f = 600$ K.

parameters will be employed for this purpose. The first. termed the ˙product fraction thickness˙ in this work. is an integral measure which relates to the mole fraction of reactant converted to product in the mixing layer at a given downstream location. The second parameter is an integral measure of the total amount of product in the layer and will be referred to here as 'product mass thickness'.

The fractional conversion to chemical product can be related. for conditions of constant pressure. to the ratio of the enthalpy rise at a given measured temperature to the corresponding enthalpy rise indicated by the adiabatic flame temperature. Integration of the time-averaged value of this quantity across the width of the layer allows definition of the normalized ˙product fraction thickness˙

$$\frac{\delta_P}{\delta_1} \equiv \frac{1}{\delta_1} \int_{-x}^{x} \frac{\overline{\Delta H(y)}}{\Delta H(T_f)} \, dy. \tag{29}$$

In this definition each value of the product fraction thickness. δ_P. is normalized by the corresponding local 1 % width. δ_1. which varies. as the case may be. for each value of heat release (as indicated in figure 3). In representing the mole fraction occupied by chemical product. (29) serves as a measure of the efficiency of the mixing and chemical reaction processes in the layer. Relating the enthalpy rise to the measured temperature rise allows writing

$$\frac{\delta_P}{\delta_1} \equiv \frac{1}{\delta_1} \int_{-x}^{x} \frac{\overline{\Delta T(y)}}{\Delta T_f} \, dy. \tag{30}$$

This definition of normalized product fraction thickness was employed by Dimotakis (1987). and is identical to (29) in the case of low heat release where the mixture specific heat can be regarded as constant. Equation (30) was used in this investigation to calculate the values of normalized product fraction thickness. At the highest temperatures of the present study. the actual enthalpy of the gas mixture at the flame temperature differs from the value calculated using a constant specific heat and flame temperature rise by up to 8%. Since the average flow temperature at any given location results from the passage of both hot and cold regions of gas. the actual error in representing (29) by (30) is less.

The product fraction thickness defined by (30) can be simply related to the normalized 'product thickness' used by Mungal & Dimotakis (1984) to relate the temperature rise to the amount of product

$$\frac{\delta_{P_t}}{\delta_1} \equiv \frac{1}{\delta_1} \int_{-\infty}^{\infty} \frac{\hat{C}_p \overline{\Delta T}(y)}{c_{02} \Delta Q} dy, \tag{31}$$

where $\hat{C}_p$ is the molar specific heat capacity at constant pressure and ΔQ is the molar heat release of the chemical reaction. If the specific heat is taken to be constant, and neglecting any effects of differential diffusion of heat or reactant species, the adiabatic flame temperature rise can be given as

$$\Delta T_f = \frac{1}{1+\phi} \frac{c_{02} \Delta Q}{\hat{C}_p} \tag{32}$$

This corresponds to the case where ϕ is varied by keeping c_{02} fixed and increasing c_{01}. Inserting the adiabatic flame temperature rise into (30) and comparing with (31) thus yields the relation $\delta_P \doteq (1 + \phi)\delta_{P_t}$.

An alternative definition for a product thickness based on the actual density of product can be obtained by integrating the local product fraction multiplied by the local fluid density, as follows

$$\frac{\delta_{P_m}}{\delta_1} \equiv \frac{1}{\delta_1} \int_{-\infty}^{\infty} \frac{\overline{\Delta T}(y)}{\Delta T_f} \frac{\bar{\rho}(y)}{\rho_0} dy. \tag{33}$$

The thickness defined by this relation will be termed the normalized 'product mass thickness'. The motivation for this alternative definition is to account for the decrease in the concentration of product, as the density in the layer decreases, owing to heat release. The earlier definition, the product fraction thickness defined in (30), could tend to a finite value even in the limit of infinite temperature rise (zero density) in the layer. The product mass thickness tends to the product fraction thickness in the limit of a very small temperature rise (i.e. small density changes). Relating the density to the local mean temperature gives

$$\frac{\delta_{P_m}}{\delta_1} \equiv \frac{1}{\delta_1} \frac{T_0}{\Delta T_f} \int_{-\infty}^{\infty} \frac{\overline{\Delta T}(y)}{T_0 + \overline{\Delta T}(y)} dy. \tag{34}$$

Relation (34) was used to compute the values of normalized product mass thickness.

Estimates of the product fraction thickness for this investigation are presented in figure 17. Some of the low-heat-release results calculated from the data of Mungal & Dimotakis (1984) and Wallace (1981) are included for comparison. For the present investigation, some decrease in the product fraction thickness for all stoichiometric mixture ratios with heat release can be inferred, amounting to a reduction of approximately 18% for a mean density decrease of 24%. By contrast, the data suggest an increase in product volume thickness with heat release between the low-heat-release results in this work and the results reported by Mungal & Dimotakis (1984) and Wallace (1981). The relatively complicated behaviour of the product fraction thickness shown in figure 17 is the consequence of many competing physical mechanisms, which may result in temperature-induced changes in the volumetric entrainment ratio (see §5.3), the intermittency, and the probability density of the mixed fluid. These issues are discussed in Hermanson (1985).

The results of the total product calculation suggested by the product mass fraction (34) are shown in figure 18. It is seen that the total amount of product (analogous also
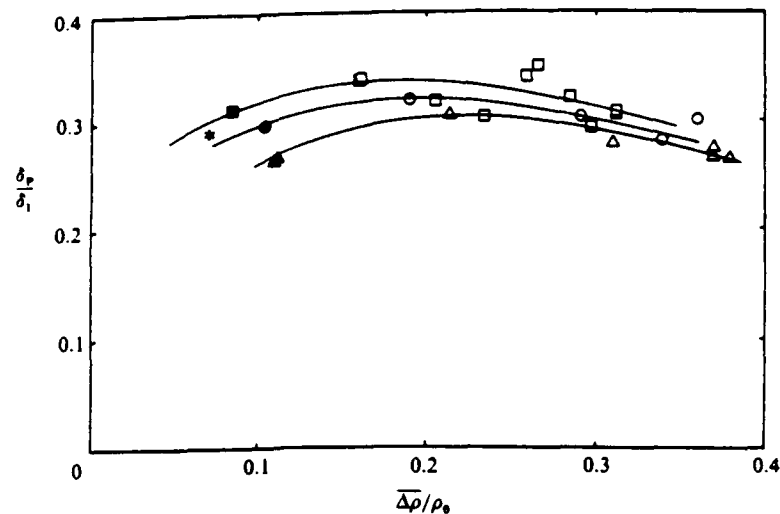
FIGURE 17. Product fraction thickness *vs.* heat release. □, ■, •, $\phi = 1$: O, ●, $\phi = \frac{1}{2}$: △, ▲, $\phi = \frac{1}{4}$. Solid symbols. Mungal & Dimotakis (1984); open symbols, present work; asterisk. Wallace (1981).
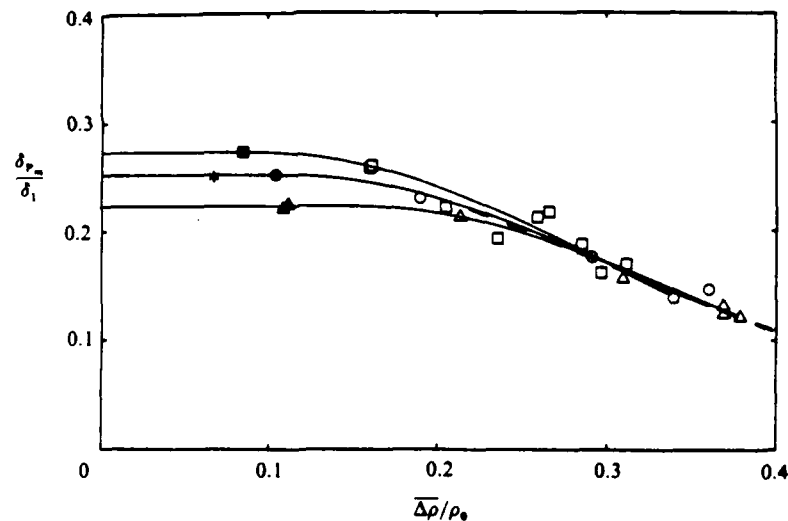

FIGURE 18. Product mass fraction thickness *vs.* heat release. □, ■, •, $\phi = 1$: O, ●, $\phi = \frac{1}{2}$: △, ▲. $\phi = \frac{1}{4}$. Solid symbols. Mungal & Dimotakis (1984); open symbols, present work; asterisk. Wallace (1981). Dashed line is representative fit to data for all ϕ at high heat release.

to the total amount of heat release) decreases substantially with increasing temperature. This is partially due to the decrease in the product fraction in the layer at higher temperatures discussed previously. but appears to be mostly a consequence of the strong reduction owing to heat release in the entrainment of the reactants into the layer. It is also seen in figure 18 that while there is a noticeable dependence for the cases at low temperature rise on the amount of product with stoichiometric mixture ratio at a fixed level of heat release (i.e. fixed $\overline{\Delta\rho}/\rho_0$). this dependence appears to weaken considerably for higher values of heat release. In fact. beyond roughly $\overline{\Delta\rho}/\rho_0 = 0.2$. the product mass fraction data for all values of stoichiometric mixture ratio can apparently be represented by a single curve.

(a)

(b)

FIGURE 19. Spark schlieren photographs at low and high heat release. (a) $2\%F_2 \cdot 2\%H_2$. $\Delta T_f = 186$ K; (b) $6\%F_2 \cdot 16\%H_2$. $\Delta T_f = 847$ K.

The data in figure 18 may suggest a measure for determining some characteristic value o the heat-release parameter. $\overline{\Delta\rho}/\rho_0$. below which the effects of heat release can be ignored. Wallace (1981) suggests $\overline{\Delta T}_{max}/T_0 = 0.35$ as the threshold of maximum mean temperature above which heat release ceases to be passive. as seen by a deviation of the measured maximum mean temperature from that predicted using the non-reacting probability density functions of Konrad (1976). The threshold value suggested by Wallace corresponds to $\overline{\Delta\rho}/\rho_0 \approx 0.12$. which is roughly consistent with the speculative breaks in the curves shown in figure 18. This characteristic value could be defined as the break-point in each (constant-ϕ) curve. Assuming that the curves n figure 18 tend to a constant value as $\overline{\Delta\rho}/\rho_0$ tends to zero suggests a possible means for extrapolating the product fraction thickness data. as presented in figure 17. to lower values of heat release. It should be remarked that the physical significance of the two product measure definitions used in this discussion cannot be regarded as being fully established. and that furthermore the trends shown in figures 17 and 18 may be. to some extent. artifacts of the definitions themselves.

7. Large-scale structure dynamics

The investigations of Wallace (1981) and Mungal & Dimotakis (1984) showed that the large-scale structures that characterize non-reacting shear layers are also found in reacting layers at low heat release. Large-scale organization is also observable in shear flows at high temperatures. as shown by the work of Ganji & Sawyer (1980). Pitz & Daily (1983). and Keller & Daily (1983). Large-scale structures were also observed at all values of heat release in this investigation. Sample spark schlieren photographs. corresponding to the lowest and to one of the highest levels of heat release in this investigation. are presented in figure 19 (a. b). The schlieren sensitivity

was reduced for the high-heat-release case, figure 19(b), from the low-heat-release run shown in figure 19(a), making qualitative comparison of the fine details between the two flows difficult: in both sample photographs, however, the large-scale structures can be clearly discerned. Ganji & Sawyer (1980) argued that the schlieren visibility of the structures suggests that the large structures retain their predominately two-dimensional nature even as the heat release increases.

In the present work, large-scale vortex statistical information was obtained over the full range of heat release from motion picture data. The location of the apparent centre of each identifiable vortex was digitized. The phenomenon of vortex amalgamation occasionally made identification of individual vortices difficult: in some frames it was difficult to pick out any large-scale structures. Ganji & Sawyer (1980) pointed out that heat release might render the boundary between two merging structures invisible, while they might still be two separate fluid entities in the fluid-mechanical sense. Nonetheless, a typical motion picture was digitized to provide, typically, about 1600 points corresponding to individual vortex locations. Normally about 1300 frames were digitized, corresponding to about 2.8 s of run time, during which over 300 large-scale structures were convected through the test section and field of view. Redigitization of several runs suggested that this technique produced mean statistics accurate to about 5%. For cases with zero streamwise pressure gradient, little variation was observed with downstream distance in the local mean vortex spacing normalized by downstream distance and generally no significant difference in vortex statistics upstream and downstream of the mixing transition region.

Sample vortex-spacing histograms of four different runs, each with a different amount of heat release, are presented in figure 20(a–d). The histograms show the relative frequency of each value of vortex spacing normalized by the value of the 1% temperature thickness of the layer, δ_1, at the station halfway between the two vortices in question, assuming linear layer growth. Increasing temperature appears to have caused a decrease in the mean normalized vortex spacing, l/δ_1. The corresponding standard deviation of the histograms, σ, also appears to have been reduced with heat release. The solid lines in figure 20(a–d) represent the lognormal distribution proposed by the statistical theory of vortex circulation formulated by Bernal (1981):

$$P_\lambda(\lambda) = \frac{1}{(2\pi)^{\frac{1}{2}}\hat\sigma\lambda}\exp\left[-\frac{1}{2\hat\sigma^2}\left(\ln\left(\lambda/\bar\lambda\right)+\frac{\hat\sigma^2}{2}\right)^2\right].$$ (35)

Here $\lambda \equiv l/\delta_1$, and the parameter $\hat\sigma$ is related to the variance of the experimentally determined distribution, σ, by

$$\hat\sigma^2 = \left(\frac{l}{\delta_1}\right)^2(e^{-\sigma^2}-1).$$ (36)

The values of $\hat\sigma$ for the theoretical distributions shown in figure 20(a–d) were calculated using the l/δ_1 and σ indicated by the experimental data.

The parameter $\hat\sigma$ in (35) was shown by Bernal to be related to the relative frequencies of vortex pairing, tripling and tearing. Bernal found a value of $\hat\sigma = 0.28$ in the unreacting layer and showed that this value implies that pairing is the dominant vortex amalgamation mechanism. Increasing the relative frequency of tripling would result in a larger value of $\hat\sigma$: increasing tearing, a smaller value. In the present work, the values of $\hat\sigma$ calculated from the measured results were oserved to be nearly constant over the entire range of heat release, with a mean value of $\hat\sigma = 0.25$. The near-constancy of $\hat\sigma$ suggests that the relative frequencies of pairing,
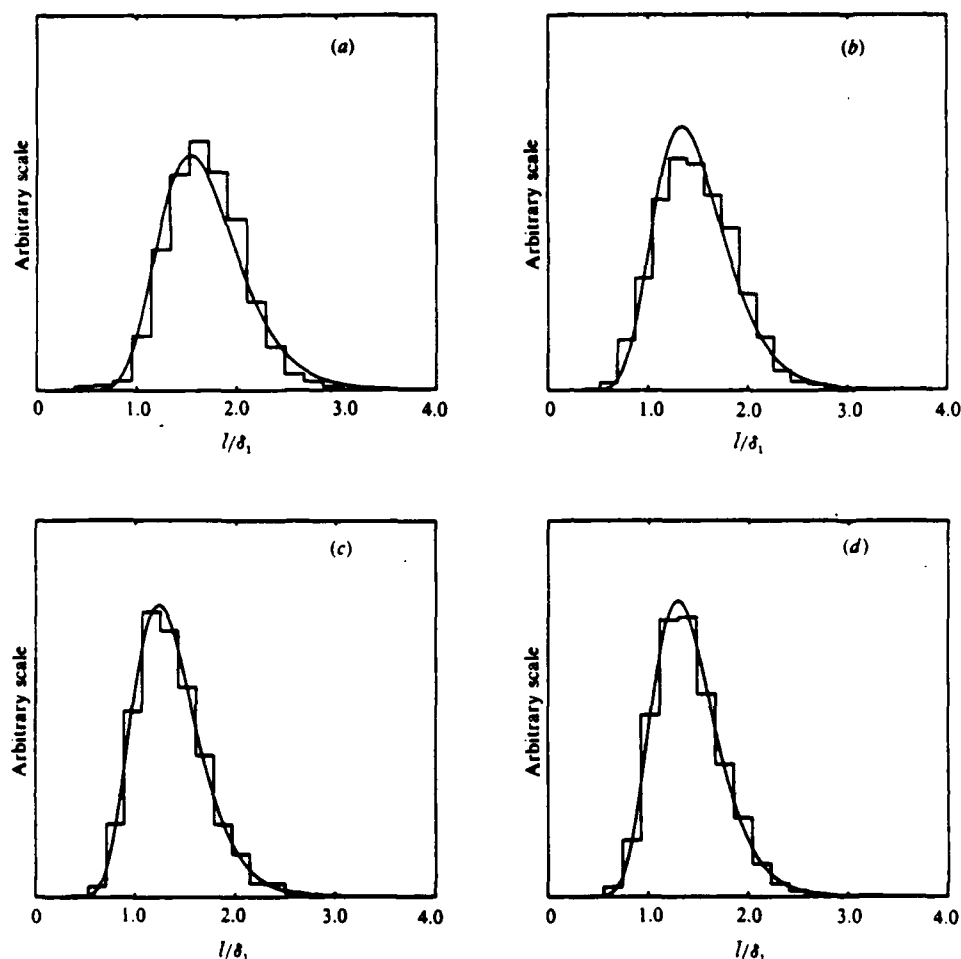
FIGURE 20. Vortex-spacing histograms. (a) $2\%F_2 : 2\%H_2$. $\Delta T_f = 186$ K. $l/\delta_1 = 1.69$. $\sigma = 0.43$. $\dot{\sigma} = 0.25$: (b) $4\%F_2 : 4\%H_2$. $\Delta T_f = 368$ K. $l/\delta_1 = 1.48$. $\sigma = 0.39$. $\dot{\sigma} = 0.26$: (c) $6\%F_2 : 6\%H_2$. $\Delta T_f = 554$ K. $l/\delta_1 = 1.36$. $\sigma = 0.35$. $\dot{\sigma} = 0.25$: (d) $6\%F_2 : 12\%H_2$. $l/\delta_1 = 1.25$. $\sigma = 0.30$. $\dot{\sigma} = 0.24$.

tripling, and tearing are not affected by heat release, though an increase (or decrease) of both tripling and tearing relative to pairing could also yield an unchanging value of $\dot{\sigma}$.

The decreasing trend in mean normalized vortex spacing, l/δ_1, with heat release is shown in figure 21. The decrease was substantial, as large as 25 % for a mean density reduction of 40 % in the layer. Because the vortex spacing decreased proportionally faster with heat release than the layer thickness, one could argue that the mechanism of vortex amalgamation was inhibited, to some extent, by heat release.

Schlieren flow visualization in the non-reacting case in this experiment was accomplished by using nitrogen and a density-matched mixture of helium and argon as free-stream fluids. The measured mean normalized vortex spacing is in fair agreement with the corresponding results from Brown & Roshko (1974), Bernal (1981), and Koochesfahani et al. (1979), which are included in figure 21 for comparison.

The decrease in mean vortex spacing has implications for the volumetric
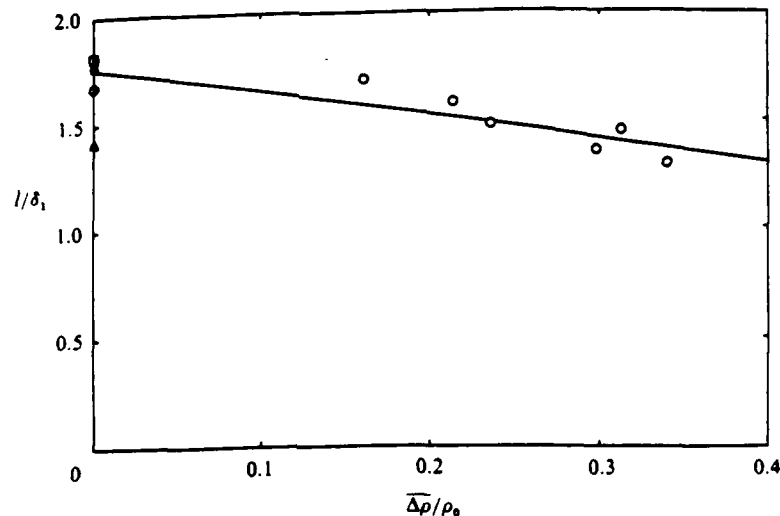
FIGURE 21. Mean vortex spacing *vs.* heat release: ○. present results: □. Brown & Roshko (1974): △. Bernal (1981): ●. Koochesfahani *et al.* (1979).

entrainment ratio into the layer. In Dimotakis (1986). the following expression is proposed for estimating the entrainment ratio:

$$E_v = s^{\frac{1}{2}}\left(1 + \frac{l}{x}\right). \tag{37}$$

This implies that the reduction in vortex spacing is accompanied by a reduction in the volumetric entrainment ratio in favour of more entrained fluid from the low-speed free stream. The observed decrease in mean vortex spacing indicates. using (37). a decrease in entrainment ratio of roughly 4% over the range of heat release in this investigation, which is within the range of entrainment ratio changes estimated in §5.3.

The persistence of large-scale structures at elevated temperatures has an interesting implication for the mean density in a layer with heat release. The mean density reduction parameter. $\overline{\Delta\rho}/\rho_0$. is of course a function of the adiabatic flame temperature rise, ΔT_f. This dependence is shown for the present investigation in figure 22. Some results calculated from the data of Mungal & Dimotakis (1984) and Wallace (1981) are also included. The mean density changed rapidly (with adiabatic flame temperature) at low heat release but less rapidly at high temperatures. These data suggest that there may be a limiting value of $\overline{\Delta\rho}/\rho_0$ at very high flame temperatures. and the present data suggest that the limiting value for a reacting shear layer is substantially less than unity. A limiting value of the mean density reduction might be expected if large-scale structures persist at all levels of heat release. resulting in the flow consisting of alternating regions of hot. low-density structure fluid and cold. high-density free-stream fluid. This would imply that even in the extreme case of infinitely high temperatures. where the cores of the structures would consist of fluid with essentially zero density. the regions of cold. unreacted free-stream fluid between structures would result in a finite mean density and a value of $\overline{\Delta\rho}/\rho_0$ less than unity.

The corresponding value of mean density reduction for the $U_2 = 0$ shear layer of
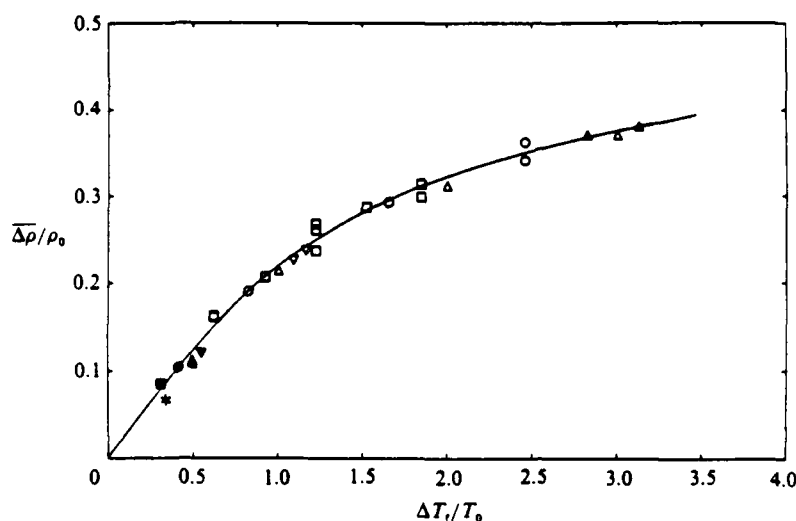
FIGURE 22. Mean density reduction vs. adiabatic flame temperature rise: $\square$. $\blacksquare$. $*$. $\phi = 1$: $\bigcirc$. $\bullet$. $\phi = \frac{1}{2}$: $\triangle$. $\blacktriangle$. $\phi = \frac{1}{4}$. Solid symbols: Mungal & Dimotakis (1984): open symbols. present work: asterisk. Wallace (1981).

Ganji & Sawyer (1980) is $\overline{\Delta\rho}/\rho_0 \approx 0.65$ for $\Delta T_f/T_0 = 4.5$. It should be pointed out that their U_2' layer reattached and thus was characterized by the recirculation and re-entrainment of hot products into the low-speed side. This caveat may explain the difference between their results and the present data. On the other hand. their $U_2'/U_1' \approx 0$ shear-layer data may not necessarily be directly comparable to the $U_2'/U_1' \approx 0.4$ data presented here.

8. Results for non-zero streamwise pressure gradient

A pressure gradient in the present investigation was imposed by fixing the sidewalls for the reacting flow in a position corresponding to zero pressure gradient in the unreacting flow. This yielded a naturally induced favourable pressure gradient in the case of flow with chemical reaction. the magnitude of which increased in proportion to the level of heat release. The results with favourable pressure gradient. combined with those at zero pressure gradient discussed earlier allow comparison of flows with the same level of heat release but with different streamwise pressure gradients. In the present study. favourable pressure gradient runs were made at reactant concentrations of up to 6% fluorine and 6% hydrogen. corresponding to an adiabatic flame temperature rise of up to 554 K. The amount of heat release was sufficient to induce a pressure decrease. Δp. over the distance from the splitter plate tip to the measuring station. of about half of $\frac{1}{2}\rho_2 U_2'^2$. the low-speed free-stream dynamic head. This served to increase the high-speed velocity from the nominal 22 m/s to 23.1 m/s and the low-speed velocity from 8.8 m/s to 11.3 m/s in the distance between the splitter tip and the measuring station. corresponding to a 22% decrease in the speed ratio. U_2'/U_1'.

8.1 Shear-layer growth

For a given level of heat release. the thickness of the layer. at a fixed measuring station. appeared to decrease for each favourable-pressure-gradient case. relative to

the corresponding flow with no streamwise pressure gradient. The thinning caused by pressure gradient is not surprising in an accelerating flow. In particular. the change in layer growth rate can be accounted for in terms of the change with downstream distance in speed ratio induced by the pressure gradient. as quantified in the following discussion.

For non-reacting shear layers with equal free-stream densities. a commonly used expression for relating the growth rate to the speed ratio was given by Brown & Roshko (1974) (this is a special case of the more general form of (4). §5.1):

$$\frac{\delta_{\text{vis}}}{(x-x_0)} = 0.38\frac{1-r}{1+r}. \tag{38}$$

where δ_{vis} is the visual thickness of the layer. For the moderate values of the streamwise pressure gradient in this investigation. it is interesting to take this similarity relation as holding locally†, i.e.

$$\frac{\mathrm{d}\delta_1}{\mathrm{d}x} = \Lambda(\hat{q})\frac{1-r(x)}{1+r(x)}. \tag{39}$$

where the parameter $\Lambda(\hat{q})$ is a growth-rate parameter. taken to depend only on the amount of heat release. The speed ratio, $r(x) \equiv U_2(x)/U_1(x)$, is a local function of the downstream distance in the presence of a pressure gradient. Thus in this formation the growth rate is expressed as a product of two factors. one that relates only to the heat release. the other that depends on the magnitude of the pressure gradient. Equation (39) is essentially a statement that the layer is in local equilibrium, that is. that the speed ratio changes slowly compared with the rate at which the layer growth adjusts to it. A changing speed ratio with downstream distance in (39) due to pressure gradient thus indicates a nonlinear growth rate. It should be remarked that the speed ratio appears to impact the mean vortex spacing normalized by the layer thickness. as shown by the results of Browand & Troutt (1985). This effect is not strong. however. and could be expected for the largest amount of pressure gradient discussed here to result in a normalized vortex spacing change of about 1%. This should be compared to the observed variation in layer thickness with pressure gradient of up to 8%. The change in normalized vortex spacing is not directly addressed by the present analysis.

Integration of (39) gives the layer growth as a function of downstream distance, i.e.

$$\delta_1(x) = \Lambda(\hat{q})\int_0^x \frac{1-r(x)}{1+r(x)}\,\mathrm{d}x. \tag{40}$$

From (40) the thickness of a layer with heat release but at zero pressure gradient, $\delta_{1_0}(x)$. is

$$\delta_{1_0}(x) = \Lambda(\hat{q})\frac{1-r_0}{1+r_0}x. \tag{41}$$

where $r(x) \equiv r_0 =$ constant in the absence of a pressure gradient. Consideration of two layers at the same level of heat release (i.e. same value of $\Lambda(\hat{q})$) but with and without pressure gradient allows normalization of (40) by (41) to give

$$\frac{\delta_1(x)}{\delta_{1_0}(x)} = \frac{1}{x}\frac{1+r_0}{1-r_0}\int_0^x \frac{1-r(x)}{1+r(x)}\,\mathrm{d}x. \tag{42}$$

---

† Suggested by M. M. Koochesfahani in private discussions.

% F_2/% H_2	ΔT_f (K)	$\overline{\Delta\rho}/\rho_0$	$\dfrac{dp}{dx}$ (torr/cm)	$\kappa(\hat{q})$ (cm^{-1})	δ_1 (cm)
2/2	186.3	0.153	≈ 0	≈ 0	7.13
2/2	186.3	0.156	-0.0022	-0.0027	7.00
4/4	368.2	0.260	≈ 0	≈ 0	7.04
4/4	368.2	0.257	-0.0032	-0.0053	6.49
6/6	553.8	0.313	≈ 0	≈ 0	6.72
6/6	553.8	0.312	-0.0042	-0.0080	6.45

TABLE 2. Representative pairs of runs without and with streamwise pressure gradient. $dp/dx \equiv$ pressure gradient; $\kappa(\hat{q}) \equiv$ pressure gradient parameter (see text); $\delta_1 \equiv$ layer thickness at measuring station based on 1 % points of mean temperature rise profile. Flows at nominally zero pressure gradient have values of $\kappa(\hat{q}) < \pm 0.0003$ cm^{-1}.

The lower limit of integration in (40) and (42) is taken as $x = 0$; this analysis thus does not explicitly consider the effects of a virtual origin, x_0. By neglecting the virtual origin, it is essentially assumed that both the layer with a pressure gradient and the corresponding layer at zero pressure gradient attain the growth rate suggested by (39) in a downstream distance that is small compared with the distance from the splitter tip to the measuring station. In §5.1 the virtual origin for the zero-pressure-gradient case was seen to be typically about 7 % of the total distance to the measuring station. It should be noted that the layer in this investigation was not self-similar in the presence of a streamwise pressure gradient. This conclusion follows from the work of Rebollo (1973), who showed that, in order to have similarity, the layer growth must be linear and the free-stream dynamic heads must be matched. Neither condition was met in the present work.

The free-stream velocities can be determined from the corresponding Bernoulli equations, assuming that the streamwise pressure gradient dp/dx does not depend on downstream distance for the particular flow in question. The results are

$$U_1^{\cdot 2}(x) = U_{01}^{\cdot 2} - \frac{2}{\rho_1}\left[\frac{dp}{dx}\right]x \qquad (43a)$$

and

$$U_2^{\cdot 2}(x) = U_{02}^{\cdot 2} - \frac{2}{\rho_2}\left[\frac{dp}{dx}\right]x, \qquad (43b)$$

where $U_{01}^{\cdot}$ and $U_{02}^{\cdot}$ are the high-speed and low-speed free-stream velocities, respectively, at some reference point, e.g. at the start of the test section ($x = 0$). The values of dp/dx and the observed layer thickness at the measuring station are given in table 2 for several values of heat release.

The speed ratio as a function of downstream distance can be expressed by combining (43a) and (43b). The result is

$$r(x) = r_0\left[\frac{1 - 2\kappa(\hat{q})\,x}{1 - 2\kappa(\hat{q})\,r_0^2\,sx}\right]^{\frac{1}{2}}. \qquad (44)$$

where

$$\kappa(\hat{q}) \equiv \frac{dp/dx}{\rho_2\,U_{02}^{\cdot 2}}$$

is introduced here as the pressure gradient parameter, which has units of inverse length, and $r_0 \equiv U_{02}^{\cdot}/U_{01}^{\cdot}$ is the initial velocity ratio (at $x = 0$). For the fixed geometry in this work, $\kappa(\hat{q})$ depends directly on the level of heat release employed. The product
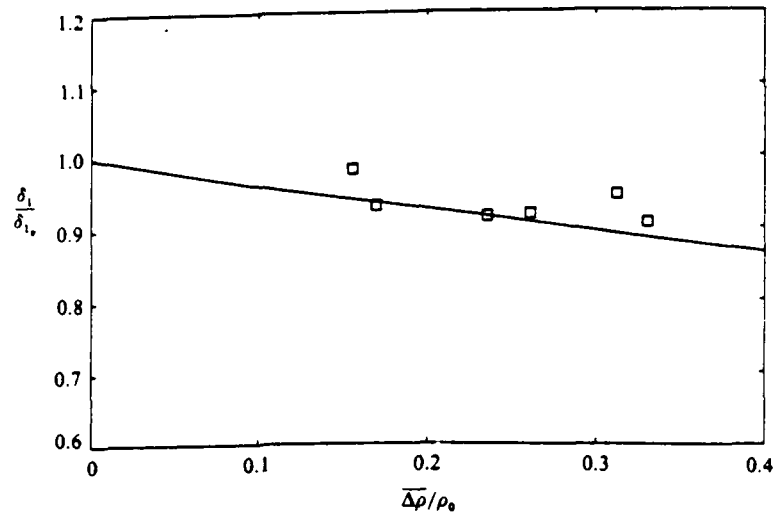
FIGURE 23. Normalized layer thickness with streamwise pressure gradient: ———. theory: □. experiment. δ_{1_0} is layer width at given level of heat release with no pressure gradient.

$\kappa(q) x$ is dimensionless and can be thought of as characterizing the cumulative effect of the pressure gradient over the length x. A non-dimensional parameter similar to $\kappa(\hat{q}) x$.

$$\beta \equiv \frac{d_j}{\rho_j u_j^2} \frac{dp}{dx},$$

was presented by Stårner & Bilger (1980) as a means of parameterizing reacting jet flows with streamwise pressure gradient. Here d_j is the jet diameter. ρ_j and u_j the jet fluid density and velocity, respectively.

The effect of a favourable pressure gradient is seen from (44) to increase the speed ratio (i.e. drive it toward unity): and to decrease it (drive it toward zero) for an adverse pressure gradient. The speed ratio is affected less by a favourable pressure gradient than by an adverse one of similar magnitude.

The trend in layer thinning over the full range of heat release and pressure gradient of this investigation is shown in figure 23, where the normalized layer thickness (δ_1/δ_{1_0}) at the measuring station is given against $\overline{\Delta\rho}/\rho_0$. The curve shown results from (42) and (44). In this calculation the values of dp/dx versus $\overline{\Delta\rho}/\rho_0$ were determined by a linear least-squares fit to the experimental data. The fit was on average accurate to about 6%. Values of $r_0 = 0.38$ and $s = 1$ were representative of the cases at zero pressure gradient considered here and were employed in the calculation.

Figure 23 thus indicates how the layer thickness for a given amount of heat release with the pressure gradient induced by the fixed wall locations of this experiment compares with the corresponding layer with zero streamwise pressure gradient. The experimental results are seen to be consistent with the predicted trend. The above analysis appears to adequately represent the layer growth and the changes in the free-stream conditions for the values of heat release and pressure gradient in this investigation. It is not clear whether these arguments will continue to be valid for larger values of favourable pressure gradient and higher flow temperatures. or for adverse pressure gradients.

The mean velocity profiles at the measuring station. other than showing a change
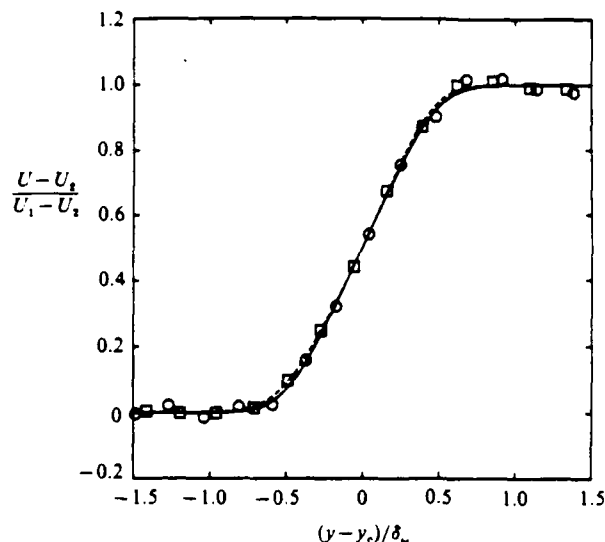
FIGURE 24. Mean velocity profile comparison. $6\%F_2:6\%H_2$. $\Delta T_f = 554$ K. $\bigcirc$. $\kappa(\dot{q}) \approx 0$. $\delta_\omega/(x-x_0) = 0.072$: $\square$. $\kappa(\dot{q}) = -0.0080/cm$. $\delta_\omega/(x-x_0) = 0.068$.

in maximum slope corresponding to a change in layer thickness. did not exhibit any significant differences in shape between the corresponding cases with and without pressure gradient. The normalized velocity profile for the maximum amount of pressure gradient in this invest'zation is compared with the corresponding profile at zero pressure gradient in figur .4.

8.2. Temperature rise and amount of product formation

It could be argued that. in reacting flows with substantial density variations and appreciable pressure gradients. an additional mixing mechanism might be operative. resulting from a possible relative acceleration between light fluid elements and heavy fluid elements. This mechanism is referred to as 'pressure gradient diffusion' by Bray & Libby (1981) and by Spalding (1986). The efficacy of such a mechanism would of course depend on the scales at which the density variations would occur and their relation to the viscous small scales of the flow. If the hot/cold fluid elements are very closely interlaced. viscous effects might not permit substantial relative motions to be established and little or no augmentation of the mixing would result.

The results of this experiment indicate little change in either the peak temperature or the amount of product formation as a result of the favourable pressure gradient. This is seen in figure 25. where three of the resulting mean temperature profiles. at the highest heat release and largest value of pressure gradient attained in this investigation. are compared. The profiles for $\kappa(\dot{q}) < 0$ were shifted as in figure 12 to aid comparison. These results indicate a maximum possible augmentation in product as indicated by the product volume fraction defined in §6. of about 8%. The cases with pressure gradient were seen to be. for all values of heat release. on average less than 5% higher in product thickness than the corresponding flows without pressure gradient. Bearing in mind that the estimated accuracy of the experimental results is 3-5%. these data also admit the possibility that the effect may be considerably smaller.

A small increase in product can be accounted for by the change in Reynolds
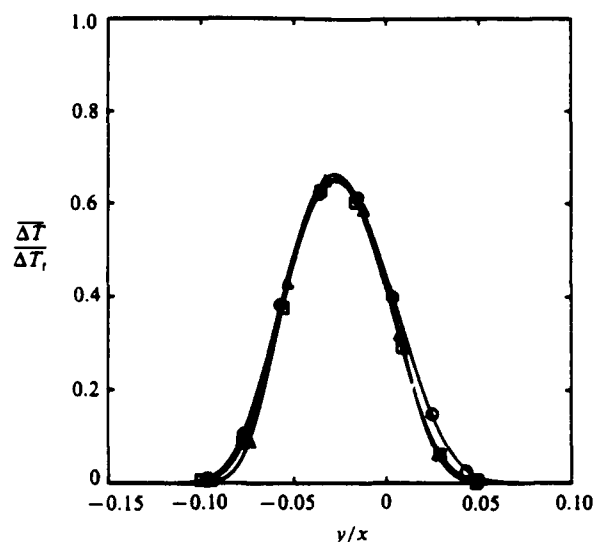
FIGURE 25. Pressure gradient effect on mean temperature profile. $6\%F_2 : 6\%H_2$, $\Delta T_f = 554$ K. $\bigcirc$. $\kappa(\dot{q}) \approx 0$: $\square$. $\kappa(\dot{q}) = -0.008\Gamma$ $\blacksquare$: $\triangle$. $\kappa(\dot{q}) = -0.0088/$cm. Profiles shifted to coincide with peak of $\kappa(\dot{q}) = 0$ case.
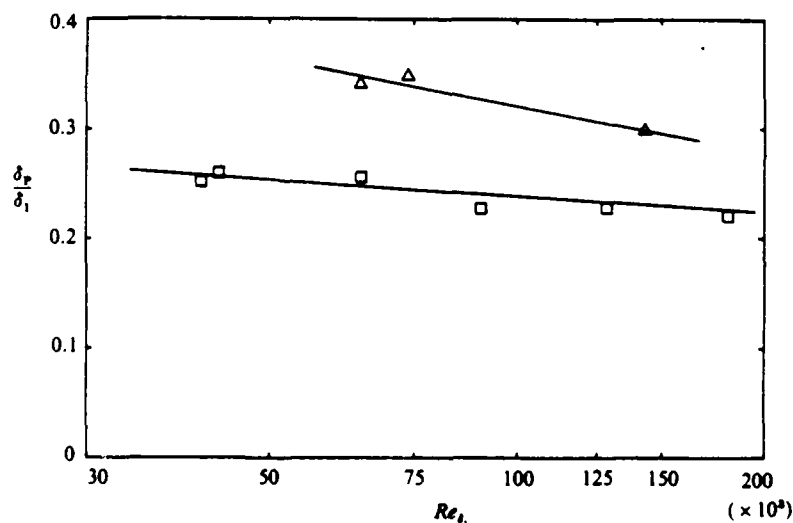
FIGURE 26. Reynolds-number effect on product volume thickness: $\square$. Mungal *et al.* (1985) $\phi = \frac{1}{8}$. $\Delta T_f = 186$ K: $\triangle$. present results. $\phi = 1$. $\Delta T_f = 368$ K.

number of the flow caused by pressure gradient. The local value of Reynolds number. $Re_{\delta_1} \equiv \Delta U \delta_1/\nu$. at a given downstream location. decreases with a favourable pressure gradient. This is because δ_1 decreases and. in addition. ΔU decreases owing to free-stream acceleration. The result is a modest decrease in Reynolds number. The nominal Reynolds number at the measuring station of $Re_{\delta_1} \approx 6.4 \times 10^4$ decreased to as little as $Re_{\delta_1} \approx 5.2 \times 10^4$. for the runs with the largest heat release and pressure gradient.

$ \cdot $ w the amount of product in the layer depends on the Reynolds number was in stigated at low heat release by Mungal *et al.* (1985). That work suggested an

increase in product formation amounting to roughly 20% per factor of 10 decrease in Reynolds number. How that trend might change with heat release was investigated by running 4% fluorine and 4% hydrogen ($\Delta T_f = 368$ K) at elevated free-stream speeds. $U_1 = 44$ m/s. $U_2 = 17.6$ m/s. The results of these runs. along with those of Mungal *et al.* are shown in figure 26. The trend of product decrease with Reynolds number at low heat release appears to persist at higher values of heat release.

The data in figure 26 suggest. for the present investigation. that the naturally induced pressure gradient could be expected to result in an increase in product formation of up to approximately 5% at the highest temperature and pressure gradient of this investigation. That this result already accounts for most of the small observed increase in product formation suggests that 'pressure gradient diffusion'. at least for the values of temperature and pressure gradient reported here. does not play a significant role in enhancing the mixing and combustion in a reacting shear layer.

9. Conclusion

The hydrogen–fluorine chemical reaction was used to study the effects of large heat release in a planar. turbulent shear layer at high Reynolds number. A range of reactant concentrations was employed to produce adiabatic flame temperature rises from 186 K up to 940 K. resulting in a maximum mean density reduction in the layer of up to 60%.

The growth rate of the shear layer, in spite of large heat release and large density changes. did not increase and instead appeared to show a slight decrease. even as the displacement thickness of the layer increased substantially with heat release. The decrease in growth rate. at zero streamwise pressure gradient. was observed to be up to 15% for a mean density reduction in the layer of 40%. Accordingly the volumetric entrainment of free-stream fluids into the layer was substantially reduced by heat release. The observed reduction in entrainment appears to more than offset the additional displacement of the layer owing to heat release. *Ex post facto* arguments suggest that a large decrease in turbulent momentum transport. as represented by the turbulent shear stress in the layer. accompanies increasing flow temperatures. This decrease in shear stress can be accounted for by the change in density in the core regions of the large-scale structures, and is shown to be consistent with the reduced layer growth.

The mean temperature-rise profiles. normalized by the adiabatic flame temperature. did not change significantly in shape over the entire range of heat release investigated. A slight decrease in normalized mean temperature was observed. which indicates that the relative efficiency with which the layer generates chemical product decreases slightly with increasing heat release. This further suggests that the probability density function of the mixed-fluid concentration is altered. to some extent. by heat release.

Large-scale structures persisted in the shear layer at all levels of heat release. The mean structure spacing. normalized by the layer width. decreased with increasing heat release. This suggests that the mechanisms of large-structure coalescence are. to some extent. inhibited by heat release.

The imposition of a favourable pressure gradient resulted in additional layer thinning at all levels of heat release. This change in growth rate can be related to the change in free-stream speed ratio induced by the favourable pressure gradient. The pressure gradient had little effect on the amount of mixing and chemical product

formation in the layer. The slight measured increase in product appears to be largely accounted for by the decrease in the local Reynolds number resulting from the acceleration of the free-streams and the layer thinning. The increase in the amount of product with decreasing Reynolds number is in accord with earlier results obtained at low heat release.

REFERENCES

BATT. R. G. 1975 Some measurements on the effect of tripping the two-dimensional shear layer. *AIAA J.* **13**, 245–247.

BAULCH, D. L., DUXBURY. J., GRANT. S. J. & MONTAGUE. D. C. 1981 Evaluated kinetic data for high temperature reactions, vol. 4. *J. Phys. Chem. Ref. Data*, **10**, Suppl. 1.

BERNAL. L. P. 1981 The coherent structure of turbulent mixing layers: I. Similarity of the primary vortex structure. II. Secondary streamwise vortex structure. Ph.D. thesis. California Institute of Technology.

BERNAL. L. P., BREIDENTHAL. R. E., BROWN. G. L., KONRAD. J. H. & ROSHKO. A. 1979 On the development of three-dimensional small scales in turbulent mixing layers. In *Turbulent Shear Flows 2, Seond Intl Symp. on Turbulent Shear Flows*, July 1979, p. 305. Springer.

BRADSHAW. P. 1966 The effect of initial conditions of the development of a free shear layer. *J. Fluid Mech.* **26**, 225–236.

BRAY, K. N. C. & LIBBY. P. A. 1981 Countergradient diffusion in pre-mixed turbulent flames. *AIAA J.* **19**, 205–213.

BREIDENTHAL. R. E. 1981 Structure in turbulent mixing layers and wakes using a chemical reaction. *J. Fluid Mech.* **109**, 1–24.

BROADWELL. J. E. & BREIDENTHAL. R. E. 1982 A simple model of mixing and chemical reaction in a turbulent shear layer. *J. Fluid Mech.* **125**, 397–410.

BROWAND. F. K. & LATIGO. B. O. 1979 Growth of the two-dimensional mixing layer from a turbulent and non-turbulent boundary layer. *Phys. Fluids* **22**, 1011–1019.

BROWAND. F. K. & TROUTT. T. R. 1985 The turbulent mixing layer: geometry of large vortices. *J. Fluid Mech.* **158**, 489–509.

BROWN. G. L. & ROSHKO. A. 1971 The effect of density differences on the turbulent mixing layer. In *Turbulent Shear Flows*; *AGARD-CP-93*, 23.1–23.12.

BROWN. G. L. & ROSHKO. A. 1974 On density effects and large structure in turbulent mixing layers. *J. Fluid Mech.* **64**, 775–816.

BROWN. J. L. 1978 Heterogeneous turbulent mixing layer investigations utilizing a 2-D 2-color laser Doppler anemometer and using a concentration probe. Ph.D. dissertation. University of Missouri at Columbia.

CALDWELL. F. R. 1962 Thermocouple materials. *National Bureau of Standards Monograph* 40. United States Department of Commerce. National Bureau of Standards.

COHEN. N. & BOTT. J. F. 1982 Review of rate data for reactions of interest in HF and DF lasers. *The Aerospace Corporation Rep.* SD-TR-82-86.

DIMOTAKIS. P. E. 1986 Entrainment and growth of a fully developed, two-dimensional shear layer. *AIAA J.* **24**, 1791–1796.

DIMOTAKIS. P. E. 1987 Turbulent shear layer mixing with fast chemical reactions. *United States–France Joint Workshop on Turbulent Reacting Flows. Rouen. France. July 1987* (submitted to *J. Fluid Mech*).

DIMOTAKIS. P. E. & BROWN. G. L. 1976 The mixing layer at high Reynolds number: large-structure dynamics and entrainment. *J. Fluid Mech.* **78**. 535–560.

EFFELSBERG. E. & PETERS. N. 1983 A composite model for the conserved scalar PDF. *Combust. Flame* **50**. 351–360.

GANJI. A. T. & SAWYER. R. F. 1980 Experimental study of the flowfield of a two-dimensional. premixed turbulent flame. *AIAA J.* **18**. 817–824.

HERMANSON. J. C. 1985 Heat release effects in a turbulent. reacting shear layer. Ph.D. thesis. California Institute of Technology.

HERMANSON. J. C.. MUNGAL. M. G. & DIMOTAKIS. P. E. 1987 Heat release effects on shear layer growth and entrainment. *AIAA J.* **25**. 578–583.

KEE. R. J.. MILLER. J. A. & JEFFERSON. T. H. 1980 CHEMKIN: A general purpose. problem independent. transportable. Fortran chemical kinetics code package. *SANDIA Rep.* SAND80-8003.

KELLER. J. O. & DAILY. J. W. 1983 The effect of large heat release on a two-dimensional mixing layer. *AIAA Paper* 83-0487 *21st Aerospace Sciences Meeting, January 1983*.

KOLLMAN. W. & JANICKA. J. 1982 The probability density function of a passive scalar in turbulent shear flows. *Phys. Fluids* **25**. 1755–1769.

KONRAD. J. H. 1976 An experimental investigation of mixing in two-dimensional turbulent shear flows with applications to diffusion-limited chemical reactions. Ph.D. dissertation. California Institute of Technology.

KOOCHESFAHANI. M. M.. CATHERASOO. C. J.. DIMOTAKIS. P. E.. GHARIB. M. & LANG. D. B. 1979 Two-point LDV measurements in a plane mixing layer. *AIAA J.* **17**. 1347–1351.

KOOCHESFAHANI. M. M. & DIMOTAKIS. P. E. 1986 Mixing and chemical reactions in a turbulent liquid mixing layer. *J. Fluid Mech.* **170**. 83–112.

KOOP. C. G. & BROWAND. F. K. 1979 Instability and turbulence in a stratified fluid with shear. *J. Fluid Mech.* **93**. 135–159.

LANG. D B. 1985 Laser Doppler velocity and vorticity measurements in turbulent shear layers. Ph.D. thesis. California Institute of Technology.

MARBLE. F. E. & BROADWELL. J. E. 1977 The coherent flame model for turbulent chemical reactions. *Project SQUID Tech. Rep.* TRW-9-PU.

MASUTANI. S. M. & BOWMAN. C. T. 1986 The structure of a chemically reacting plane mixing layer. *J. Fluid Mech.* **172**. 93–126.

McMURTRY. P. A.. JOU. W.-H.. RILEY. J. J. & METCALFE. R. W. 1986 Direct numerical simulations of a reacting mixing layer with chemical heat release. *AIAA J.* **24**. 962–970.

McMURTRY. P. A. & RILEY. J. J. 1987 Mechanisms by which heat release affects the flow field in a chemically reacting. turbulent mixing layer. *AIAA Paper* 87-0131. *25th Aerospace Sciences Meeting. January 1987*.

MUNGAL. M. G. & DIMOTAKIS. P. E. 1984 Mixing and combustion with low heat release in a turbulent shear layer. *J. Fluid Mech.* **148**. 349–382.

MUNGAL. M. G.. HERMANSON. J. C. & DIMOTAKIS. P. E. 1985 Reynolds number effects on mixing and combustion in a reacting shear layer. *AIAA J.* **23**. 1418–1423.

MUNGAL. M. G. & FRIELER. C. E. 1985 The effects of Damköhler number on a turbulent shear layer – experimental results. *GALCIT Rep.* FM85-01.

PARANTHOEN. P.. LECORDIER. J. D. & PETIT. C. 1982 Influence of dust contamination on frequency response of wire resistance thermometers. *DISA Information* **27**. 36–37.

PITZ. R. W. & DAILY. J. W. 1983 Combustion in a turbulent mixing layer formed at a rearward-facing step. *AIAA J.* **21**. 1565–1570.

POPE. S. B. 1981 A Monte Carlo method for the PDF equations of turbulent reactive flow. *Combust. Sci. Tech.* **25**. 159–174.

PRANDTL. L. 1925 Bericht über Untersuchungen zur ausgebildeten Turbulenz. *Zr. angew. Math. Mech.* **5**. 136–139.

RAJAGOPALAN. S & ANTONIA. R. A. 1981 Properties of the large structure in a slightly heated turbulent mixing layer of a plane jet. *J. Fluid Mech.* **105**. 261–281.

REBOLLO. M R 1973 Analytical and experimental investigation of a turbulent mixing layer of different gases in a pressure gradient. Ph.D. thesis. California Institute of Technology

SCADRON. M. D. & WARSHAWSKY. I. 1952 Experimental determination of time constants and Nusselt numbers for bare-wire thermocouples in high-velocity air streams and analytic approximation of conduction and radiation errors. *NACA Tech Note* 2599.

SPALDING. D. B. 1986 The two-fluid model of turbulence applied to combustion phenomena. *AIAA J.* **24**. 876–884.

SPENCER. B. W. & JONES. B. G. 1971 Statistical investigation of pressure and velocity fields in the turbulent two stream mixing layer. *AIAA Paper* 71-613. *11th Aerospace Sciences Meeting, January 1971.*

STÄRNER. S. H. & BILGER. R. W. 1980 LDA measurements in a turbulent diffusion flame with axial pressure gradient. *Combust. Sci. Tech.* **21**. 259–276.

WALLACE. A. K. 1981 Experimental investigation of the effects of chemical heat release in the reacting turbulent plane shear layer. Ph.D. thesis. The University of Adelaide: also *AFOSR Rep.* TR-84-0650.

WINANT. C. D. & BROWAND. F. K. 1974 Vortex pairing: the mechanism of turbulent mixing-layer growth at moderate Reynolds number. *J. Fluid Mech.* **63**. 237–255.

Appendix C

ZHUANG, M., KUBOTA, T. and DIMOTAKIS, P. E. [1989] "On the Instability of Inviscid. Compressible Free Shear Layers", submitted for publication, *AIAA J.* .

On the Instability of Inviscid, Compressible Free Shear Layers

by
Mei Zhuang[*], Toshi Kubota[**] and Paul E. Dimotakis[†]

*Graduate Aeronautical Laboratories
California Institute of Technology
Pasadena, California 91125*

Abstract

The linear spatial instability of inviscid compressible laminar mixing of two parallel streams, comprised of the same gas, has been investigated with respect to two-dimensional wave disturbances. The effects of the velocity ratio, temperature ratio, and the temperature profile across the shear layer have been examined. A nearly universal dependence of the normalized maximum amplification rate on the convective Mach number is found, with the normalized maximum amplification rate decreasing significantly with increasing convective Mach number in the subsonic region. These results are in accord with those of recent growth rate experiments in compressible turbulent free shear layers and other similar recent calculations.

Introduction

The instability of inviscid, laminar, two-dimensional shear layers in both incompressible and compressible flow has been studied in the past.

For incompressible parallel flow, the linear spatial instability of the hyperbolic tangent and Blasius mixing layers was investigated for different values of the ratio between the difference and sum of the velocities of the two co-flowing streams by Monkewitz & Huerre[1]. They found that the maximum growth rate is approximately proportional to the velocity ratio.

---

[*] Graduate student, Aeronautics.

[**] Professor, Aeronautics.

[†] Professor, Aeronautics & Applied Physics. Member AIAA.

1

For compressible flow, the instability of the free mixing layers with respect to two and three dimensional temporally growing disturbances was considered by Lessen, Fox & Zien[2,3] for both subsonic and supersonic disturbances. Under the assumption that the flow was iso-energetic, they found that the flow is unstable with respect to supersonic disturbances, although the amplification rate is smaller than that for subsonic disturbances and that the increasing of the angle between the disturbance wave number vector and the principle flow direction tends to increase the instability. With spatially growing disturbances, Gropengiesser[4] studied this instability problem using Crocco-Busemann relation as the mean temperature profilesof the flows. He carried out the inviscid instability calculations at various free stream Mach numbers and temperature ratios. In order to simplify the stability problem, which were considered by Lessen *et al.*, Blumen, Drazin & Billings[5] studied this problem by assuming that the thermodynamic state of a compressible inviscid free mixing layer is constant. They showed that there is instability of two-dimensional disturbances at all values of the Mach number and that there exists a second unstable supersonic mode. For compressible flow, however, the effects of shear layer Mach number, temperature ratio, velocity ratio, and temperature profile on the stability characteristics are very complicated. These authors offer no prediction about what the combined influences of these flow parameters will be. Recently, Ragab & Wu[6] studied the influence of the velocity ratio on the stability characteristics of the compressible shear layer, and they also investigated the effect of the convective Mach number, as proposed by Papamoschou & Roshko[7]. Their results indicate the convective Mach number is a parameter which correlates the compressibility effects on the spreading rate of mixing layers.

Papamoschou & Roshko performed experiments on compressible shear layers and suggested the convective Mach number (M_c) as the appropriate parameter scaling the effects of compressibility. This is defined for each stream as:

$$M_{c1} = \frac{U_1 - U_c}{a_1} \ , \qquad M_{c2} = \frac{U_c - U_2}{a_2} \ , \qquad (1)$$

where U_1, U_2 and a_1, a_2 are the free stream velocities and speeds of sound. The quantity U_c is the convective velocity of the large scale structures and was estimated as $\bar{U}_c$ by Papamoschou & Roshko assuming that the dynamic pressure match at stagnation points in the flow (Coles[8], Dimotakis[9]). For compressible isentropic flow, i.e. (Papamoschou & Roshko)

$$\left(1 + \frac{\gamma_1 - 1}{2}\tilde{M}_{c1}^2\right)^{\frac{\gamma_1}{\gamma_1 - 1}} = \left(1 + \frac{\gamma_2 - 1}{2}\tilde{M}_{c2}^2\right)^{\frac{\gamma_2}{\gamma_2 - 1}}, \tag{2}$$

where γ_1, γ_2 are the ratios of the specific heats of the two streams, and

$$\tilde{M}_{c1} = \frac{U_1 - \tilde{U}_c}{a_1}, \qquad \tilde{M}_{c2} = \frac{\tilde{U}_c - U_2}{a_2}. \tag{3}$$

For γ_1 equals γ_2, $\tilde{U}_c$ can be obtained by

$$\tilde{U}_c = \frac{a_2 U_1 + a_1 U_2}{a_1 + a_2}, \tag{4}$$

which, for equal static free stream pressures and specific heats, reduces to the incompressible expression[9]. They suggested that the growth rate of a compressible shear layer, normalized by the growth rate for an incompressible shear layer, might be expressible as a universal function of the convective Mach number $\tilde{M}_{c1}$, which is valid over a wide range of velocity and temperature ratios of a shear layer. They also found that the normalized growth rate decreases significantly with increasing $\tilde{M}_{c1}$.

Jackson & Grosch[10] presented their results of a study of the inviscid spatial stability of a parallel compressible mixing layer with one stream moving and the other stream stationary. It is shown that if the Mach number of the moving stream exceeds a critical value, there are always two groups of unstable waves. One of these groups is fast with phase velocity greater than 1/2, and the other is slow with phase velocity less than 1/2.

The numerical calculations described here were performed under the assumptions of linear instability theory. The convective velocity is estimated as the phase velocity of the disturbances, i.e. $\hat{U}_c = C_p$ (Mack[11] considered $\hat{U}_c = C_r$ for neutral disturbances). Therefore, a convective Mach number ($\hat{M}_c$) for each stream can be written as:

$$\hat{M}_{c1}^2 = \frac{U_1 - C_p}{a_1}, \qquad \hat{M}_{c2}^2 = \frac{C_p - U_2}{a_2}, \tag{5}$$

where C_p is chosen to be the phase velocity of the most unstable eigenvalue. We think the definition given by Eq. (5) is more appropriate since the phase velocity of the disturbances is available from our computations.

The purpose of the present studies is to investigate the combined influence of the convective Mach number ($\hat{M}_c$), which is different from the one used by Ragab & Wu ($\bar{I}_c$), the velocity and temperature ratios, and the temperature profiles of the flow on the linear stability behavior of compressible shear layers. Studies are made of the case of inviscid flow under the assumptions that the gases in the two streams are the same, the main flow can be treated parallel, and that the disturbances in the flow are of small amplitude. The range of the unstable frequencies and wave numbers were numerically calculated for a two-dimensional, spatially growing disturbance.

Basic disturbance equations

We consider a two-dimensional flow of two parallel streams. With upper stream quantities as the reference and the local layer thickness δ as the length scale, the dimensionless quantities of the flow in Cartesian co-ordinates can be written as usual

$$u_x = \bar{U} + u', \ u_y = v', \ T = \bar{T} + T',$$

$$\rho = \bar{\rho} + \rho', \ p = \bar{p} + p',$$

or, for the general field quantity

$$Q(x,y,t) = \bar{Q}(y) + Q'(x,y,t),$$

where $\bar{Q}$ is a profile of the main flow, and Q' is the corresponding disturbance amplitude.

Consider now the disturbance to be a wave propagating in the x-direction. The disturbance quantities in dimensionless form can be expressed as[2]

$$\{u',v',T',\rho',p'\} = \{f(y),\alpha\phi(y),\theta(y),r(y),\pi(y)\}\exp[i\alpha(x-ct)], \tag{6}$$

where α is a complex wave number, and c is a complex wave velocity. In the case of negligible viscous effects, the linearized disturbance equations for a 2-D compressible fluid with the same gas constants and specific heats are given by[2]:

Continuity:
$$i(\bar{U}-c)r + \bar{\rho}(\phi'+if) + \bar{\rho}'\phi = 0 \tag{7a}$$

Momentum:
$$\gamma M_1^2 \bar{\rho}[i(\bar{U}-c)f + \bar{U}'\phi] = -i\pi \tag{7b}$$

$$\gamma M_1^2 \alpha^2 \bar{\rho}[i(\bar{U} - c)\phi] = -\pi' \tag{7c}$$

Energy:

$$\bar{\rho}[i(\bar{U} - c)\theta + \bar{T}'\phi] = -(\gamma - 1)(\phi' + if) \tag{7d}$$

State:

$$\frac{\pi}{\bar{p}} = \frac{r}{\bar{\rho}} + \frac{\theta}{\bar{T}} , \tag{7e}$$

where M_1 is the upper stream Mach number and primes here correspond to d/dy. These equations can be reduced to the second order differential equation for the pressure disturbance[2], i.e.

$$\pi'' - \left(\frac{2\bar{U}'}{\bar{U} - c} - \frac{\bar{T}'}{\bar{T}} \right)\pi' - \alpha^2 \left[1 - \frac{M_1^2}{\bar{T}}(\bar{U} - c)^2 \right]\pi = 0 . \tag{8}$$

Asymptotic Behavior of the Eigenfunctions

The asymptotic behavior of the eigenfunction $\pi(y)$ for $y \to \pm\infty$ is found from Equation (8). With $y \to \pm\infty$, $\bar{U}$ and $\bar{T}$ are constants, and $\bar{U}'$, $\bar{T}'$ are zeros. In that limit, Equation (8) becomes

$$\pi'' - \lambda_k^2 \pi = 0 , \tag{9}$$

with

$$\lambda_k^2 = \alpha^2 \left[1 - \frac{M_1^2}{\bar{T}_k}(\bar{U}_k - c)^2 \right] = \Lambda_k = \Lambda_{kr} + i\Lambda_{ki} , \tag{10}$$

and $k = 1, 2$. Therefore, from (10) we get

$$\lambda_k = \lambda_{kr} + i\lambda_{ki} = \pm\Lambda_k^{1/2}$$

and the solution for large $|y|$ can be written as

$$\pi = A_k exp(-\lambda_k|y|) , \tag{11}$$

where A_k is a complex constant.

Since we have only considered the case of amplified disturbances ($\alpha_i < 0$), the boundary conditions for both supersonic and subsonic disturbances can be expressed by $\pi_r(y \to \pm\infty) \to 0$ and $\pi_i(y \to \pm\infty) \to 0$. In order to satisfy the boundary conditions, we set $\lambda_{kr} > 0$, and get

$$y = y_1 \to +\infty , \qquad \pi = A_1 exp(-\lambda_1 y) \qquad (12a)$$

$$y = y_2 \to -\infty , \qquad \pi = A_2 exp(\lambda_2 y) , \qquad (12b)$$

where

$$\lambda_k = \lambda_{kr} + i\lambda_{ki} = \left[\tfrac{1}{2}(|\Lambda_k| + \Lambda_{kr})\right]^{1/2} + i\, sign\{\Lambda_{ki}\}\left[\tfrac{1}{2}(|\Lambda_k| - \Lambda_{kr})\right]^{1/2} .$$

Formulation of the Eigenvalue problem

The eigenvalue problem is defined as follows. For a given real disturbance frequency β ($\beta = \alpha c$), the eigenvalues α_r and α_i are to be determined in such a way that the eigenfuctions $\pi_r(y)$ and $\pi_i(y)$ satisfy the boundary conditions. Specifically, we used a Runge-Kutta method to solve the eigenvalue equation, with (12a) and (12b) as boundary conditions. The equation was integrated from one side of the boundary ($y = y_1$) to the other side ($y = y_2$). The correct α was obtained for a given β by matching to the boundary conditions.

Velocity and Temperature Distributions

Lock's[12] numerical calculation of the velocity distribution for a compressible laminar boundary layer was approximated by Gropengiesser using a generalized hyperbolic tangent profile with three free constants. To simplify the problem, we assume that the dimensionless mean velocity profile is described by a hyperbolic tangent profile represented by the form

$$\bar{U}(y) = \eta(y) + U_R[1 - \eta(y)] , \qquad (13)$$

where $U_R = U_2/U_1$ is the velocity ratio across the shear layer, and $2\eta(y) - 1$ is approximated by a hyperbolic tangent. See mean velocity profiles $\bar{U}(y)$ in Fig. 1.

We note that the linearized flow equations do not prescribe the mean temperature profile. Accordingly, two different kinds of temperature profiles have been considered. One conforms to the Crocco-Busemann[13,14] relation, wherein the total temperature profile $T_t(y)$ for an equal ratio of the specific heats of the two free streams is represented by

$$T_t(y) = T_{t1}\eta(y) + T_{t2}[1 - \eta(y)] , \qquad (14)$$

where T_{t1}, T_{t2} are the free stream total temperatures. This yields the dimensionless mean static temperature profile,

$$\bar{T}(y) = c_1 + c_2 \bar{U}(y) - \frac{(\gamma - 1)M_1^2}{2} \bar{U}^2(y), \tag{15}$$

where M_1 is the upper stream Mach number and c_1, c_2 are constants which satisfy the boundary conditions on the temperature profile. Such mean temperature profiles $\bar{T}(y)$ for $M_1 = 5$ are shown on Fig. 2. The other kind of dimensionless temperature profile is obtained by assuming that the dimensionless density distribution across the shear layer can also be approximated by a hyperbolic tangent profile, i.e.

$$\bar{\rho}(y) = \eta(y) + \rho_R[1 - \eta(y)]\,, \tag{16}$$

where $\rho_R = \rho_2/\rho_1$ is the density ratio across the shear layer. Therefore, for a shear layer comprised of the same gas, the dimensionless temperature profile is $\bar{T}(y) = 1/\bar{\rho}(y)$. See Fig. 3.

Results

For a given combination of free stream Mach number M_1, temperature ratio T_R (T_2/T_1) and velocity ratio U_R, the linear instability characteristics were calculated, yielding the most unstable eigenvalue ($\alpha_m = \alpha_{mr} + i\alpha_{mi}$) and its corresponding real frequency β_m. The phase velocity C_p of the disturbances was obtained as β_m/α_{mr}. This yields the convective Mach number $\hat{M}_{c1}$ and $\hat{M}_{c2}$ from Eq.(5).

For a free mixing layer with subsonic disturbances, there is only one unstable mode propagating with the phase velocity C_p approximately equals to $\bar{U}_c$, which is constant for given U_R and T_R. As the Mach number of the stream M_1 approaches or exceeds a critical value, there are always two unstable modes. The one is with the phase velocity C_p less than $\bar{U}_c$ and the other is with the phase velocity greater than $\bar{U}_c$. These two unstable modes are called supersonic mode 1 and mode 2 respectively. If we increase the Mach number M_1, the phase velocities of the two modes will further increase or decrease (see Fig. 4).

Different combinations of velocity and temperature ratios using a velocity and temperature profile from Eqs.(13) and (15) were investigated for a convective Mach number $\hat{M}_{c1}$ from 0 to about 1.5. The velocity profiles for $U_R = 0.25$, 0.5, 0.75 appear in Fig. 1 and the temperature profiles for $T_R = 0.5$, 1.0, 1.5 in Fig. 2. In the region of supersonic convective

Mach numbers, the modes with C_p less than $\bar{U}_c$ are more unstable than the modes with C_p greater than $\bar{U}_c$ in the most cases of the velocity and temperature profiles given by Figs. 1 and 2. Therefore, we only considered the mode with C_p less than $\bar{U}_c$ for supersonic convective Mach number. Results shown in Figs. 5 − 10, which were obtained from nine different combinations of T_R and U_R, indicate that if the most unstable eigenvalue for a compressible shear layer is normalized by its value corresponding to an incompressible shear layer(at the same velocity and temperature ratio), the ratio is well approximated as a function of the convective Mach number only, i.e.

$$\frac{\delta_x(\hat{M}_{c1})}{\delta_x(0)} \simeq \frac{max\{-\alpha_i(U_2/U_1, T_2/T_1, \hat{M}_{c1})\}}{max\{-\alpha_i(U_2/U_1, T_2/T_1, \hat{M}_{c1} = 0)\}} \simeq F(\hat{M}_{c1}) , \qquad (17)$$

where $\delta_x = d\delta/dx$ for the shear layer of the particular free stream conditions and δ is the local layer thickness. The solid line estimate of $\delta_x(\hat{M}_{c1})/\delta_x(0)$ in Figs. 5 − 10 was computed by using all the data of the nine different cases, and least squares fitting the normalized maximum amplification rate versus the convective Mach number $\hat{M}_{c1}$, for the range of $\hat{M}_{c1}$ from 0 to about 1.5 with a function of the form

$$\frac{\delta_x(\hat{M}_{c1})}{\delta_x(0)} \simeq 1 + p_0(e^{-(p_2\hat{M}_{c1}^2 + p_3\hat{M}_{c1}^3 + p_4\hat{M}_{c1}^4)} - 1) , \qquad (18)$$

where

$$p_0 = 0.928286 \qquad p_2 = 1.78285$$

$$p_3 = -2.16428 \qquad p_4 = 2.68579.$$

Note that $\delta_x(\hat{M}_{c1} \to \infty)/\delta_x(0) = 1 - p_0$, and that the coefficient p_2 is related to the second derivative at $\hat{M}_{c1} = 0$, etc. Note also that these results suggest that $F(\hat{M}_{c1} = 0) = 0$, as might have been argued a priori. The results, shown in Figs. 5 − 10, also suggest that the normalized maximum amplification rate decreases significantly with increasing $\hat{M}_{c1}$ for the subsonic convective Mach numbers. In the region $\hat{M}_{c1} > 1.5$, this normalized amplification rate decreases continuously untill zero as the convective Mach number is increseased.

In the second set of calculations, the mean temperature profile was specified via Eq.(16), i.e. $\bar{T}(y) = 1/\bar{\rho}(y)$. The resulting temperature profiles for $T_R = 0.67$, 1, and 2 are plotted in Fig. 3. The velocity ratio $U_R = 0.5$ with each of these three temperature ratios was studied for the convective Mach number $\hat{M}_{c1}$ from 0 to about 1.5. The results, shown in Fig. 11, substantiate the convective Mach number as the relevant compressibility parameter and also display good agreement with the plot $\delta_x(\hat{M}_{c1})/\delta_x(0)$ vs. $\hat{M}_{c1}$ obtained from Eq.(18), even though these two mean temperature profiles are very different at supersonic convective Mach numbers (see Figs. 2, 3).

With $\tilde{U}_c$ calculated from Eq.(4) and C_p obtained from the numerical calculations under the linear theory, $\tilde{M}_{c1}$ does not necessarily equal $\hat{M}_{c1}$. In fact, the phase velocity C_p approximately equals to $\tilde{U}_c$ for subsonic convective Mach numbers; but because of the existence of second unstable modes for supersonic convective Mach numbers[10], C_p is not unique and can not be estimated by $\tilde{U}_c$. Blumen, Drazin & Billings[5] have noted this behavior for a shear layer of an inviscid fluid with two-dimensional temporally disturbances[5]. We can see that, for both temperature profiles (Eq.(15) and Eq.(16) with $\bar{T}(y) = 1/\bar{\rho}(y)$), there are very small differences between $\hat{M}_{c1}$ and $\tilde{M}_{c1}$ from the plot of $(\hat{M}_{c1} - \tilde{M}_{c1})/\hat{M}_{c1}$ vs. $\hat{M}_{c1}$ for $\hat{M}_{c1} \leq 1$, but the differences only become substantial when $\hat{M}_{c1} > 1$. See Figs. 12, 13. We only studied the cases for $\hat{M}_{c1} < 1.5$, since shock waves can exist in a shear layer at high convective Mach numbers and therefore, the validity of a linear description of these phenomena would be suspect.

A comparison of our estimate of $\delta_x(\hat{M}_{c1})/\delta_x(0)$ with Ragab's numerical data and with Papamoschou's experimental data is made in Fig. 14. The data from our calculations are very close to Ragab & Wu's. The difference between $\hat{M}_{c1}$ and $\tilde{M}_{c1}$, though not small in the region $\hat{M}_{c1} > 1$, does not affect the results, since the normalized amplification rates are very small in this region. According to Papamoschou & Roshko's experimental data, the growth rate of the shear layer tapers off as the convective Mach number becomes supersonic. As opposed to their findings, however, the growth rate of our calculations decreases to zero as $\hat{M}_{c1} \gg 1$. Preliminary calculations suggest that a larger value for the growth rate at large M_{c1} is exhibited by more complex velocity and/or density profiles. Also, Sandham & Reynolds[15] showed that a large value of the growth rate can be obtained for three-dimensional wave disturbances at convective Mach numbers above 0.6.

Conclusion

The influences of the convective Mach number, the velocity and temperature ratios and the temperature profiles of the flow on the linear spatial instability characteristics of a plane shear layer, formed by the same gas, were investigated. It was found that there is a nearly universal dependence of the normalized maximum amplification rate on the convective Mach number, and this amplification rate decreases significantly with increasing $\hat{M}_{c1}$ in the region of $\hat{M}_{c1} < 1$.

Acknowledgement

References

1. MONKEWITZ, P. A. and HUERRE, P. [1982] "Influence of the Velocity Ratio on the Spatial Instability of Mixing Layers", *Phys. Fluids.* **25**(7), 1137-1143.

2. LESSEN, M., FOX, J. A. and ZIEN, H. M. [1965] "On the Inviscid Stability of the Laminar Mixing of Two Parallel Streams of a Compressible Fluid", *J. Fluid Mech.* **23**, 355-367.

3. LESSEN, M., FOX, J. A. and ZIEN, H. M. [1965] "Stability of the Laminar Mixing of Two Parallel Streams with respect to Supersonic Disturbances", *J. Fluid Mech.* **25**, 737-742.

4. GROPENGIESSER, H. [1970] "Study of the Stability of the Boundary Layers in Compressible Fluids", NASA TT-F-12, 786.

5. BLUMEN, W., DRAZIN, P. G. and BILLINGS, D. F. [1975] "Shear Layer Instability of an Inviscid Compressible Fluid", *J. Fluid Mech.* **71**, 305-316.

6. RAGAB, SAAD A. and WU, J. L. [1988] "Instabilities in the Free Shear Layer Formed by Two Supersonic Streams", AIAA Paper No. 88-0038.

7. PAPAMOSCHOU, D. and ROSHKO, A. [1986] "Observations of Supersonic Free Shear Layers", AIAA Paper No. 86-0162.

8. COLES, D. [1981] "Prospects for Useful Research on Coherent Structure in turbulent shear flow", *Proc. Indian Acad. Sci.* **4**(2), 111-127.

9. DIMOTAKIS, P. E. [1986] "Two-Dimensional Shear-Layer Entrainment", *AIAA J.* **24**(11), 1791-1796.

10. JACKSON, T. L. and GROSCH, C. E. [1988] "Spatial Stability of a Compressible Mixing Layer", ICASE REPORT NO. 88-33.

11. MACK, L. M. [1975] "Linear Stability and the Problem of Supersonic Boundary-Layer Transition", *AIAA J.* **13**, 278-289.

12. LOCK, R. C. [1935] "The Velocity Distribution in the Laminar Boundary Layer Between Parallel Streams", *Quart. J. Mech. Appl. Math.* **4**, 42-63.

13. CROCCO, L. [1932] "Sulla trasmissione del calore da una lamina piana a un fluido scorrente ad alta velocita", *L'Aerotecnica* **12**, 181-197.

14. BUSEMANN, A. [1935] "Gasstromung mit Laminarer Grenzschicht Entlang einer Platte", *ZAMM* **15**, 23-25.

15. SANDHAM, N. and REYNOLDS, W. [1989] "The Compressible Mixing Layer: Linear Theory and Direct Simulation", AIAA paper No. 89-0371.
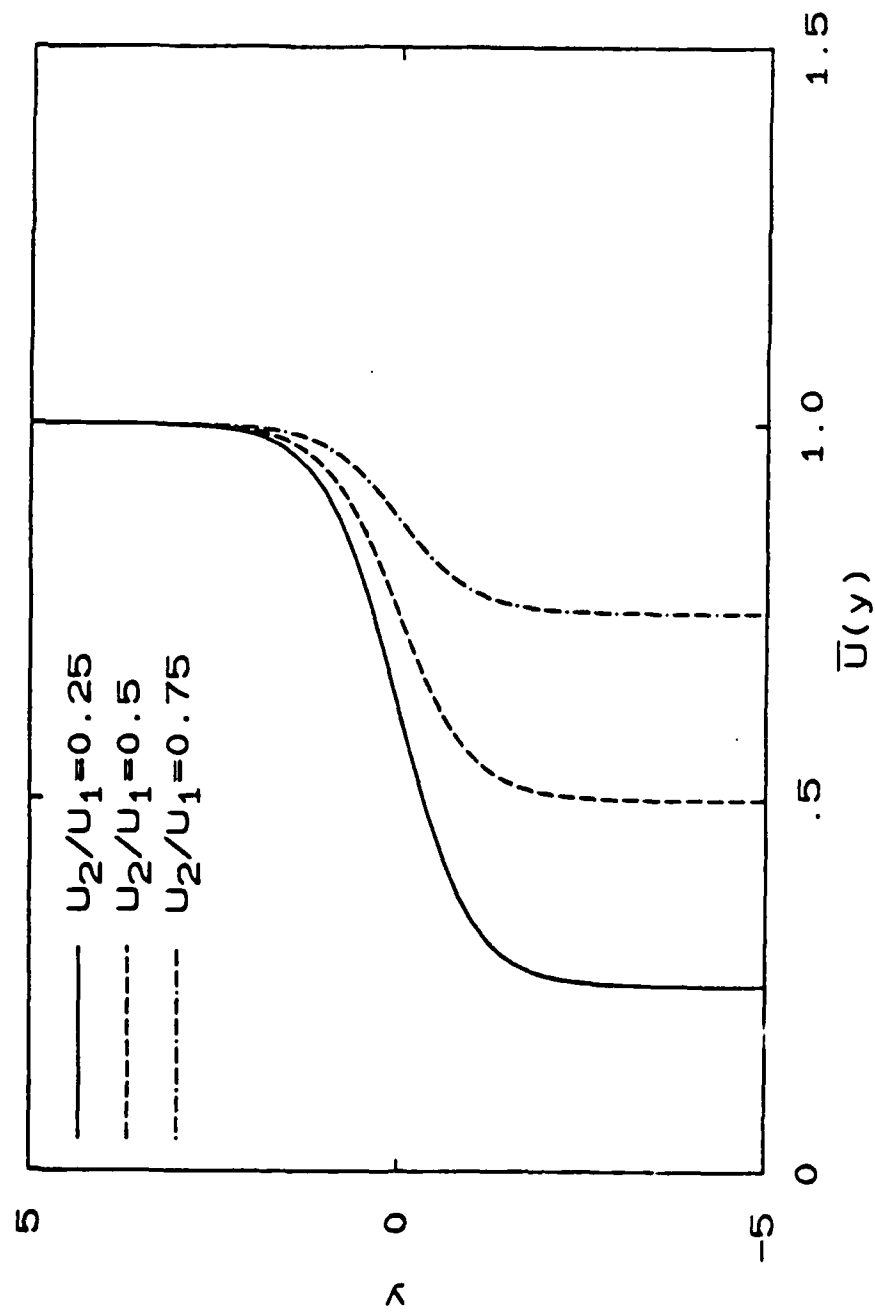
FIG. 1 Hyperbolic tangent mean velocity profiles for different values of the velocity ratio U_2/U_1.
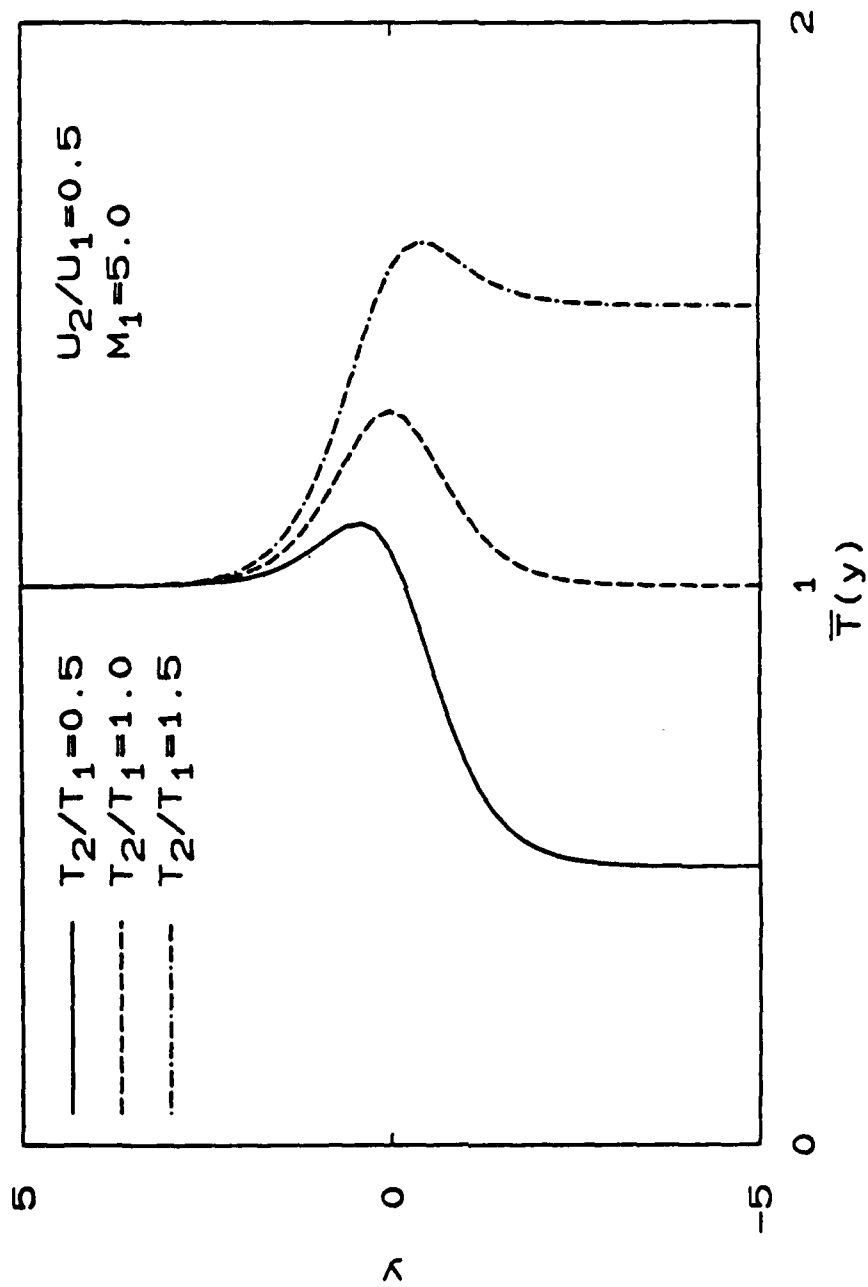
FIG. 2 Crocco-Busemann mean temperature profiles for different values of the temperature ratio T_2/T_1 for the case $U_2/U_1 = 0.5$ and $M_1 = 5.0$.
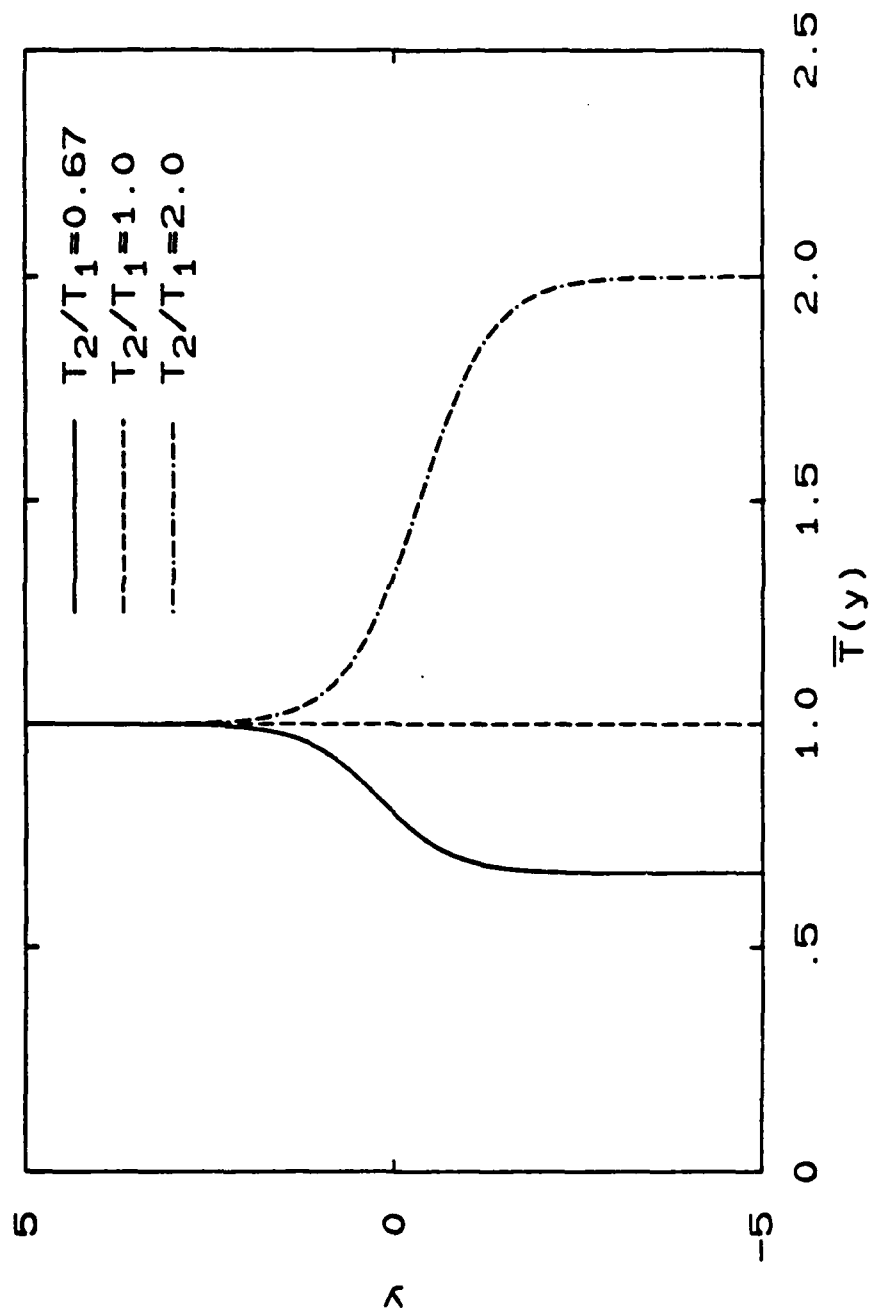
FIG. 3 Hyperbolic tangent $\overline{T}(y)$ mean temperature profiles for different values of the temperature ratio T_2/T_1.
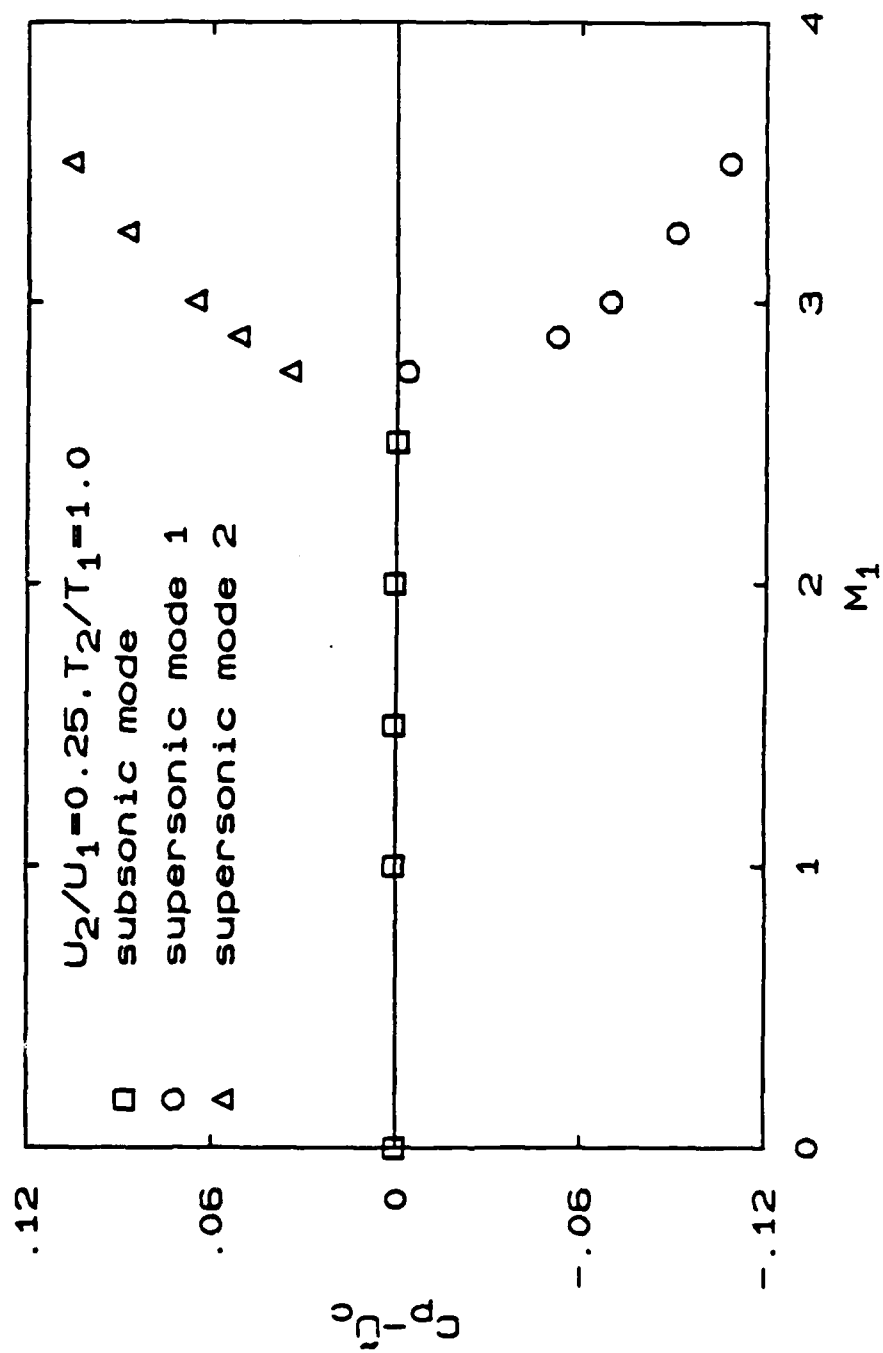
FIG. 4 The difference between C_p and $\bar{U}_c$ vs the free stream Mach number M_1.
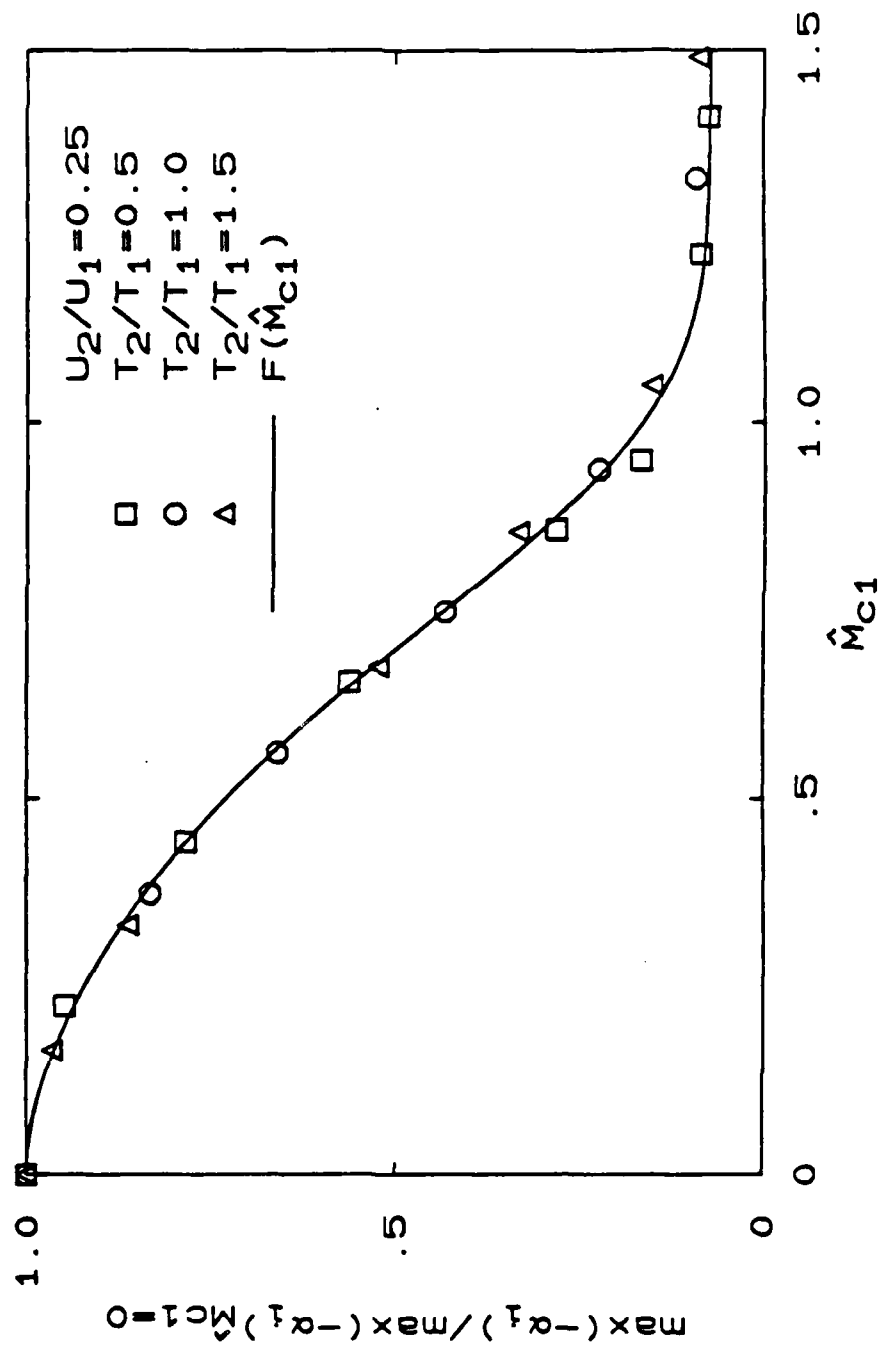
FIG. 5 Normalized maximum amplification rate vs $\hat{M}_{c1}$.
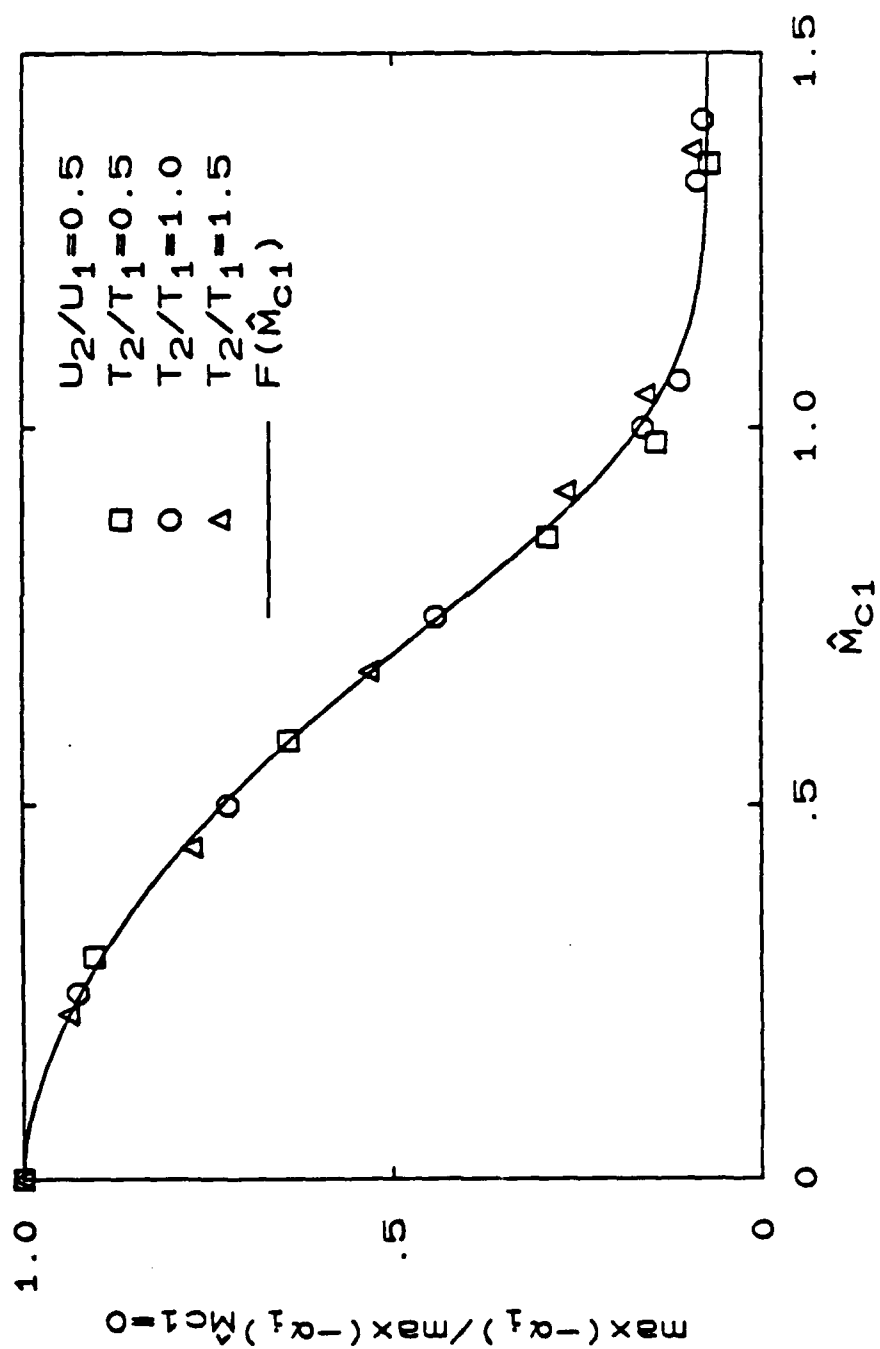
FIG. 6 Normalized maximum amplification rate vs $\hat{M}_{c1}$.
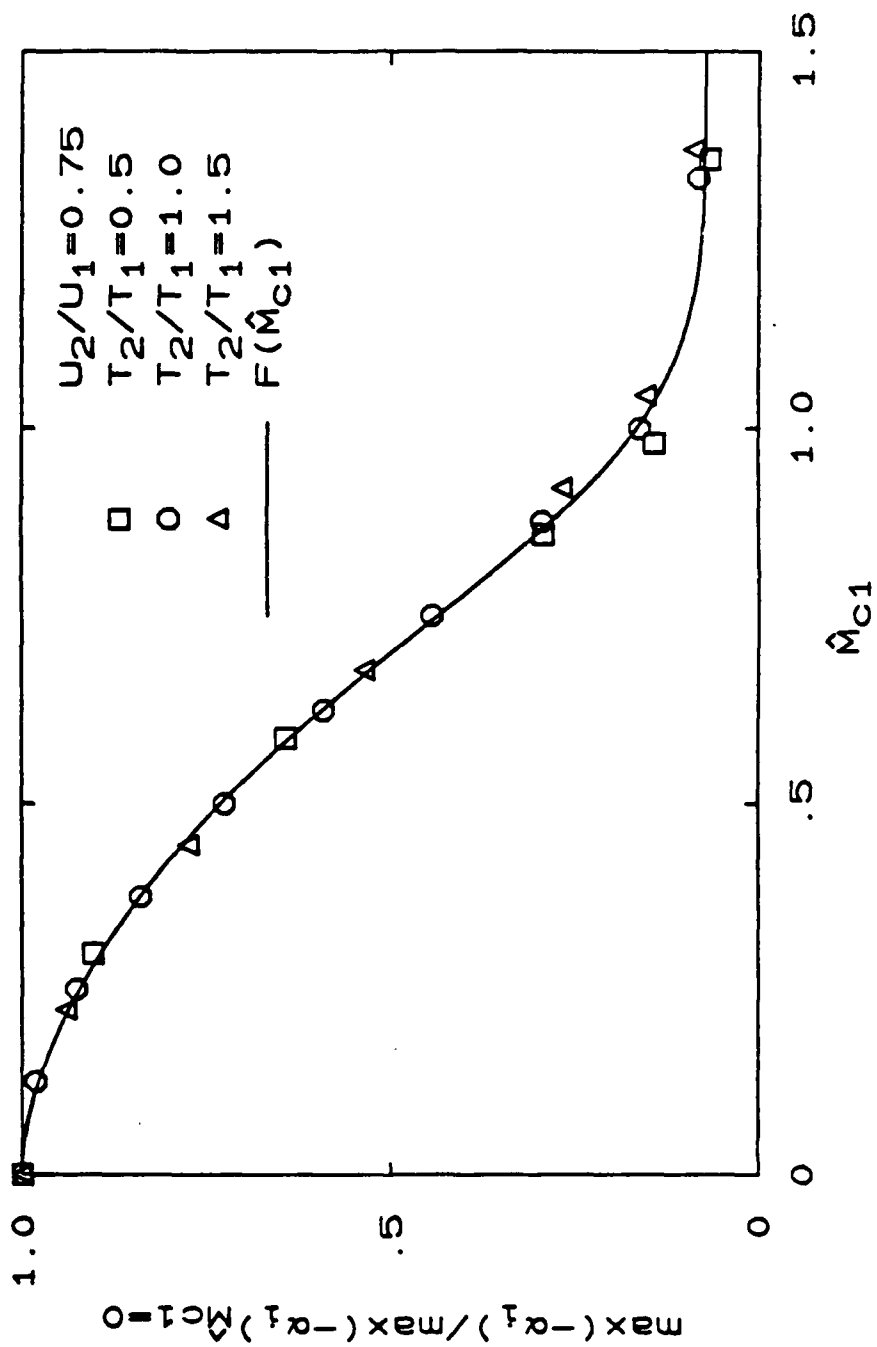
FIG. 7 Normalized maximum amplification rate vs $\hat{M}_{c1}$.
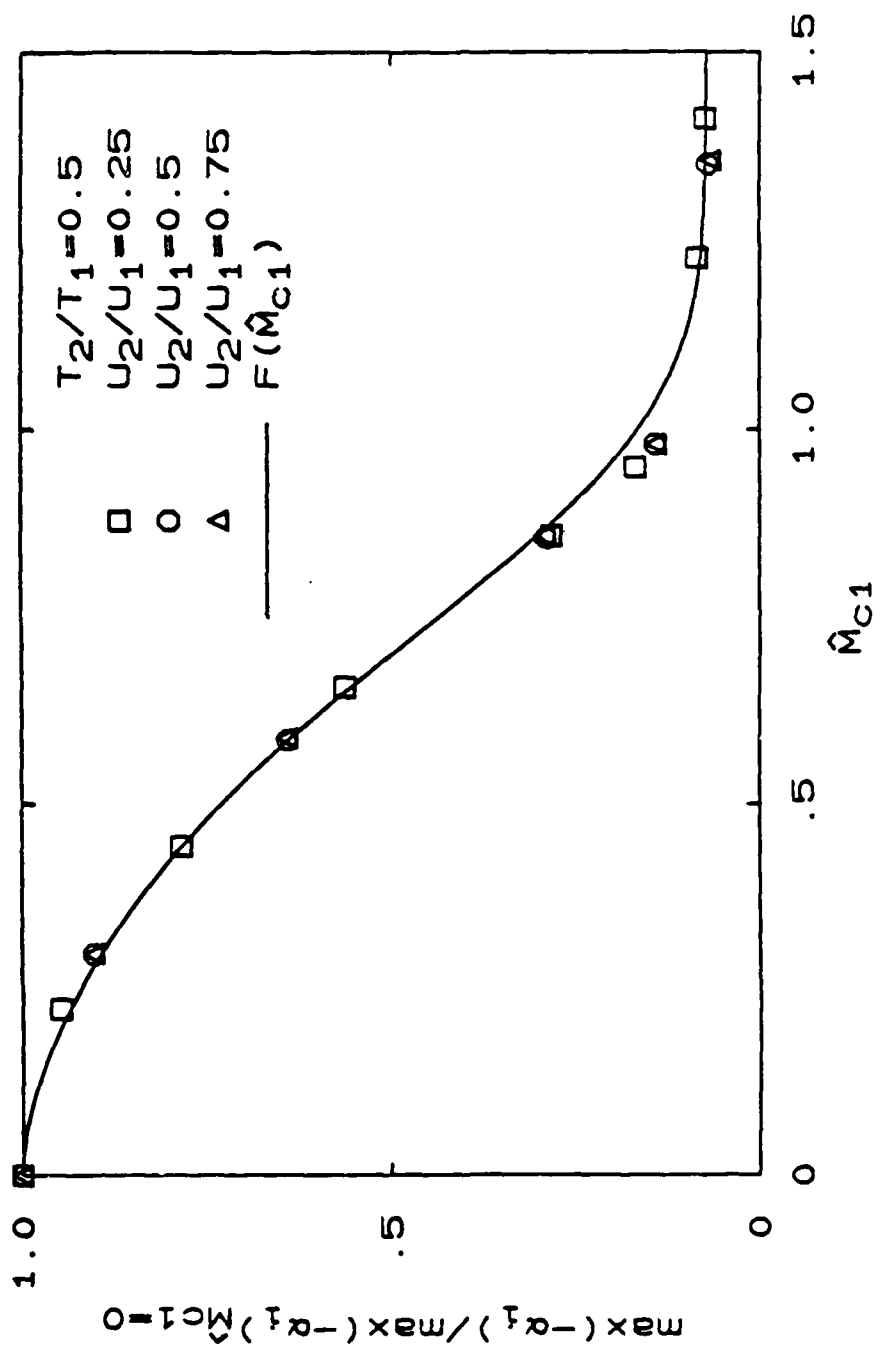
FIG. 8 Normalized maximum amplification rate vs $\dot{M}_{c1}$.

FIG. 9 Normalized maximum amplification rate vs $\hat{M}_{c1}$.

$T_2/T_1 = 1.5$

$\square$ $U_2/U_1 = 0.25$

$\bigcirc$ $U_2/U_1 = 0.5$

$\triangle$ $U_2/U_1 = 0.75$

—— $F(\hat{M}_{c1})$

$\hat{M}_{C1}$

$\max(-\alpha_i)/\max(-\alpha_i)_{\hat{M}_{C1}=0}$
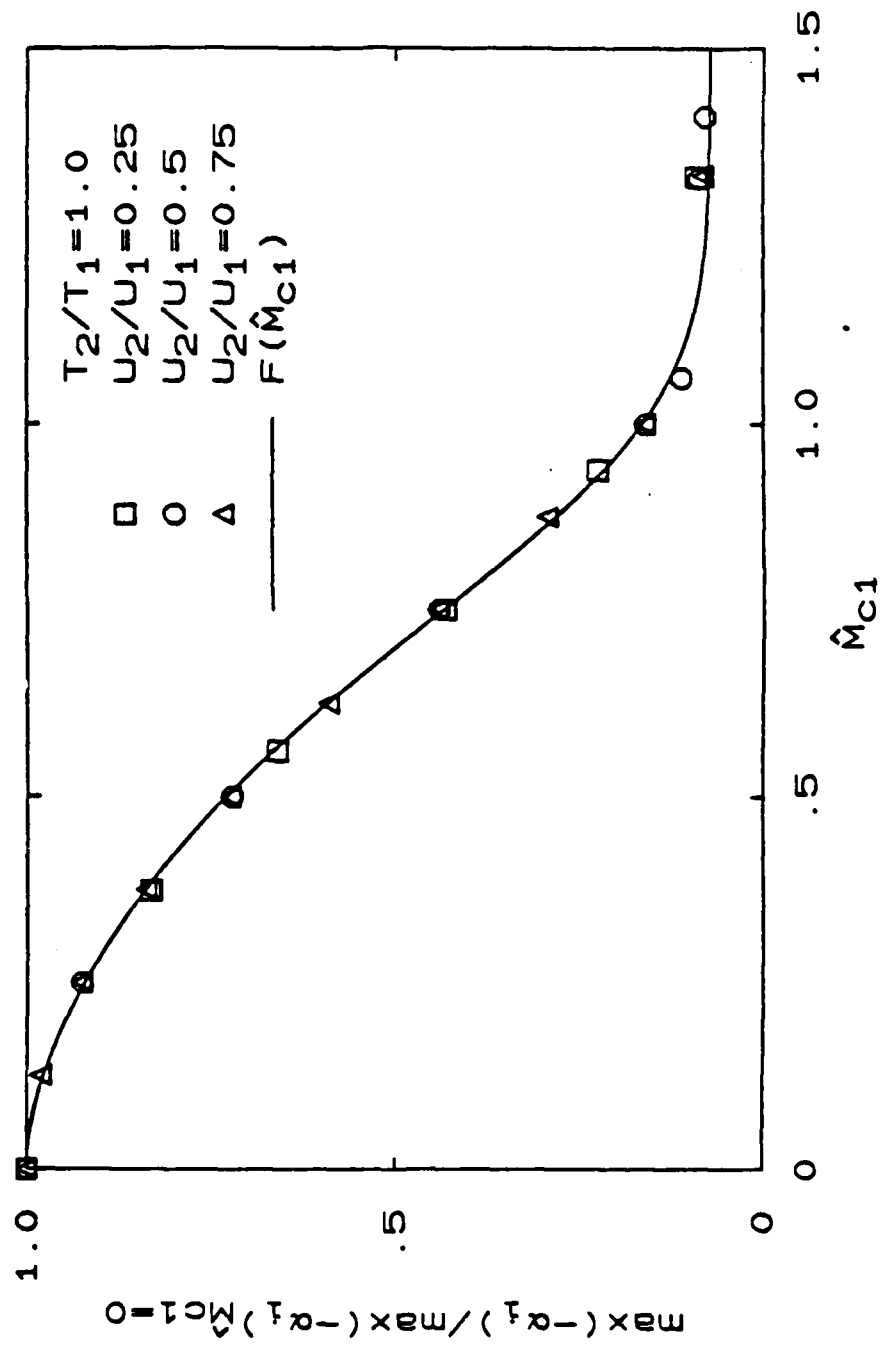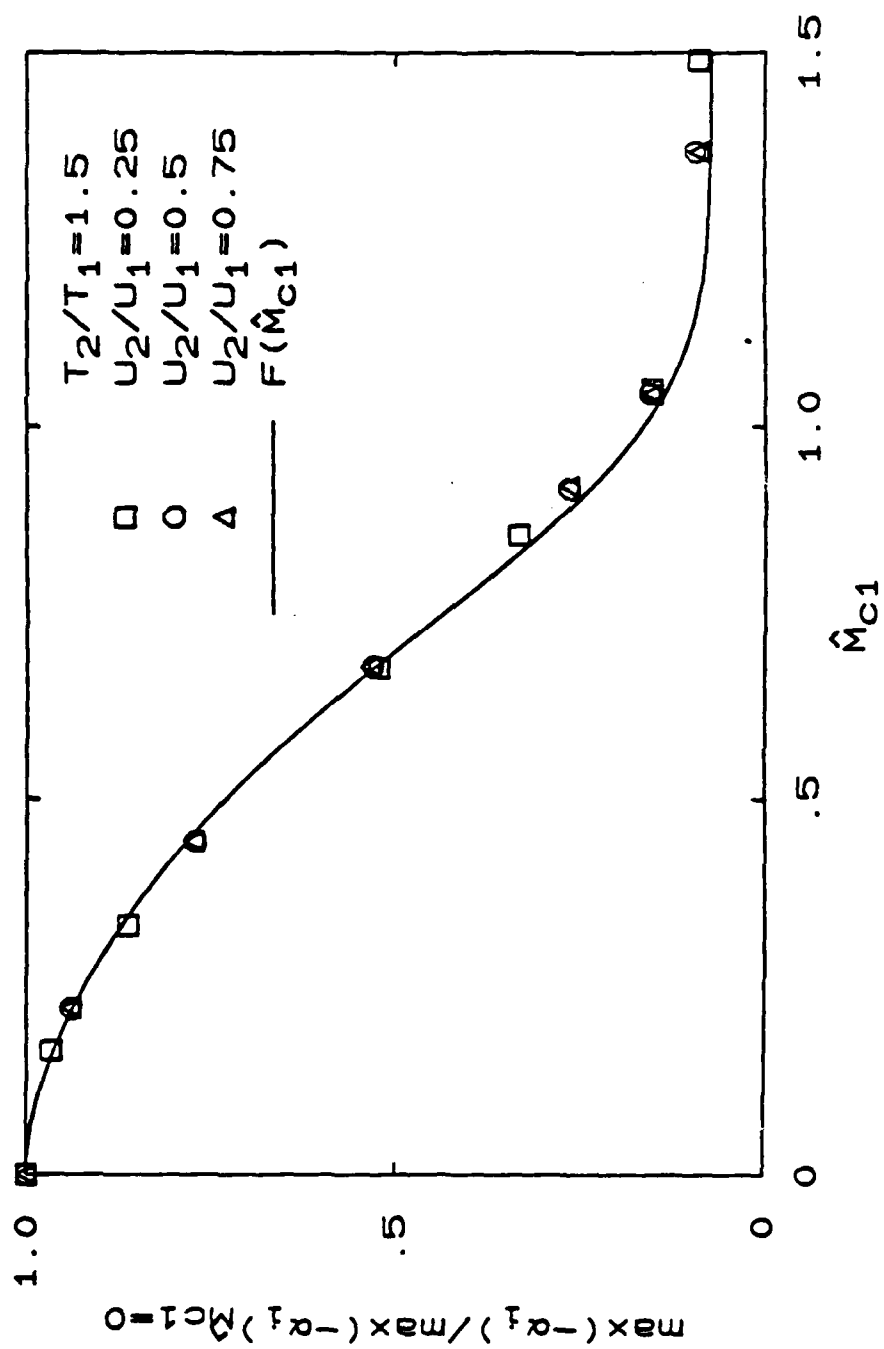
FIG. 10 Normalized maximum amplification rate vs $\hat{M}_{c1}$.
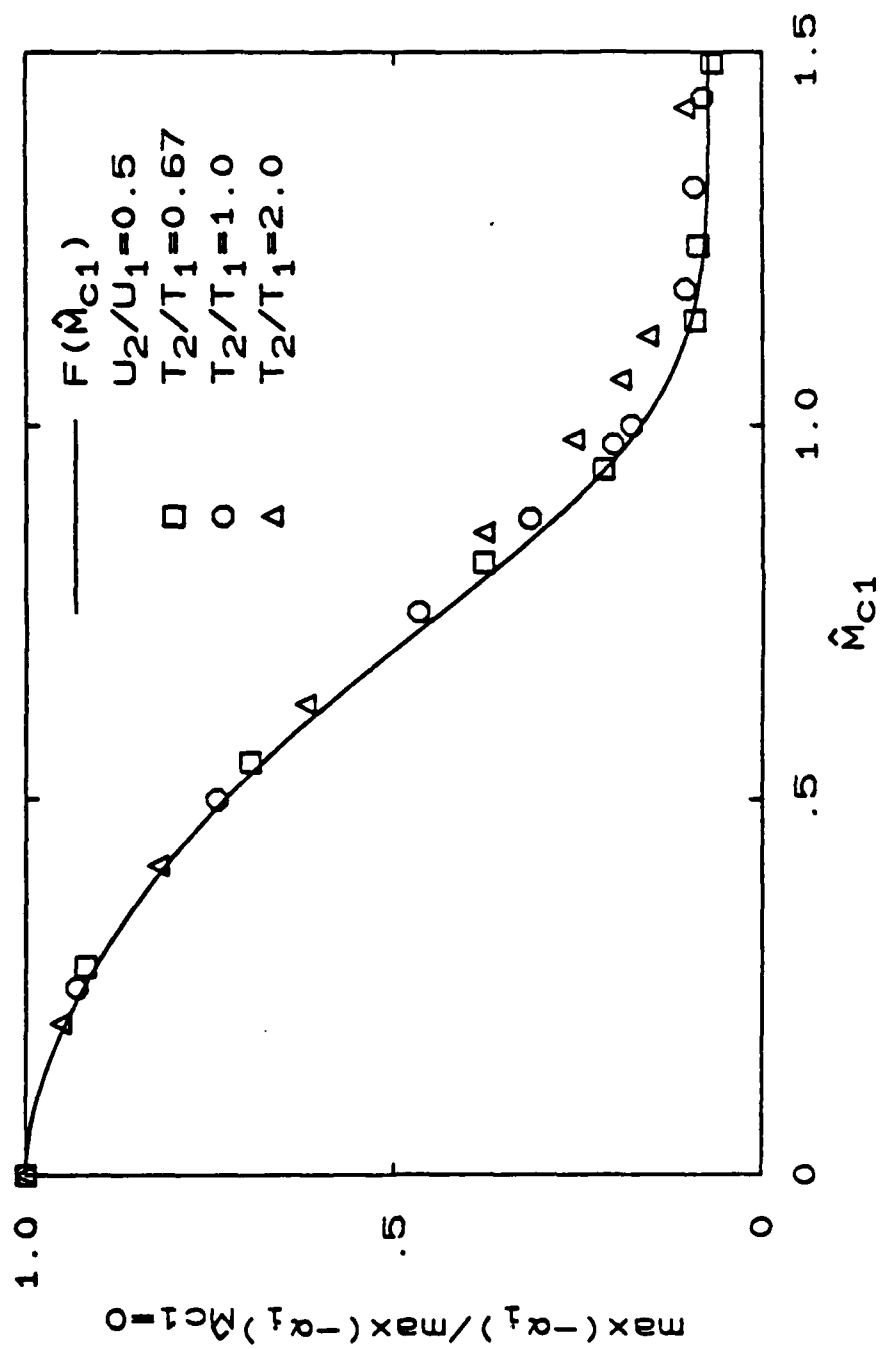
FIG. 11 Normalized maximum amplification rate vs $\dot{M}_{c1}$ for hyperbolic tangent mean temperature profiles comparison with $F(\dot{M}_{c1})$.
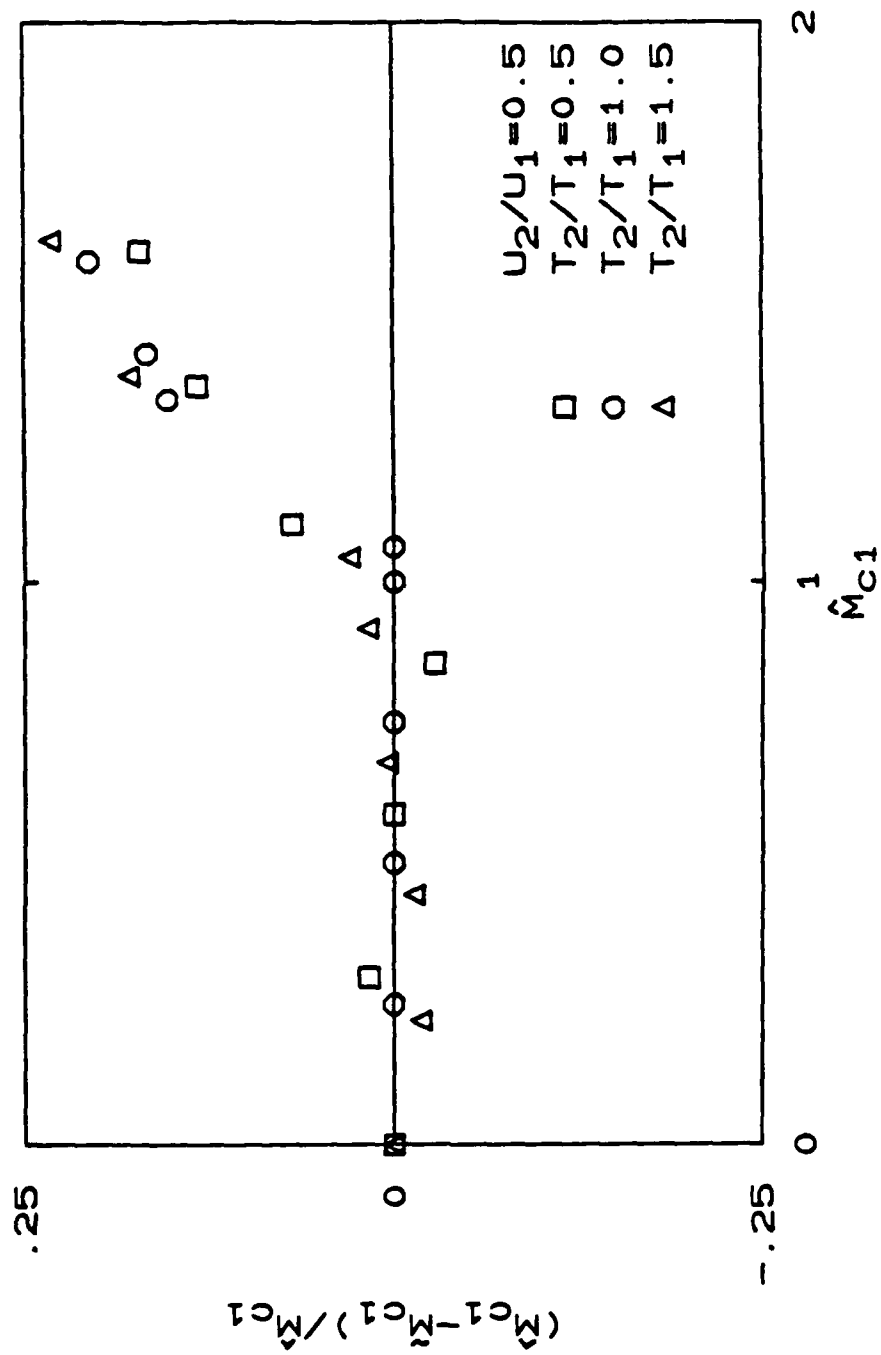
FIG. 12 Normalized difference between $\dot{M}_{c1}$ and $\hat{M}_{c1}$ vs $\dot{M}_{c1}$.
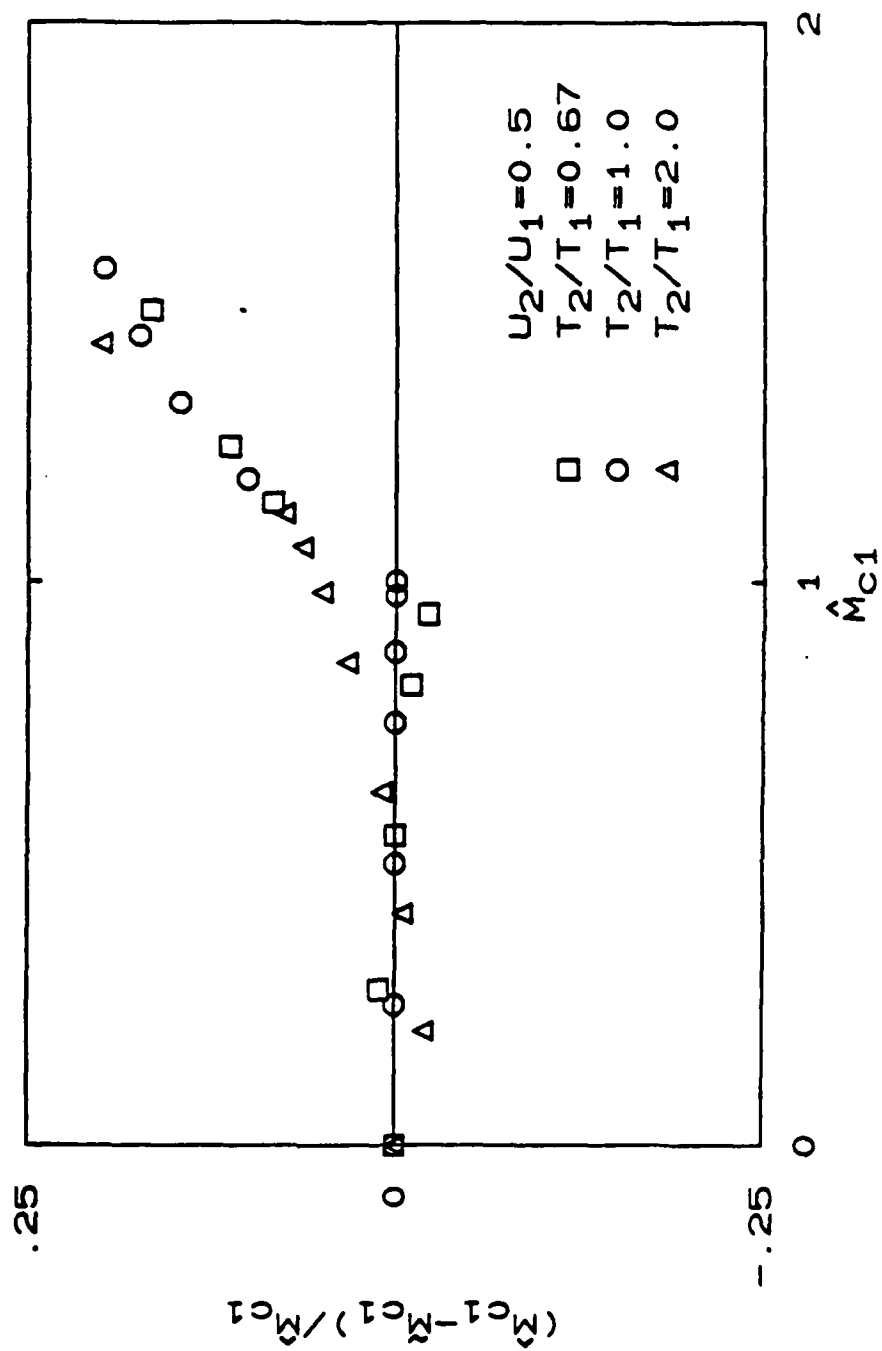
FIG. 13 Normalized difference between $\dot{M}_{c1}$ and $\tilde{M}_{c1}$ vs $\hat{M}_{c1}$ for hyperbolic tangent mean temperature profiles.
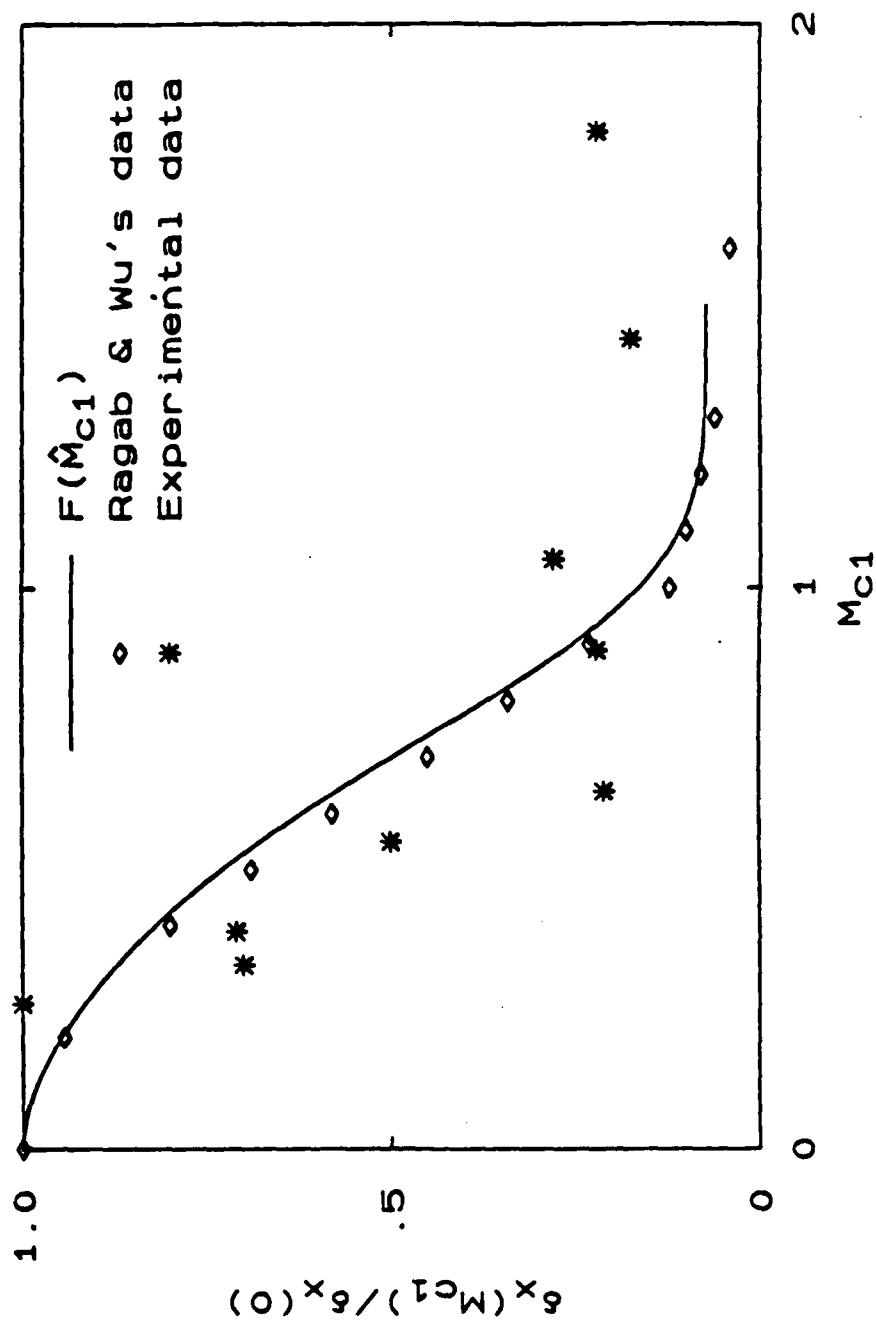
FIG. 14 A comparison of $F(\hat{M}_{c1})$ with Ragab & Wu's numerical data and with Papanoschou & Roshko's experimental data.

Appendix D

MILLER, P. L. and DIMOTAKIS, P. E. [1989] "Stochastic Geometric Properties of Scalar Interfaces", *ASME Fluids Engineering Conference* (La Jolla, California), 10–12 July 1989. session on *Fractal Structures*.

Stochastic geometric properties of scalar interfaces[*]

by
Paul L. Miller[**] and Paul E. Dimotakis[†]

Graduate Aeronautical Laboratories
California Institute of Technology
Pasadena, California 91125

Abstract

Experiments were conducted in which the behavior of scalar interfaces in turbulent jets was examined, using laser induced fluorescence (*LIF*) techniques. The experiments were carried out in a high Schmidt number fluid (water), near or on the jet centerline, over a jet Reynolds number range of $1,000 \leq Re \leq 24,000$. Both two-dimensional scalar data, $c(r,t)$ at fixed x/d, and one-dimensional scalar data, $c(t)$ at fixed x/d and r/x, were analyzed using standard one- and two-dimensional fractal box-counting algorithms. Careful treatment was given to the handling of noise. Both long and short records as well as off-axis measurements were also investigated. No evidence was found of a constant fractal dimension over the substantial range of Reynolds numbers studied. Our results are consistent with the computed behavior of a simple model of interface geometry.

Introduction

The proposals of Mandelbrot (1975, 1977a, 1977b, 1983) to account for the stochastic geometry of turbulent interfaces in terms of fractal, power law similarity generated considerable hope in the turbulence community. The proposed formalism held the promise of an alternate interpretation of a variety of important quantities in turbulence related to energy spectra and dissipation as well a description of the behavior of the interfacial surface of scalars and mixing on a molecular diffusion scale (*e.g.* Gouldin 1988, Sreenivasan *et al.* 1989).

---

[*] Originally presented at the ASME Fluids Engineering Conference (La Jolla, California), 10–12 July 1989, session on *Fractal Structures*, extended for submission to *Physics of Fluids*.

[**] Graduate student, Applied Physics.

[†] Professor, Aeronautics & Applied Physics.

2

We have had the ability, in our own laboratory, to record and analyze high time and space resolution, one- and two-dimensional scalar data using laser induced fluorescence (*LIF*) techniques for the last 12 years, or so. The availability of these data led to a search for a fractal description early on, *i.e.* a similarity scaling wherein the number of elements $N(\lambda)$, of an extent λ, required to cover the scalar interface would be given by

$$N(\lambda) \propto \lambda^{-D} .$$ (1)

In the work presented here, we have investigated the behavior of scalar interfaces in turbulent jets in water using *LIF* techniques.

Experimental description
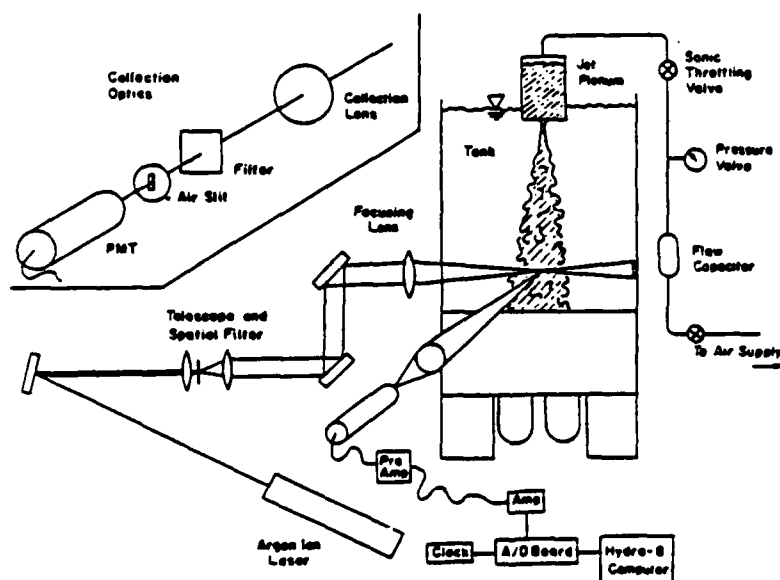
FIG. 1 Experimental apparatus.

The experiments were carried out utilizing the facility shown in Fig. 1. A large rectangular water tank of about two cubic meters volume (Dimotakis *et al.* 1983, Dahm & Dimotakis 1987) acts as the jet reservoir. Large windows on all sides of the tank provide optical access. To establish the flow, the jet plenum is filled with water tagged by a fluorescent laser dye (sodium fluorescein), and air is sonically metered to drive the jet fluid at constant velocity through a 0.1 *in.* nozzle at the base of the plenum. The beam from an argon ion laser is passed through appropriate optics and aligned radially through the centerline of the jet. A beam stop prevents reflections from the opposite window.

Previously, measurements were made in this facility in which a line segment centered on the jet centerline at an x/d of 300 was imaged onto a linear photodiode array. The array was then scanned during a run, providing streak image data of concentration in one spatial dimension $vs.$ time (Dimotakis et $al.$ 1983, Losi & Green 1985, Dahm & Dimotakis 1987). In the present measurements, the laser beam optics were designed to generate a small Gaussian waist at the focus, with a small Rayleigh range. The measurements were made utilizing a low f# lens to image light from a very short segment centered at the waist of the focused laser beam (on the jet centerline at an x/d of 100) onto a photomultiplier tube, yielding single-point concentration values $vs.$ time. An optical low-pass filter eliminates background laser light, passing only the red-shifted fluorescence. A slit spatial filter defines the length of the laser line segment sampled, and is chosen such that the sampling volume is roughly cubic in shape. Data acquisition is computer-controlled, with the data stored on disk for transferral to a larger computer for subsequent processing.

Results and discussion

Single-point concentration measurements as a function of time were made on the jet centerline for a range of Reynolds numbers from $2,940$ to $23,400$. The Reynolds number used here is defined as

$$Re = \frac{u_0 d}{\nu} , \qquad (2)$$

where u_0 is the jet nozzle velocity, d is the jet nozzle diameter, and ν is the kinematic viscosity. Careful consideration was given to the treatment of noise. Specifically, power spectra of the data were calculated, allowing the optimal (least mean squared error) Wiener filter (Wiener 1949, Press et $al.$ 1986, Dowling 1988, Dowling et $al.$ 1988) to be obtained. The data were then convolved with the Wiener kernel to obtain the optimal signal, consistent with detection noise levels. Sample spectra before and after the filtering process are compared in Fig. 2.

The Wiener-filtered data were subsequently thresholded and transitions, or crossings of the threshold value, were located. The threshold chosen was the local mean concentration because it is an unambiguous choice, it is close to both the mode of the concentration PDF and the value for which the most transitions are obtained, and is the value towards which the local scalar field is driven by the diffusion process (scalar dissipation). Our results were found to be insensitive to modest changes in this choice. The resulting record of transition locations was then processed using a one-dimensional fractal box-counting algorithm.

The box-counting algorithm produces a plot of the logarithm of the number of 'tiles', or contiguous constant length segments, required to cover the transition locations on a record, as a function of the logarithm of the tile size (such as Fig. 3 below). D_λ, the negative derivative of the line on this plot, may then be interpreted as the associated fractal dimension.
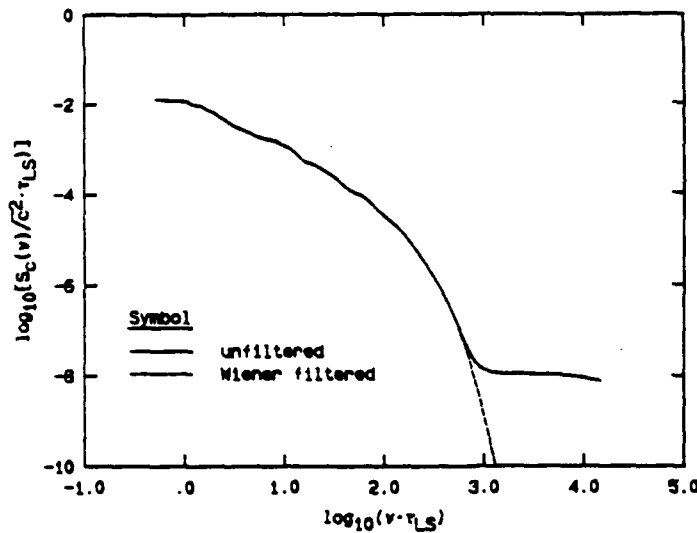
FIG. 2 Demonstration of Wiener filter.

It became apparent, after some early attempts at using many points per decade in our fractal calculations, that there are some subtle end-effects which can occur. If the record submitted for box-counting is a non-integral number of a particular tile size in length, the last tile extends past the end of the record, 'hanging off the edge'. If there is a transition under the portion of this tile which lies on the record, then there is no ambiguity, and the tile can be counted. However, if no transition occurs, it is unclear whether there would have been a transition under the portion of the tile extending beyond the end of the data record. Some type of weighting scheme of this fractional end tile may suggest itself, but such weighting requires the (ad hoc) assignment of the appropriate probability.

Numerical experiments we have conducted utilizing the one-dimensional Cantor set have displayed sawtooth oscillations which vary in wavelength as a function of tile size, consistent with end-effects. We verified that various weighting schemes do not correct the difficulty. As a result, we decided that the tile sizes used in these fractal calculations should all be powers of 2 and the total record size analyzed should also be a power of 2.

The result of a Cantor set calculation using integral tiles is included in Fig. 3. The constant slope region is clearly visible, although there is some fluctuation about the expected analytic value. This may be the result of the oscillations observed by Smith et al. (1986) in numerical calculations of the fractal dimension for this set. We argue, and have confirmed to our satisfaction by varying the effective record length, that the deviation of the numerical result from the analytical value, at the smaller and largest scales, is a result of the finite range of scales included in the simulation. The calculated points were joined by straight lines in the plots to aid the eye. It is significant to note that, using only integral tiles, the log-log curves must be non-increasing with increasing tile size. Without belabor-
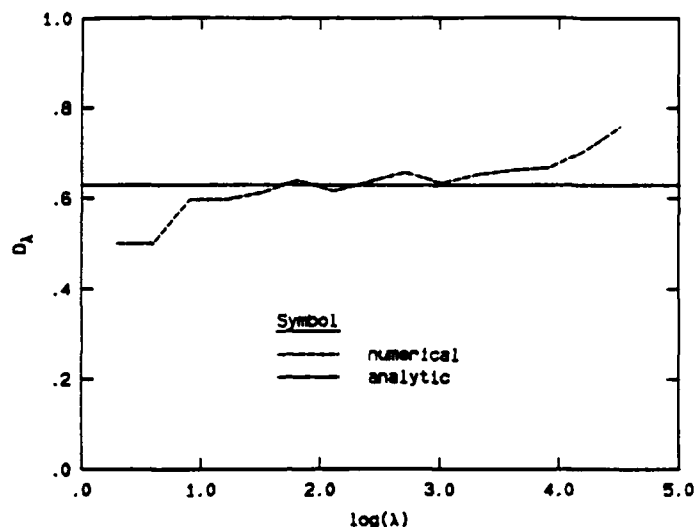
FIG. 3 Calculation for the Cantor set.

ing the logic, it is clear that it cannot require more larger tiles than smaller ones to cover the same transitions. Note, also, that increases in the log-log curve would yield a negative fractal dimension for the corresponding range of scales. This is, of course, inadmissible, even in the presence of noise.

It is tempting to fit a straight line to the log-log plot to assign a (constant) fractal dimension. There is, however, the ambiguity of deciding which segment of the curve to fit with the line. In our case, there is in fact no need to resort to such a fit, as the statistics of our processed data are of sufficient quality to permit direct differentiation of the log-log curve to determine its local slope. A constant dimension should then appear as a constant value in a plot of this derivative. We chose to use three-point central differencing in this computation. Higher order schemes were considered to be unwarranted for this task. The log-log plots and plots of the resulting D_λ are shown in Fig. 4, where the length scale (estimated from the calculated mean velocity) has been expressed in absolute length (meters).

As can be seen, *there is no evidence of a constant value* on the D_λ plots, other than the limiting values of 0 and -1. This is despite the fact that the spatial range spans from below the Kolmogorov scale to the outer large scales of the flow. The limiting value of -1 at the large tile sizes indicates that every tile of sufficient length covers transitions. This is to be expected for scales on the order of the jet diameter (about $11\,cm$ in Fig. 4b), or larger, since over such a distance (or corresponding time) a crossing of the mean concentration level is almost certain. Failure to reach this asymptotic value indicates that either the data record was insufficient in length to capture the largest scales of the flow, or that the processing algorithm stopped at a tile size shorter than these largest scales.
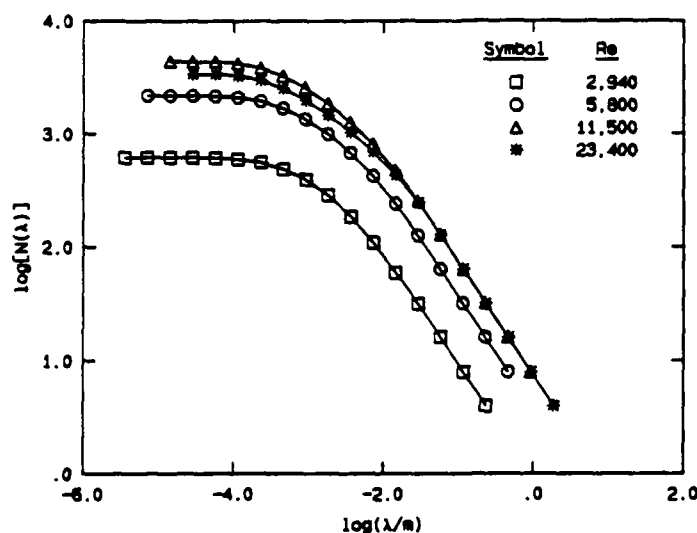
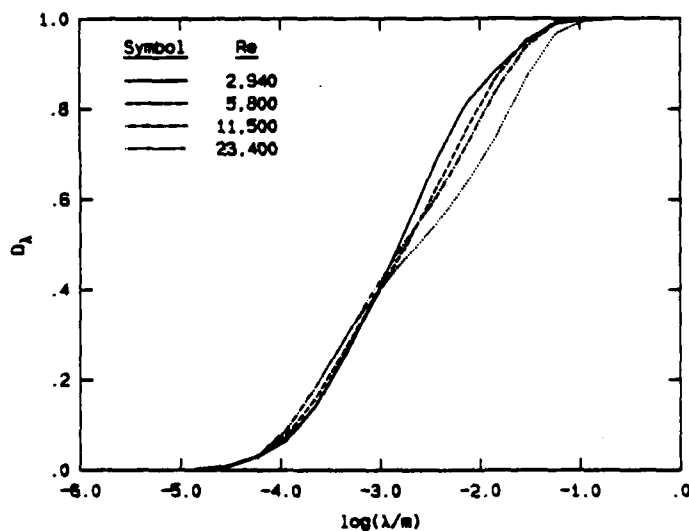FIG. 4a Log-log tiling plots of centerline data for four Reynolds numbers $(x/d = 100)$.

FIG. 4b Corresponding D_λ plots (note that $\log \delta/m \simeq -1.0$).

Note that the spatial resolution of the measurements used for the values in Fig. 4b is about $80\,\mu m$, and the Kolmogorov scales[‡] range from roughly 50 to $250\,\mu m$. It can be seen that all four curves merge in the vicinity of $80\,\mu m$ in the figure, consistent with our estimate of the resolution. We recognize, however, that it may be necessary to measure

[‡] The Kolmogorov scale was estimated directly from its definition in terms of the mean energy dissipation rate, using the result of Friehe *et al.* (1971) for the dissipation rate on the centerline of a turbulent jet (*cf*. Dowling 1988).

scales well *below* the Kolmogorov scale for several reasons. One is that the fractal dimension is calculated as a finite difference of the log-log curve. This makes slope values somewhat sensitive to resolution of the next smallest point. Another caveat is that the Kolmogorov scale, as a local scale, is subject to fluctuations which have some distribution. This distribution may have a significant contribution at scales less than the Kolmogorov scale based on the mean energy dissipation rate. Finally, the Batchelor (1959) diffusion scale is, in this case, a factor of 25 below the Kolmogorov scale. It is, in fact, the smallest spatial scale expected in the scalar field.

While recognizing the issues at the smallest scales, it should be kept in mind that these data represent some of the highest resolution measurements made in a turbulent, high Schmidt number jet. In addition, over a million single-point measurements are made in each run, spanning four to five decades of spatial scales. Nevertheless, taking into account the effects discussed above, it may be that this is still insufficient resolution to quantify the small scale behavior of the D_λ curves at the higher Reynolds numbers that were investigated.
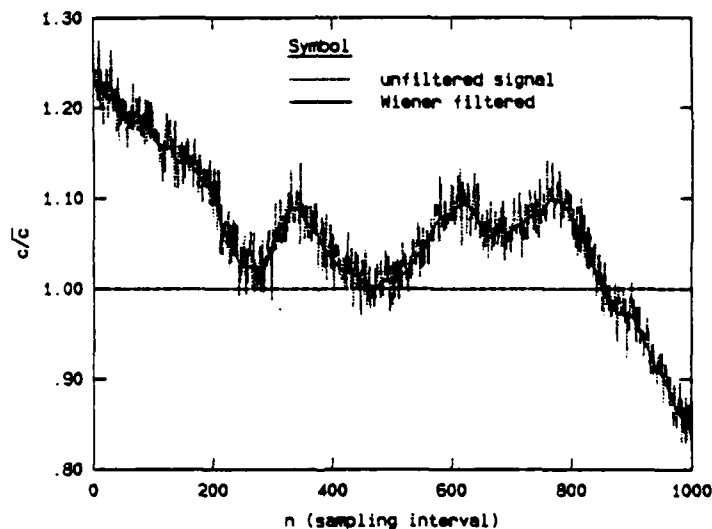
FIG. 5a Effect of noise on transitions ($Re = 2940$).

It has been known for some time that the presence of noise in a signal can profoundly effect the statistics of level crossings (Rice 1954). Since the box-counting algorithm utilizes level crossings or transitions, the issue of noise is an important one. To illustrate this effect, Fig. 5a displays a small segment of a normalized, unfiltered signal and the corresponding optimally (Wiener) filtered signal. It is apparent that noise grossly affects the crossings of the mean level, and that a proper treatment of this aspect of the data is thus an essential component of the data processing. As all measurements are subject to noise, this is an issue which must be addressed.
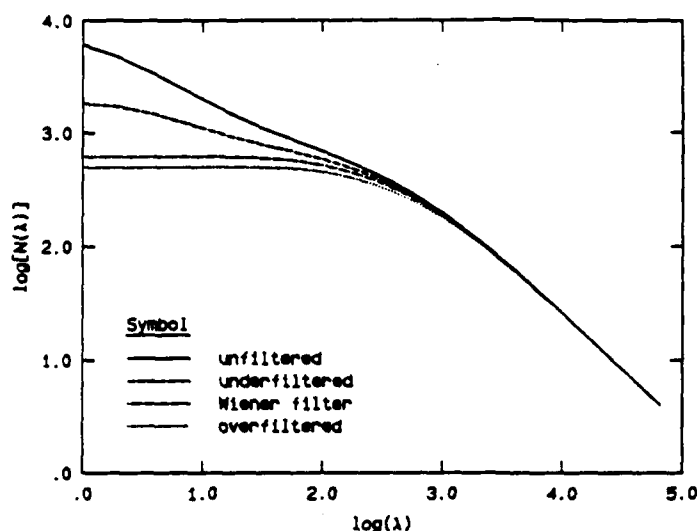
8

FIG. 5b Effect of noise on results ($Re = 2940$).

As a demonstration of the effect of noise on the box-counting algorithm's results, data from a particular run was processed both unfiltered, with a variety of Gaussian filters of differing widths, and using the optimal filter. The Gaussian filter, if chosen with an appropriate width (which, however, is not known *a priori*), may serve as an adequate approximation to the Wiener filter. Figure 5b shows the results for no filtering, insufficient filtering, optimal filtering, and over filtering. It is evident that the presence of noise in the data may result in a region of nearly constant slope on the log-log plots. With the correct degree of filtering, however, which is totally determined from the power spectrum and has no adjustable parameters, this constant slope has disappeared.

While the approach documented above to determine D_λ is one we have converged on in favor of many alternatives, several suggestions have been made in the literature which we felt we should assess. These include the effect of analyzing shorter data records rather than the entire run as one long record, measuring in the intermittent off-axis region of the jet, and comparing true one-dimensional spatial data and two-dimensional streak data with the single-point measurements (*cf*. Sreenivasan & Meneveau 1986 and Prasad & Sreenivasan 1989).

Shorter records have been suggested because of the possibility that scalar interfaces might display a particular fractal behavior on a local length or time scale, but that over larger scales, fluctuations or variations in the local properties could smear out the effect. To examine the behavior of shorter record lengths, rather than ensemble averaging either the log-log plots or the D_λ curves for many short records, we superimpose all of the results on one plot (Fig. 6). The results shown are for a Reynolds number of 2,940. Not only do the individual realizations fail to exhibit a constant slope region, but the ensemble average
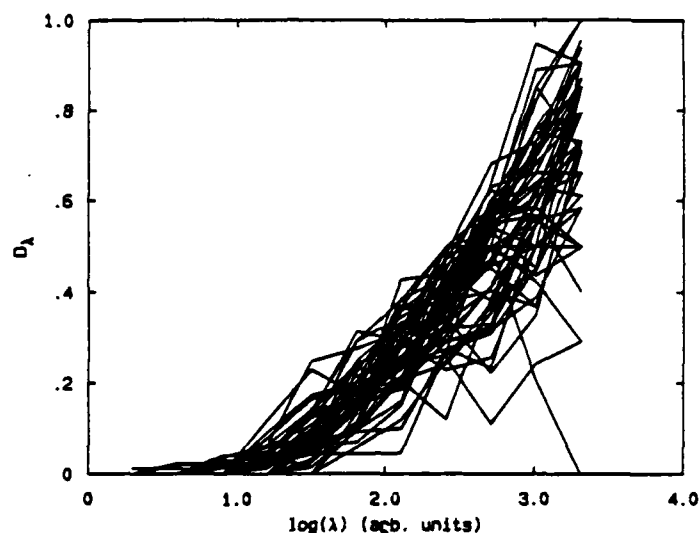
FIG. 6 Many individual short records $(Re = 2,940)$.

resembles the result displayed in Fig. 4. Even shorter records were also analyzed, for the entire range of Reynolds numbers, and the outcome was the same for record lengths of all sizes, down to ones so small that the D_λ curve would barely begin to rise before the record length was reached.
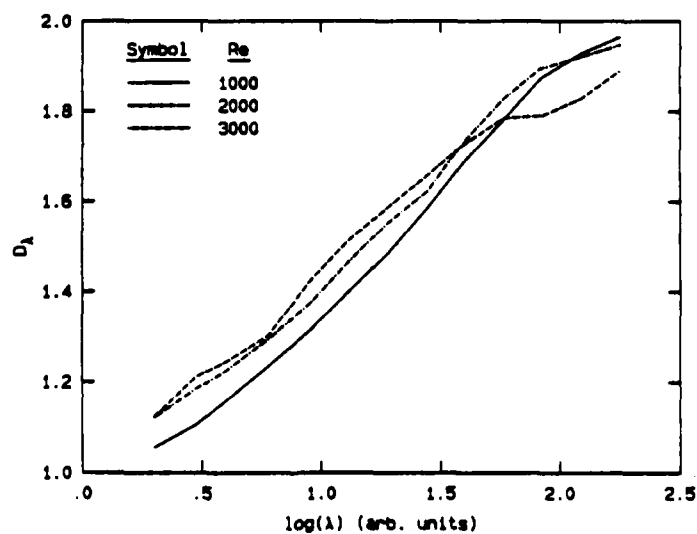

FIG. 7 Two-dimensional results.

In addition to the one-dimensional box-counting algorithm, a two-dimensional tiling program was also employed on the streak image data. Streak images were taken at Reynolds

numbers of $1,000$, $2,000$, and $3,000$, providing full resolution of the Kolmogorov scale in each case (Green & Losi 1985). The data acquisition rate was adjusted proportional to the local flow velocity. The results are shown in Fig. 7.
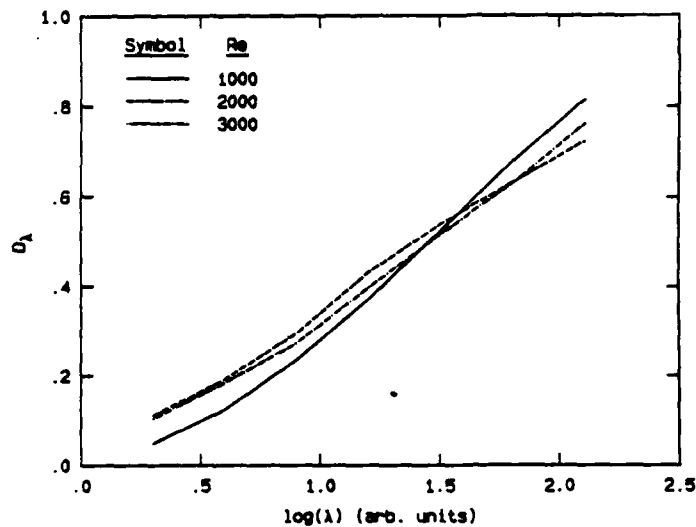
FIG. 8 One (spatial) dimension results.

These streak images were also analyzed line by line, as successive, one-dimensional spatial images. Since the array used contained only 512 pixels, the dynamic range of the spatial data is much smaller than the single-point measurements. These results are included as Fig. 8. Finally, single-point measurements were made off the jet centerline at $\eta = r/x$ of 0.06 and 0.13, at a Reynolds number of $8,500$. The results are shown in Fig. 9, and compared with a corresponding centerline curve.

Regardless of the approach, *no evidence was found of a power law similarity*, corresponding to a (constant) fractal dimension. It is for this reason that we have denoted the logarithmic derivative of the $N(\lambda)$ curve by the symbol D_λ, rather than simply D.

In an effort to model this behavior, we utilized a simple description of the threshold crossings. A program was written which produced a record of transitions which were randomly spaced with log-normal probability. *PDF*'s of our measured transition spacings show that the log-normal distribution is a good approximation. Two parameters, the location of the maximum and the width of the distribution, were allowed. Figure 10 includes the result for the lowest Reynolds number of $2,940$. The agreement is good.
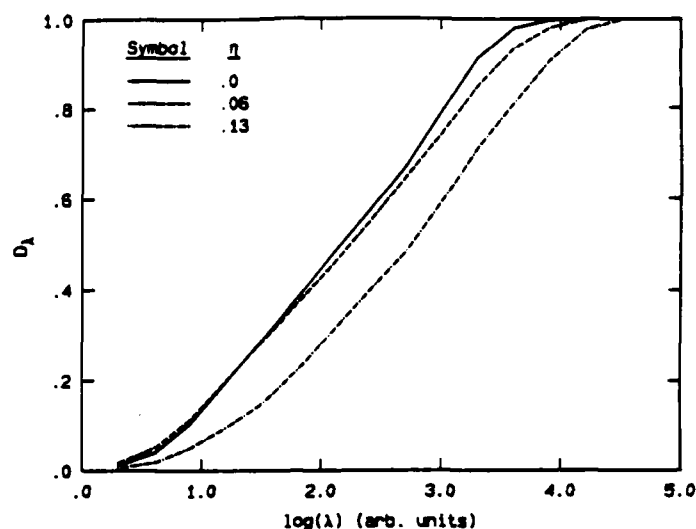
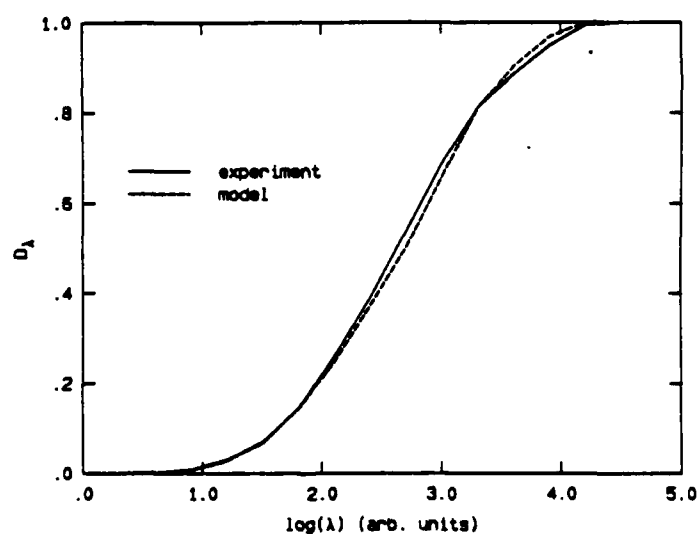FIG. 9 Off-axis single-point results ($Re = 8,600$, $\eta = r/x$).

FIG. 10 Comparison of model and experiment ($Re = 2,940$).

Conclusions

There has been a number of papers documenting experimental measurements of fractal dimension in turbulent flows, e.g., Sreenivasan & Meneveau (1986), Sreenivasan et al. (1989), Meneveau (1989), and Prasad & Sreenivasan (1989). These authors have concluded that power law (fractal) similarity is applicable to the description of scalar interfaces. We appreciate that our results are at variance with documented evidence, which led us to

expend considerable care in examining possible reasons for this discrepancy. In summary, we have performed experiments in the far field of turbulent jets, yielding high resolution scalar field measurements. We have examined single-point measurements, one-dimensional line images, two-dimensional streak images, ensembles of long records, short records, on-axis and off-axis data, in jet flows spanning over a decade in Reynolds number, and find no evidence of a power law similarity.

There are many possible explanations for this discrepancy. Available documentation of previous experiments and the analysis of the resulting data make no mention of the treatment of noise, which we have shown may have an important effect on the results. We have also examined the merits of short *vs.* long records in the search of a constant fractal dimension, as it was suggested by Sreenivasan & Meneveau (1986, Fig. 14), that large scale fluctuations in very long records may mask this behavior. We note, however, that their short records (for which they claim a constant D_λ) only have on the order of 20 transitions, or so, in the region of interest. The confidence level of the statistical inferences from such small samples could well be low. Additionally, we also note that in the same figure, increases in $\log N(\epsilon)$ can be seen with increasing $\log \epsilon$. Such increases are, of course, not admissible by the analysis and suggest that the algorithms that were employed may be at fault (see also *ibid.*, Figs. 10, 15, and 19). Non-integral tiles were apparently used in that analysis, with no explanation of how end-effects were treated. No test case is shown using their box-counting algorithm. We should also raise a caveat concerning fitting a straight line directly to log-log curves, rather than computing the derivative directly, in some way. We feel that straight line fitting may often obscure systematic curvature. The reader is invited to sight along log-log curves edge-on to reveal this effect.

There is also an issue of Reynolds number. The only referenced value for jet flow in Sreenivasan & Meneveau (1986) is a Reynolds number of 2,500 (Fig. 9, caption). Unfortunately, the jet Reynolds number is not cited in the more recent paper by Prasad & Sreenivasan (1989). Judging by the photograph (Fig. 1) and the resolution claims in that paper, it would appear to be close to 1,000. Previous experiments in water (*e.g.* the Weddel experiments documented in Hottel 1953, Dahm 1985), however, have shown that jet flow has not attained asymptotic behavior, by a variety of criteria, until a Reynolds number of at least 3,000. Power spectra (Dowling 1988, gas phase mixing) of the scalar field are also not characterized by a constant power law region for Reynolds numbers as high as 5,000 to 10,000. Our own measurements of scalar spectra in water corroborate this finding. Entrainment measurements in gas phase jet flows (Ricou & Spalding 1961) have shown that quasi-asymptotic behavior is not attained until a Reynolds number of 25,000.

Findings of a constant and universal fractal dimension are thus all the more surprising, since the jet flows utilized in the reported experiments may not be bona fide turbulent, certainly not in the sense of displaying a well-developed inertial cascade with a (near) $-5/3$ power law exponent. Conversely, our data and analysis force us to conclude that, at

least in the far field of turbulent jets, *scalar interface geometry cannot be described in terms of a constant fractal dimension*, at least under any of the flow conditions we have examined in our experiments. This conclusion was the reason for avoiding the word fractal in our title, as that was coined by Mandelbrot to denote the power law of Eq. 1. We appreciate that the flow in the far field of turbulent jets is characterized by a host of similarity properties, indeed spanning the full spectrum of scales (Dowling 1988). We note, however, that power law behavior is not compelled by similarity.

Acknowledgements

References

BATCHELOR, G. K. [1959] "Small-scale variation of convected quantities like temperature in turbulent fluid. Part 1. General discussion and the case of small conductivity", *J. Fluid Mech.* **5**, 113–133.

DAHM, W. J. A. [1985] *Experiments on Entrainment, Mixing and Chemical Reactions in Turbulent Jets at Large Schmidt Numbers*, Ph.D. thesis, California Institute of Technology.

DAHM, W. J. A. and DIMOTAKIS, P. E. [1987] "Measurements of Entrainment and Mixing in Turbulent Jets", *AIAA J.* **25**(9), 1216-1223.

DIMOTAKIS, P. E., MIAKE-LYE, R. C. and PAPANTONIOU, D. A. [1983] "Structure and Dynamics of Round Turbulent Jets", *Fluid Dynamics Trans.*, **11**, 47-76.

DOWLING, D. R. [1988] *Mixing in gas phase turbulent jets*, Ph.D. thesis, California Institute of Technology.

DOWLING, D. R., LANG, D. B. and DIMOTAKIS, P. E. [1988] "An Improved Laser-Rayleigh Scattering Photodetection System", submitted to *Exp. in Fluids* .

FRIEHE, C. A., VAN ATTA, C. W. and GIBSON, C. H. [1971] "Jet turbulence: Dissipation rate measurements and correlations", AGARD *Turbulent Shear Flows* CP-93, 18.1-7.

14

HOTTEL, H. C. [1953] "Burning in Laminar and Turbulent Fuel Jets", 4th (International) Symposium on Combustion (The Williams and Wilkins Co.), 97.

GOULDIN, F. C. [1988] "Interpretation of Jet Mixing Using Fractals", *AIAA J.* **26**(11), 1405–1407.

GREEN, S. and LOSI, G. [1985] "Fractal Dimension of a Turbulent Jet", Ae 104 experimental report (experiments under the supervision of and collaboration with Werner Dahm and Paul Dimotakis).

MANDELBROT, B. B. [1975] "On the Geometry of Homogeneous Turbulence, with Stress on the Fractal Dimension of the Iso-Surfaces of Scalars", *J. Fluid Mech.* **72**(2), 401–416.

MANDELBROT, B. B. [1977a] *Fractals. Form, chance, and dimension* (W. H. Freeman & Co., San Fransisco).

MANDELBROT, B. B. [1977b] "Fractals and Turbulence: Attractors and Dispersion", *Lecture Notes in Mathematics* **615** (Springer-Verlag), 83–93.

MANDELBROT, B. B. [1983] *The Fractal Geometry of Nature* (W. H. Freeman & Co., San Fransisco).

MENEVEAU, C. [1989] "The Multifractal Nature of Turbulence", Ph.D. thesis, Yale University.

PRASAD, R. R. and SREENIVASAN, K. R. [1989] "Scalar interfaces in digital images of turbulent flows", *Exp. in Fluids* **7**, 259–264.

PRESS, W. H., FLANNERY, B. P., TEUKOLSKY, A. A. and VETTERLING, W. T. [1986] *Numerical Recipes. The Art of Scientific Computing.* (Cambridge Univ. Press).

RICOU, F. P. and SPALDING, D. B. [1961] "Measurements of Entrainment by Axisymmetrical Turbulent Jets", *J. Fluid Mech.* **11**, 21–32.

RICE, S. O. [1954] "Mathematical Analysis of Random Noise", *Selected Papers on Noise and Stochastic Processes* (Dover), 133–294.

SMITH, L. A., FOURNIER, J–D. and SPIEGEL, E. A. [1986] "Lacunarity and Intermittency in Fluid Turbulence", *Phys. Lett.* **114A**(8,9), 465–468.

SREENIVASAN, K. R. and MENEVEAU, C. [1986] "The Fractal Facets of Turbulence", *J. Fluid Mech.* **173**, 357–386.

SREENIVASAN, K. R., RAMSHANKAR, R. and MENEVEAU, C. [1989] "Mixing, Entrainment, and Fractal Dimensions of Surfaces in Turbulent Flows", *Proc. Roy. Soc. London A* **421**, 79–108.

WIENER, N. [1949] *Extrapolation, Interpolation and Smoothing of Stationary Time Series* (John Wiley & Sons).

Appendix E

BROADWELL, J. E. and MUNGAL, M. G. [1988] "Molecular Mixing and Chemical Reactions in Turbulent Shear Layers", *22nd Symposium (International) on Combustion* (The Combustion Institute), 579–587.

MOLECULAR MIXING AND CHEMICAL REACTIONS IN TURBULENT SHEAR LAYERS

JAMES E. BROADWELL

Graduate Aeronautical Laboratories
California Institute of Technology
Pasadena, CA 91125

AND

M. GODFREY MUNGAL

Department of Mechanical Engineering
Stanford University
Stanford, CA 94305

A model is proposed for describing chemical reactions in a turbulent shear layer. The model exhibits explicitly the effects on the overall reaction rate of equivalence ratio and of the Schmidt, Reynolds and Damköhler numbers. The model predictions compare favorably with experimental results in which all of these parameters are varied. The comparisons imply that the Reynolds number influences the effective reaction rate for Re as high as 10^5 and that the reaction rate becomes mixing-limited for values of the Damköhler number, based on time of flight to the measuring station and the overall reaction time, of about 40.

Introduction

In this paper the model proposed in Ref. 1 for treating fast chemical reactions in turbulent shear layers is extended to allow the treatment of arbitrary chemical reaction rate. To provide a background for the development, the basic ideas on which the model is based are reviewed and the earlier comparisons with fast chemical reaction experiments in both gases and liquids are summarized. The experiments of Mungal and Frieler[2] in which the reaction rate in a turbulent shear layer was varied from zero to mixing limited conditions was the motivation for the work and it is with their data that the model is compared.

The essential concept upon which the model is based is the idea that the molecular mixing takes place during, and at the end of, a Kolmogorov-like cascade from the largest to the smallest scales in the flow. Successive cascades begin as fluid from the two streams enter the shear layer and form large-scale structures. During the cascades, flame sheets form between the reactant streams and here the molecular transport coefficients influence directly the molecular mixing rate. It is in the treatment of these effects that the model predictions differ most significantly from those based on the notion of turbulent eddy diffusion.

Basic Ideas

The basic ideas upon which the model rests came primarily from the experiments of Konrad[3] and of Breidenthal,[4] experiments following the seminal work of Brown and Roshko.[5] The essential observations were: 1) more reaction product was present, at a given Reynolds number, in a reaction in gases than in water, and 2) the ratio of high speed fluid to low speed fluid in the molecularly mixed fluid was virtually independent of the lateral coordinate. These early experiments have been followed by others confirming the observations and providing many more supporting details. Results from the experiments of Koochesfahani and Dimotakis[6] in water (Fig. 1) illustrate, strikingly, the nearly constant in the lateral direction composition of the molecularly mixed fluid. Konrad's observations in gases, also in Fig. 1, show that the composition is not quite so flat in gases. These measurements will be discussed in the context of the model after it has been developed.

It is concluded from the experimental observations and from numerical calculations such as those of Corcos and Sherman,[7] Lin and Corcos,[8] and Lowery and Reynolds,[9] that the scalar behavior arises from the fact that instabilities lead to regions of concentrated vorticity, which causes freestream fluids
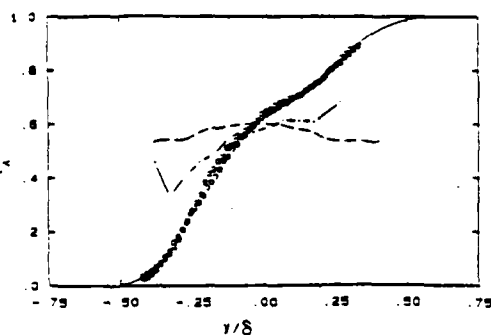
Fig. 1. High speed fluid concentration. The symbols denote mean concentration and the dashed line the mean concentration of the molecularly mixed fluid in water. Koochesfahani and Dimotakis.[8] Dashdot line is the mean concentration of the molecularly mixed fluid in gases. Konrad.[3]

to enter the shear layer in streams with dimensions of the order of the layer thickness. δ. The model formulation is based largely on these observations and proceeds as follows. (It is helpful in following the model development to have in mind the flow fields described in these references.)

It is postulated that in the limit Re $\rightarrow \infty$, no mixing takes place until the scale of these entering streams is reduced. by inviscid motions, to the Kolmogorov scale. $\lambda_k \sim \delta/Re^{3/4}$, where Re is the Reynolds number based on the shear layer thickness. δ, and velocity difference. ΔU. When the scale of the concentration fluctuations in the streams reaches λ_k, it is shown in Refs. 1 and 10, and outlined below. that the time required for diffusion to "homogenize" the mixture is negligible compared to the time to reach λ_k from δ, i.e. compared to $\delta/\Delta U$. The quantity. or volume fraction. of molecularly mixed fluid so formed is. therefore, independent of both the Reynolds number and the Schmidt number. Sc $= \nu/D$. where ν and D are the viscosity and diffusion coefficients. In the limit Re $\rightarrow \infty$ then, the rate of molecular mixing is a constant as is the rate of entrainment into the layer. These assumptions parallel those made in turbulence theory concerning dissipation. that it is independent of Reynolds number and takes place at the Kolmogorov scale.

When the Reynolds number is below the asymptotic range Re $\rightarrow \infty$, but still such that (ReSc)$^{1/2}$ $>> 1$ and the inertial cascade takes place, diffusion layers form at the boundaries of the entering streams. At the large scale their thickness. λ_r, scales with the large scale variables. U and δ, and is given by

$$\lambda_r \sim \delta/(ScRe)^{1/2} \sim \delta/Pe^{1/2}$$

where Pe is a Peclet number $\Delta U \delta/D$. Since the surface area per unit volume. S. of these diffusion sheets scales only with δ^{-1} at the large scale, their fractional volume $(S \cdot \lambda_r)$ is proportional to Pe$^{-1/2}$.

In the original formulation of the model. the diffusion layers are called strained laminar flames. Connection is made with the preceding discussion by noting that if these layers are in diffusive equilibrium with the local large scale strain $\epsilon \sim \Delta U/\delta$. their thickness λ_r is proportional to $(D/\epsilon)^{1/2}$ $\sim \delta/Pe^{1/2}$ in agreement with the above expression. (See Carrier. Fendell. and Marble[11] for a discussion of these flames.) When Sc $= 1$. λ_r is the Taylor scale. a fact brought to our attention by H. W. Liepmann. who points out that they are. in the mathematical sense. internal boundary layers.

In this case. also. when all scales in the entering stream are reduced to the Kolmogorov scale. the mixture is homogenized as before. In this Lagrangian description of the path from the free stream to the molecularly mixed state. the same quantity of fluid is involved whatever the Reynolds or Schmidt number. Therefore. the fractional volume of mixed fluid produced by diffusion at the Kolmogorov scale is independent of these parameters. The diffusion at the scale λ_r causes mixing that is "early" or upstream. in the Eulerian viewpoint.

At any axial station. then. the molecularly mixed volume fraction. V_m, can be written.

$$V_m = A + B/(ScRe)^{1/2} \quad \begin{array}{l} Re >> 1 \\ (ScRe)^{1/2} >> 1 \\ Re >> \ln Sc^2 \end{array} \quad (1)$$

in which A is the average volume fraction generated when the entrained fluid reaches the scale λ_k and B is proportional to the average non-dimensional surface are per unit volume. i.e.. to S measured in terms of δ. The notation ScRe is used instead of Pe because of the need to state the conditions of applicability of the model.

The restrictions written for Eq. (1) are to be interpreted as follows. The requirement that Re $>> 1$ insures that the flow is turbulent. The condition that (ScRe)$^{1/2} >> 1$ insures that the Taylor layer thickness is small relative to the shear layer thickness. The need for the restriction Re $>> \ln Sc^2$ arises from the requirement that the homogenization time at the scale λ_k be small compared to δ/U. Batchelor[10] shows that local straining reduces λ_k to $\delta/(Re^{3/4} Sc^{1/2})$ in a time $(\delta/U)(1/Re^{1/2})\ln Sc$. Then since the time for diffusion across the reduced scale is only $(\delta/U)/Re^{1/2}$. the larger time $(1/Re^{1/2})\ln Sc$ is controlling and is the restriction given relative to Eq. (1). For ordinary substances. the requirement for turbulent flow. Re $>> 1$. automatically satisfies Re $>> \ln Sc^2$.

In the shear layer. the strained flames or Taylor

layers will be considered to be stagnation point flows formed between the two free streams. When the reaction is simple and fast, an exact solution is available in the reference just mentioned. Complex reactions with finite rates must be treated numerically as is done, for instance, in Dixon-Lewis et al.[12] The exact solution and an approximate integral treatment for a special case are described in a following section.

While large scale unsteadiness is an inherent feature of the flows being considered, the model attempts to deal only with their averaged consequences.

It is seen that this picture of the flow, and the model derived from it, describe the two essential experimental features discussed above. In the limit $ScRe \rightarrow \infty$, a condition that the water experiments appear to meet, the delay after the freestream fluids enter the layer, before mixing takes place, together with the large-scale vortical motion explains the uniform lateral mixed fluid composition. At lower values of $ScRe$, as in the gas experiments, the strained laminar layers account both for the larger amount of product than in liquids and for the slight lateral variations in the mixed fluid composition.

The Chemical Reactions

The picture developed above will be used first for a discussion of the H_2-F_2 reaction in the shear layer discussed above. Mungal and Dimotakis,[13] and the subsequent one, Mungal and Frieler,[2] in which the chemical rate coefficient was varied.

The reaction takes place between H_2 and nitric oxide, NO, carried in one nitrogen stream and F_2 in the other. In most of the experiments the high and low speed velocities were 22 m/s and 8.8 m/s, but several runs were made at 44 m/s and 17.6 m/s. In the part of the experimental results to be discussed here, the H_2 concentration was varied between one and eight percent molar and was in the high speed stream, the F_2 concentration was one percent molar, and that of the NO (needed to initiate the reaction) varies between 0 and 0.03 percent molar. With these concentrations, the mean temperature rise is only about 100° K so that the density change is small and the fluid mechanics is little influenced.

The important reactions are:

$$F + H_2 \xrightarrow{k_1} HF + H \qquad (2)$$

$$F_2 + H \xrightarrow{k_2} HF + F \qquad (3)$$

$$F_2 + NO \xrightarrow{k_3} NOF + F \qquad (4)$$
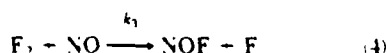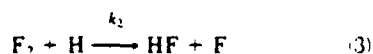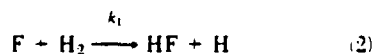
described by the equations:

$$\frac{d[H_2]}{dt} = -k_1[F][H_2]$$

$$\frac{d[F_2]}{dt} = -k_2[F_2][H] - k_3[NO][F_2]$$

$$\frac{d[NO]}{dt} = -k_3[F_2][NO]$$

It was shown in Mungal and Frieler[2] that this kinetic system can be represented by a single reaction

$$H_2 + F_2 \xrightarrow{k} 2HF \qquad (5)$$

governed by the rate equation

$$\frac{d[HF]}{dt} = k[H_2][F_2] \qquad (6)$$

where k is a function of the initial nitric oxide concentration. $[NO]_i$.

Model Formulation

The picture of the motions postulated in the foregoing is illustrated schematically in Fig. 2. The v's are volume fluxes per unit length into the various states, with v_1 and v_2 the fluxes from the high and low speed stream into the layer. The entrainment ratio, $E(>1)$, is v_1/v_2 and it is determined by the free stream density and velocity ratios.[5] In this work, however, the former is taken to be unity, but the general ideas should apply to the more general case.

When the molecular diffusion coefficients of the constituents are equal, the flame sheets consist of equal volumes from the two free streams. The excess high speed fluid, therefore, becomes part of the homogeneous mixture, directly, only when the Kolmogorov scale is reached.

The homogeneous mixture volume flux increases with axial distance x by the addition of a volume flux per unit length, v_h, made up of the flame sheet flux, v_f, and of the flux directly from the high speed stream, v_d. It is easy to show that v_h is made up of v_d and v_f in the proportions

$$v_d = \frac{E - 1}{E + 1} v_h, \quad v_f = \frac{2}{E + 1} v_h.$$

In the present formulation, it is assumed as a simplification that the flame sheets are formed only between pure fluid from the two streams and, in addition, that their thickness is in equilibrium with the local large-scale strain. Furthermore, the ho-
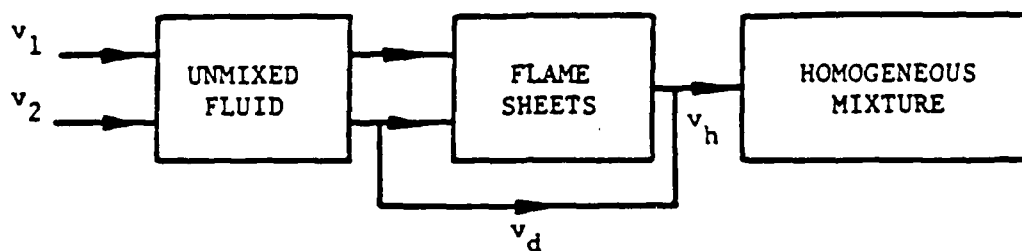
FIG. 2. Schematic diagram of shear layer mixing.

mogeneous mixture is taken to be at a single composition.

In the experiments under discussion, the amount of product in the shear layer is characterized by the "product thickness," δ_P, defined at a particular axial measuring station by

$$\delta_P = \int_{-\infty}^{\infty} \frac{C_P(y)}{C_x} dy$$

where C_P is the molar product concentration and C_x is the fluorine concentration in the low-speed stream. In accordance with the discussion above, the contributions of the flame sheets and the homogeneous mixture are considered separately as follows:

$$\delta_P = \int_{-\infty}^{\infty} \frac{C_P}{C_x} dy = \int_{-\infty}^{\infty} \frac{(C_P)_h}{C_x} \alpha(x,y) dy$$
$$+ \int_{-\infty}^{\infty} \frac{(C_P)_f}{C_x} \lambda_\tau \cdot S \, dy \quad (7)$$

where $(C_P)_h$ and $(C_P)_f$ denote the homogeneous mixture and *average* flame sheet product concentrations, in moles per unit volume of homogeneously mixed fluid and of flame sheet fluid, respectively. The fractional volume of the former is denoted by $\alpha(x,y)$ and that of the flame sheet by $\lambda_\tau \cdot S$, as discussed above.

As already noted, $(C_P)_h$ is independent of y at any x and $\alpha(x,y) = \alpha(\eta)$, where $\eta = y/\delta$ and δ is the shear layer thickness, here taken to be distance between the one percent of maximum of the product profiles. The homogeneous mixture term can, consequently, be written

$$\frac{(C_P)_h}{C_x} \delta \int_{-\infty}^{\infty} \alpha(\eta) d\eta.$$

Carrier et al.[11] show that $\lambda_\tau = a(D/\epsilon)^{1/2}$, where a is a constant of order one. As stated above, we take ϵ to be the large-scale strain. $\Delta U/\delta$ and as-

sume that λ_τ and $(C_P)_f$ are also independent of y at fixed x. Since S scales with $1/\delta$, we put $S = \beta(\eta)/\delta$ and write for the flame sheet term

$$\frac{(C_P)_f}{C_x} \lambda_\tau \int_{-\infty}^{\infty} \beta(\eta) d\eta = a \frac{(C_P)_f}{C_x} \left(\frac{D\delta}{\Delta U}\right)^{1/2} \int_{-\infty}^{\infty} \beta(\eta) d\eta$$
$$= \frac{a \cdot (C_P)_f}{C_x} \delta(ScRe)^{-1/2} \int_{-\infty}^{\infty} \beta(\eta) d\eta.$$

With these expressions, Eq. (7) becomes

$$\frac{\delta_P}{\delta} = A(C_P)_h/C_x + B(ScRe)^{-1/2}(C_P)_f/C_x \quad (8)$$

where $A = \int_{-\infty}^{\infty} \alpha(\eta) d\eta$ and $B = a\int_{-\infty}^{\infty} \beta(\eta) d\eta$ are the constants in Eq. (1).

Observe that A and B have to do only with the molecular mixing; all the chemical kinetic effects appear in $(C_P)_h$ and $(C_P)_f$. Strictly, A and B must be determined for each free stream velocity; it is likely, however, from the arguments leading to the model, that they are weak functions of these variables.

Consider first the application of Eq. (8) to shear layer reactions that are diffusion limited. Under these conditions, $(C_P)_h/C_x$ is easily determined for the H_2-F_2 reaction as follows. To specialize to the experimental situation, let the low speed stream reactant be one percent fluorine and the high speed stream carry various concentrations of hydrogen (together with sufficient nitric oxide to insure that the reaction is fast). Define the equivalence ratio, ϕ, as the ratio of the freestream concentration of fluorine to that of hydrogen, $\phi = (C_F)_x/(C_H)_x$. Now we use a result of Konrad[3] that the homogeneous mixture consists of E($=1.3$) parts high speed fluid and one part low speed. The fluorine will, therefore, be consumed completely when the hydrogen concentration in the mixture is such that $\phi \leq 1.3$. Calling 2HF the product, we have for $\phi \leq 1.3$.

$$(C_P)_h/C_x = 1/(E + 1) = 0.43.$$

As was mentioned above, when the reactions are fast and consist of a single step forward process as in the case here. the chemical reactions in the flame sheet can be treated exactly when the flame structure is in equilibrium with the strain. (See Carrier. et al.) The solution gives for the moles of product per unit flame sheet area. κ_P.

$$\kappa_P = (2/\pi)^{1/2}(\phi - 1)e^{-\Lambda^2}(D/\epsilon)^{1/2}C_x$$

$$= (2/\pi)^{1/2}(\phi + 1)e^{-\Lambda^2}C_x\delta/(ScRe)^{1/2} \quad (9)$$

where $\Lambda = \mathrm{erf}^{-1}(\phi - 1)/(\phi - 1)$. With the use of this expression and the result above. Eq. (8) becomes. for $\phi \leq 1.3$.

$$\frac{\delta_P}{\delta} = A/(E - 1)$$

$$+ B(2/\pi)^{1/2}(\phi + 1)e^{-\Lambda^2}/(ScRe)^{1/2}. \quad (10)$$

To proceed further. we need to determine A and B. The most straight-forward and accurate procedure is to use the measured δ_P/δ for $\phi = 1/8$ from the H_2-F_2 fast reaction experiment[13] under discussion and the corresponding value from the experiment in water.[6] We need not be concerned with the details of the latter experiment, needing only to note that it was for Re $= 2.3 \cdot 10^4$, $\phi = 1/10$ and Sc $= 600$. The H_2-F_2 experiment. for Re $= 6.6 \cdot 10^4$, Sc $= 0.70$ and $\phi = 1/8$ yielded $\delta_P/\delta = 0.24$ and the water experiment gave $\delta_P/\delta = 0.13$. (As will be pointed out later. the H_2-F_2 experiments were not quite at mixing limited conditions; consequently. Eq. (10) is only approximately applicable. To avoid complicating an already complex exposition. this inconsequential inconsistency will be ignored.)

These two results and two sets of conditions substituted into Eq. (10) give two equations from which it follows that $A = 0.28$ and $B = 54$. This result implies that in gases at this Reynolds number. the product is almost equally divided between the flame sheets and the homogeneous mixture. In water, on the other hand. the flame sheet contribution is negligible.

With A and B fixed. the model prediction of the effects of equivalence ratio and Reynolds and Schmidt numbers. can be compared with the experimental findings. When the reaction is fast. Eq. (10) as it stands can be applied. For slower reaction rates Eq. (8) must be used and $(C_P)_h/C_x$ and C_{Pf}/C_x in this equation determined. An approximate analysis of the flame sheet for arbitrary reaction rates is given in the next section. The homogeneous mixture. which can be treated exactly, is considered afterwards.

Approximate Analysis of Strained Flames

A two-dimensional strained flame is formed when two streams carrying reactants meet at a stagnation point as sketched in Fig. 3. Under our conditions. the overall conservation equation is

$$\frac{\partial u}{\partial x} + \frac{\partial v}{\partial y} = 0.$$

If v is a linear function of y.

$$v = -\epsilon y, \quad \frac{\partial u}{\partial x} = \epsilon. \quad (11)$$

When ϵ is constant and the reaction is fast relative to diffusion. the reaction takes place on a plane parallel to x and the exact solution of Carrier. et al.[11] is applicable.

When the reaction rate is finite, a boundary layer integral approach applied to the control volume indicated by dashed lines in Fig. 3 yields approximate results. (It would. perhaps. also be possible to use a perturbation procedure here.) To obtain a simple solution. we specialize from the beginning to small values of ϕ. the condition of the variable reaction rate experiment.[2] Further. only average values for the concentrations are considered. Note first that from Eqs. (11) $v(-\lambda_r/2) = \epsilon\lambda_r/2$ and $u = \epsilon\Delta x$. The conservation equations for H_2 and F_2 in the control volume are

$$-v(+\lambda_r/2)(C_H)_x\Delta x - k(C_F)_f(C_H)_f\lambda_r\Delta x$$

$$= (C_H)_f\epsilon\lambda_r\Delta x \quad (12)$$

$$v(-\lambda_r/2)(C_F)_x\Delta x - k(C_F)_f(C_H)_f\lambda_r\Delta x$$

$$= (C_F)_f\epsilon\lambda_r\Delta x \quad (13)$$

From Eq. (12).

$$(C_H)_f = \frac{1}{2}\frac{(C_H)_x}{\left[1 + \dfrac{k}{\epsilon}(C_F)_f\right]}$$

Putting this expression into Eqs. (12) and (13). and solving for $(C_F)_f$ in the limit $(C_F)_x \to 0$ (to approximate $(C_H)_x/(C_F)_x \gg 1$). we get

$$(C_F)_f = \frac{1}{2}\frac{(C_F)_x}{\left[1 + \dfrac{k(C_H)_x}{2\epsilon}\right]}, \quad (C_H)_f = \frac{(C_H)_x}{2}. \quad (14)$$
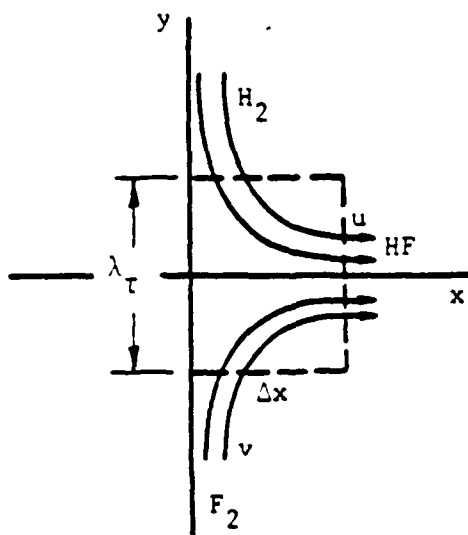
The product concentration. $(C_P)_f$. is given by

FIG. 3. Strained flame control volume.

$$,C_P)_f = \frac{k(C_H)_x}{4\epsilon} \frac{(C_F)_x}{\left[1 - \frac{k(C_H)_x}{2\epsilon}\right]} \qquad (15)$$

a result consistent with the requirement that $(C_P)_f + (C_F)_f = (C_F)_x/2$. To compare these results with the exact solution, note that the amount of product per unit flame sheet area, $\kappa_P = (C_P)_f \cdot \lambda_\tau$ is, from Eq. (15) with $k \to \infty$, given by

$$\kappa_P = (a/2)(C_F)_x(D/\epsilon)^{1/2}. \qquad (16)$$

while Eq. (9) is the exact solution. Thus the dependence on the parameter (D/ϵ) is the same in the two expressions, and with the constant, a, set equal to 6.8, the two expressions match.

For small k, Eq. (15) reduces to

$$(C_P)_f = \frac{(C_H)_x(C_F)_x}{4} (k/\epsilon) \qquad (17)$$

a result in agreement with the analysis of Norton.[14]

In summary, Eqs. (15) and (16) are approximations for all k for $(C_F)_x/(C_H)_x = \phi \ll 1$, while Eq. (9) is the exact solution for $k(C_H)_x/\epsilon \gg 1$ for all ϕ.

Analysis of the Homogeneous Mixture

In this section, expressions for the reactant and product concentrations in the homogeneous mixture are derived. The connection between v_h, the addition rate to the homogeneous mixture, and α.

the homogeneously mixed volume fraction, is derived first. The shear layer is considered to be fully developed so that $\delta = C_1 x$ and α and U are functions of $\eta = y/\delta$. Let $U = U g(\eta)$ where $U = (U_1 + U_2)/2$, then

$$v_h = \frac{d}{dx} \int_{-x}^{x} \alpha(\eta) U(\eta) dy = c_1 G U \qquad (18)$$

where

$$G = \int_{-x}^{x} \alpha(\eta) g(\eta) d\eta. \qquad (19)$$

When fluorine is carried in the low speed stream, no fluorine "enters" the homogeneous flux directly, it is homogenized only after becoming part of a flame sheet. The fluorine and hydrogen conservation equations for the homogeneous mixture are, under these conditions,

$$\frac{d}{dx} \int_{-x}^{x} (C_F)_h \alpha(\eta) U(\eta) dy$$
$$= - \int_{-x}^{x} k(C_H)_h(C_F)_h \alpha(\eta) dy - \frac{2(C_F)_f}{E-1} v_h \qquad (20)$$

$$\frac{d}{dx} \int_{-x}^{x} (C_H)_h \alpha(\eta) U(\eta) dy$$
$$= - \int_{-x}^{x} k(C_H)_h(C_F)_h \alpha(\eta) dy + \left[\frac{2}{E+1} (C_H)_f + \frac{(E-1)}{(E-1)} (C_H)_x\right] v_h \qquad (21)$$

Eq. (20) describes the change in the fluorine flux in the mixture, the l.h.s., caused by the consumption of F_2 in the chemical reaction, the first r.h.s. term, and the addition from the flame sheets, the last term. The same meanings apply to the first three terms in Eq. (21). The final term is the direct flux from the high speed stream into the homogeneous mixture. Using Eqs. (18) and (19), we find,

$$\frac{d}{dx}[\pi(C_F)_h] = \frac{-k(C_H)_h(C_F)_h x}{U} - \frac{2(C_F)_f}{(E-1)} \qquad (22)$$

$$\frac{d}{dx}[x(C_H)_h] = \frac{-k(C_H)_h(C_F)_h x}{U}$$
$$+ \left[\frac{2}{(E+1)} (C_H)_f + \frac{(E-1)}{(E-1)} (C_H)_x\right] \qquad (23)$$

in which the approximation

$$G = \int_{-\infty}^{\infty} \alpha(\eta) g(\eta) d\eta \cong \int_{-\infty}^{\infty} \alpha(\eta) d\eta$$

has been made. The approximation used in the flame sheet analysis. i.e., that the hydrogen depletion by chemical reaction can be neglected, is introduced next. With $(C_H)_f = (C_H)_\infty/2$, Eq. (23) yields

$$(C_H)_h = \frac{E}{(E+1)} (C_H)_\infty,$$ (24)

The hydrogen from the free stream is again simply diluted in the homogeneous mixture by the low speed free stream fluid. With this result, Eq. (22) becomes

$$\frac{d}{dx^*} [x^*(C_F)_h] = -\frac{E}{(E+1)} x^*(C_F)_h - \frac{2(C_F)_f}{(E+1)}$$ (25)

where $x^* = k(C_H)_\infty x / \bar{U}$.

Since $\epsilon = \Delta \bar{U}/\delta$, in which $\Delta \bar{U}$ is simply related to $\bar{U}$ and $\delta = c_1 x$ with $c_1 = 0.16$, Eq. (14) shows that $(C_F)_f$, also, is a function of x^* only. Eq. (25) can, therefore, be solved by standard methods to yield $(C_F)_h$ as a function of x^* and, since

$$(C_P)_h / C_\infty + (C_F)_h / C_\infty = 1/(E+1),$$ (26)

the variation of the product concentration at the (fixed x) measuring station with the reaction rate. Interestingly, the over-all solution is dependent only upon the Damköhler-like variable, x^*, which arises naturally in the analysis.

It is helpful to note that when $x/\bar{U}$ is replaced

by t in Eqs. (22) and (23), they become equations describing exactly the fluorine and hydrogen concentrations in a closed homogeneous i.e., well-stirred) reactor to which streams of flame sheet and freestream fluid are steadily added.

Model Comparison with Experiment

Consider the diffusion limited conditions first. Figure 4 shows a comparison of δ_P/δ from Eq. (10) with results from the H_2-F_2 gas experiment[13] and the water experiment.[6] The two solid symbols are the experimental points from which A and B were determined. A plot of this form is useful in that it shows clearly the nature of the model. Consider first the curve for Sc = 600, in which there is negligible contribution from the flame sheets. For a fixed low speed stream reactant concentration, say one percent, the amount of product rises linearly from zero with the high speed stream concentration. i.e., with $1/\phi$, to the value $1/E$ at which condition all the low speed reactant has been converted to product. Further increases in the high speed concentration have no effect. The dashed line, for gases. Sc = 0.70, comes from adding at each ϕ the flame sheet contribution to that of the homogeneous mixture, the solid line.

Consider next the effect of changing the reaction rate of the H_2-F_2 reaction. Recall that the rate coefficient can be varied simply by varying the initial NO concentration, leaving the fluid mechanics essentially unchanged. Some of the results and the model predictions (with the values of A and B already determined as described earlier) are given in Fig. 5. In the figure Da is defined as $k(C_H)_\infty x / \bar{U}$
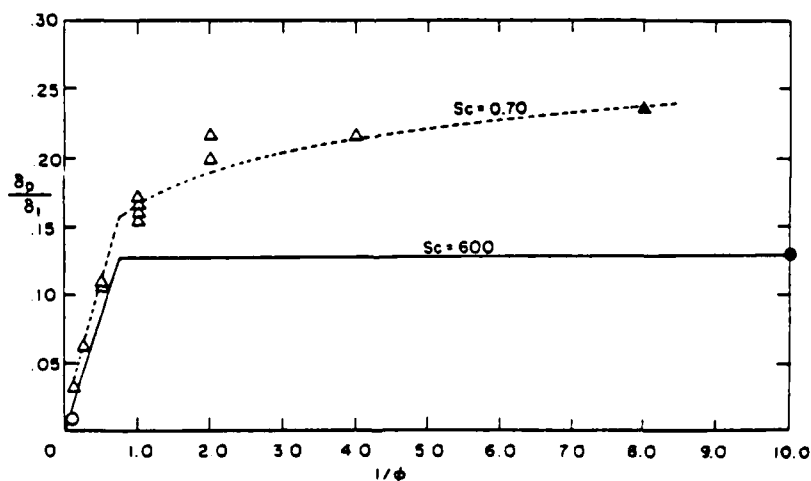

FIG. 4. Dependence of product thickness on equivalence ratio. Triangles are experimental results in gases. Mungal and Dimotakis;[13] circles are from experiments in water. Koochesfahani and Dimotakis.[6] Dashed and solid lines are the corresponding model predictions.
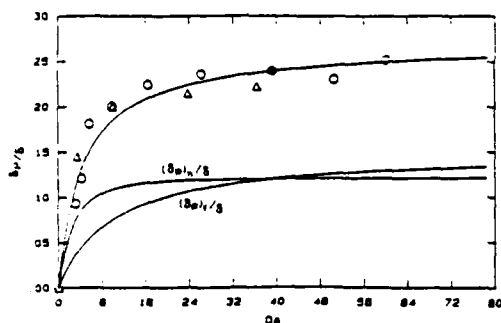
FIG. 5. Dependence in shear layer of product on Damköhler number. Da = $k(C_H)_\infty x/U$. δ_p, total product thickness, $(\delta_p)_f$, flame sheet product, $(\delta_p)_h$, homogeneous mixture product; δ, shear layer thickness. The symbols are experimental data from Mungal and Frieler[2] for two different velocities at the same velocity ratio.

where x the distance of the measuring station from the location of the turbulence transition (See Ref. 2 for details). The separate contributions of the flame sheets $(\delta_p)_f$ and the homogeneous zones $(\delta_p)_h$ are shown, with the latter seen to reach its limiting value more quickly.

It is useful next to discuss effects of the Reynolds number on the reaction because when Re is increased by increasing the velocities, there is an accompanying change in the Damköhler number. Figure 6 shows the theoretical product amount for several values of the gas reaction rate. the full lines, together with the measurements of Mungal, Hermanson and Dimotakis.[15] the circles. The solid symbols mark the same conditions as in Fig. 4. The curve marked $k/k^* = 1$ is to be compared with the
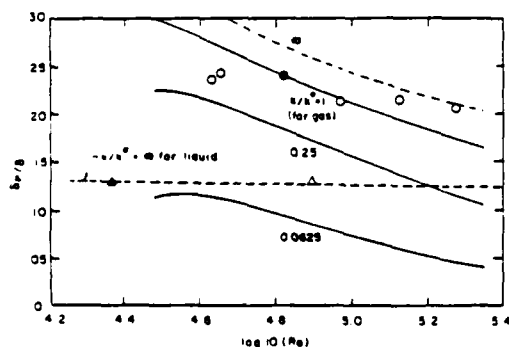
experimental H_2-F_2 values. That for infinite reaction rate, $k/k^* = \infty$, illustrates the effect of Reynolds number alone in gases compared to the dashed line for liquids. Data for a wider range of Reynolds number would, of course, be valuable.

Conclusions

It should be noted that the two constants in the model which must be determined from the experiment are fixed by results from two measurements with fast chemical reactions, one in gas and the other in water. They cannot, therefore, be adjusted to fit the data when the equivalence ratio, the Damköhler number, or the Reynolds numbers are varied. In its final form the model displays explicitly the effects on the overall reaction rate of changes in these parameters.

The results imply that when the Schmidt number is of order one, the Reynolds number influences the reaction rate to values of the Reynolds number at least as large as 10^6. In addition, the reaction rate becomes mixing limited at a Damköhler number of about 40, where Da is the ratio of the time of flight between the measuring station and the station at which the flow becomes turbulent and the effective reaction time.

Acknowledgments

Nomenclature

|	
A	average volume fraction of fluid mixed at λ_k.
B	constant, proportional to non-dimensional surface area per unit volume
C	molar concentration
D	molecular diffusion coefficient
E	entrainment ratio, v_1/v_2
k	overall reaction rate coefficient
Pe	Peclét number, $\Delta U\delta/D$
Re	Reynolds number, $\Delta U\delta/\nu$
S	flame sheet area per unit volume
Sc	Schmidt number.
U	mean streamwise velocity
ΔU	$(U_1 - U_2)$
U	$(U_1 + U_2)/2$
V_m	molecularly mixed fluid volume fraction
v	volume flux per unit length
x	streamwise coordinate
y	lateral coordinate

FIG. 6. Dependence of product thickness on Reynolds number and reaction rate in gas and liquids. Circles are experimental results in gas. Mungal. et al..[15] and triangles are results in water. Koochesfahani and Dimotakis.[4] Solid and dashed lines are the corresponding model predictions.

α fractional volume of homogeneous mixture
β $S \cdot \delta$
δ shear layer thickness
δ_P product thickness
ϵ strain rate, $\Delta U / \delta$
η y / δ
κ_P moles of product per unit flame sheet area
λ_κ Kolmogorov scale
λ_τ Taylor scale
ν viscosity
ϕ equivalence ratio, $(C_F)_\infty / (C_H)_\infty$

Subscripts

1 high speed stream
2 low speed stream
d directly from freestream
f flame sheet
F fluorine
h homogeneous mixture
H hydrogen
P product
∞ freestream

REFERENCES

1. Broadwell, J. E. and Breidenthal, R. E.: J. Fluid Mech. 25, 397 (1982).
2. Mungal, M. G. and Frieler, C. E.: Comb. Flame 71, 23 (1988).
3. Konrad, J. H.: An Experimental Investigation of Mixing in Two-Dimensional Turbulent Shear Flows with Applications to Diffusion-Limited Chemical Reactions. Ph.D. Thesis, California Institute of Technology, 1976; also available as Project SQUID Technical Report CIT-8-PU, December, 1976.
4. Breidenthal, R. E.: J. Fluid Mech. 109, 1 (1981).
5. Brown, G. L. and Roshko, A.: J. Fluid Mech. 64, 4 (1974).
6. Koochesfahani, M. M. and Dimotakis, P. E.: J. Fluid Mech. 170, 83 (1986).
7. Corcos, G. M. and Sherman, F. S.: J. Fluid Mech. 73, 241 (1976).
8. Corcos, G. M. and Lin, S. J.: J. Fluid Mech. 139, 67 (1984).
9. Lowery, P. S. and Reynolds, W. C.: Numerical simulation of a spatially-developing forced, plane mixing layer. Stanford University Department of Mechanical Engineering, Report No. TF-26, 1986.
10. Batchelor, G. K.: J. Fluid Mech. 5, 113 (1959).
11. Carrier, G. F., Fendell, F. E. and Marble, F. E.: SIAM J. Appl. Math. 28, 463 (1975).
12. Dixon-Lewis, G., David, T., Gaskell, P. H., Fukutani, F., Jinno, H., Miller, J. A., Kee, B. J., Smooke, M. D., Peters, N., Effelsberg, E., Warnatz, J. and Behrendt, F.: Twentieth Symposium (International) on Combustion, p. 1893. The Combustion Institute, 1985.
13. Mungal, M. G. and Dimotakis, P. E.: J. Fluid Mech. 148, 349 (1984).
14. Norton, O. P.: The Effects of a Vortex Field on Flames with Finite Reaction Rates. Ph.D. thesis, California Institute of Technology, 1983.
15. Mungal, M. G., Hermanson, J. E. and Dimotakis, P. E.: AIAA J. 23, 1418 (1985).

COMMENTS

J. C. Hermanson, United Technologies Research Center, USA. The analysis of Carrier et al., which was employed in representing the amount of product resident in the flame sheets, does not consider differential diffusion effects. For the case of unequal reactant diffusivities, the reactant consumption rate exhibits a different dependence on equivalence ratio than that for the case of equal reactant diffusivities. What impact would including this effect have on the correspondence between the proposed model and the H_2/F_2 reaction results shown in Fig. 4?

Author's Reply. Other approximations in the model are probably much more serious than the neglect of differential diffusion. The model as formulated, however, allows the treatment of diffusional processes of whatever complexity is appropriate. Numerical computation of the flame sheet would then be required, as would be the case, also, for complex chemical kinetic systems. We do not expect that the results in Figure 4 would change significantly if differential diffusion were considered.

Appendix F

DOWLING, D. R., LANG, D. B. and DIMOTAKIS, P. E. [1988] "An Improved Laser-Rayleigh Scattering Photodetection System", submitted to *Exp. in Fluids* .

An improved laser-Rayleigh scattering photodetection system

D. R. Dowling*, D. B. Lang and P. E. Dimotakis

Graduate Aeronautical Laboratories, California Institute of Technology, Pasadena, CA 91125, USA

Abstract. An improved photodetection system for high resolution laser-Rayleigh scattering measurements has been developed that utilizes a solid state detector coupled to a custom-designed, low-noise, transimpedance amplifier. The resulting system, based on a PIN photodiode is less expensive, inherently safer, less delicate and, depending on the detected light level, may exhibit higher signal-to-noise ratios than photodetection systems based on photomultiplier tubes. The frequency response of the system was designed to be uniform (3% peak variation) from DC to nearly 100 kHz. Concentration fluctuation spectra of a high scattering cross-section label (jet fluid) gas discharging into a density-matched, low scattering cross-section quiescent reservoir gas were measured using this system. Spectral signal-to-noise ratios as high as 7 decades were achieved under some conditions in parts of the spectrum.

1 Introduction

Laser-Rayleigh scattering is a well-established diagnostic for single-point, time- and space-resolved measurements of the mole fraction of a binary gas mixture in turbulent mixing flows (Graham et al. 1974; Dyer 1979; Pitts and Kashiwagi 1984; Niwa et al. 1984; Arcoumanis 1985; Pitts 1986, Haumann et al. 1987). It has also been used for two-dimensional imaging of the near field of turbulent jets (Escoda and Long 1983; Namazian et al. 1987), and for the measurement of temperature in reacting flows (Dibble and Hollenbach 1980). The diagnostic is nonintrusive and potentially capable of high spatial and temporal resolution. In most experimental configurations, the signal-to-noise ratio (SNR) of this technique is determined by the available laser power, the scattering cross-section (extinction coefficient) of the gas mixture under study, and the characteristics of the photodetection system. A detailed discussion of the technique is available in Pitts and Kashiwagi (1983). The relevant physical principles are documented in McCartney (1976) and Jackson (1975).

The single-point Rayleigh scattering studies referenced above relied on a photomultiplier tube (PMT) as the photo-detecting element. The shot noise of the photodetection process imposes an upper limit on the dynamic range of PMT measurements (Robben 1971). The effectiveness of the detection process is governed by the quantum efficiency of the photocathode of the photomultiplier tube, η_t (typically about 10% at optical wavelengths near 500 nm), and the stage gain of the photomultiplier tube, θ_t (Robben 1971; Pitts and Kashiwagi 1983). The relationship between η_t, θ_t and the SNR of a PMT system is given in Sect. 3. Other noise sources can usually be made insignificant compared to the photodetection noise by using the PMT at high gain, as we will discuss below.

We should recognize, however, that photomultiplier tubes are delicate instruments. They can be easily damaged by normal indoor lighting, and require special handling to prevent mechanical shocks and stresses (Engstrom 1980). They also require a relatively high operating voltage (~1kV); not an insignificant safety concern, especially in the presence of combustible gases. These considerations, plus the high quantum efficiencies available from silicon detectors prompted a study of alternative systems of Rayleigh scattering photodetection. In this paper, we describe the outcome of this study and, in particular, the resulting, improved photodetection scheme, which is based on a mechanically and optically rugged solid-state photodetector, requiring a low voltage (~15 V) supply. The detector, a PIN photodiode, has quantum efficiency, η_d, of nearly 70% at optical wavelenghts near 500 nm. The improved system utilizes a special, low-noise, wide-band transimpedance amplifier that amplifies the detected photocurrent to produce an output voltage of sufficient amplitude for subsequent processing. The noise limit for this system is a combination of the shot noise associated with the detected photocurrent, the thermal (Johnson) noise of the resistor that the detected photocurrent passes through, and the amplification noise of the transimpedance amplifier.

We note here, that the use of photodiodes to detect Mie scattered light is well developed in laser Doppler velocimetry (LDV) investigations. The discussion presented here shows that recent advances in the quality of both photodiodes and

* Present address: Boeing Aerospace, MS 8H-29, P.O.B. 3999, Seattle, WA 98144, USA

transimpedance amplifiers makes this combination a competitor of PMT photodetection in Rayleigh scattering studies, even though the effective optical cross section in the latter case is orders of magnitude lower than for Mie scattering, which is usually employed in LDV experiments.

The performance of the current system and a PMT system has been calculated and measured. The performance formulae for these calculations are described in Sects. 2 and 3. Comparisons and discussions of the predicted and measured performance of both systems are contained in Sect. 4. The conclusions are presented in Sect. 5.

2 The transimpedance amplifier

Relative to a PMT, the main disadvantage of a PIN photodiode is that it has no internal amplification. Consequently, it is necessary to use a very low noise electronic amplifier to amplify the photoelectrically induced signal current. Conversely, for the PIN photodiode system to be a competitive replacement for a PMT system, the electronic amplifier noise must not be such as to offset the quantum efficiency advantage it enjoys relative to a PMT.

Figure 1 shows block diagrams for both a conventional amplifier and a transimpedance amplifier. The spectral noise current for both amplifier circuits is given by the equation

$$i_n^2(f) = 2 q_e (I_S + I_L) + i_a^2 + e_a^2 \left[\frac{1}{R_L^2} + (2\pi f C)^2 \right] + \frac{4 k_B T}{R_L}. \quad (1)$$

In this expression, f is the frequency (in Hz), $q_e = 1.602 \times 10^{-19} C$ is the charge of an electron, I_S is the photoelectrically induced signal current, I_L is the leakage current of the photodiode, i_a is the amplifier input noise current (in

Transimpedance Amplifier

Conventional Amplifier

Fig. 1. Photodiode amplifiers

$A \sqrt{Hz}$). e_a is the equivalent input noise voltage of the amplifier (in $V \sqrt{Hz}$), and R_L is the load resistance through which I_S passes. The capitance C is the total capacitance of the photodiode, amplifier input, and load resistor. $k_B = 1.38 \times 10^{-23} J \cdot K$ is Boltzmann's constant, and T is the absolute temperature in Kelvin. The first term in Eq. (1) is the photodiode shot noise term, the second term is the amplifier input noise current term (including amplifier shot noise), the third is the amplifier input voltage noise term, and the last term is the thermal Johnson noise term (see also Lang 1985, Appendix D).

To minimize the thermal (Johnson) noise term, R_L was chosen to be as large as possible (100 MΩ). This value gives a thermal noise term of 0.013 pA $\sqrt{Hz}$. For a conventional amplifier, the amplifier bandwidth is given by $\Delta f \approx (2\pi R_L C)^{-1}$ Hz. Unfortunately, even if the total capacitance C is as low as 20 pF, this value of R_L gives a bandwidth of $\Delta f \approx 80$ Hz! A transimpedance amplifier, on the other hand, has a bandwidth of $\Delta f \approx G_a (2\pi R_L C)$, where G_a is the (absolute value of) the transimpedance amplifier gain. Accordingly, a gain of $G_a \approx 1,200$ is needed for 100 kHz bandwidth.

Note that the e_a^2 term in Eq. (1) is multiplied by $(2\pi f C)^2$, a factor proportional to f^2. If the amplifier input noise voltage is not to be a limiting factor, the product $(2\pi f C) e_a$ must be less than $\sqrt{4 k_B T R_L}$. At a frequency of 100 kHz, this gives a target upper bound for the amplifier equivalent input noise voltage of $e_a < 1.0$ nV $\sqrt{Hz}$. Combined with the previous result, this imposes the simultaneous requirements:

$e_a < 1.0$ nV $\sqrt{Hz}$ and $i_a < 0.013$ pA $\sqrt{Hz}$.

To minimize the contributions of e_a and i_a in Eq. (1), a discrete Junction Field Effect Transistor (JFET) was used in the input stage of the transimpedance amplifier, along with a special compensation circuit that gives it the DC stability of monolithic JFET op-amps. The values of e_a and i_a achieved thereby were 2.5 nV $\sqrt{Hz}$ and 0.002 pA $\sqrt{Hz}$, respectively. Note that the higher value of e_a will cause an increase in the amplifier noise above 30 kHz. Nevertheless, this is still appreciably lower than the 12 nV $\sqrt{Hz}$ input noise voltage presently available from the best monolithic JFET op-amps.

Figure 2 shows the measured frequency response of the photodiode transimpedance amplifier system. These measurements were made by illuminating the photodiode with a red light-emitting-diode (LED), driven by a sinusoidal voltage plus a DC offset. The amplitude of the system response was then recorded as the LED driving frequency was swept from 10 Hz to 10^6 Hz. The frequency at which the response of the photodiode transimpedance amplifier system fell to ~0.70 of its pass-band response level was about 130 kHz.

3 Performance equations

For experimental measurements of electrical currents, the SNR can be expressed as the ratio of the signal current, I_S,
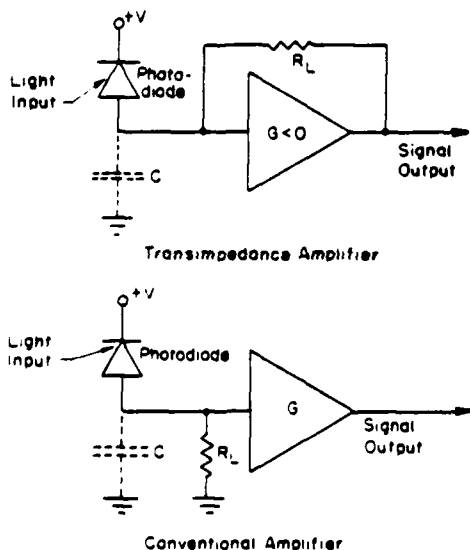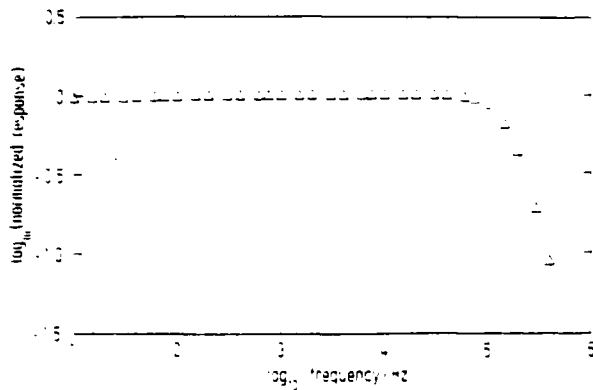
Fig. 2. Measured frequency response of the photodiode system

to the root mean square (rms) of the current fluctuations that arise from noise sources. i_{rms}, i.e.

$$SNR = 20 \log_{10}\left(\frac{I_s}{i_{rms}}\right).$$ (2)

The root mean square of the noise current is, in turn, expressible as the integral over the spectral noise current $i_n^2(f)$, i.e.

$$i_{rms}^2 = \int_0^r |H(f)|^2 i_n^2(f)df \approx \int_0^{\Delta f} i_n^2(f)df,$$ (3)

where $H(f)$ is the transfer function of the signal processing system, and Δf is the effective bandwidth (Hz), as implicitly defined in this equation.

For laser-Rayleigh scattering measurements, the average signal current I_s can be estimated for either photodetection system from the relation

$$I_s = q_e \frac{\eta_Q P_L}{E_{ph}} x_T \Delta y \eta_c.$$ (4)

In this expression, q_e is the charge of an electron, η_Q is the quantum efficiency of the photodetector, P_L is the power of the laser beam, E_{ph} is the average photon energy, and x_T is the total Rayleigh scattering extinction coefficient of the gas mixture. The quantity Δy is the effective length of the laser beam segment which is imaged onto the photodetector, and η_c is the optical collection efficiency of the detection optics, i.e. the fraction of total light scattered along Δy that is collected on the detector.

For a pure gas, the Rayleigh scattering extinction coefficient x is given by (e.g. Jackson 1975):

$$x = \frac{2 k^4}{3 \pi N} (n-1)^2.$$ (5)

where $k = 2\pi / \lambda$ is the wave number of the laser radiation of wavelength λ, n is the index of refraction of the gas, and N is the number density of the gas molecules. For a binary gas mixture, the total extinction coefficient is just the number-

weighted sum of the corresponding pure gas extinction coefficients, i.e.

$$x_T = x_1 X - x_2(1 - X),$$ (6)

where X is the mole fraction of the gas whose extinction coefficient is given by x_1, and x_2 is the extinction coefficient of other gas. At constant temperature and pressure, Eqs. (4) and (6) combine to make I_s a linear function of X, which is the basic utility of the laser-Rayleigh scattering diagnostic.

For the PMT system, a transimpedance amplifier with a FET input op-amp (LF 356) was used to bring the output signal current $I_{out} = G_t I_s$ to useable levels, where (for a k-stage PNT modeled with a gain of θ_t per stage) $G_t = \theta_t^k$ denotes the overall gain of the photomultiplier tube. For this photodetection system, the noise current spectrum (referenced to the PMT input) $i_n^2(f)$ was calculated from the relation

$$i_n^2(f) = 2 q_e M_t I_s + \frac{1}{G_t}\left\{i_a^2 + e_a^2\left[\frac{1}{R_L^2} + (2\pi Cf)^2\right] + \frac{4 k_B T}{R_L}\right\}.$$ (7a)

The first term is the photodetection shot noise term. This includes the PMT multiplication noise M_t, which can be approximated by (e.g. Engstrom 1980)

$$M_t \approx \frac{1 - 1 \theta_t^{k-1}}{1 - 1 \theta_t} = 1 + \frac{1}{\theta_t} + \frac{1}{\theta_t^2} + \dots + \frac{1}{\theta_t^k}.$$ (7b)

The terms inside the braces play the same role as the corresponding terms in Eq. (1).

4 Results and discussion

To measure the performance of the photodetection systems, some simple experiments were performed in a sealed test cell that could be filled with a pure gas. A laser beam was focused to a waist inside the test cell and the Rayleigh-scattered light from a small segment of the beam was imaged one-to-one onto the photodetector of the system that was being tested. A diagram of this setup is shown in Fig. 3. The signal from the photodetection system was digitized with a 12-bit, A D converter controlled by a computer data acquisition system based on a (DEC) LSI 11 73 CPU. The digitization rate was 180 kHz. The analog signal was low-pass (analog) filtered with a 3-pole, Butterworth filter prior to digitization. The "knee frequency" of this filter was set to 90 kHz, in accordance with the Nyquist criterion.

The performance of the photodiode system and of a PMT system was measured under the same conditions and compared to each other and to the expected results [Eqs. (1), (4) and (7)]. The laser was a CR-10 argon-ion system with a new Innova plasma tube, run at all the available lines to produce a 21 W beam. The 2%-98% beam width near the waist was measured to be 120 ± 10 μm. The collection optics had an f number of about 2.5.
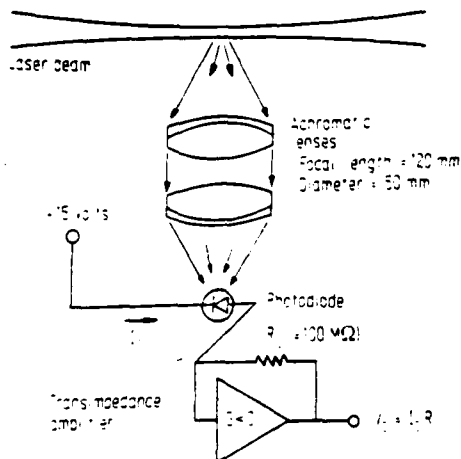
Fig. 3. Collection optics and photosensor

Fig. 4. Computed and measured signal current I_s vs. laser power P_L

For the measurements described below, the PMT used was an RCA # 8645 with an aperture limit provided by a precision 200 μm pinhole. The photodiode provided its own aperture limit, possessing a sensitive-area diameter that was also 200 μm (United Detector Technologies # PIN-HS008). The scattering medium was pure argon gas at room temperature and 1 atm pressure. Figure 4 is a plot of the signal current I_s vs. laser power P_L for the photodiode system under the conditions described above. Small deviations from perfect linearity are within the error produced by the slight imprecision of the power meter used to monitor the laser beam intensity. The predicted line, which is about 15% higher than the measurements, was computed from Eq. (4) with $\eta_Q = 0.65$. $E_{ph} = 3.97 \times 10^{-19}$ J. $\Delta y = 200$ μm. $z = 1.45 \times 10^{-5}$ m. and $\eta_c = 0.0092$. The 15% discrepancy is most likely the result of a slight overestimation of the collection efficiency η_c.

Figure 5 is a plot of the predicted and measured curves of $i_n^2(f) I_s^2$ for the PMT and photodiode systems. The predicted curve for the photodiode system was computed using Eq. (1) and the measured value of I_s at $P_L = 21$ W, corresponding to a signal current of $I_s = 127$ pA. The other parameters in Eq. (1) were taken from the manufacturer's data sheets, looked up, or measured. The numerical values are: $I_L = 20$ pA. $i_a = 0.002$ pA $\sqrt{Hz}$. $e_a \approx 2.5$ nV/$\sqrt{Hz}$. $R_L = 100$ MΩ. $C = 20$ pF and $T = 300$ K. We note that with these values, the Johnson noise term in Eq. (1) accounts for about three quarters of the total spectral noise current for $f < 10$ kHz.

The predicted curve of $i_n^2(f) I_s^2$ for the PMT system was computed from Eq. (7) with I_s taken to be a factor of 7.22 ($= \eta_d \eta_t$) less than the measured value of I_s for the photodiode system. The PMT had an S-20 spectral response, a quantum efficiency of $\eta_t \approx 0.09$ at 500 nm. and 10 amplification stages. The precise value of I_s from the PMT system could not be determined because G_t was not accurately known and the measurements yielded the product $I_s G_t$.
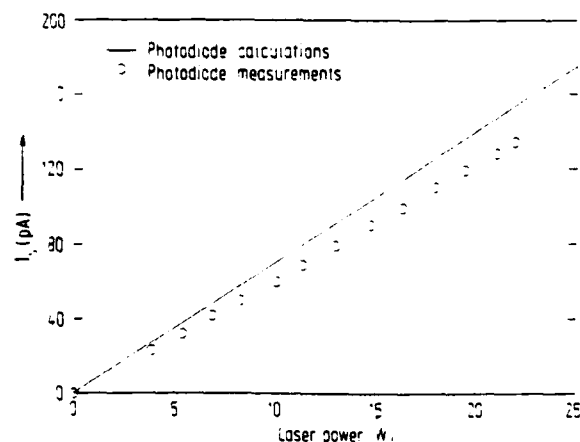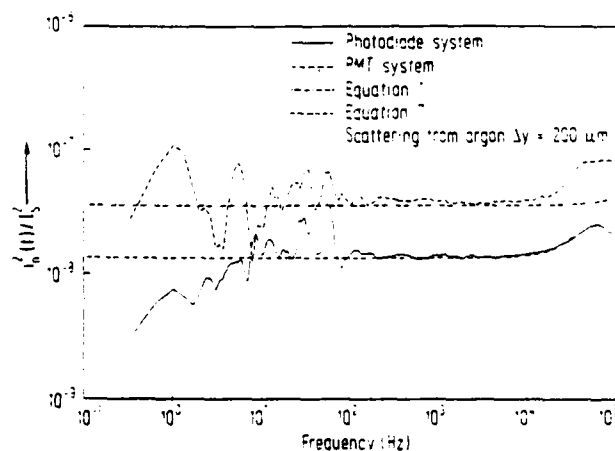
Fig. 5. Predicted and measured estimates of $i_n^2(f) I_s^2$

When G_t was "back calculated" from the estimate of I_s (≈ 18 pA) obtained from the photodiode measurement. a value of $G_t \approx 10^4$ was obtained. The stage gain of the PMT was then estimated to be about 2.5. The other numerical values used in Eq. (7) were: $i_a = 0.01$ pA/$\sqrt{Hz}$. $e_a = 15$ nV/$\sqrt{Hz}$. $R_L = 1.0$ MΩ. $C \approx 15$ pF. and $T = 300$ K. Under these conditions, the calculated value of the first term in Eq. (7) accounts for 85% of the spectral noise current for $f < 100$ kHz.

The measured spectra in Fig. 5 were each computed from 2^{19} ($> 500,000$) individual measurements and smoothed by convolving with a one-tenth decade (≈ 1 3-octave) averaging filter for plotting. The overall normalization of each spectrum is given by Eq. (3). Neither spectrum can be considered reliable below 1 or 2 Hz because of insufficient statistical confidence at those frequencies. The peaks in both spectra at 30 Hz are probably attributable to the current regulator of the CR-10 laser system. The peaks at 60 Hz come from the laboratory electrical environment. Details of

the spectral estimation algorithm are discussed in Dowling (1988).

As can be seen, there is good agreement between the calculated and measured values of $i_n^2(f)/I_S^2$. The only real discrepancy shows up in the PMT results where the measured spectrum turns up at a lower frequency than the one calculated. This disagreement is acceptable since the estimate of the effective capacitance C for the PMT system could have been in error by a large factor. The "roll-off" in the measured spectra at the highest frequencies is the result of the 3-pole Butterworth analog pre-filter.

The most important result of the data in Fig. 5 is that the normalized noise spectrum from the photodiode system is more than a factor of two lower than that of the PMT system, even at the low signal levels derived from argon scattering. This can be important in sensitive measurements that require the highest SNR since:

$$\text{SNR} = -10 \log_{10}\left(\int_0^{\Delta f} \frac{i_n^2(f)}{I_S^2} df \right). \tag{8}$$

Because the difference in $i_n^2(f)/I_S^2$ between the two systems depends on the magnitude of I_S, it is possible to estimate the value of I_S where the two noise-to-signal ratios are matched, i.e.

$$\left[\frac{i_n^2(f)}{I_S^2} \right]_{PMT} = \left[\frac{i_n^2(f)}{I_S^2} \right]_{diode}. \tag{9}$$

from Eqs. (1) and (7). Using only the shot and Johnson noise terms of Eq. (1), the first term of Eq. (7), and the same parameter estimates used in the computations for Fig. (5), the value of the photodiode system current that satisfies the conditions in Eq. (9) is about $I_S \approx 50$ pA. Above this value of I_S, the photodiode system will have superior performance when compared to an optimal, i.e. shot-noise-limited, PMT system with a stage gain of $\theta_t = 2.5$.

The preceding discussion implies that the present photodetection scheme should provide superior SNR performance for values of the laser power much less than 20 W. In particular, using Eq. (4) with $\eta_c = 0.0078$ (the measured value), 8.3 W of laser power and a imaged segment of $\Delta y = 200$ μm are required for a photodiode system yield of $I_S \approx 50$ pA. If lower spatial resolution is acceptable, e.g. $\Delta y = 1$ mm, the photodiode system will be superior at 1.65 W (or more) of laser power. We should note that these calculations were based on the estimated performance of both systems assuming pure agon as the Rayleigh scattering gas: a relatively poor Rayleigh scatterer. In many situations where this diagnostic is applied, the total extinction coefficient x_T will typically be higher, resulting in a yet lower "cross-over" laser power where the photodiode system is the one of choice, or, for a fixed laser power, in a higher SNR for the photodiode system.

Finally, we recognize that while the performance of the PMT system could be improved by increasing the stage gain

θ_t, a factor as small as 1.3 would result in an average PMT output current far larger than the optimum recommended by the manufacturer for this particular unit. The RCA # 8645 was chosen for comparison with the present system because it has good spectral response at optical wavelengths near 500 nm, and it can be used at current gains which might be considered low for many PMT applications. In fact, one of the main reasons that the present detection system fairs so well against the PMT is that the signal current levels of this study are really too large for optimal operation of a PMT. Hence, one important conclusion of the present discussion is the location of the "cross-over" signal current level between the competing photodetection technologies, namely, $I_S \sim 50$ pA.

Even considering these factors, the present system has the added advantage of flexibility, which allows it to be tailored to the characteristics of the photosignal to be measured. For example, the "flat" noise level seen in Fig. 5 could be lowered further by using a larger load resistor and or cooling it. The location of the "turn-up" point of the spectral noise current could be pushed to higher frequencies by a lower value of the input capacitance C, perhaps obtainable from a different input JFET. The width of the uniform portion of the system, pass-band can be adjusted, within the feedback loop stability limits, by changing G_a, C or R_L.

The present system has been succesfully used for the measurement of the time- and space-resolved mole fraction in the mixing region of a round turbulent jet at a Reynolds number of 16,000. Figure 6 is a plot of the power spectrum of the mole fraction fluctuations measured at a point located 30 jet-exit diameters downstream of the nozzle exit ($z d = 30$), and halfway between the centerline and the edge of the jet. The mean mole fraction of the jet fluid (propylene) at this location was about $\bar{X} = 0.063$. The horizontal portion of the unfiltered spectrum at high frequencies is the noise level of the new detection system. Mie scattering from dust parti-
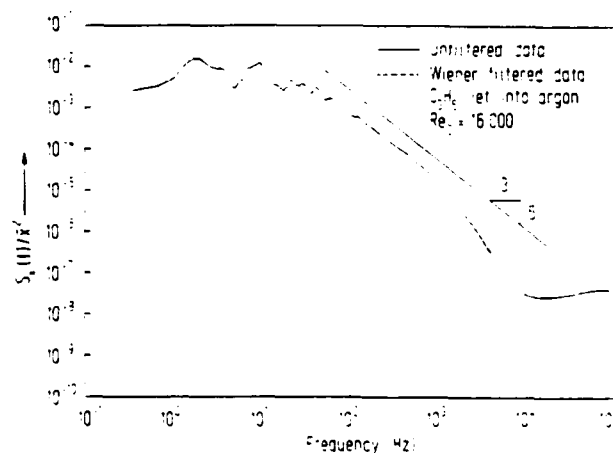

Fig. 6. Mole fraction power spectra of $X(t)$ and the Wiener-filtered mole fraction $\hat{X}(t)$
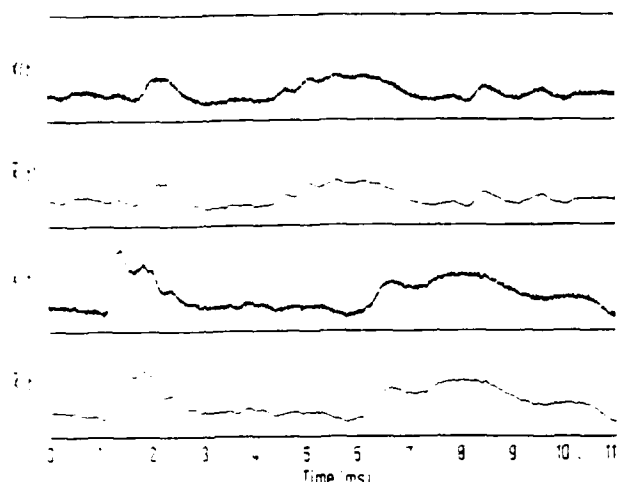
Fig. 7. Unfiltered jet fluid mole fraction $X(t)$ and Wiener-filtered $\hat{X}(t)$ record samples

cles was removed from the sampled data with a matched-filter detection scheme, and some simple interpolation software (see Dowling 1988, Appendix E, for aditional details).

The high signal-to-noise ratio and the form of the noise spectrum lend themselves to further processing of these data using (optimal) Wiener (1949) filtering. This, in effect, further improves the dynamic range of these measurements beyond the 6 orders of magnitude seen for the unfiltered data in Fig. 7. Sample time histories of the mole fraction measurements $X(t)$, and the corresponding Wiener-filtered time trace $\hat{X}(t)$ are depicted in Fig. 7. The spectrum of the Wiener-filtered mole fraction records appears as the dashed line curve in Fig. 6. Further details of the turbulent jet data are discussed in Dowling (1988) and Dowling and Dimotakis (1988).

5 Conclusions

It has long been appreciated that at relatively high detection levels solid state photodetectors can yield improved signal-to-noise characteristics. Our calculations and measurements of performance demonstrate, however, that it is possible to substantially improve on the SNR obtainable from a "shot-noise-limited". PMT-based photodetection system even at light levels derived from laser-Rayleigh scattering by a gas at atmospheric pressure. This can be realized with a high quantum efficiency, solid-state photodetector coupled to a well-designed, matched transimpedance amplification system. The improved photodetection system is also safer and perhaps easier to use than conventional PMT-based systems because it is mechanically and optically rugged, less expen-

sive, less delicate, and does not require a high operating voltage.

References

Arcoumanis. C. 1985: A laser Rayleigh scattering system for scalar transport studies. Exp. Fluids 3. 103–108

Dibble. R. W.; Hollenbach. R. E. 1980: Laser Rayleigh thermometry in turbulent flames. In: 18th Int. Symp. Combustion. pp. 1489–1499. The Combustion Institute

Dowling. D. R. 1988: Mixing in gas phase turbulent jets. Ph. D. Thesis. California Institute of Technology

Dowling. D. R.; Dimotakis. P. E. 1988: On mixing and structure of the concentration field of turbulent Jets. In: Proc. 1st Nat. Fluid Dyn. Cong. Vol. 2. pp. 982–988 Cincinatti: A.I.AA.

Dyer. T. M. 1979: Rayleigh scattering measurements of time-resolved concentration in a turbulent propane jet. AIAA J. 17. 912–914

Engstrom. R. W. 1980: Photomultiplier handbook. Lancaster: RCA Corporation

Escoda. M. C.; Long. M. B. 1983: Rayleigh scattering mesurements of the gas concentration field in turbulent jet. AIAA J. 21. 81–84

Graham. A. J.; Grant. A. J.; Jones. J. M. 1974: Transient molecular concentration measurements in turbulent flows using Rayleigh light scattering. AIAA J. 21. 1140–1142

Haumann. J.; Wu. G.; Leipertz. A. 1987: Low power laser Rayleigh probe for mixing studies. Exp. Fluids 5. 230–234

Jackson. J. D. 1975: Classical electrodynamics 2nd edn. New York: Wiley

Lang. D. B. 1985: Laser doppler velocity and vorticity measurements in turbulent shear layers. Ph. D. Thesis. California Institute of Technology

McCartney. E. J. 1976: Optics of the atmosphere. New York: Wiley

Namazian. M.; Schefer. R. W.; Kelly. J. 1987: Sandia Report No. SAND 87-8652 Comb. Flame (in press)

Niwa. C.; Ichizawa. J.; Yoshikawa. N.; Ohtake. K. 1984: Time-resolved concentration measurements of jets by laser Rayleigh method. In: Proc. 14th Int. Symp. Space Technology Science. pp. 469–476. Tokyo

Pitts. W. M. 1986: Effects of global density and Reynolds number variations on mixing in turbulent axisymmetric jets. NBS Report No. NBSIR 86-3340

Pitts. W. M.; Kashiwagi. T. 1983: The application of laser-induced Rayleigh light scattering to the study of turbulent mixing. NBSIR 83-2641

Pitts. W. M.; Kashiwagi. T. 1984: The application of laser-induced Rayleigh light scattering to the study of turbulent mixing. J. Fluid Mech. 141. 391–429

Robben. F. 1971: Noise in the measurement of light with photomultipliers. Appl. Optics 10. 776–796

Wiener. N. 1949: Extrapolation. interpolation and smoothing of stationary time series. New York: Wiley